Air Force Institute of Technology

AFIT Scholar

3-2020

Neutron Energy Effects on Asteroid Deflection

Lansing S. Horan IV

Follow this and additional works at: https://scholar.afit.edu/etd

Part of the Nuclear Engineering Commons, and the Other Astrophysics and Astronomy Commons

Neutron Energy Effects on Asteroid Deflection

THESIS

Lansing S. Horan IV, Civilian

AFIT-ENP-MS-20-M-101

DEPARTMENT OF THE AIR FORCE
AIR UNIVERSITY

AIR FORCE INSTITUTE OF TECHNOLOGY

Wright-Patterson Air Force Base, Ohio

DISTRIBUTION STATEMENT A
APPROVED FOR PUBLIC RELEASE; DISTRIBUTION UNLIMITED

The views expressed in this document are those of the author and do not reflect the official policy or position of the United States Air Force, the United States Department of Defense or the United States Government. This material is declared a work of the U.S. Government and is not subject to copyright protection in the United States.

Neutron Energy Effects on Asteroid Deflection

THESIS

Presented to the Faculty

Department of Engineering Physics

Graduate School of Engineering and Management

Air Force Institute of Technology

Air University

Air Education and Training Command

in Partial Fulfillment of the Requirements for the

Degree of Master of Science

Lansing S. Horan IV, BS

Civilian

March 2020

Neutron Energy Effects on Asteroid Deflection

THESIS

Lansing S. Horan IV, BS
Civilian

Committee Membership:

Dr. Darren E. Holland
Chair

Dr. Megan B. Syal
Member

Maj James E. Bevins, Ph.D.
Member

Dr. John W. McClory
Member

Abstract

In the future, a hazardous asteroid will find itself on a collision course with Earth. It is an inevitability; the question is not if, but when. For asteroids of moderate size or larger, a nuclear device is one of humanity's only technologies capable of mitigating this threat via deflection on a timescale of less than a decade. This work examined how changing the output neutron energy from a nuclear device detonation affects asteroid deflection. The notional asteroid target was 300 meters in diameter and composed of silicon dioxide at a bulk density of 1.855 g/cm^3.

To calculate the energy deposition in the asteroid that results from a neutron source, the Monte Carlo radiation-transport code, MCNP6.2, was applied. MCNP6.2 simulations were performed for neutrons of various energies radiating towards the asteroid surface. The neutron energy was found to have an impact in terms of 1) the energy deposition spatial profile, and 2) the energy coupling efficiency.

To model the mechanical response of the asteroid due to a spatially-varying energy deposition, the hydrodynamics code, ALE3D, was employed. The energy deposition outputs from MCNP6.2 served as inputs into the model representation of the asteroid in ALE3D. The momentum impulse imparted onto the asteroid body due to rapidly-evolving melted and/or vaporized blow-off ejecta was quantified.

From this, the asteroid velocity change, or δV, was determined for two different neutron yields (50 kt and 1 Mt) and for two different source neutron energies (14.1 MeV from fusion and 1 MeV from fission). Underexplored in literature, the distribution of deposited energy and the energy coupling were both found to affect the asteroid deflection. The magnitude of energy deposition, as determined by the neutron energy and the coupling, generally appears to be the more significant factor.

Acknowledgements

There are many people to thank and acknowledge, yet not enough space to do so adequately. First, my research advisor, Dr. Darren Holland of AFIT, for spending approximately 8,000,000 hours in discussions throughout my research process, and for providing useful help and feedback. Also, my three other committee members, for various insights and for their willingness and/or reluctance to read through this thesis. Dr. Megan Syal of LLNL, who is the LLNL planetary defense team lead, especially for providing subject-matter expertise on asteroid deflection. Maj James Bevins of AFIT, especially for first informing me of this thesis topic as an available option. Dr. John McClory of AFIT, especially for working to admit me, a lowly civilian, into AFIT. Additionally, Dr. Joseph Wasem of LLNL, who also works with their planetary defense group, for further feedback and expertise.

My instructors from my undergraduate degree from Texas A&M University, for preparing me well for graduate school, and also my instructors here at AFIT, for pummeling us with such an excessive amount of work that the quantity itself was previously thought by scientists to be impossibly and unacheivably large. Uh, what I meant was, for providing a rigorous, yet worthwhile, set of courses.

The developers of ALE3D, especially Andy Anderson, Albert Nichols III, and Chad Noble, for hosting the ALE3D Introductory Class at LLNL, and for their extended support in answering my onslaught of emails with various questions.

My peers at AFIT, for making the school experience much more interesting, and also for their help and collaboration with various homeworks, projects, and exams. Erm, I mean, not the exams. No, there was no collaboration on exams, of course.[1]

My parents, for their continuous love and support.

---

[1] I'd like to make it abundantly clear that this is definitely a joke, and that I know of zero violations of academic conduct by me or anyone else at AFIT. Please don't court-martial anybody.

Last, but obviously not least, I owe this all to God, the Creator of the universe, and the most accomplished Nuclear Engineer of all time and for all time.

Lansing S. Horan IV

Table of Contents

List of Figures

List of Tables

Neutron Energy Effects on Asteroid Deflection

I. Introduction

1.1 Motivation

In May 2012, a previously-unseen asteroid roughly 100 to 300 meters in diameter was spotted. Estimates placed a less-than-1% chance of it colliding with Earth in April 2020. Over the next several months, however, the probability increased to 10%, and eventually 100%, a certainty. The question of collision was no longer if, but where. If the point of impact ended up in a remote area or over an expanse of ocean, then mitigation might not be necessary.

Various organizations — including the National Aeronautics and Space Administration (NASA), Department of Defense (DoD), State Department, European Space Agency, International Asteroid Warning Network (IAWN), international Space Missions Planning Advisory Group (SMPAG), and more — began to trade information on various asteroid deflection capabilities and methods. In 2014, NASA launched a probe to rendezvous with the asteroid's path and collect more data at a close range. In December 2014, astronomers calculated that the asteroid was on a collision course with Denver, Colorado, and that the city would be completely destroyed with such an impact.

Several mitigation options were considered, the chief among them being nuclear devices and kinetic impactors. National and international political obstacles and disagreements made it more difficult for a nuclear device to be quickly contemplated. In addition, many environmental groups were opposed out of concern for potential

1

accidents involving the nuclear material; while perhaps well-intentioned, these worries were based in common misunderstandings and falsehoods, though understandably such stories were amplified by the media all-the-same. As a result, the nuclear payload option was mired in controversy.

Major space powers — the United States, the European Union, Russia, China, Japan — therefore began the rapid assembly of six kinetic impactor shuttles that would intercept and ram into asteroid to push it off its collision path. Half of these vehicles ultimately failed to intercept the asteroid target due to technical faults, but the remaining three of the six impactors hit the asteroid in August 2017. Almost a year later, when the asteroid came back into Earth's view, astronomers saw that while the main body was deflected, a 60 meter fragment had broken-off in the process. This fragment appeared to be headed towards the Eastern region of the United States.

Now, given the shortened window of potential response time, only a nuclear device could stop this fragment from soon crossing paths with Earth. The United States government debated shipping a nuclear-armed rocket out into space to intercept, but policy disagreements slowed this plan down significantly. This delay, along with the lack of a delivery system at-the-ready, eventually eliminated this possibility. No options remained, and Earth would have to take the hit. Six months out, it was only known that the asteroid fragment would hit somewhere in the New York area.

Two months before impact, it was determined that the body was hurtling towards New York City. FEMA, the Federal Emergency Management Agency, struggled to evacuate such a large population in that timeframe. In April 2020, the fragment reached the atmosphere traveling at 69,000 kilometers per hour and exploded 15 kilometers above Central Park, releasing the energy equivalent of 1000 Hiroshima nuclear explosions. Total devastation and destruction spread to a 15-mile radius surrounding Manhattan, moderate damage out to 45-miles, and minor damage out

2

to 68-miles away from the asteroid fragment's point-of-disintegration.

The observant and clever reader will realize that this did not actually happen. However, the events and timelines depicted in the above scenario are intended to be as realistic as possible. In May 2019, around 200 astronomers, engineers, and emergency response personnel participated in the biennial Planetary Defense Conference (PDC). The above sequence of events was exactly how the 2019 PDC simulated scenario played out [1, 2]. Practice sessions like this help reveal how we might respond, what kind of timelines we might face, and determine what sort of technology we might want to have at-the-ready when faced with incoming asteroids in the future.

There are at least two lessons to be learned. One, humanity has a long way to go in preparing to defend the planet from future asteroid threats. Two, as long as petty politics can be overcome, nuclear devices could one day save life on Earth from a looming asteroid threat.

The broad mission of the DoD is "to protect the security of our country" [3]. The United States Strategic Command (USSTRATCOM) within the DoD is the organization tasked with "strategic deterrence; nuclear operations; space operations; joint electronic spectrum operations; global strike; missile defense; and analysis and targeting" [4]. With these mission sets and skill sets of USSTRATCOM and the DoD at large, it is only natural that the DoD would be intimately involved in efforts to mitigate threats from hazardous asteroids, especially when using nuclear devices to do so.

Even though the likelihood of a 1 kilometer or larger asteroid strike is low, occurring once every 500,000 years or so, the consequences of such a collision are so catastrophic (an estimated 25% of the world's population would perish) that the annual probability of an individual's death from very large asteroids is on the order of 5×10^{-5} % [5]. While this number might seem absurdly small, it is in fact comparable

3

to the risk of death from a commercial airplane crash [6].

Asteroids approximately 100 meters in diameter are considerably greater in number than 1+ kilometer bodies in our solar system. Because of this large population increase, objects of this class hit Earth much more frequently: about once every 300 years [5]. Due to their smaller-size, their maximum collision yield is reduced, and there is a chance that these objects might disintegrate and release their energy in the atmosphere before reaching the ground. Therefore, the effects of these "smaller" asteroid impacts are far more localized. Rather than the world at-large, only people in the general regional vicinity of such a collision would risk death. Due to these differences, the annualized probability of an individual's death from $\sim$100 meter asteroids is $\sim 3.3 \times 10^{-6}$ %, about 15 times less than 1-kilometer-or-greater objects [5].

The magnitude of the damage that could result from these fairly-rare, one-off impact events makes the planetary defense mission a prudent pursuit. Asteroid collisions pose an array of threats. What is at stake? Everything — human life, animal and plant life, the environment, the world economy, the very course of history. With everything to lose, we also have everything to gain by being prepared to combat asteroids by any available means. This paper explores how the neutron energy from nuclear detonations affects asteroid deflection and aims to serve as an ever-so-small contribution towards the grand planetary defense mission.

1.2 Background

1.2.1 Asteroid Survey

Asteroids are small rocky objects that orbit the Sun either directly or indirectly. They are thought to be the leftovers from the very formation of our solar system. 4.6 billion years ago, a large cloud of dust and gas collapsed. Most of the material fell towards the center, forming the Sun. Some grouped elsewhere and formed planets

4

and moons. A small amount of the condensing dust instead cooled into small chunks of debris that were not incorporated into larger bodies; this debris material became the asteroids [7]. Asteroids exist in abundance — as of 19 December 2019, there are 932,365 discovered asteroids, although in total there are millions and millions more that are yet to be found [8]. Most of the asteroids in the solar system are located in the asteroid belt between the Mars and Jupiter, as visualized by the green dots in Figure 1.1.

Asteroids come in a wide variety of sizes, shapes, and compositions. Some of these bodies are very small, with the smallest asteroid ever closely studied being TC25, a rock only about 2 meters (6 feet) in diameter. Others are indeed massively sized, the largest discovered thus far being Ceres, a body that is 940 kilometers (583 miles) wide, only slightly smaller than the width of the state of Texas (660 miles). Despite numbering in the millions or more, the total mass of all asteroids combined is less than the mass of Earth's moon [10]. This is in large part due to the fact that asteroids follow an approximate power-law size distribution — small asteroids are much more abundant than very large asteroids [11].

Most asteroids are jagged and irregularly shaped, though some are roughly spherical. They often have many craters and indentations on their surface, like the asteroid Vesta. Some asteroids are solid or rigid, cohesive rock, while others are rubble piles, consisting of numerous rock fragments held together by gravitational pull [8]. Most asteroids are believed to be rubble piles, consisting of numerous rock fragments held together by gravitational pull. However, there is a wide range of possible internal structures and geotechnical properties for asteroids.

The first way often used to classify asteroids is by their composition. There are 14 classifications (A,B,C,D,E,F,G,M,P,Q,R,S,T,V), though the vast majority of asteroids fall into three categories — C, M, and S. The rest are quite rare in comparison. C-

5
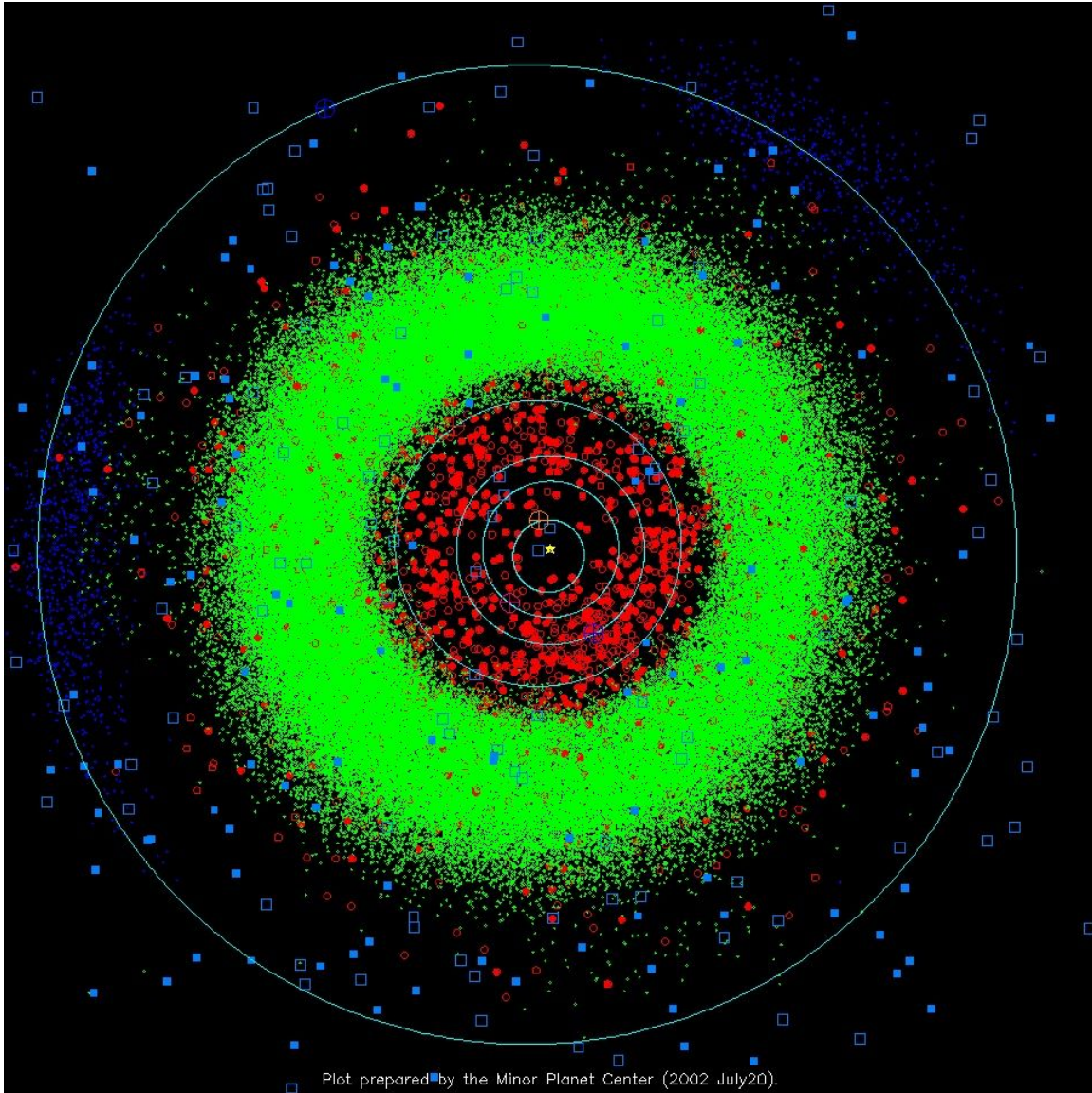
Figure 1.1. Asteroid belt depiction. The golden star in the center is the Sun. In order of increasing radius, circular paths represent the planetary orbital paths of Mercury, Venus, Earth, Mars, and Jupiter. The green dots are the asteroids of the asteroid belt between Mars and Jupiter. The red dots are asteroids with orbits outside the asteroid belt that pose a potential threat to Earth. Taken from [9]. Image prepared by the Minor Planet Center on 20 July 2002. © MPC, CBAT, Harvard CfA, IAU.

type asteroids are carbonaceous. They are the most common, approximately 75% of known asteroids, are greyish in color, and are likely composed of clay and stony rocks. S-type or siliceous asteroids are made of silicate materials and some nickel-iron. They are green-to-red in color and make up less than 17% of the discovered asteroids. M-type asteroids are metallic, made of large amounts of nickel-iron. These asteroids are rusty-red in color and account for most of the remaining asteroid body-types, less than 8% of the asteroid population. C-type asteroids are most common in the outer asteroid belt, farthest from Earth, while M-type asteroids are generally found in the middle of the belt. S-type asteroids are typically found in the inner asteroid belt, closest to Earth [10, 12, 13].

1.2.2 Near-Earth & Potentially Hazardous Objects

Of particular interest are asteroids that fall in the near-Earth object (NEO) categorization. A NEO is "an asteroid or comet that comes within 1.3 astronomical units (au) of the Sun," where Earth's orbit is defined as the 1.0 au standard [14]. This requires that the minimum orbit intersection distance (MOID) between the object and Earth is 0.3 au (about 50 million kilometers) or less. On the grand scale of the solar system, these distances are small, and NEOs are indeed near-Earth. When the NEO is an asteroid, occasionally NEA (near-Earth asteroid) is used.

Figure 1.2 depicts, as of 2017, the known population of NEAs as a function of asteroid size, alongside the fraction of discovered asteroids in each size-class. The red line shows the estimated distribution of asteroid size, which is described by an approximate power-law; smaller asteroids are considerably more abundant than larger asteroids. The blue line represents the percent of NEAs that have been discovered for all size classes. Scientists estimate that most of the very large NEAs have been discovered, while very few of the smaller asteroids have been found. Most NEOs and

7

NEAs are discovered with telescopes surveying space for faint glowing points that are moving against the stationary background stars. These spots of moving light are often asteroids, reflecting sunlight back towards Earth, just like planets. Of course, because asteroids are significantly smaller and darker (less reflective) than planets, their surfaces reflect a much smaller amount of light, making asteroids much harder to find. In general, a larger object reflects more light and therefore is more easily detected with a telescope. This is why there is confidence that most of the larger, more easily-spotted NEAs have been found, while the majority of the smaller NEAs are likely still lurking in the shadows, as-yet undetected [15].

Figure 1.3a is a similar presentation of the numbers of NEAs discovered, though it is current (as of 7 February 2020) and binned into five size-classes. As of 7 February 2020, 22,105 total NEAs have been discovered. Figure 1.3b shows how this cumulative total has changed over years of surveying space.

Not all NEOs and NEAs are at risk of colliding with Earth. A potentially hazardous object (PHO) or asteroid (PHA) satisfies the following two criteria: 1) the body approaches Earth at a distance of 0.05 au (7.5 million kilometers) or closer, and 2) the object is at least 140 meters or greater in diameter [14]. If a large asteroid with a diameter approximately 140 meters or greater were to collide with Earth, such an impact could cause significant damage to population centers on the regional level (Figure 1.2). A 140-meter sized asteroid impact would release approximately 100 megatons (Mt) of TNT-equivalent, which represents a severe-damage risk to a sizeable region. This amount of energy would be larger than the 50 Mt yield of Tsar Bomba, the Soviet nuclear device, which was the largest nuclear explosion in the history of the nuclear test era [18]. For PHAs of increasing size, the energy released and subsequent impact devastation could reach the continental regime, or even rise to a potential existential threat with global consequences [19]. Figure 1.4 shows the orbits

8

arth Objects (NEOs) are asteroids and comets that come close to or pass across Earth
the Sun.[1] They range in size from small "meteoroids" only a few meters across, to muc
several kilometers wide. When NEO orbits bring them into Earth's atmosphere, smaller
ssly fragment and disintegrate, while larger objects can cause local damage or even
ation. The shaded background of Figure 1 shows roughly how impact damage varie
d size.[2] Figure 1 also shows the known population of near-Earth asteroids, or NEAs[3] (gree
rent estimate of the total NEA population (red line), and the estimated completeness of
(blue line).
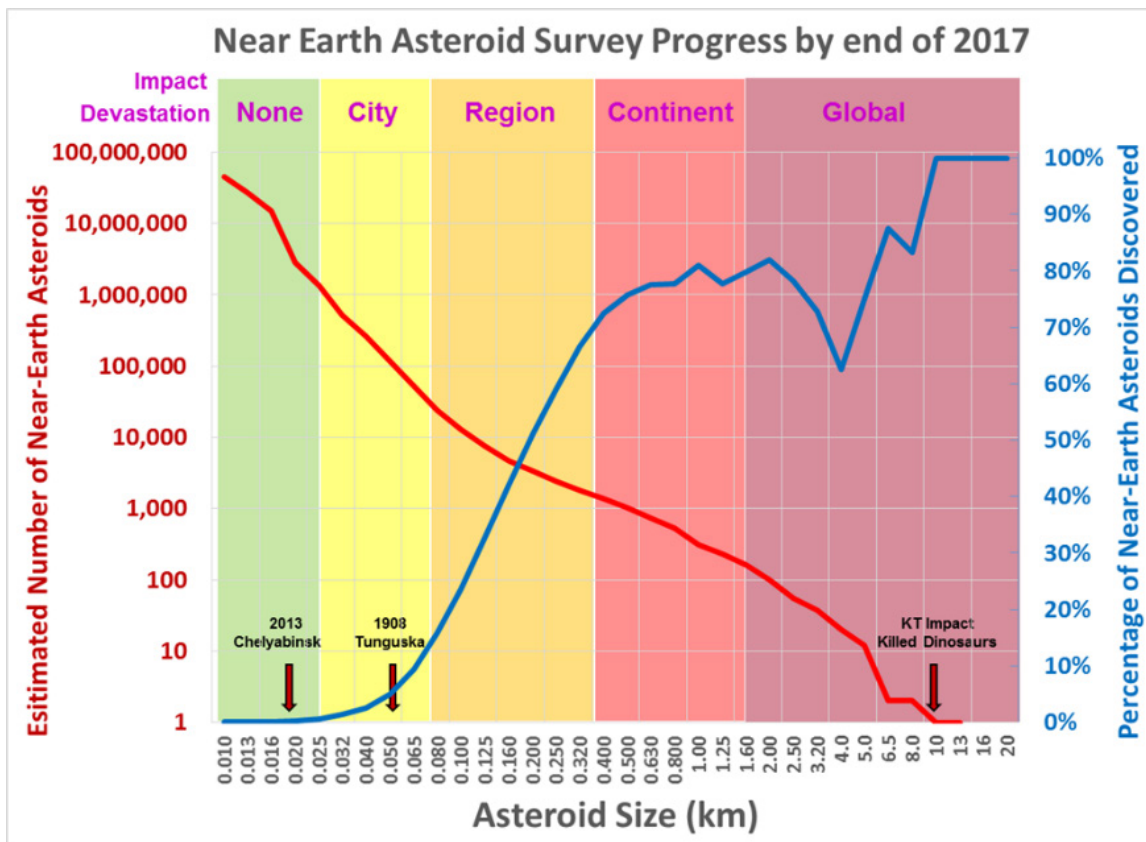
Figure 1.2. Near-Earth asteroid (NEA) size distribution estimations alongside the frac-
tions discovered as of 2018. The red line represents the estimated power-law distribution
of NEA sizes, while the blue line shows the fraction of asteroids of each size-class that
have been discovered. The purple scale at the top provides an idea of the damage mag-
nitude anticipated from a collision as a function of asteroid size. The three arrows at
the bottom are placed over three well-known historical asteroid impacts — Chelyabinsk
in 2013, Tunguska in 1908, and the K-T dinosaur extinction event. Taken from [16].

mpacts of varying size could have major environmental, economic, and geop
uences detrimental to the United States, even if the impact is outside U.S. territory. Th
from a NEO impact depend on its size, composition, and impact speed. Small, rocky NI
o explode before hitting the ground, resulting in an airburst that could produce a wider
ate damage compared with a similarly sized metallic object that would strike the grou
eavier, more localized devastation.

nall NEOs can have significant destructive effects. For example, on February 15, 2013, an a
imately 20 meters in size created an airburst near Chelyabinsk, Russia, with roughly 20-3
nergy than that released by the first atomic bombs. It damaged thousands of buildin
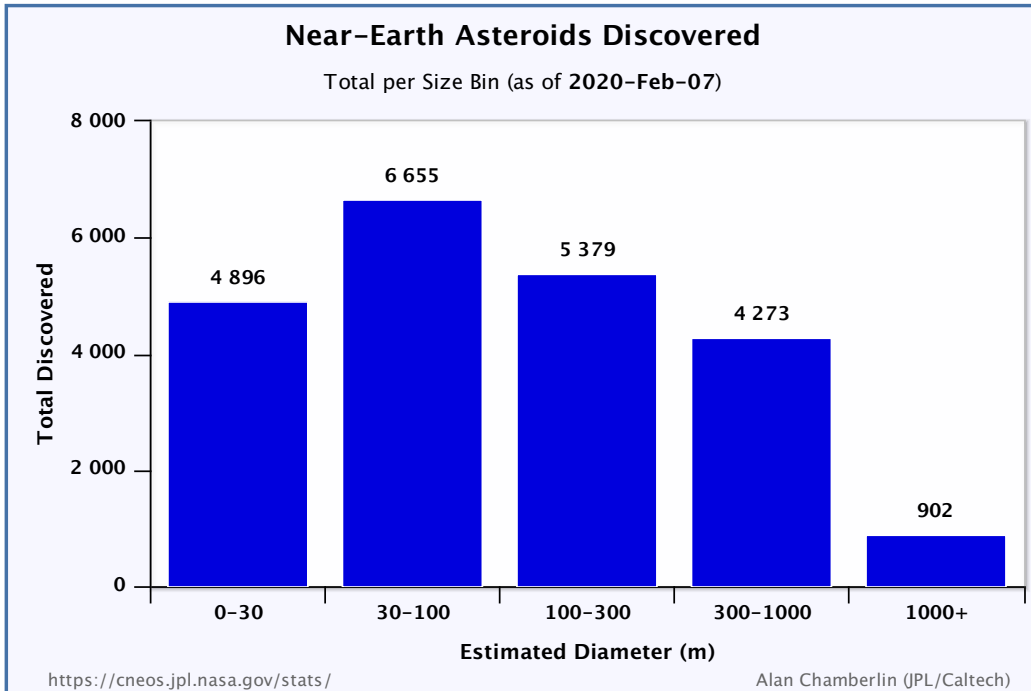
(a) The current total number of known NEAs grouped according to their estimated sizes.
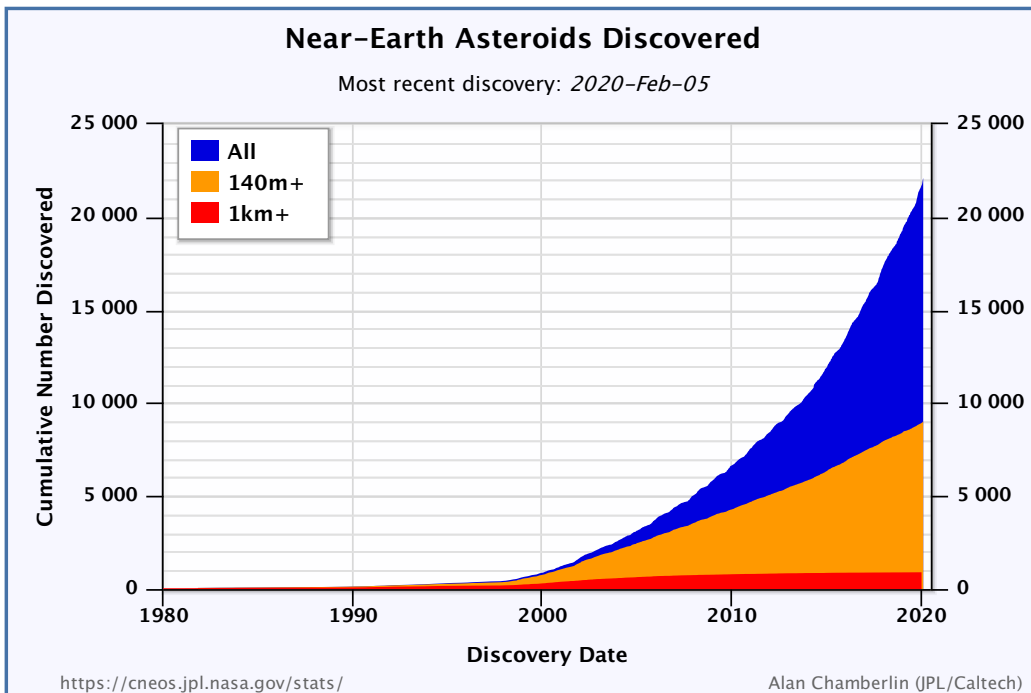
(b) The cumulative number of known NEAs versus time.

Figure 1.3. The discovery statistics of near-Earth asteroids. Taken from [17].

of the ~1,400 PHAs found before 2013. At the current time, zero discovered PHAs are expected to collide with Earth within the next 100 years [20].
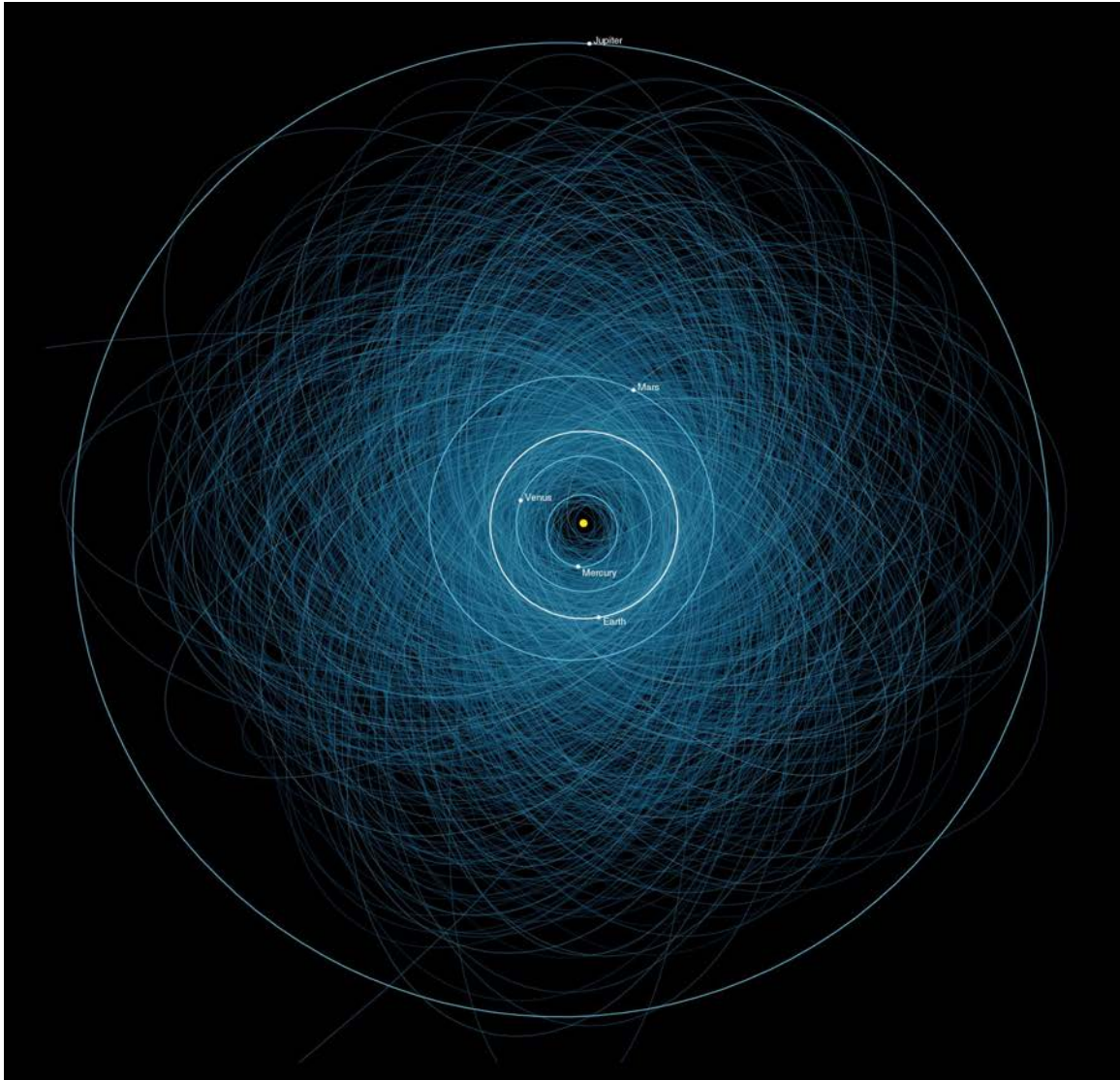
Figure 1.4. Orbits of all the known Potentially Hazardous Asteroids (PHAs) alongside the Sun and the paths of inner planets. Image generated in 2013, when the number of known PHAs was a bit over 1,400. Taken from [20].

NEAs are divided into four orbital classes — Atira, Aten, Apollo, and Amor — based on their perihelion distances (q), aphelion distances (Q), and semi-major axes (a) [21]. The perihelion distance is the closest distance between the asteroid and the Sun along the asteroid's orbit. The aphelion distance is the farthest distance between

11

the asteroid and the Sun. The semi-major axis is half of the longest diameter of the asteroid's elliptical orbit. These parameters are visualized in Figure 1.5.
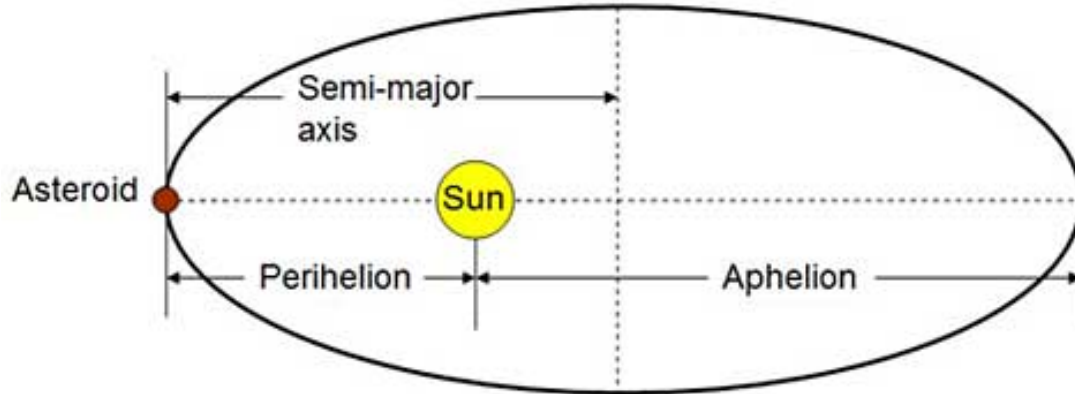
Figure 1.5. Parameters defining an elliptical orbit. Taken from [22].

Figure 1.6 shows the four different orbit types, each taking its namesake after a well-known named asteroid. Of particular note are Apollo- and Aten-type NEAs, whose paths cross Earth's orbit, of course making it possible for the two bodies to collide at some point in the future. In contrast, Amors and Atiras asteroids do not present an immediate impact threat because their paths do not cross Earth's; however, some of these objects are close-enough to be a potential concern should their orbits be perturbed after a close approach to Mercury or Venus. Most PHAs are Earth-crossing Apollo or Aten asteroids, though a small amount are Amors with perihelion distances of 1.05 au or less.

As of 7 February 2020, 9,009 NEOs with diameters greater than 140 meters have been discovered, and of these, 2,057 are classified as PHAs [17]. At the end of 2016, it was estimated that the NEO population of size 140 meters or greater amounts to $\sim$27,100 $\pm$ 2,200 in total, meaning that approximately 33.2% $\pm$ 2.7% of such NEOs have been found at the start of 2020 [23]. For the PHA subset population, in 2002, NASA's asteroid-search component of the Wide-field Infrared Survey Explorer

12

Amors

Earth-approaching NEAs with orbits
exterior to Earth's but interior to Mars'
(named after asteroid (1221) Amor)
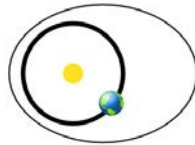
$a > 1.0$ AU
1.017 AU $< q < 1.3$ AU

Apollos

Earth-crossing NEAs with semi-major
axes larger than Earth's
(named after asteroid (1862) Apollo)

$a > 1.0$ AU
$q < 1.017$ AU

Atens

Earth-crossing NEAs with semi-major
axes smaller than Earth's
(named after asteroid (2062) Aten)

$a < 1.0$ AU
$Q > 0.983$ AU

Atiras

NEAs whose orbits are contained
entirely within the orbit of the Earth
(named after asteroid (163693) Atira)

$a < 1.0$ AU
$Q < 0.983$ AU

$(q = \text{perihelion distance}, Q = \text{aphelion distance}, a = \text{semi-major axis})$

Figure 1.6. **Near-Earth object (NEO) orbit types. NEOs fall into one of four orbital types — Amors, Apollos, Atens, or Atiras — each having different characteristics. Taken from [21].**

(NEOWISE) analyzed 107 known PHAs and extrapolated an estimated $4{,}700 \pm 1{,}500$ total PHAs with diameters larger than 100 meters [24]. If this figure is accurate, then $43.8\% \pm 13.8\%$ of the PHAs in existence have been found thus far.

1.2.3 Historical Asteroid Impacts

The far-right arrow in Figure 1.2 marks the massive asteroid impact that brought about the K-T (Cretaceous period K and Tertiary period T) dinosaur extinction event. Around 65 million years ago, an asteroid with a diameter of 10 kilometers collided with Earth, releasing extreme amounts of energy and creating a 150 kilometer crater that still exists today, buried in the Yucatan region of Mexico. Debris from the explosion was lofted into the atmosphere, severely altering Earth's climate and harming both plant and animal life. Near the region of impact, high temperatures from the explosion spewed numerous fires, earthquakes from the violent collision arose, tsunami tidal waves traveled the seas, and hurricane-level winds and an immense shockwave traversed the atmosphere, all contributing further to the devastation. All of these conditions resulted in a mass extinction event whereby 70% of Earth's species disappeared in a very short amount of time [25, 26]. Luckily, due to the asteroid size power-law limiting the numbers of large asteroids, and due to the relative ease of detecting larger objects in space, 95% or more of the global-catastrophe-inducing NEAs have already been discovered and have been determined not to be a threat anytime soon [27].

Objects smaller than 140 meters are not counted among the PHAs, by definition. However, this is not to imply that NEAs smaller than this would not result in damage upon collision, that they are not also "hazardous." The remaining two of the three arrows in Figure 1.2 support this point. These arrows denote the size of two recent and noteworthy asteroid collisions with Earth. In 1908, a $\sim$60 meter asteroid

impacted Earth near Tunguska in the Siberian region of Russia [28]. As no impact crater was found, this body is believed to have disintegrated in the atmosphere a few kilometers above the ground. 2,000 square kilometres of forest and 80 million trees beneath this airburst were flattened and destroyed from the shockwave [15]. The yield equivalent is estimated to have been 10-20 megatons [28]. In 2013, a 19 meter asteroid fell towards Chelyabinsk, Russia [29]. The resulting airburst injured 1,500 people and damaged around 7,000 buildings [15]. The Chelyabinsk asteroid yield was approximately 500 ± 100 kilotons [29]. Both of these events were under the 140 meter PHA threshold, and neither impacted the ground, but both were clearly hazardous in their own right.

Because asteroids of this size are rather "small," however, it is likely that near-future collisions in this regime will occur with minimal warning time (on the order of hours or days), if at all. This conclusion recognizes that only a very small fraction of smaller NEAs have been found up to this point (the blue line in Figure 1.2). Additionally, in 2019 alone, Earth experienced slightly over 80 so-called asteroid "close-approaches," where an asteroid passes closer to Earth than the Moon (one lunar distance is 0.0025696 au, or 384,410 kilometers). Most of these objects were 50 meters or smaller in diameter. Over 50% of the close-approaches were not discovered until *after* the asteroid had already flown-by Earth, and only ∼5% were detected more than one week before the close approach. Figure 1.7 is a pie-chart visualizing the close-approaches in 2019 by time of discovery of the asteroids.

1.2.4   Mitigation Timelines for Asteroid Threats

If an asteroid was bound by fate to collide with Earth, could we do anything to stop it? The answer depends on the warning time, or how much time in advance we are able to detect and predict the impact event, as well as whether we have to spend

15
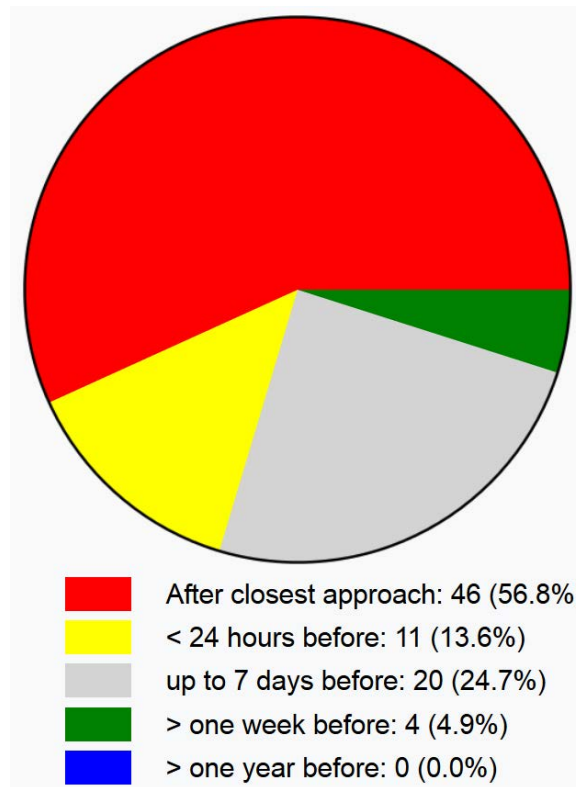
Figure 1.7. Asteroid close-approaches to Earth in 2019. Time of discovery of asteroids which came closer to Earth than the moon in 2019. Taken from [30].

time to build the mitigation technology or instead we have it pre-constructed and at-the-ready.

A numbers game, the warning time will most strongly depend upon the size of the asteroid in question. To have a warning time at all, the asteroid must first be spotted. Unless national and international efforts in locating all NEAs and PHAs greatly increase, little-to-no warning time for small incoming asteroids can be expected, as seen in Figure 1.7. On the other hand, sizeable amounts of the larger (140+ meter) NEAs and PHAs have already been found. Additionally, it is believed to be feasible to locate most of the 140+ meter NEAs/PHAs within the next few years or decades[1] [32]. As more and more of these objects are found, and as more time passes to allow for tracking observations and subsequent orbital predictions to accumulate, it is increasingly likely that PHAs will be among the objects whose collision dates could be predicted with enough confidence and warning time to allow for a potential mitigation response. While orbital predictions do not expect any discovered PHA to be a threat over the next century, most of these objects are yet to be discovered [20]. For the 140+ meter NEAs that have already been found, as their orbits are increasingly known and watched as more observation time is accrued, it is possible that warning times of a few years might be provided if any of the orbits of these objects are perturbed to enter an eventual collision course with Earth.

Yet another factor is the amount of time that would be required to plan and execute an asteroid intercept mission. Presently, while the kinetic and nuclear mitigation technologies are relatively mature, there is not a launch vehicle and spacecraft set aside for delivery of these mitigation methods. Because of this, if it was announced tomorrow that an asteroid was on track to hit Earth in ten years, some of the mis-

---

[1]In 2005, Congress tasked NASA with identifying 90% of asteroids larger than 140 meters in diameter by 2020. Funding was not supplied as needed, however. In 2013, the National Research Council estimated that $50 million per year would be needed to reach the 90% goal by 2030, but current funding has only been about $20 million per year [31].

17

sion hardware would need to be built or procured, taking more time to respond. In addition, the actual mission would have to be planned and coordinated, and determining the favorable launch window would be necessary. Due to these factors and more, in 2013, expert testimony to the United States Congress included an estimate that NASA would need a minimum of five years of preparation time before a mission to intercept an asteroid could be launched [33]. Note that this is only the notional amount of time that would be spent on getting a launch ready. According to other testimony in this same hearing: "Travel times to the [asteroid] target could be several months but could range up to a couple of years depending on the details of the NEO's orbit." Once the interceptor arrives at the NEO, depending on the mitigation approach used and the details of the asteroid size and orbit, it might take several more years or even decades for the initial delivered impulse to integrate to an Earth-missing deflection distance. The times required for mission planning and execution, travel, and mitigation effectiveness should make it clear why sufficient warning time is an absolute necessity for a human response to an incoming asteroid to even be possible.

1.2.5   Mitigation Strategies for Asteroid Threats

Several methods of combating asteroids on a collision course with Earth have been envisioned. These strategies can be divided into two categories of approach: disruption or deflection. Mitigation methods can be notionally classified by the time it takes the technology to act, as well. Deflection can operate in two time regimes — impulsive (rapid) or slow-push (gradual), while disruption operates only in the former domain.

Disruption aims to completely destroy the asteroid, shattering the object into a countless number of smaller pieces and fragments. With enough energy causing the disruption, the debris field is rapidly dispersed and none of the original mass collides

18

with Earth.

Disruption may be the most effective option when an asteroid is "small"[2] and/or when the warning time of an impending asteroid collision is very short. Disruptions executed even just months in advance of an impact date with Earth can be very successful at dispersing the fragments and allowing all material to generously miss Earth [34].

Numerical simulations show that most of these pieces are usually given large deflection velocities and typically miss Earth, even for relatively late-time disruption scenarios [34]. However, with our limited knowledge of asteroid composition and structure, it is unlikely that we would know from the onset exactly how the asteroid would shatter. Since disruption is a somewhat stochastic process, it would be important to conduct sensitivity studies over a range of asteroid material properties.

Deflection is the alternative, gentler approach. When two bodies are headed towards each other, one or both must be moved in order to avoid a collision. In the case of Earth facing an incoming asteroid, the "obvious solution, dodging, is precluded due to the cumbersome nature of Earth. It is easier, and sufficient, to force the intruder to dodge" [35]. Deflection is the act of pushing the asteroid onto a new trajectory by changing its velocity. According to a study by David Dearborn, it is best to apply the force along the direction of the asteroid's travel, either speeding up or slowing down the asteroid [36]. Deflecting an asteroid perpendicular to its path is generally much less effective in altering the orbit. If the magnitude of the velocity change, δV, is great enough, and if enough time is left before the asteroid approaches close to Earth, then the orbits of the asteroid and Earth will be de-phased and the

---

[2]That is, small enough where a successful deflection would be challenging. If deflection requires a velocity change that is nearing or exceeding the object's escape velocity in order to be effective, then the asteroid would likely suffer undesirable fragmentation in the process. Smaller asteroids typically have less mass, and by Equation 1.2, the v_{escape} threshold is lower. This makes deflection more difficult to execute on smaller objects.

fated collision is avoided entirely.

For asteroids where both disruption and deflection are possible, deflection is usually the preferred option, so long as the warning time is sufficient for it to be viable. Deflection is the approach that works by providing a gentle "push," and by this very nature, it is less likely to generate a difficult-to-predict and potentially dangerous debris field, at least compared to the more violent, shattering disruption option. A downside of deflection is that only small changes in asteroid velocity (usually on the order of millimeters or centimeters per second) are achievable without risking fracture and disruption. Typically years or a decade or more of warning time would be needed for for this level of velocity change to cause enough deflection for the asteroid to miss Earth [37].

There are many different ways to deflect an asteroid. Deflection strategies are either impulsive, being effective nearly instantaneously, or slow-push, acting gradually over an extended period of time. Impulsive methods include the following: conventional explosives (detonated at or beneath the surface of the asteroid), nuclear explosives (detonated stand-off, at, or beneath the surface of the asteroid), and kinetic impacts [38]. Conventional explosives are perhaps self-explanatory, involving an explosive force to push the asteroid and alter its momentum. Nuclear explosives would work in a somewhat similar way, as discussed in greater detail in Section 1.2.6. Kinetic impacts refer to kinetic impactors, or slamming a high-speed, high-mass spacecraft into the asteroid to impart momentum directly and push it off course [6].

Some of the slow-push deflection methods that have been considered are: focused solar, pulsed lasers, mass drivers, gravity tractors, asteroid tugs, and the enhanced Yarkovsky effect [38]. Focused solar would be using a large mirror to focus solar energy into a small region of the asteroid's surface to heat and "boil-off" material over time. A pulsed laser could be affixed to a rocket that is sent to rendezvous with

a PHA, upon which a laser is pointed at the surface to similarly "boil-off" material and change the momentum of the asteroid. Mass drivers would function like a mining operation, where a shuttle would drop-off a machine on an asteroid that would break-up material and eject it outwards into space at high-speeds. A gravity tractor would be the act of a spacecraft reaching a PHA and orbiting it in close-proximity over a long period of time, allowing gravitational attractions to nudge the object off-course. The asteroid tug involves attaching a rocket engine onto an asteroid and then turning it on to push. Lastly, the enchanced Yarkovsky effect operates by changing the albedo (reflectivity) of the surface of a rotating asteroid, perhaps by painting it white, so that more of the incident solar spectrum is reflected off of the surface, thereby turning sunlight into a push-force.

Of course, not every mitigation method is equally efficient or effective. Not all mitigation technologies are suitable for all asteroid threats — "each technique works *up* to a certain size NEO and *down* to a certain advance warning time" (emphasis mine) [33]. The Near-Earth Object Survey and Deflection Analysis of Alternatives, a NASA report to Congress, assessed the "launch, orbit transfer, technology development, and object characterization requirements" for each of these deflection technologies, and applied them to a set of five scenarios representing a range of probable asteroid threat-types [38]. It found that kinetic impactors are the most mature approach, and could be used in some deflection scenarios involving asteroids that are small and solid. While chemical explosives are irrelevant — the kinetic energy per unit mass of a spacecraft traveling at typical intercept velocities (many kilometers per second) dwarfs the chemical energy per unit mass contained in high explosives — nuclear charges are the most effective way to deflect a PHO. Additionally, in general the "slow-push" methods were found to be the most expensive, the least mission-ready, and even for small asteroids only possibly effective over decades of warning time.

21

Another source, the National Near-Earth Object Preparedness Strategy and Action Plan from the Office of Science and Technology Policy, listed kinetic impactors, nuclear devices, and gravity tractors as the most mature in-space concepts for deflection [16]. Another study examined six technologies — nuclear interceptor, solar collector (focused solar), mass driver, low-thrust propulsion (asteroid tug), gravity tug (gravity tractor), and kinetic impactor — by various performance criteria: ease of deflection/deviation, cost of the mission, complexity of the approach, readiness of the deviation strategy, and response time. It concluded that the solar collector and nuclear interceptor offered the best deviation per mass of the technology and required the lowest amount of warning time to be effective, with the nuclear option being better for Apollo and Apophis orbits. Kinetic impactors and low-thrust propulsion offer comparable performance for smaller asteroids below 10^{10} kilograms in mass [39]. Ahrens and Harris reached a similar conclusion: kinetic impactors and mass drivers are impractical for asteroids larger than 100 meters, while nuclear explosion radiation would be an alternative and the only practical option for kilometer-scale objects [6].

In terms of timing, Adams et al. estimated that the nuclear interceptor could deflect smaller NEOs (100 to 500 meters) if applied two years prior to impact, and larger NEOs with five years of warning [40]. A single kinetic impactor could only be effective for NEOs up to 100 meters. Although multiple kinetic impactors would possibly be effective for asteroids up to 300-400 meters in diameter, this would require at least 8-10 years of warning time. Solar collectors could be used for deflection if they are able to operate for longer operation times. In 2013, the United States Congress Committee on Science, Space, and Technology collected expert testimony in hearings pertaining to "Threats from Space: A Review of U.S. Government Efforts to Track and Mitigate Asteroids and Meteors." These sessions found that one or multiple stand-off nuclear blasts would work for the largest known NEOs (10-20 kilometers)

with a five year warning time, and for medium NEOs with a one year warning time. Using several kinetic impactors could deflect 1-2 kilometer NEOs if applied several decades before impact, and for 100 meter NEOs with a few years of warning. Slow-push techniques, namely the gravity tractor, could deflect asteroids on the order of several hundred meters with many decades of notice, and for NEOs up to 100 meters with one to two decades of warning [33]. Sanders' sources told him that non-nuclear methods required "tens, hundreds, or even thousands of years to sufficiently divert" one kilometer objects [41].

There is a clear and consistent pattern to be realized from these many sources — broadly speaking, nuclear detonations are the most efficient means of deflecting asteroids. In fact, NASA found that nuclear stand-off explosions are 10-100 times more effective than non-nuclear alternatives [38]. A nuclear device is also by-far the most mass-efficient technology for storing and delivering usable energy, a practical consideration of the utmost importance given the payload constraints of rockets when launching material into space. The energy released from the fissioning or fusing of nuclei is rooted in the aptly-named strong force, the strongest of the four fundamental forces. Nuclear energy densities are nearly one million times greater than chemical bonds [42]. The outputs and effects of nuclear explosions are also known and well-characterized; nuclear devices are a mature technology. These factors make the nuclear option a prime choice for combating asteroids on a collision path with Earth [36].

With current technologies, nuclear devices are one of the only viable options for mitigating an incoming 140 meter or larger hazardous asteroid on a less than decadal timescale. For objects of this size, other mitigation technologies require decades or longer to be successful. Even for longer warning times, a recent study found that objects similar in size to the Bennu asteroid (500 meters) may require a nuclear

deflection in order to *safely* miss Earth [43].

Nuclear explosives could be used in disruption or deflection scenarios. This thesis focuses on deflection via stand-off nuclear detonations because deflection is generally regarded as safer, more desirable, and more elegant than disruption [37].

1.2.6   Deflection via Stand-off Nuclear Detonations

For deflection with the lowest probability of disruption, the nuclear device is detonated at a stand-off distance away from the asteroid's surface, as opposed to a surface or sub-surface detonation, which would pose a higher risk of accidental and undesirable disruption. In an ideal, perfectly symmetric detonation, the source radiations (x-rays, neutrons, and gamma-rays) form thin spherical shells of energy that expand radially outwards in all directions. Depending on the detonation's stand-off distance and the asteroid's shape, some fraction of the total source energy impinges upon some fraction of the asteroid surface area.

The prompt x-rays, neutrons, and gamma-rays are formed within the last microsecond of the detonation initiation. After these particles quickly stream through the vacuum of space and reach the target surface, they deposit their energies in the asteroid material via absorption and scattering reaction mechanisms in a very short time (also on the order of microseconds). Given the penetrative nature of neutrons and gamma-rays, the target material will not mechanically respond in such a short time due to inertia, thereby allowing the energy deposition to be understood as an instantaneous increase in the internal energy of the asteroid surface material [44]. This is not strictly true for x-rays, as their energy is deposited in such a small volume (in extremely thin layers beneath the surface) that a rapid ablative material response can occur.

If the detonation yield is large enough and the stand-off distance is close enough,

24

the energy deposited at and beneath the surface might exceed the sublimation energy threshold of the asteroid's material. If so, as soon as the material can respond to its sudden internal energy spike, the outer surface immediately phase-changes from solid to gas or plasma, and some mass beneath the surface will be liquefied. The highly-energetic melted and/or vaporized material quickly expands outwards and blows-off the surface, hence the common parlance of "blow-off" in the planetary defense community. Because the blow-off is moving very quickly and predominately outwards and away from the asteroid surface, this is a rocket-like exhaust momentum imparted over a short time. With the blow-off pushing off of and departing the surface, and with the intense and sudden temperature increases, a pressure wave is formed in the asteroid that propagates throughout the object. As a result, an equal and opposite momentum is imparted to the asteroid, changing its speed and therefore orbit [37,45]. Figure 1.8 visualizes this process, showing snapshots of how the radiation from a stand-off nuclear explosion induces a velocity change in the asteroid. If this velocity change is sufficient, the orbits of Earth and the asteroid would be de-phased, and collision is avoided entirely.

Typically, in most published literature involving asteroid nuclear deflection simulations, the neutron source component is simply assumed to be either the Watt fission spectrum or fusion reaction energies, such as mono-energetic 2.45 MeV or 14.1 MeV neutrons. Examples of past works using the Watt spectrum, 2.45 MeV, and 14.1 MeV neutron sources are [46], [47], and [48], respectively. These are the predominate neutron energies produced from nuclear explosions. However, to the authors' knowledge, there is little-to-no finalized or wholesale published research exploring neutron source energies in a comparative lens, so as to determine which neutron energies are best for asteroid deflection.

Previous work on *disruption* found that "preliminary hydrodynamics simulations

with a planet or by gravitational perturbations that eject them into hyperbolic orbits.

Earth-crossing asteroids have been recognized telescopically since 1932, when Reinmuth[1] discovered 1862 Apollo, and Gilbert's work[6] on Meteor Crater, Arizona, and subsequent studies, made it apparent that the impacts of Earth-crossing asteroids and comets have produced the ~120 known meteorite impact craters on the Earth and virtually all the craters on the Moon. That the impact of any asteroid or comet with the Earth
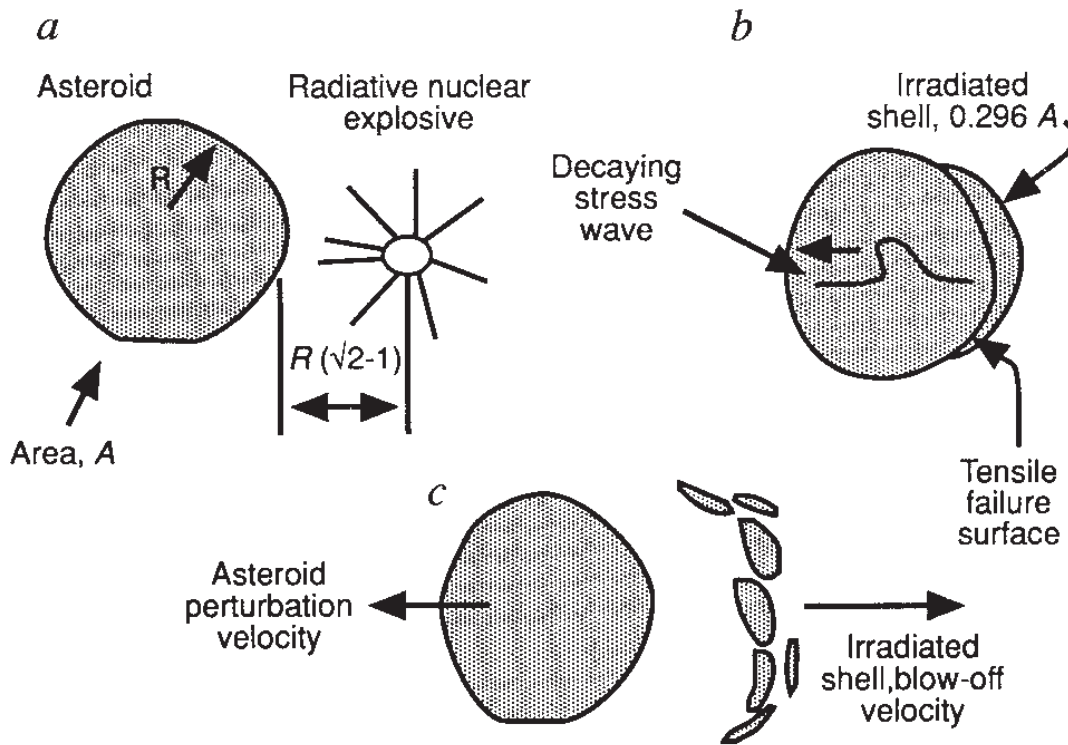
Figure 1.8. How nuclear explosive radiation could be used to induce a velocity change in an asteroid target. First, at time "a," a nuclear device is detonated at some stand-off distance away from the asteroid surface. Some of the nuclear radiation reaches the target, and at time "b," some portion of the asteroid surface has been irradiated, reaching melting and/or vaporizing thresholds. Soon after, at time "c," the highly-energetic melted/vaporized irradiated material blows-off the surface, and an equal-and-opposite momentum is imparted on the remaining asteroid body, thus changing its velocity. Taken from [6]. Reprinted by permission from Springer Nature: Nature, Thomas J. Ahrens and Alan W. Harris, "Deflection and fragmentation of near-Earth asteroids," 03 December 1992.

26

conducted suggest that the spatial variations in energy deposition in an asteroid can have a significant effect on the resulting degree of disruption" [49]. If the neutron energy significantly changes the energy deposition profiles, perhaps this will also have an effect on the *deflective* response. A study on deflection found that a factor η_K, called the "kinetic coupling" fraction representing the ratio of the asteroid's resultant kinetic energy to the total deposited energy from a neutron source, is possibly greater for lower-energy neutrons [41]. This would suggest that fission (lower-energy) neutrons might be more ideal for deflection than fusion (high-energy) neutrons, with respect to this "kinetic" coupling. However, in both of these works, these findings were regarded as preliminary and were not the primary focus of the respective efforts. The search for which neutron energies are most effective for asteroid mitigation, and why, is still an open-question.

1.3 Problem & Hypothesis

In broad terms, this research investigates how the incident neutron energy affects asteroid deflection. More specifically, this work will examine the impact that neutron energy has on both the spatial distribution of energy deposition and the energy coupling efficiency in a notional asteroid. For two different neutron source energies, the resulting impact on the asteroid's deflection, δV, is then determined.

It is anticipated that differences both in the spatial distribution of deposited energy and in energy coupling, which themselves result from differences in the source neutron energies, will impact the asteroid deflection performance. To begin to assess the overall impact of neutron energy on asteroid deflection, this work focuses on the spatial energy deposition profiles and the energy coupling efficiencies for two nominal neutron energies, 14.1 MeV and 1 MeV, and the resulting change in aster-

27

oid velocity, δV, for each source energy.[3] 14.1 MeV neutrons are generated from deuterium-tritium (D-T) fusion reactions, which are given off by boosted fission and thermonuclear devices, and 1 MeV neutrons are generated from fission reactions (with this energy corresponding to near the peak of the Watt spectrum) [50]. These energies were chosen to roughly represent the notional energy differences between neutrons characteristic of fusion and fission processes.

1.3.1   Research Objectives

The goals of this work are to answer the following questions:

1. What do the energy deposition profiles look like for various neutron source energies, and how do they compare?

2. How does energy coupling efficiency change with the energies of the incident neutrons?

3. In changing the energy deposition profile and energy coupling, what effect does neutron energy (indirectly) have on asteroid deflection?

4. What is the optimal neutron energy or energy spectrum for asteroid deflection?

Questions #1 and #2 are answered by generating energy deposition profiles via Monte Carlo radiation transport simulations. Monte Carlo N-Particle 6.2 (MCNP6.2) from Los Alamos National Laboratory (LANL), a well-known code in the field of radiation transport, is used in this work. MCNP6.2 is a general-purpose Monte Carlo

---

[3]In actuality, the "1 MeV" source is energy group #21 of the DPLUS bin structure, and the "14.1 MeV" source is group #3. These sources were uniformly sampled between the bin boundaries of 0.96164 and 1.1080 MeV for group #21 and 13.840 and 14.191 MeV for group #3. The midpoint or average energy for each group is quite close to 1 and 14.1 MeV, respectively, and for the sake of brevity these sources will be referred to as 1 MeV and 14.1 MeV in this thesis.

code that can be used for neutron, photon, charged particle, or coupled neutron/photon/charged particle transport in 3-D geometries [51]. Nuclear cross-sections for interaction probabilities were pulled from the US Evaluated Nuclear Data Library (ENDF) B-VII.1 (ENDF71x) library [52].

Question #3 is answered by applying the generated MCNP6.2 energy deposition spatial profiles as inputs to initialize a hydrodynamic transport code and thereby quantify the asteroid's mechanical deflection response following energy deposition. ALE3D, an Arbitrary Lagrangian–Eulerian (ALE) hydrodynamics code capable of running two- and three-dimensional geometries developed by Lawrence Livermore National Laboratory (LLNL), is used in this work [53].

Question #4 is answered in part by comparing the δV resulting from a 14.1 MeV neutron source to the δV resulting from a 1 MeV neutron source. This comparison is the first step in answering this broad question. The foundation for future work is laid from this thesis. For a given asteroid size and composition, 46 energy deposition profiles (adhering to the 46-group DPLUS group structure[4]) spanning the full, relevant range of the neutron energy spectrum are generated. With this data, a potential optimization process for calculating *the* ideal neutron energy spectrum that results in the maximum asteroid deflection is possible.

1.3.2 Assumptions & Limitations

Numerous assumptions were made throughout this work, but care was taken to make them as reasonable and as justifiable as possible. These were all necessary in some form or fashion to obtain timely results. Some of the implications of some of the assumptions limit this research more than others. This section serves to quickly list and discuss the major assumptions made in this research.

---

[4]The DPLUS group structure is based on the DABL69 library, which has been used in radiation shielding problems in defense-applications [54].

29

Only the neutron component of radiation from a nuclear detonation is investigated. The energy from a nuclear explosion is emitted principally in the form of x-rays, gamma-rays, and neutrons. Typically, most (roughly 50-70%) of the prompt energy is in the form of x-rays [55]. Neutrons from a fission device usually account for 1% of the total yield, and around 20% from a fusion device output [39]. These numbers are only notional, as classified details of device designs can alter the energy partitionings. The device "yield" in this work refers to the *neutron* yield,

$$Y_n = [\text{src-n}] \cdot E_n, \tag{1.1}$$

or the amount of detonation energy emitted in the form of neutrons. The parameter [src-n] refers to the number of source neutrons, and E_n is the weighted-average energy of each source particle (i.e. MeV/src-n). For a uniformly-sampled energy bin source, like the DPLUS energy groups used in this work, E_n is the midpoint energy. Neutrons were the only radiation form considered because neutrons are generally the most effective source type for deflection [47]. This greater efficiency from neutrons is because prompt gamma-ray radiation is typically a very small fraction of the device yield, and prompt x-rays deposit their energy only a few microns beneath the surface [36]. Most neutrons have a penetration depth on the order of centimeters in most materials, meaning that neutrons can heat greater amounts of material and are more effective at generating blow-off on a per-source-particle basis than x-rays.

The neutron yield of the detonation source is assumed to be either fifty kilotons (kt) or one megaton (Mt). For each neutron source energy E_n, the number of source neutrons src-n is selected so that Y_n is either 50 kt or 1 Mt (Equation 1.1). Setting the incident yields equal for differing source neutron energies allows for the asteroid deflection to be fairly evaluated. The 50 kt and 1 Mt numbers themselves were somewhat arbitrary. These yields are discussed in more detail later

in Section 4.1.2.

A detonation is treated as an isotropic (perfectly symmetric) point-source. Considering that a nuclear device is small and at a decent stand-off distance away from a much larger asteroid, treating the detonation as a point-source is acceptable and is a common assumption made in literature. In the MCNP6.2 models, the neutrons are all generated at a point and travel outwards evenly in all directions throughout a 4π steradian space. In reality, there is some angular dependence to the neutron emission (this is device dependent). However, isotropic emission is a reasonable approximation.

The neutron energy spectrum is discretized into a 46-group bin structure. The DPLUS library was used to approximate a continuum of neutron energies, spanning 10 μeV up to 19.64 MeV, into a finite 46-group structure. DPLUS is based on the DABL69 library, which has been used in radiation shielding problems in defense-applications [54]. Energy deposition profiles were generated for neutron sources with energies uniformly-sampled between the lower and upper bounds of each DPLUS group. This was intended to capture the wide range of neutron energies into convenient groups for the purposes of a full neutron energy spectrum optimization.

This works focuses on two neutron source energies: 14.1 MeV and 1 MeV. These energies were meant to correspond to typical neutron energies from fusion and fission reactions, respectively. 14.1 MeV is the standard energy of a neutron from the most predominate fusion channel, and 1 MeV is close to the most probable neutron energy from fission, as explained in Section 2.4.

A fixed stand-off distance is assumed for comparing deflection performance with different neutron source energies. The stand-off distance, or height of burst (HOB), examined in this work is $\left(\sqrt{2} - 1\right) R$, or $\sim$0.414 times the asteroid radius, which is the geometrical "optimal" HOB derived by Hammerling and Remo [56].

31

This is the distance where the sum of two fractions, f (the fraction of the asteroid surface area that is irradiated) and g (the fraction of device yield that reaches the asteroid target), is maximized. It is not anticipated that the HOB will have a significant, if any, effect on which neutron energies perform best for deflection. As such, this was a somewhat arbitrary choice of HOB, and it is expected that comparing deflection performance between different neutron source energies at HOBs other than this will produce similar relative results.

Contributions from secondary particles are included in energy profiles. In addition to the direct energy deposition from neutron scattering and absorption, energy from the paths and collisions of secondary particles is also included in the deposition tallies. All charged particles (namely protons and alpha particles) were treated as locally deposited for computational savings because their path lengths are quite small (microns or tens of microns) in comparison with the size of the spatial discretization [51]. Secondary photons (i.e. gamma-rays resulting from radiative capture and/or inelastic scattering) were tracked and the energy deposition was distributed along their true path. Past work recognized that some gamma-ray energy deposition occurs at much-later times, and opted to be more conservative and disregard energy deposition from secondary gamma-rays entirely [41]. In this work, however, capture gamma-rays were included, based on the assumption that excited nuclei decay and emit these photons extremely quickly[5] (in about 10^{-14} to 10^{-9} seconds), which is within the same time-period that the neutrons are depositing energy [58].

The MCNP6.2 cell resolution is on the order of millimeters to centime-

---

[5]There are a select few isotopes known as isomers that can be exist in a metastable state of excitation for very long time. For instance, ^{180m}Ta is estimated to have a half-life of 1.2×10^{15} *years*, which is longer than the age of the universe. There are at least 2469 isomers with half-lives of 10 nanoseconds or longer [57]. However, isomers are not relevant to, or considered in, this work. ^{32}Si and ^{33}Si are both isomers, but very few (if any) of these isotopes are expected to be produced from the ^{28}Si starting material, and even so, their half-lives are still quite short (in the tens of nanoseconds range).

ters in the radial direction, and tens to hundreds of centimeters in the angular direction. The details of this are explained and central to Sections 3.1.1 and 3.1.1.3. In brief, the selected resolution in the radial direction was informed by the neutron mean-free-path. In the angular direction, the resolution was determined by how the asteroid curvature affects a fixed penetration depth. In total, there were MCNP6.2 cell tallies for energy deposition at 256,470 spatial locations, with 498 in the radial direction and 515 in the angular direction.

Energy from neutrons is deposited into the asteroid approximately instantaneously. As discussed in Section 1.2.6, most nuclear-scale interactions occur over much shorter timescales than the time it takes for materials to overcome inertia and physically respond. Assuming instantaneous energy deposition allows for the radiation-transport simulations and the hydrodynamic simulations to be de-coupled, or run separately; otherwise a "rad-hydro" (combined radiation-transport + hydrodynamics) code would be required. Previous work has similarly treated energy deposition as instantaneous [47, 49, 59, 60]. However, the method of sourcing in spatial energy profiles in ALE3D was not compatible with truly instantaneous energy deposition, though the initial timestep could be controlled and set arbitrarily close to zero. A 1×10^{-5} microsecond window for energy deposition was selected, which is approximately instantaneous considering that significant material response is on the order of tens of microseconds.

Logarithmic interpolation of the MCNP6.2 energy deposition profiles is used to initialize the spatial energy deposition in ALE3D. Interpolation of some form is required because it was not possible or desirable to exactly match the MCNP6.2 cell resolution in the ALE3D mesh structure. The energy deposition drops-off in somewhat of an exponential fashion in the radial direction, making logarithmic interpolation much more appropriate than the linear alternative. This trend is less

33

accurate in the angular direction, but logarithmic is still a better choice in this case as well.

The asteroid inspected in this work is 300 meters in diameter, perfectly spherical, non-rotating, monolithic with strength, and composed of pure silicon dioxide (SiO_2) at standard solid density (2.65 g/cm^3) with a porosity of 30%. Like the stand-off HOB distance, it is not expected that the asteroid size will have a significant effect on which neutron energies perform best for deflection. This made the choice of a 300 meter diameter somewhat arbitrary. However, this size in particular was still chosen for a few reasons. A somewhat sentimental reason is that this is roughly the size of Apophis, a well-known asteroid first spotted by astronomers in June 2004. Later that year, Apophis was rediscovered, and initial orbital calculations estimated that the asteroid had a 2.7% chance of impacting Earth in 2029, which caused a bit of a frenzy. Luckily, it is now known that Apophis will closely-approach, and not collide with, Earth on 13 April 2029 [61]. Based on the deflection performance and warning times required, a 300 meter Apophis-sized body such as this has been considered as near the boundary where kinetic impactor missions would become "heroic" and nuclear deflection would be the much more practical choice [34]. If such an asteroid was to collide with Earth, this size-class also falls within the definition of a PHA, and thus has a fair chance of being detected in the near future (see Section 1.2.4). Lastly, as seen in Figure 1.2, many NEAs of this size are yet to be discovered. There is perhaps a greater chance that an asteroid of this size might sooner pose a threat to Earth, at least when compared to the very-large asteroids (of which most have already been discovered and deemed *not* imminent threats).

The perfectly spherical nature of this hypothetical asteroid is a bit non-ideal, considering that most asteroids are irregularly shaped [8]. However, in conglomer-

ate, perhaps a spherical shape is a good representation of asteroids on the average. Additionally, perfect spheres greatly simplified the geometry setup for the energy deposition and hydrodynamic simulations.

While many asteroids have some degree of rotation about an axis, the ALE3D simulations were easier to work with without rotation, and past work has found that rotation (or lack thereof) does not significantly affect deflection [62].

Assuming that the asteroid is monolithic and that it has material strength simplifies the hydrodynamic simulations. This is a reasonable approximation for some asteroids, but other asteroids are loose rubble-piles bound only by gravitational attraction and therefore are not well-represented by this assumption. Based on measured rotation periods from asteroid light curves, most asteroids are believed to be rubble-piles. However, as of 2019, there are 887 known objects with short-enough rotation periods requiring that they have some cohesive strength (such fast rotators are potentially, but not necessarily, monoliths), most of them being stony NEAs with diameters of less than 1 kilometer [63].

SiO_2, or quartz, was selected as the asteroid material for a few reasons. First, it is a well-studied and well-characterized material, being a major component of many of Earth's soils. Second, S-type (siliceous) asteroids are the most common in the inner asteroid belt, closest to Earth. Lastly, a complete material model for SiO_2 was available for use. The SiO_2 in the MCNP6.2 phase of this work was composed entirely of ^{28}Si and ^{16}O constituent isotopes. This is another reasonable assumption. According to the chart of the nuclides, there are three stable isotopes of silicon, and ^{28}Si is 92.2% abundant. There are also three stable isotopes of oxygen, yet 99.76% of all oxygen nuclei are ^{16}O [64].

Densities and porosities among asteroid bodies are highly variable. The standard density of SiO_2 is 2.65 g/cm^3, the density chosen for this problem. However, due to

35

an asteroid porosity, Φ, of 30%, the bulk or effective density is 1.855 g/cm^3. $\Phi = 0.30$ was selected both because it is a reasonable value and because the resulting bulk material density is close to 2 g/cm^3, which is typical of the asteroid densities that have been measured [65].

In summary, this asteroid was intended to be a rough representation of a potential PHA where nuclear deflection would be appropriate. This research sought to develop a process to compare the deflection performance based on differing source neutron energies. Due to the wide range of asteroid sizes, compositions, densities, shapes, and other parameters, and due to the amount of time and effort involved in procuring quality energy deposition profiles and hydrodynamic simulations, the goal was not, and never could have been, to answer the question of "best neutron energy" for every asteroid in existence. The same procedures for energy deposition and hydrodynamic response in this work could be applied to other asteroids in the future.

A material model for silicon dioxide at 290 K, with strength, was used. This material model was developed by Eric Herbold of LLNL's Computational Geosciences Group. It belongs to the GEODYN library, and references Livermore Equation of State (LEOS) #2210 for silicon dioxide. The Cap model contributes strength characteristics to the material, making the asteroid a rigid or cohesive body rather than rubble. The reference temperature is 290.1112 K, or room temperature on Earth, which was the initial temperature of the asteroid in this work [66]. However, typical asteroids are believed to have average temperatures around 100-200 K [67]. Considering that the neutron energy deposition in this research heats the surface to thousands of Kelvin, or even tens of thousands of Kelvin, this difference in initial temperature conditions is not expected to have any perceptible impact.

Heat transfer (both via conduction and radiation) is neglected. The prompt blow-off momentum from melting and vaporization concludes a few hundred

36

microseconds after the energy deposition from a stand-off nuclear detonation. The resulting shockwave formed in the asteroid traverses the object back-and-forth over the course of seconds [68]. Conductive heat transfer requires much more time than hundreds of microseconds, or even a few seconds, to be significant. Thus, after neutron energy deposition, it is the hydrodynamic physics that dominate the accuracy of asteroid deflection by blow-off. As a result, simulations are run "hydro-only," with thermal energy transfer turned off, simplifying the problem and saving computational time. While radiative heat transfer is somewhat more significant for super-heated materials in the energy deposition region, this mode of thermal energy transfer is also not implemented. These types of assumptions have been made in past work [69].

ALE3D mesh resolution is on the order of centimeters in the energy deposition region. Except at the molecular level and below, homogeneous material behaves as a continuum at the macro-scale. Any discretization in the hydrodynamic simulations is therefore an approximation of real materials, but it is of course necessary. Due to computational limitations, centimeter-scale resolution was the most that could be afforded in the energy deposition region of the asteroid in ALE3D. As discussed in more detail later in Section 4.1.2, the level of discretization was informed by past work inspecting the blow-off momentum error as a function of the mesh resolution [47].

In the ALE3D setup, gravity is neglected, and the escape velocity condition for blow-off fragments from the asteroid is constant throughout space and time. Gravity physics are not enabled in the hydrodynamic calculations. Instead, the escape velocity, which is the speed that an object must reach in order to break free from the gravity well of (in this case) an asteroid and leave it without further propulsion, is calculated analytically and used as a threshold in the simulations.

37

The formula is

$$v_{escape} = \sqrt{\frac{2GM}{r}}, \tag{1.2}$$

where G is the universal gravitational constant, M is the mass of the body to be escaped from, and r is the distance between the escaping object and the larger body's center-of-mass [70]. As material is ablated and blows-off the surface and escapes, the mass of the asteroid body M changes. However, because the blow-off mass is minuscule in comparison, dwarfed entirely by the much-greater asteroid mass, the escape velocity for any subsequent blow-off is barely affected. The distance r is also slightly different depending on where the blow-off fragment originates, and the center-of-mass of the asteroid is changing slightly over time as well. Given that M and r should not change very much for deflection scenarios, a constant escape velocity was implemented.

The asteroid simulation is run in a two-dimensional, axisymmetric geometry. In other words, the 3-D spherical asteroid is represented as a 2-D semi-circle in ALE3D. This is done to save computational time and memory, and such an assumption has been made in past work [34]. This approach also allows for a finer spatial mesh resolution for a given number of elements or zones. If the available computational resources were unlimited, a full 3-D simulation would be preferable. However, given an isotropic point-source with the perfectly spherical asteroid, the resulting energy deposition profiles are symmetric, meaning that a 2-D axisymmetric setup is appropriate.

1.4 Novel Research Contributions

Energy deposition profiles and coupling efficiencies in an asteroid for various neutron energy sources were calculated using the MCNP6.2 radiation-transport code. The velocity changes that resulted from a set of simulated detonations were deter-

mined through the ALE3D hydrodynamic code. Throughout this process, several research objective questions were answered in part, and many more uncovered. A few noteworthy achievements were accomplished along the way. Some of these, listed below in no particular order, might contribute in a small way to the field of asteroid mitigation simulations, or rather help set-up other interesting research.[6]

- Developed MCNP6.2 input-generator system to calculate energy deposition spatial profiles with an informed discretization.

- Showed how energy deposition profiles change with, and re-affirmed that energy coupling efficiencies depend on, the source neutron energy.

- Visualized how the energy deposition profiles from Monte Carlo simulations are, in some cases, significantly different than a commonly-used analytical approximate equation [41, 46, 47, 60].

- Analyzed how asteroid deflection changes due to differing neutron sources, showing that differences in both the energy deposition profiles and the energy coupling result in different δV velocities.

- Compiled a high-fidelity, 46-group energy deposition data-set for potential future work to determine the optimal neutron energy spectrum for one type of asteroid.

- Ensured, single-handedly, that the world will be saved from any future asteroid doom.

---

[6]The author will grant the possibility that one of the listed items might be a small, very slight embellishment.

II. Theory

2.1 The Atom

All matter is made of atoms. An atom is the "smallest unit" of a chemical element that still retains the properties of that chemical element. In other words, it is the fundamental building block of bulk material [71].

However, it is not *the* fundamental unit of physical matter. The atom itself is composed of still-smaller objects. There are three particles that define an atom — the neutron, the proton, and the electron.[1] Neutrons and protons are called nucleons, as these are the quantum-bound particles that form the nucleus, or the densely-packed central core of an atom. Electrons surround the nucleus in an electron cloud, showing both wave-like and particle-like characteristics [72].

A proton has a unit-one positive-charge and a mass of 938.27 MeV/c^2. An electron has a unit-one negative-charge and a mass of 0.511 MeV/c^2. A neutron is a neutral (chargeless) particle with a mass of 939.56 MeV/c^2. One electron-volt (eV) is equivalent to 1.602×10^{-19} Joules (J), or the energy gained by an electron when it is accelerated in a potential gradient of one volt (V). Nuclear energies in the nucleus are commonly expressed in terms of MeV, or millions of electron-volts [73].

2.2 Nuclear Reaction Mass-Energy

The law of conservation of mass and the law of conservation of energy are both widely known. However, in reality, it is really the composite quantity *mass-energy* that is conserved at all times. This is expressed in Einstein's famous equation, the

---

[1]And of course, physicists now know that these three particles are themselves made of even smaller elementary particles (quarks, leptons, and gluons). Are *these* the fundamental, unbreakable units of matter? Only time will tell![2]

[2]But they probably are the true elementary particles.[3]

[3]You know, maybe.

40

fundamental result from his special theory of relativity,

$$E = mc^2, \qquad (2.1)$$

where E is energy, m is mass, and c is the speed-of-light universal constant equaling 2.99792458×10^8 m/s [73]. In macro-scale physics involving chemical and mechanical interactions, both mass and energy are (separately) conserved because there is no exchange between mass and energy. However, because nuclear reactions involve the conversion of mass into energy and energy into mass, Equation 2.1 is required for conservation. This equation also provides an alternative definition for c^2: 931.502 MeV/u, where "u" is shorthand notation for the atomic mass unit (amu), which is the unit of mass in the periodic table.[4] The proton's mass is 1.00728 u, the electron's mass is 0.00055 u, and the neutron's mass is 1.00867 u [73].

Because the value of c^2 is so large, for every reaction with even a very, very small change in nuclear mass, there is an enormous amount of energy involved. Nuclear reactions can be either exothermic (releasing energy by destroying mass) or endothermic (requiring energy in order to create mass). Following from Equation 2.1,

$$Q = \left(m_{initial} - m_{final} \right) c^2, \qquad (2.2)$$

where $m_{initial}$ is the initial mass of the reactants prior to a reaction, m_{final} is the resulting mass of the products following a reaction, and Q is the amount of energy released or absorbed. This is the so-called "Q-value" calculation for nuclear reactions. If the Q-value is negative, then the reaction is endothermic and requires energy to occur (because mass is created from this energy). If the Q-value is positive, then the reaction is exothermic and releases energy (because nuclear mass is destroyed in the

---

[4]The atomic mass unit was defined in reference to the ^{12}C atom; indeed, one amu is identically $1/12^{th}$ the mass of ^{12}C [74]. This is why the ^{12}C isotope has a mass of exactly 12.000 u [64].

41

reactive process) [71].

2.3 Binding Energy of the Nucleus

Consider the mass of an atom of plutonium-239 (^{239}Pu), which is one of the isotopes (i.e. nuclides) of elemental plutonium. According to the chart of the nuclides (analogous to the periodic table of elements, but for isotopes), the atomic mass m_A of ^{239}Pu is 239.0521565 u [64]. ^{239}Pu has 94 protons, 94 electrons, and 145 neutrons. The sum of these individual components is $m_{sum} = 94m_p + 94m_e + 145m_n$, which is about 240.99317 u. Notice that the measured atomic mass m_A for ^{239}Pu is not equal to the sum of the constituent particles m_{sum}. Rather, $m_A < m_{sum}$, and in fact this relation holds true for all existing isotopes of all elements. This characteristic difference between the mass of an atom and the sum of the masses of its constituent protons, electrons, and neutrons is known as the mass deficit or mass defect, $\Delta = m_{sum} - m_A$, which is positive for all nuclei [71]. In the case of ^{239}Pu, $\Delta = 240.99317 - 239.0521565 \approx 1.9410135$ u.

How can an object (in this case, an atom) be less than the sum of its parts? It is because of mass-energy conversion within the nucleus. The nucleus is made of tightly-packed protons and neutrons, but because protons are all positively-charged and neutrons are neutral, these particles would not ordinarily stick together; rather, they would fly away from each other due to electrostatic repulsion. However, there exists a strong nuclear force (SNF), a powerful and attractive force that acts between nucleons only over the very short distances between them (about 2×10^{-15} m). For stable and long-lived radioactive isotopes, the attractive SNF overcomes the repulsive Coulombic forces and binds the nucleus together. The magnitude of mass deficit Δ is a measure of the strength of the SNF; larger values of Δ mean that more nuclear mass was converted into energy to more strongly bind the nucleus together [75]. The

42

binding energy B of the nucleus is defined as

$$B = \Delta \cdot c^2, \qquad (2.3)$$

which is merely a specific case of the Einstein mass-energy conversion formula (Equation 2.1).

More accurately, it is the binding energy *per nucleon*, or B/A for mass number A (the number of protons and neutrons in the nucleus), that is more informative. The larger the value of B/A is, the more stable the nucleus [76]. Figure 2.1 shows the curve of binding energy per nucleon as a function of mass number. The average B/A value for most nuclei, to within 10%, is about 8 MeV per nucleon [73]. The most tightly-bound nuclei are nickel-60 (Ni-60), iron-56 (Fe-56), iron-58 (Fe-58), and nickel-62 (Ni-62), coined "the iron group" by astrophysicists for their abundance in stellar processes involving the synthesis of heavy elements. All four of these species have nuclear binding energies approaching 8.8 MeV per nucleon, and all are in the vicinity of the $A \approx 60$ peak of the curve [77].

Exothermic (energy-producing/releasing) reactions are those which result in products with increased binding energy compared to the initial reactants, going from less to more stable nuclei. There are two candidate reactions for nuclear energy production: fission and fusion. Nuclear fission moves from heavy nuclei on the far-right of Figure 2.1 towards lighter nuclei with higher unit binding energies. Nuclear fusion instead begins with light nuclei on the far-left and ends with heavier nuclei closer to the B/A peak [76].
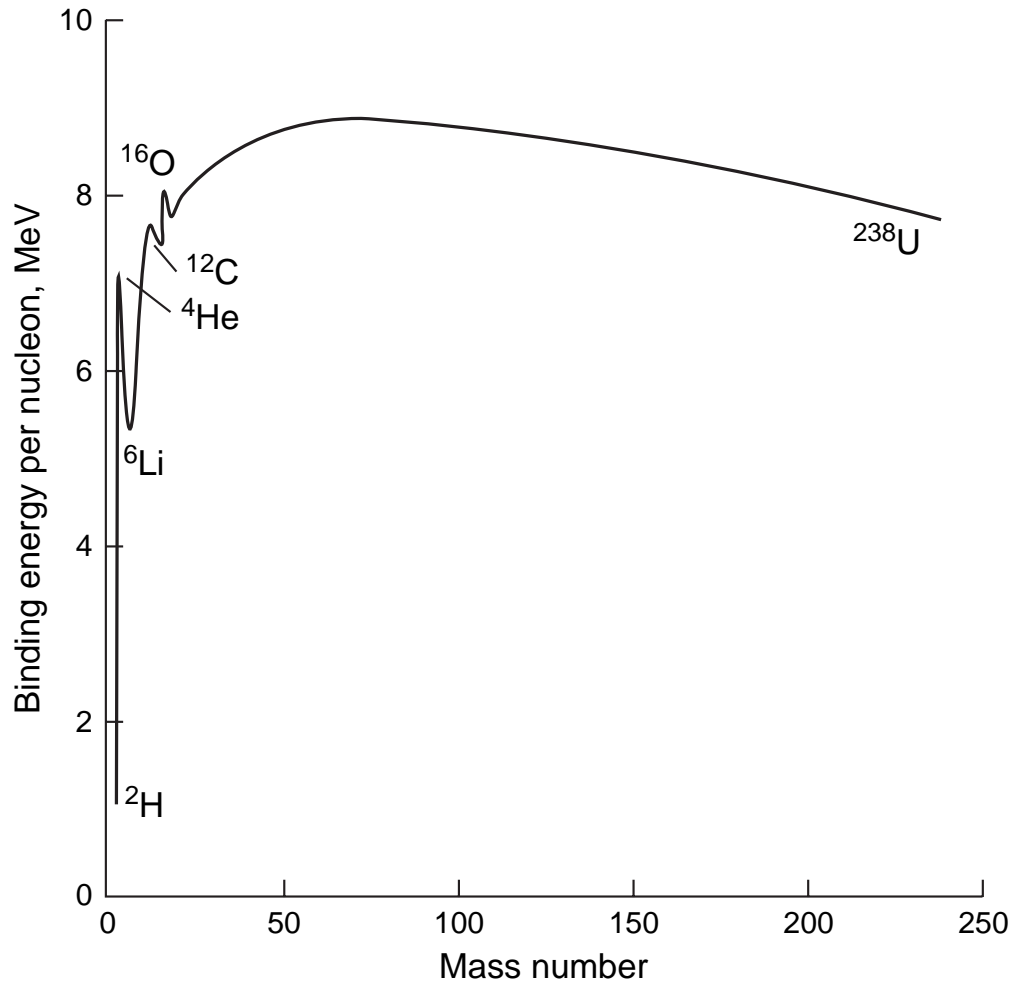
FIGURE 1.1 Curve of binding energy per nucleon.

Figure 2.1 The binding energy per nucleon. The peak occurs around $A = 60$. Nuclei with even numbers of protons and neutrons are usually more stable than their odd isotope relatives, which is why the resonance-esque peaks for certain nuclides are shown. Nuclear fission is a process that results in traveling from the far-right towards the center peak of B/A, while nuclear fusion's path is from the far-left up towards the middle. Taken from [76]. — this figure was published in "Fundamentals of Nuclear Reactor Physics," Elmer E. Lewis, pg. 8, Copyright Elsevier (2008). Reprinted by permission from Elsevier.

a heaver nuclei, higher on the binding energy curve, and fission reactions in which a heavy nucleus splits to form two lighter nuclei, each with a higher binding energy per nucleon.

1.4   Fusion Reactions

Equation (1.2) is an example of a charged particle reaction, since both nuclei on the left have atomic numbers greater than zero. Such reactions are difficult to bring about, for after the orbiting electrons

2.4 Neutrons from Fission & Fusion

Nuclear devices are designed to detonate by way of fission, fusion, or both in sequence. Fission is the process of splitting the nucleus of a large, heavy atom, breaking it into two or more so-called fission fragments, and releasing large amounts of energy in the process. Fusion is the opposite — combining two small, light nuclei to form a single heavier nucleus, also releasing excess energy [78]. Following any rapid and/or prolonged radioactive decay, both of these processes eventually culminate in stabler atoms with more binding energy per nucleon than the starting reactants, i.e. moving up the curve in Figure 2.1.

While some radioactive isotopes decay by way of spontaneous fission, controlled nuclear detonations operate via induced fission, where an initial activation source sends neutrons to collide with nuclear fuel and initiate a series of fissions. Typically, uranium and plutonium are the heavy-elements used as reactants to fuel fission reactions. Specifically, the cores of nuclear devices are metals, largely consisting of the isotopes ^{235}U and ^{239}Pu. These are two of the only known fissile isotopes, meaning that they can undergo fission with any incident neutron, even extremely low-energy (thermal) neutrons [79]. ^{235}U and ^{239}Pu also each have a favorable reproduction factor, η, because they usually release 2-to-3 free neutrons for every fission event. If the nuclear fuel has sufficient mass and density, this allows for criticality to be reached and a chain reaction to ensue — a nuclei will fission after absorbing one neutron, and the process of fission sends two or three more neutrons outwards that can fission neighboring nuclei, which each release two to three more neutrons, and so forth. In this way, both the number of fission events and neutron population grow exponentially. Because nuclear reactions like fission occur in very short timescales (on the order of "shakes," or 10^{-8} s, to microseconds), the exponential growth of the neutron population and the number of fission events occurs very quickly [55].

Eventually, enough time has passed that the surrounding nuclear device material and casing can respond, and the energy density is so high that the material and energy expands outwards rapidly, i.e. an explosion. At this point, because there is greater distance between any un-spent ^{235}U or ^{239}Pu, fissioning effectively stops, and the neutron population stops growing and is rather free to propagate outwards. For every fission reaction, approximately 200 MeV is released. This energy is distributed in various forms as shown in Table 2.1. Notably, about 5 MeV is imparted as kinetic energy to the neutrons. Given that 2-3 neutrons are released per fission, it is no surprise that the average neutron energy is approximately 2 MeV [55]. However, fission neutron energies do not follow a symmetric distribution. The energy spectrum of fission neutrons is described by the Watt distribution (or alternatively, a thermal Maxwellian distribution), visualized in Figure 2.2. At the peak of the Watt spectrum, the most probable energy for a neutron born from fission is $\sim$0.8 MeV, close to 1 MeV [50].

Table 2.1. Distribution of fission energy. Each fission reaction releases around 200 ± 6 MeV of energy, though only $\sim$180 MeV is promptly released. The first three items in this list represent prompt energy, while the latter three is energy released at later times from fission products. Most of the prompt energy is allotted to the fission fragment nuclei, but several MeV is still available for the neutrons. Taken from [55].

Energy Form	Energy (MeV)
Kinetic energy of fission fragments	165 ± 5
Instantaneous gamma-ray energy	7 ± 1
Kinetic energy of fission neutrons	5 ± 0.5
Beta particles from fission products	7 ± 1
Gamma rays from fission products	6 ± 1
Neutrinos from fission products	10

While fission chain reactions are only physically possible for a select few isotopes, fusion reactions, in principle, can occur with a wide variety of nuclides. The only requirement is furnishing the proper high-pressure, high-temperature environment that

46

For example, consider the specific fission reaction of U-235 shown in Equation (5) that produces La-147 and Br-87. The kinetic energies of the fission fragments are calculated in Eqs. (6) and (7), respectively, and the energy from the fission reaction products are shown in Table 2. As stated earlier, the ranges of fission fragments in matter are very short due to their mass and charge; the ranges of the two fission fragments used in this example are pictured in Figs. 6 and 7. The bromine-87 atom, for example, has a range of 6.29 μm in uranium metal. The spatial energy distributions of both
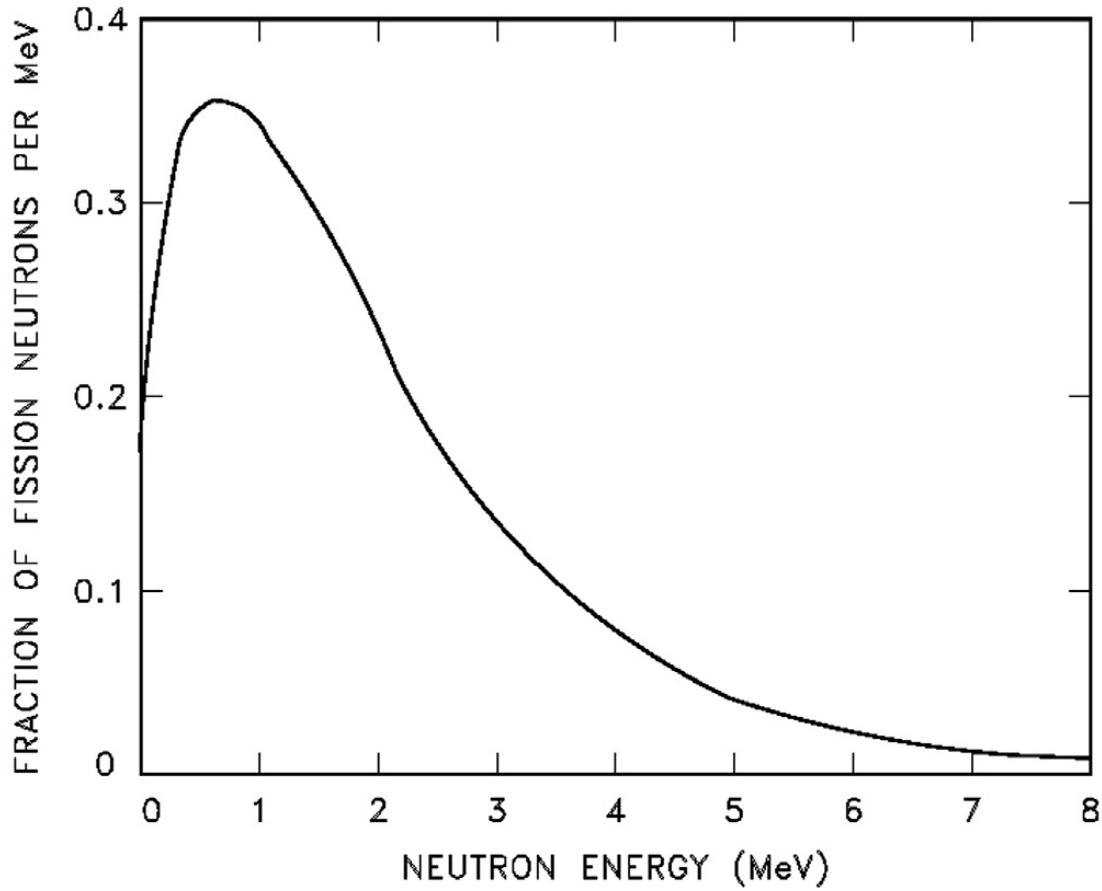
Fig. 4. Neutron energy spectrum produced by the thermal fission of U-235 (DOE-HDBK-1019/1-93, 1993). The average energy is 2 MeV, while the most probable energy is close to 1 MeV (at the peak). Taken from [80].

Fig. 5. U-2...
(DOE-HDBK...

provides nuclei with enough kinetic energy to overcome the very strong Coulombic repulsion of two positively-charged nuclei. Light-nuclei with low mass numbers A have a low number of protons and therefore a lower repulsive force to defeat. Thus, practicality limits the number of feasible fusion reaction channels in nuclear detonations. For heavy elements like uranium or plutonium, with 92 and 94 protons in their respective nuclei, the electrostatic repulsion is effectively insurmountable. For isotopes with only a single proton (i.e. elemental hydrogen), the Coulomb forces are the weakest and therefore require the least amount of energy to allow nuclei to fuse [73].

Two isotopes of hydrogen in particular are utilized in nuclear devices with fusion components. Ordinary hydrogen has a nucleus made of one proton and zero neutrons. Deuterium (^{2}H, or ^{2}D) and tritium (^{3}H, or ^{3}T) are heavy isotopes of hydrogen formed by adding a single neutron to the former's nucleus and two neutrons to the latter. With these species, there are three major fusion reactions with four total reaction outcomes:
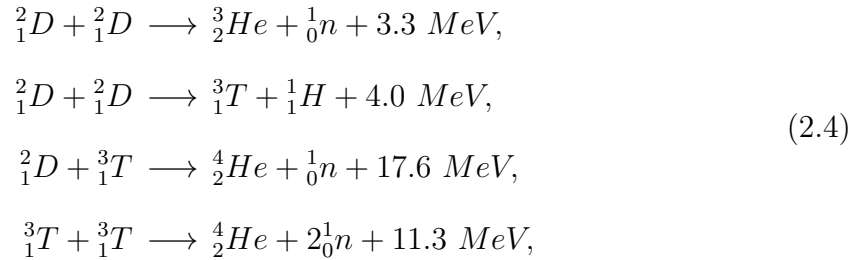
$$
\begin{aligned}
{}_1^2D + {}_1^2D &\longrightarrow {}_2^3He + {}_0^1n + 3.3 \ MeV, \\
{}_1^2D + {}_1^2D &\longrightarrow {}_1^3T + {}_1^1H + 4.0 \ MeV, \\
{}_1^2D + {}_1^3T &\longrightarrow {}_2^4He + {}_0^1n + 17.6 \ MeV, \\
{}_1^3T + {}_1^3T &\longrightarrow {}_2^4He + 2{}_0^1n + 11.3 \ MeV,
\end{aligned}
\tag{2.4}
$$

The energies listed on the product side are the Q-values, the energy released in these exothermic reactions. At the required environmental temperatures for fusion (tens of millions of K), the first two reactions (D-D fusion) occur with about equal probability. The fourth channel (T-T fusion) has an extremely low chance of occurring. The third channel (D-T fusion) has by-far the greatest cross-section, an order-of-magnitude or greater than the other paths. It is D-T fusion that is the principal fusion reaction; while the other reactions do occur, they occur in much smaller numbers and are negligible in comparison [55]. If the D-T reactant nuclei have very small kinetic

energies, then by conservation of momentum and energy, the product neutron is monoenergetic and accepts 14.1 MeV of the 17.6 MeV Q-value [73].

2.5 Neutron Interactions

A free neutron is an uncharged, ionizing form of radiation. When free neutrons enter and traverse a material medium, they are subject to exponential attenuation, which is an empirical model for neutron interactions. This is simple to consider in a slab geometry, as

$$I(x) = I_0 \, e^{-\Sigma_t x}, \tag{2.5}$$

where $I(x)$ is the number of neutrons that have survived without interacting at a penetration distance x into the material medium, I_0 is the initial or incident number of neutrons at the surface of the material medium, and Σ_t is the total macroscopic cross-section probability. Σ_t is a material-dependent parameter. If Σ_t is large, then most neutrons interact very quickly and at shallow depths x. If it is small, then neutrons penetrate further into the medium.

Broadly, there are two ways that neutrons can interact with material: scattering and absorption. These interactions are with the nucleus; it is very rare for uncharged neutrons to react at the atomic scale with charged electrons [71]. As the name suggests, scattering is the process of a neutron colliding with and then bouncing off of a nucleus. Scattering may be elastic, where kinetic energy is conserved and standard two-body kinetics apply, or inelastic, where kinetic energy of the neutron-nucleus system is not (immediately) conserved. For the latter, inelastic scattering involves some of the neutron's energy being temporarily "lost," where the target nucleus is put into an excited state. Absorption occurs when the incident neutron is absorbed by the nucleus. Absorption will result in fission only if the target nucleus is fissionable. More often, absorption is a capture-type reaction, putting the nucleus in

49

an excited state, and resulting in the emission of secondary energy and/or particles. A diagram-tree of neutron interaction types is shown in Figure 2.3.

Figure 2.1. Hierarchy of neutron interactions.
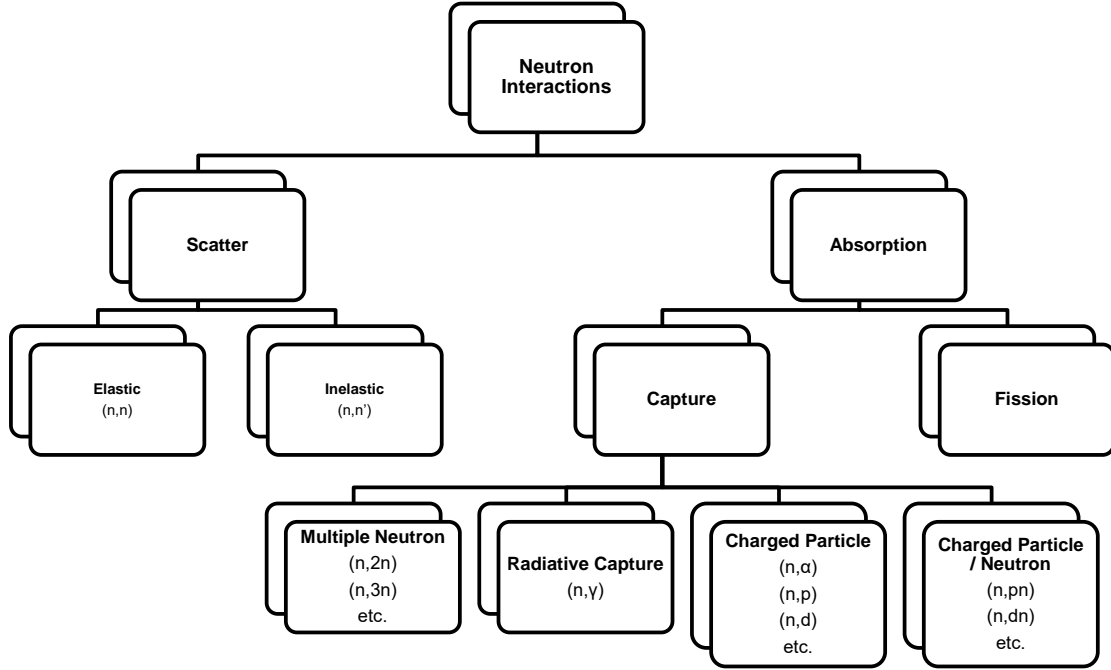
Figure 2.3. Hierarchy of neutron interactions, consisting of either scattering or absorption. Taken from [49].

2.2.1 Scattering

Elastic scattering involves a neutron bouncing off of a nucleus, with kinetic energy conserved throughout the interaction. It is denoted as (n,n), which is shorthand for stating that the reaction involves an incident neutron n and results in an ejectile neutron n. The maximum amount of energy that a neutron can lose in an elastic scatter (i.e. give-up to the nucleus) depends on the mass of the target nucleus, and is given by

When a neutron scatters off a nucleus, it transfers some portion of its kinetic energy to the nucleus. If the energy and momentum are conserved in the interaction, it is considered an elastic scattering event represented as (n,n). For a neutron undergoing elastic scatter, the maximum energy it can transfer to the nucleus, ΔE_{max} depends on the atomic mass, A, of the target nucleus and is given by

$$\Delta E_{max} = E_0 \left[1 - \left(\frac{A-1}{A+1} \right)^2 \right] = E_0 \left(1 - \alpha \right), \tag{2.6}$$

$$\Delta E_{max} = E \left[1 - \left(\frac{A-1}{A+1} \right)^2 \right] = E \left(1 - \alpha \right), \tag{5}$$

where E_0 is the initial, incident kinetic energy of the neutron and A is the mass number of the participating nucleus [49]. Assuming that the target nucleus was at rest prior to interaction, the minimum possible energy that a neutron can have after

where E is the initial energy of the neutron, and α is defined by the equation. The minimum remaining energy, E_{min}, of the neutron following the collision is found from

$$E_{min} = E - \Delta E_{max} = \alpha E. \tag{6}$$

a (n,n) reaction is

$$E'_{min} = E_0 - \Delta E_{max} = \alpha E_0, \tag{2.7}$$

where α is identified as the smallest possible remaining fraction of the neutron's energy [49]. Another parameter to describe scattering is the lethargy ξ, which is the average decrease of the logarithm of the neutron energy per scatter [81]:

$$\xi = \ln E_0 - \ln \overline{E'} = 1 - \frac{(A-1)^2}{2A} \ln \left(\frac{A+1}{A-1} \right). \tag{2.8}$$

With this, one can determine the average number of elastic scattering collisions $\overline{N}$ required to reach a certain energy level E' for a given starting neutron energy E_0:

$$\overline{N} = \frac{\ln (E_0/E')}{\xi}. \tag{2.9}$$

Table 2.2 records collision parameters for neutrons that elastically scatter off of silicon and oxygen nuclei, the constituents of silicon dioxide. ^{16}O is more effective at slowing-down neutrons and absorbing their energy via elastic scattering than ^{28}Si is.

Table 2.2. Elastic scattering parameters for ^{28}Si and ^{16}O.

Isotope	α	ξ	$\overline{N}$ for 1 MeV to 1 eV	$\overline{N}$ for 14.1 MeV to 1 eV
^{28}Si	0.86683	0.06976	199	236
^{16}O	0.77855	0.11995	116	138

Inelastic scattering is denoted by (n,n'), meaning that the reaction involves an incident neutron and results in an ejectile neutron without conservation of kinetic energy. This mode of scattering is a threshold reaction — it can only occur if the incident neutron has an energy greater than the lowest nuclear exited state of the target nucleus. After reaching an excited state, the vast majority of nuclei near-instantaneously emit a photon with an energy corresponding to the difference between

51

the excited state and a lower energy level [58].

Fission following an absorption only occurs for a select number of fissionable nuclides. In the lens of neutrons traversing all other materials, absorption is akin to neutron capture. The neutron combines with the target nucleus and forms a compound nucleus (C^*), which can form a stable isotope, though it is often unstable and in an excited nuclear state [73]. If the latter, similarly to inelastic scattering, most excited nuclei typically decay extremely quickly, resulting in a recoil nucleus and a ejectile particle. The two-body reactants and products, with the intermediate compound nucleus, are represented in reaction formula by

where the 2.225 MeV is the Q-value of the reaction. Another possibility is the emission of one or more nucleons. In this case, the reaction is of the form

$$M_1 + M_2 \stackrel{}{\longrightarrow} C^* \stackrel{}{\longrightarrow} M_3 + M_4, \tag{2.10}$$

where M_1 is the mass of the initial neutron, M_2 is the mass of the target nucleus, M_3 is the mass of the recoil nucleus, and M_4 is the particle mass of resulting ejecta (if any). Figure 2.4 is a diagram of this pathway [49].

where M_1 and M_2 are the mass of the neutron and target atom, and M_3 and M_4 are the mass of the resultant atom and emitted nucleon(s) as shown in Figure 2.2.

Figure 2.2. Nuclear reaction.
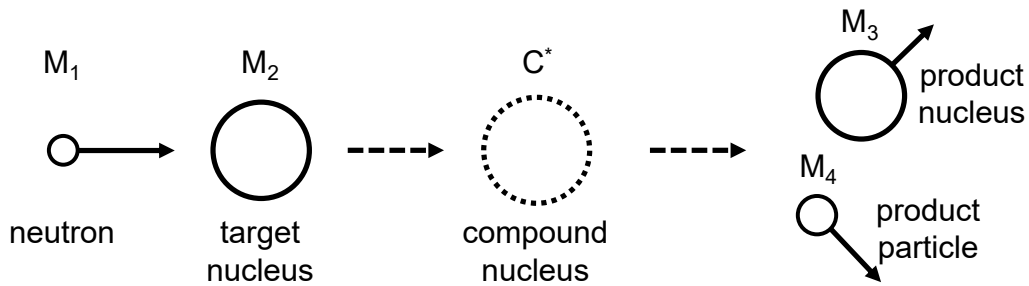
Figure 2.4. Nuclear capture reaction diagram. Note that M_4 *mass is not formed in all capture reactions; sometimes only radiative energy (a photon) is emitted. Taken from [49].*

If $M_1 + M_2 > M_3 + M_4$, then the reaction is energetically possible for any incident neutron energy. However if $M_1 + M_2 < M_3 + M_4$, there is an energy threshold which must be overcome for the reaction to take place.

If the capture reaction is exothermic, then the mass of the reactants is greater than the mass of the products ($M_1 + M_2 > M_3 + M_4$), and the Q-value is greater than zero. This energy of magnitude Q is released on the product side, split between M_3 and

The Q values, in MeV, for all the reactions and isotopes examined in this paper are shown in Table 2.2. If the value is positive, then the reaction is possible for any incident neutron energy. However, a negative value represents the energy deficit of the reaction. This energy deficit does not, however, represent the threshold energy that the reaction requires to occur. According to Turner, "The neutron must have

www.manaraa.com

M_4 according to conservations of momentum and energy. Because energy is produced by burning mass, there is no energetic threshold that the neutron must satisfy for exothermic reactions to occur. However, if the mass of the products is greater than the mass of the reactants, then the Q-value is negative, and the capture reaction is endothermic. There *is* an energy threshold for these reactions because energy is required for them to occur in the first place. The threshold (minimum) energy E_{th} that must be supplied by the incident neutron for an endothermic reaction to occur is

$$E_{th} = Q \cdot \left(1 + \frac{M_1}{M_3 + M_4 - M_1} \right).\tag{2.11}$$

E_{th} is not simply Q due to the continued motion of the center of mass of the colliding particles after the collision [71]. When $Q < 0$, energy is burned to produce mass, meaning that there is a net loss of energy throughout the system.

Capture reactions are denoted by the type of emission they produce. (n,γ) is radiative (massless) capture that releases a gamma-ray. (n,α) means that neutron absorption led the emission of an alpha particle, (n,p) refers to the release of a proton, (n,d) for a deuteron exile, (n,t) for a triton, (n,2n) for one neutron absorption resulting in two neutrons being emitted, and so forth. Using Equation 2.2 for exothermic reactions and Equation 2.11 for endothermic reactions, Table 2.3 lists the +Q energies created from, along with the -E_{th} energies required for, various capture reaction channels in silicon and oxygen. The first excited nuclear state -E_1^* is also listed (recall that inelastic scattering is also a threshold reaction based on this value).

2.6   Nuclear Cross-Sections

Neutron interactions are probabilistic. The physics of interactions at this level are complex, non-intuitive, and non-linear. It is known and observed that reaction probabilities depend on isotopic material properties and on the energy of the free

Table 2.3. Neutron reaction energies for ^{28}Si and ^{16}O. Q-values for exothermic capture reactions are positive to signify that this energy is produced, and E_{th} values for endothermic capture reactions are negative to signify that this energy is required (and lost). The energy level of the first excited state E_1^* for each nuclei is also listed, negative with the recognition that inelastic scatter requires neutrons with this energy or more. All values are in MeV. Reproduced from [49].

Isotope	Capture Reaction						E_1^*
	(n,γ)	(n,p)	(n,d)	(n,t)	(n,α)	(n,2n)	
^{28}Si	8.474	-3.466	-9.698	-16.743	-2.749	-17.799	-1.7790
^{16}O	4.143	-9.669	-10.527	-15.391	-2.355	-16.651	-6.0494

neutron.

Nuclear physics experiments and simulations have generated microscopic cross-sections for as many isotopes and neutron energies as possible. The macroscopic cross-section Σ depends on the microscopic cross-section σ,

$$\Sigma = N\sigma = \frac{\rho N_A}{M}\sigma, \tag{2.12}$$

where N is the number density of the material, ρ is the density of the material, N_A is Avogadro's number, and M is the molecular weight. N only depends on bulk physical properties, while σ depends on nuclear properties. The mean-free-path (mfp), which is the expected distance that a neutron will travel on average before colliding with a nuclei and interacting, is the inverse of Σ:

$$\lambda = \frac{1}{\Sigma} = \frac{1}{\frac{\rho N_A}{M}\sigma}. \tag{2.13}$$

Of course, because Σ depends on the properties of the nucleus, the neutron energy, and the properties of the bulk material, so too does the mfp λ.

The microscopic cross-section σ has units of area, traditionally in barns (b), which is the equivalent of 10^{-24} cm^2. In this way, the total microscopic cross-section can be

envisioned as the total area that a neutron "sees" when it approaches a nucleus. The larger the area, the larger the nucleus appears and the more likely that an interaction occurs. The likelihood of a particular reaction path being taken could be thought of as a fractional slice of the total σ area, similar to a section of a pie-chart.

For a fixed material, as the neutron energy changes, the total microscopic cross-section magnitude changes, and the available reaction channels and their relative probabilities also change. In other words, neutrons of different energies will experience different nuclear interactions as they travel through the same material. Depending on the material properties, lower energy neutrons in bulk might not penetrate as far as higher energy neutrons, and the former might be more susceptible to scatter reactions and the latter absorption. Figures 2.5a and 2.5b plot the microscopic cross-sections in ^{28}Si for neutrons of various energies. Figures 2.6a and 2.6b plot the microscopic cross-sections in ^{16}O for neutrons of various energies. Note that far-reaching logarithmic scales for both neutron energy and cross-section magnitude are required in order to capture the wide-range of reaction channel probabilities.
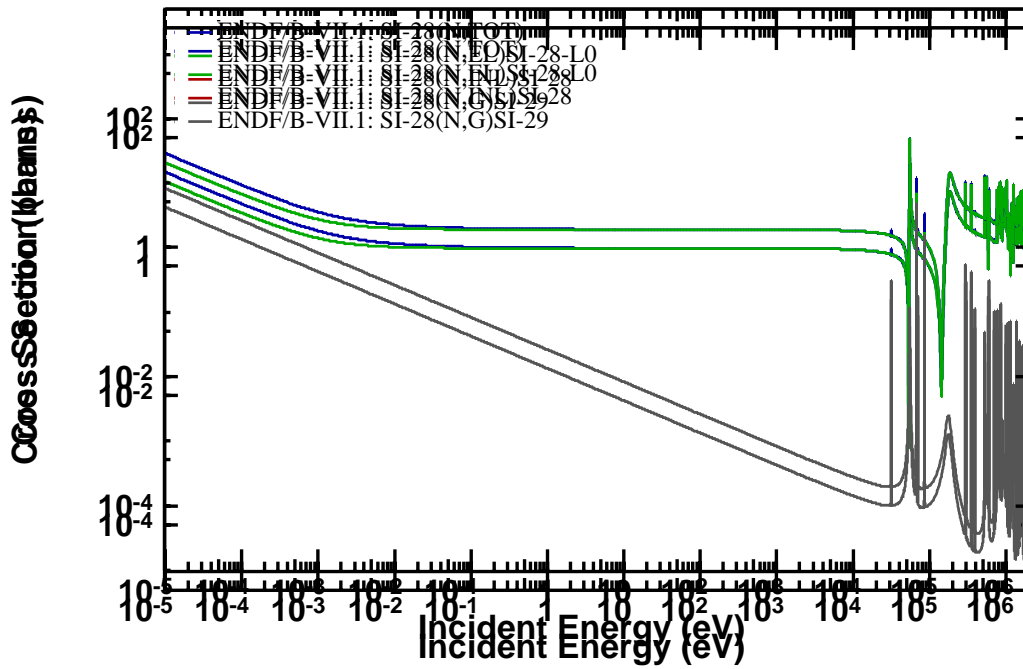
(a) ^{28}Si microsconic cross-sections for neutrons below 2 MeV

Figure 2.3. Neutron cross sections in ^{28}Si for reactions occurring at energies below 2 MeV. Created in ZVView with data from [20].

(b) ^{28}Si microscopic cross-sections for neutrons below 15 MeV

Figure 2.4. Neutron cross sections in ^{28}Si for reactions occurring at energies below 15 MeV. Created in ZVView with data from [20].

Figure 2.5. ^{28}Si microscopic cross-sections. Taken from [49].

18

(a) ^{16}O microscopic cross-sections for neutrons below 2 MeV.

Figure 2.5. Neutron cross sections in ^{16}O for reactions occurring at energies below 2 MeV. Created in ZVView with data from

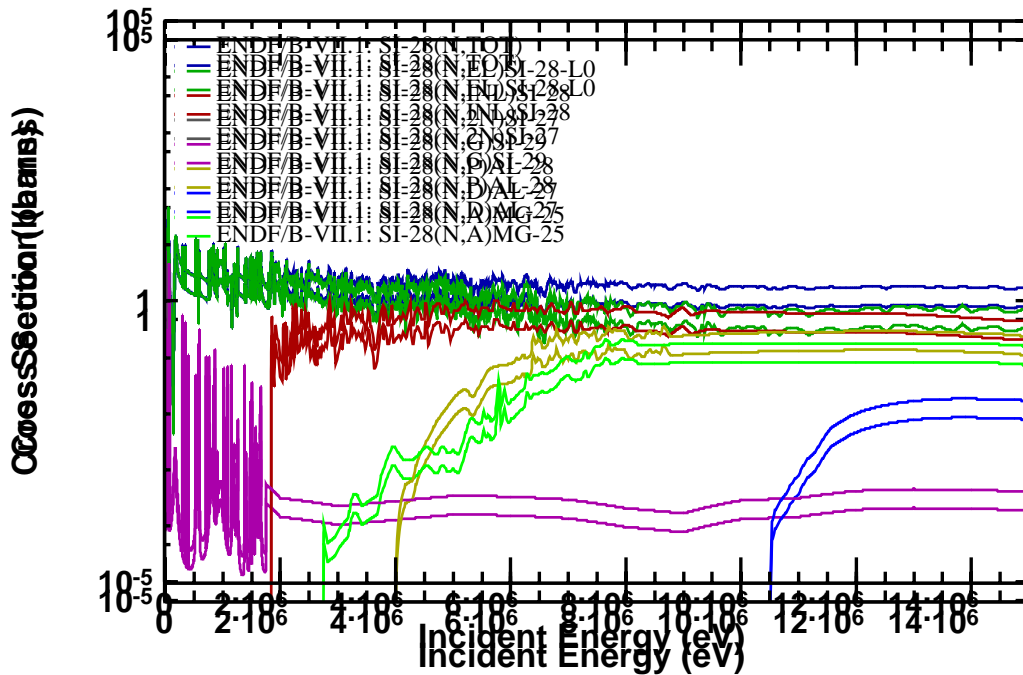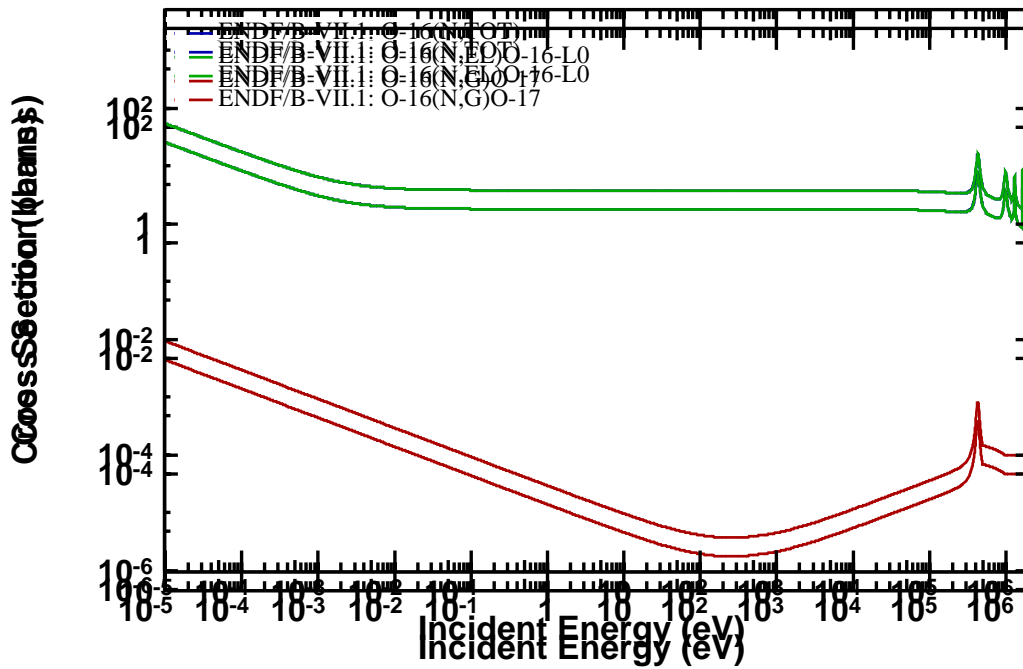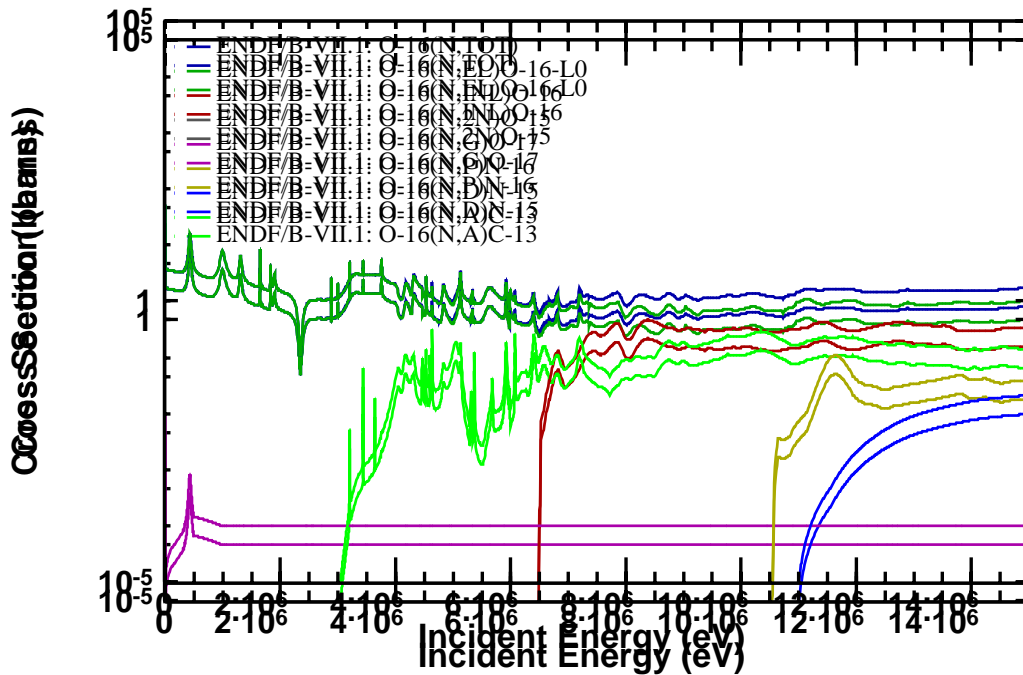(b) ^{16}O microscopic cross-sections for neutrons below 15 MeV.

Figure 2.6. Neutron cross sections in ^{16}O for reactions occurring at energies below 15 MeV. Created in ZVView with data from[20].

Figure 2.6. ^{16}O microscopic cross-sections. Taken from [49].

19

III. Neutron Energy Deposition

This chapter discusses the methodology behind, and analyzes the results from, the MCNP6.2 energy deposition calculations. Radiation-transport via MCNP6.2 allows for the calculation of energy deposition spatial profiles and coupling efficiencies for various neutron energies beneath the asteroid's surface. Obtaining accurate and precise energy deposition data specific to the selected asteroid target was a necessity for this work, especially in order to ascertain the effects of different source neutron energies. The theory from Chapter 2 pertained in large part to the underlying nuclear physics that change with neutron energy; it is precisely this theory that will inform how to appropriately tally the energy deposition and will provide a lens to interpret profile characteristics.

3.1 Methodology

There are three pieces to this section on the neutron energy deposition methodology. First, the specifics behind the MCNP6.2 approach are presented and discussed. Second, the background procedure for calculating Monte Carlo uncertainties is shown. Third, an alternative way to generate energy deposition profiles is listed to serve as a comparison to the profiles computed in this work.

3.1.1 MCNP6.2 Approach

3.1.1.1 Problem Geometry

NEOs come in a myriad of shapes, sizes, and compositions. To pare down the nearly limitless work that could be done in asteroid mitigation simulations, assumptions were made to inspect a single notional asteroid. The asteroid modeled in this work is 300 meters in diameter, perfectly spherical, and composed of pure silicon diox-

58

ide (i.e. SiO_2, quartz). The SiO_2 is taken to be at standard solid density (2.65 g/cm^3). However, due to an asteroid porosity, Φ, of 30%, the bulk or effective density is 1.855 g/cm^3. Densities and porosities among asteroid bodies are highly variable. $\Phi = 0.30$ was selected both because it is a reasonable value and because the resulting bulk density is close to 2 g/cm^3, which is typical of the asteroid densities that have been measured [65]. The general procedure of obtaining energy deposition profiles detailed in this section would remain the same for asteroids of other sizes and material compositions.

It is prudent to begin by explicitly defining the coordinate system along with the naming and mathematical conventions used for this problem. Acquiring the energy deposition from a point-source radiating towards a spherical body is a three-dimensional problem that can be reduced to a two-dimensional geometry due to symmetry. Figure 3.1a shows the 3-D Cartesian coordinate system defined in this work. The asteroid (blue sphere) of radius R is centered at the origin (0, 0, 0). The nuclear device (red point) located at position (0, -(R+HOB), 0) is treated as a point-source, which is a reasonable approximation given the asteroid size (300 m) compared to a nuclear device (on the order of a few meters). The stand-off HOB can be expressed as a scaled asteroid radius,

$$HOB = cR, \tag{3.1}$$

where c is a non-dimensional sizing factor. This representation is advantageous for two reasons — one, it allows for the HOB to be expressed by a short and unitless number, and two, it allows for easier and more efficient comparison of stand-off distances for asteroids of different sizes. For example, it likely takes less time to realize that a 40-m HOB for a 100-m asteroid is the same geometry as a 288-m HOB for a 720-m asteroid when a c of 0.4 is communicated.

59
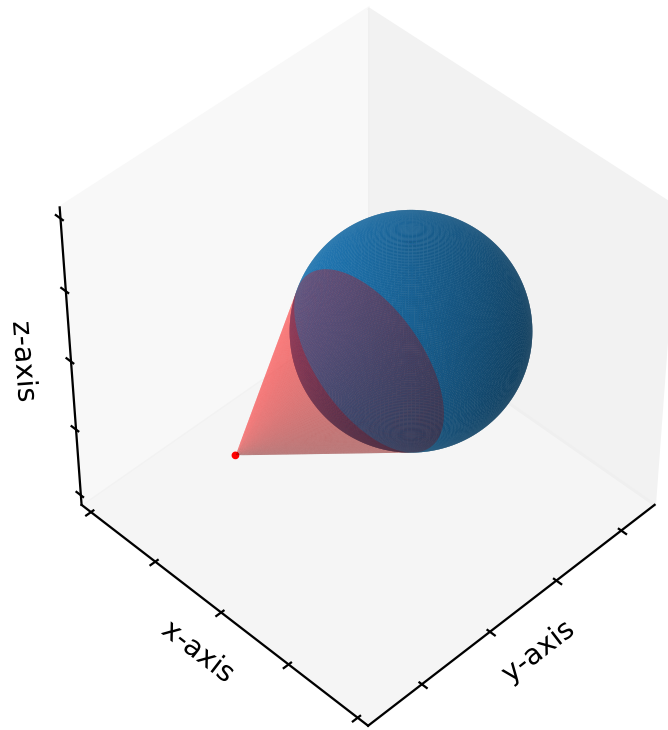
(a) Detonation-and-asteroid coordinate system definition visualizing the fraction of nuclear radiation (red cone) that is incident on the asteroid (blue sphere) from a device detonation (red point) at a fixed stand-off distance from the asteroid surface.
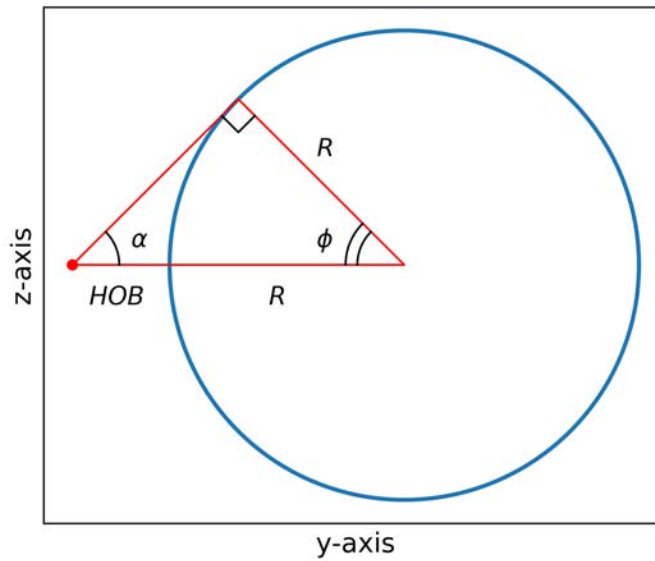
(b) Detonation-and-asteroid encounter geometry, side-view, where α is the device-centered half-angle and ϕ is the asteroid-centered half-angle.

Figure 3.1. 3-D and 2-D views of the device-asteroid geometry.

60

The angular and spatial conventions are defined as in Figure 3.1b, borrowing from the style of Hammerling and Remo [56]. α is the half-angle denoting the fraction of radiation from the detonation that is incident on the asteroid surface, while ϕ is the half-angle representing the fraction of the asteroid surface area that is irradiated. It follows that

$$\sin \alpha = \frac{R}{R + HOB} = \frac{R}{R + cR} = \frac{R}{R(1 + c)} = \frac{1}{1 + c} \tag{3.2}$$

and

$$\phi = \frac{\pi}{2} - \alpha. \tag{3.3}$$

Equation 3.2 shows that the fraction of detonation energy that hits the asteroid is a function only of the HOB scaling factor c. Equation 3.3 shows that α and ϕ have an inverse relationship — as the energy fraction increases (i.e. α increases), the surface area fraction decreases (i.e. ϕ decreases), and vice-versa.

The central HOB examined in this work is $c = \sqrt{2} - 1 \approx 0.414$, which is the "optimal" HOB derived by Hammerling and Remo [56]. This is the distance where the sum of two fractions, the fraction f of the asteroid surface area irradiated and the fraction g of the device yield that reaches the asteroid target, is maximized. Of course, this stand-off distance from the asteroid is the geometrical optimum because it is where both $\alpha = 45°$ and $\phi = 45°$. With its 300 meter diameter, the asteroid's radius is 150 m, and therefore the stand-off distance at $c \approx 0.414$ is ~62.13 m.

It is not anticipated that the HOB will have a significant, if any, effect on which neutron energies perform best for deflection. As such, this was a somewhat arbitrary choice of HOB, and it is expected that comparing deflection performance between different neutron source energies at HOBs other than this will produce similar relative results.

61

3.1.1.2 Energy Deposition Cut-Off

Several moles of neutrons are produced in real-world nuclear detonations. Given that these are massive numbers, and given that scattering and absorption interaction processes in materials are stochastic, there will be some small fraction of neutrons that survive and penetrate very deep into the asteroid. In this sense, there is not a discrete spatial cut-off for energy deposition.

The specific heat capacity definition provides a way to determine a reasonable (or *sensible*) energy deposition threshold:

$$q = c_p \Delta T. \tag{3.4}$$

Equation 3.4 represents the amount of specific thermal energy, q (J/kg), needed to heat a material with specific heat, c_p (J/kg-K), to result in a temperature change, ΔT (K). SiO_2 has a nominal c_p of ~1000 J/kg-K [82]. An energy deposition corresponding to ΔT of 1-K was selected as the arbitrary, yet reasonable, cut-off metric. A temperature change this small would not melt SiO_2 or affect shockwave formation or transmission. Using these values in Equation 3.4, and converting the units from J/kg to MeV/g, the specific energy deposition required to heat SiO_2 by 1-K is 6.242×10^{12} MeV/g.

MCNP6.2 calculates source-particle-normalized specific energy deposition values in MeV/g/src-n. In a real nuclear detonation, the number of source neutrons depends on the device design and yield. Bridgman [44] provides notional, unclassified estimates of the number of source neutrons per Mt of yield for various fuel types. For deuterium-tritium fuel, the maximum number of source neutrons that could escape the device case during detonation is about 1.5×10^{27} src-n/Mt. Assuming that 1 Mt is the maximum device yield that would be considered for this deflection scenario, the energy

deposition threshold is given as

$$\frac{6.242 \times 10^{12} \text{ MeV/g}}{1.5 \times 10^{27} \text{ src-n/Mt} \times 1 \text{ Mt}} = 4.2 \times 10^{-15} \text{ MeV/g/src-n.} \qquad (3.5)$$

This magnitude, 4.2×10^{-15} MeV/g/src-n, can serve as a rough metric for the lowest value of normalized energy deposition that needs to be tallied for fusion (i.e. 14.1 MeV) neutrons. Note that this threshold is conservative for smaller yields in that the profile extent would extend to depths with temperature increases below 1 K. It is also reasonable even for multi-Mt yields — for example, for a 10 Mt yield, the spatial extent of this profile data would allow the deepest regions to fall to about a 10 K (rather than a 1 K) increase in temperature due to heating, which is still not significant for the upcoming hydrodynamic simulations.

For 14.1 MeV neutrons shooting straight into the asteroid near ground-zero (GZ) at $\alpha = \phi = 0°$, preliminary simulations estimated that a penetration depth of $\sim$375 cm into the SiO$_2$ target at 1.855 g/cm^3 was necessary for the normalized energy deposition to drop-off to the 4.2×10^{-15} MeV/g/src-n threshold. The asteroid regions were tallied in MCNP6.2 for energy deposition up to 450 cm deep to err on the safe side.

3.1.1.3 Spatial Discretization

Considering the size of the sensible energy deposition region and the asteroid size, this problem is poorly-scaled. For the asteroid target, ρ is the material bulk/effective density of SiO$_2$ with a 30% porosity (1.855 g/cm^3), N_A is Avogadro's number, M is the molecular weight ($\sim$60 g/mol for SiO$_2$), and σ is the total microscopic cross-section (about 6×10^{-24} cm^2 for neutrons above 2 MeV in SiO$_2$) [36]. With these values, Equation 2.13 reveals that the mean-free-path for MeV-level neutrons into this asteroid is in the vicinity of 8.95 cm, or on the order of several centimeters.

This implies that the energy deposition spatial discretization in the asteroid should

63

be on the order of centimeters, and perhaps even millimeters at the surface, in the radial (depth) direction. Even for Mt-class yields, which push the heating of material to the furthest penetration depths, energy deposition as a whole is only significant up to about 4 m beneath the surface, at the most. However, the asteroid diameter is 300 m, which is significantly greater than the size of the energy deposition region in the radial direction.

Furthermore, the asteroid is spherical, making typical Cartesian meshing both undesirable and impractical. It was also quite unclear from *a priori* intuition or previous work what resolution would be necessary in the angular direction.

Pre-processing calculations based on geometry were made in a Python3 script to calculate the spatial discretization parameters needed for MCNP6.2 input decks. For the following figures, note that an exaggerated penetration depth of 45 m (rather than the 4.5 m maximum depth actually tallied for this problem) was utilized in order to provide a visual example of the discretization procedure. The resolution of the radial and angular discretizations have also been greatly decreased for this same purpose, to visualize the methodology. For the following discussion in the paragraphs below, however, the *real* 4.5 m depths will be discussed.[1]

The incident angle of a neutron from the device detonation ranges from 0° up to α (Equation 3.2). At the 0° angle, the neutron exactly hits GZ on the asteroid surface. At this angle, it may penetrate up to 4.5 m beneath this surface. At all other angles greater than 0° and less than α, the neutron paths are incident upon the asteroid surface at a non-normal angle. As such, the same 4.5 m target depth must be translated to match that same angle of incidence. Using circle-line intersection equations and trigonometric relations, a ray-tracing procedure of discrete incidence-angles from 0° up to α was performed, calculating the position beneath the asteroid

---

[1] If you think *that's* confusing, well, let's just say that you are really going to enjoy the rest of this thesis. Wait, you are reading this on Opposite Day, right?

64

surface corresponding to the same 4.5 m depth into the target [83]. The ray-tracing calculations resulted in the orange points seen in Figure 3.2a. The length of every dashed orange line, which is the distance along the device-angle of incidence from the asteroid surface to the orange point beneath the surface, is identically the 4.5 m target depth. This line of data points extended slightly beyond the surface area that is directly irradiated by the device (red dashed lines). To capture the entire energy deposition region out to 4.5 m depths, the asteroid-centered ϕ was slightly increased to also encompass this small region near the surface (green dashed lines).

Next, these device-centered 4.5 m depths were converted to asteroid-centered penetrations. The distance from the origin of each orange point (i.e. the Euclidean L2-norm) was subtracted from the asteroid radius. This amounted to calculating the asteroid-centered penetration depths d_{NEO} (which stands for "depth into the near-Earth object") as a function of the asteroid-centered ϕ, as shown by the length of the dashed purple lines in Figure 3.2b. Note that the dashed orange lines in Figure 3.2a are aligned with α angles because they are device-centered depths, while the dashed purple lines in Figure 3.2b are aligned with ϕ angles because they are asteroid-centered depths. The linear ϕ span of the asteroid-centered depths is shown in Figure 3.3a, where each d_{NEO} magnitude is the length of each dashed purple line in Figure 3.2b. As expected, at the 0° angle, the device-centered 4.5 m penetration depth is the same as the asteroid-centered penetration depth. At all other angles, the asteroid-centered d_{NEO} decreases as ϕ increases. Shown in Figure 3.3a, a piecewise linear interpolation function (the solid purple line) was fit to the discrete d_{NEO} distances (the purple points) across the span in ϕ.

Using this fit, the angular discretization was selected using the following process. For the permitted change in d_{NEO}, Δd_{NEO}, a comparatively-small tolerance of 0.875 cm was selected (this value was exaggerated to ∼3.5 m in the figures). This

65
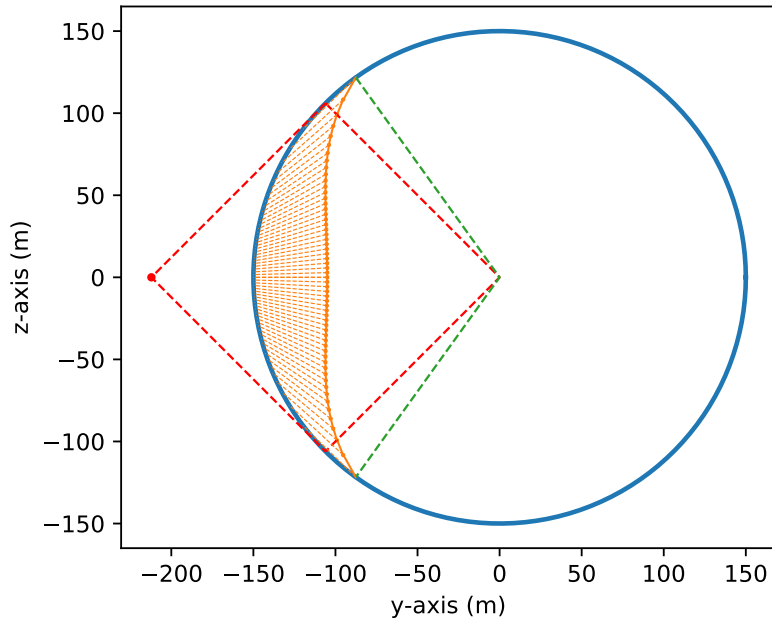
(a) Ray-tracing of 45 m penetration depth (exaggerated from 4.5 m) for all angles of incidence α at a HOB corresponding to $c = 0.414$.
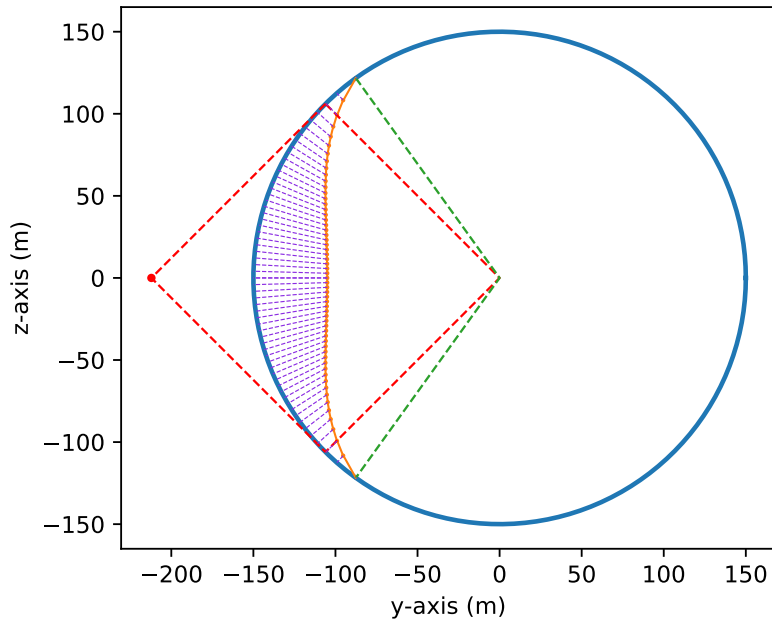
(b) The ray-traced 45 m penetration distances referenced to the device angle α are converted to asteroid-centered depths d_{NEO} (purple dashed lines) as a function of the asteroid-centered angle ϕ.

Figure 3.2. Device-centered (referenced to the α incidence angle) and asteroid-centered (referenced to the ϕ angle towards the asteroid core) penetration depths.

66
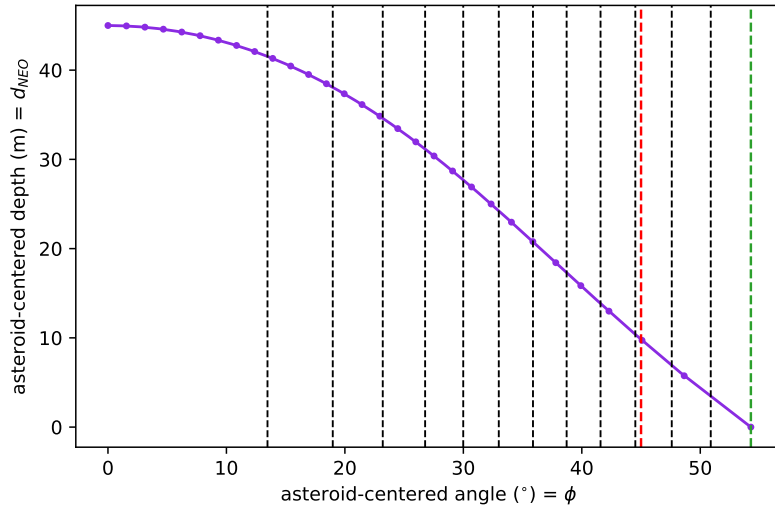
(a) Asteroid-centered penetration depth d_{NEO} versus asteroid-centered angle ϕ, from the GZ $0°$ angle up to the maximum energy deposition angle (green dashed line), with the maximum direct-surface-irradiation ϕ (red dashed line). The angular discretization (black dashed lines) is dependent on the Δd_{NEO} selection (intersection of the black lines with the purple line). Note that the spacing is non-linear because the purple d_{NEO} curve is non-linear.
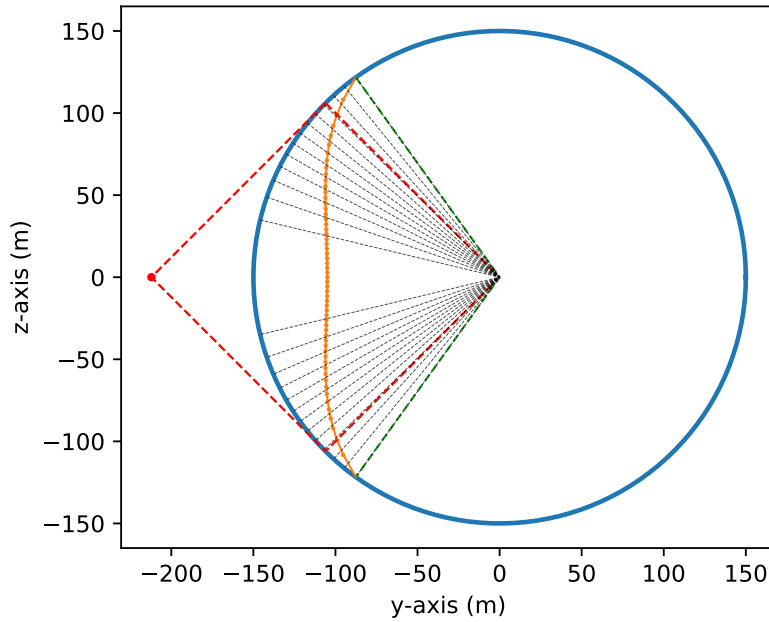
(b) YZ-plane view of the angular discretization indicated by black dashed lines. Note that these divisions are located at the same ϕ values that were determined from Figure 3.3a.

Figure 3.3. Angular discretization of the asteroid, visualizing the angular divisions throughout the asteroid energy deposition region.

choice divided the ϕ angular space into discrete regions or bins, as demonstrated by the dashed black lines in Figure 3.3a. For the $d_{NEO} = 4.5$ m (450 cm) target depth and the $\Delta d_{NEO} = 0.875$ cm tolerance, this totaled to 515 different divisions in angle from $\phi = 0°$ to $\phi = \phi_{max}$. Δd_{NEO} was chosen to be less than the 8.95 cm mean-free-path for MeV-level neutrons as was determined in the beginning of this section.

In this way, each angular bin resulting from this type of angular discretization effectively groups reasonably-similar neutron penetration depths together. For example, the first angular region (which encompasses GZ where $\phi = 0°$) collects the neutron incidence paths that penetrate to d_{NEO} depths between between 450 cm and $(450 - 0.875)$ cm. The second angular region groups d_{NEO} depths between $(450 - 0.875)$ cm and $(450 - 2 \cdot 0.875)$ cm, and so forth, with the last angular bin capturing the region where d_{NEO} approaches 0 cm.

This approach to divisioning allowed for more angular resolution where it was necessary and less where it was not. Towards the middle-to-upper ϕ angles, as seen in Figure 3.3a (or Figure 3.2b), the d_{NEO} curve changes somewhat quickly as ϕ increases. Because of this, greater angular resolution (i.e. smaller angular bins) in this region is required. For the ϕ values about GZ ($0°$), Figure 3.3a shows that d_{NEO} changes more slowly with ϕ (notice that the slope is nearly flat when walking along in angle if starting from $\phi = 0°$). Indeed, the regions near GZ can be wider in angle than they are elsewhere, because near $\phi = 0°$ the asteroid curvature does not change as much with respect to a wider range of neutron angles of incidence. Therefore, to group similar d_{NEO} depths near GZ, less angular resolution (i.e. larger angular bins) could be permitted. For these reasons, the bin surrounding $0°$ is the largest, and the bins away from GZ are smaller. This is seen in Figure 3.3a by the dashed black lines which mark the boundaries between each angular bin.

Figure 3.3b shows these angular lines in the YZ-plane side-view. Because there are 2π radians of symmetry around the y-axis (Figure 3.1), partitioning the asteroid via encapsulated cones is the best choice for this task in order to exploit the symmetry while still partitioning the asteroid in angle. That is, the discretization in Figure 3.3b is rotated 360° about the y-axis, forming conical surfaces. Figure 3.4a shows the circular bases of the cones intersecting the spherical asteroid surface in the XZ-plane device-centric view. This perspective shows the surface area of the asteroid target that the nuclear device sees. Using cones for angular discretization allowed the 3-D asteroid geometry to be converted into a 2-D (d_{NEO} and ϕ) energy deposition problem.

While the angular discretization was determined by how the asteroid curvature affects a fixed penetration depth, the radial discretization was informed by the neutron mean-free-path. Because the mean-free-path of multi-MeV neutrons is on the order of several centimeters, the energy deposition is expected to change on a centimeter or even millimeter scale beneath the surface. Because most of the energy was expected to be deposited near the surface, logarithmically-spaced concentric spherical shells with spacing of 0.5 mm at the surface up to 4 cm beneath the surface were generated, resulting in 498 total shells out to 450 cm depths. Figure 3.4b shows evenly-spaced concentric spherical shells with very large spacing to merely demonstrate the concept of radial discretization.

In summary, the symmetry about the y-axis (Figure 3.1) was fully exploited, and subsequently the 3-D asteroid was discretized in a 2-D fashion in preparation for energy deposition simulations. Figure 3.5 visualizes the (d_{NEO}, ϕ) coordinate system that has been developed from this procedure. GZ is ground-zero, the point along the asteroid surface that is closest to (i.e. most directly beneath) the stand-off detonation. Fittingly, GZ is located at the (0 cm, 0°) coordinate. The d_{NEO} depths penetrate

69
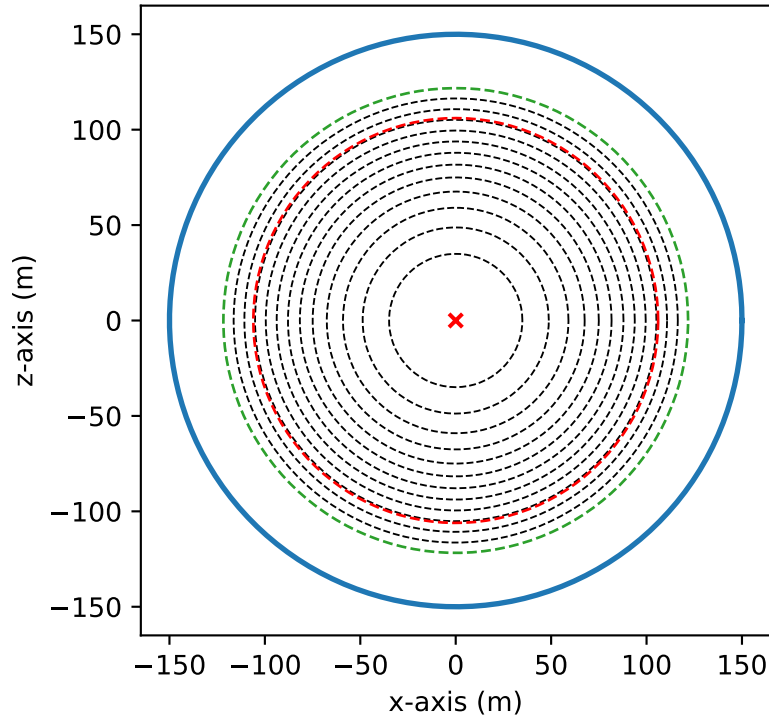
(a) Angular discretization in XZ-plane, device-centric view. The red X represents the initial location of the detonation radiation going into the page (towards the asteroid). The dashed circles are located where the circular bases of the concentric cones intersect the spherical asteroid.
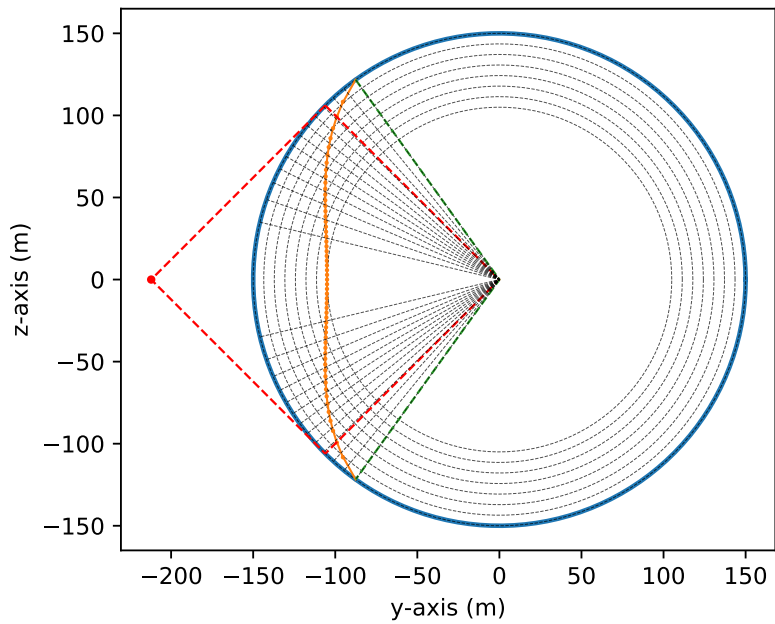
(b) Concluded radial, concentric, spherical discretization and concentric, conical angular discretization in YZ-plane cross-section, the side-view.

Figure 3.4. The angular and radial discretization visualized in the "device-view" and the "side-view."
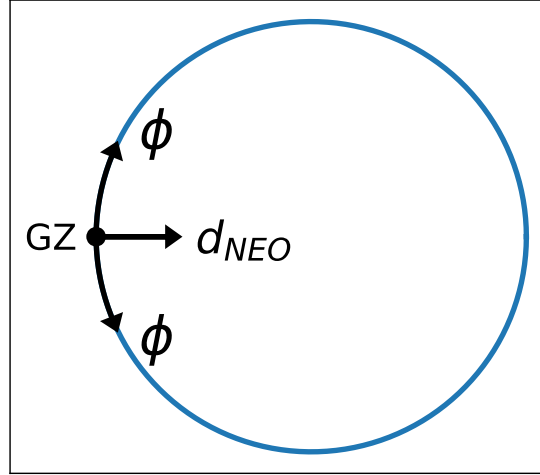
Figure 3.5. The 2-D coordinate system for energy deposition into the asteroid. The locations are of the form (d_{NEO}, ϕ), with d_{NEO} being the radial axis and ϕ the angular axis. GZ is ground-zero, located at $(0 \text{ cm}, 0°)$.

beneath the outer surface (where all points along the surface have "depths" of 0 cm), and the ϕ angles measure the distance away from GZ along the curvature of the asteroid.

3.1.1.4   MCNP6.2 Setup

The correct energy deposition is essential for correctly modeling whether or not an asteroid can be deflected by imparting a sufficient δV without undesired fracturing. If large uncertainties in the energy deposition values exist, or if the spatial refinement is too coarse to capture the heating gradients, there should be minimal confidence in the subsequent asteroid hydrodynamic response outputs. MCNP6.2 was the primary code used to explore the characteristics of neutron energy deposition beneath an asteroid's surface. MCNP6.2 is a general-purpose Monte Carlo N-Particle code that can be used for neutron, photon, charged particle, or coupled neutron/photon/charged particle transport in 3-D geometries [51]. Cross-sections for interaction probabilities were pulled from the ENDF71x library [52].

The two sources used in this study were ~14.1 MeV and ~1 MeV neutrons. As dis-

71

cussed in Section 2.4, 14.1 MeV neutrons are generated from deuterium-tritium (D-T) fusion reactions, which are given off by boosted fission and thermonuclear devices, and fission reactions create many 1 MeV neutrons (with this energy corresponding to near the peak of the Watt fission spectrum).

The simulated asteroid was 300 meters in diameter, spherical, and composed of silicon dioxide (i.e. SiO_2 quartz) at 1.855 g/cm^3 density. The cell resolution was on the order of millimeters to centimeters in the radial direction, and tens to hundreds of centimeters in the angular direction, based on the approach in Section 3.1.1.3. In total, there were 498 divisions in the radial direction out to 450 cm d_{NEO} depths and 515 divisions in the angular direction, spanning from a ϕ of 0° out to slightly more than 45°. This amounted to cell tallies for energy deposition at 256,470 spatial locations in the MCNP6.2 computations.

The detonation was modeled as an isotropic point-source. However, only the neutrons released in angles within the α half-angle — that is, within the red cone in Figure 3.1a — will ever collide with the asteroid. At the HOB of $c = \sqrt{2} - 1 \approx 0.414$, approximately 14.64% of the neutrons from an isotropic point-source detonation are emitted towards the asteroid surface; the rest of these neutrons (and their energies) are lost to the void of space. To reduce variance and run-time, directional source-biasing was implemented. The only neutrons simulated were those that fell within the acceptable range of α and were on path to intercept the asteroid.

The MCNP +F6 "collision heating" tally stored the total energy deposited into asteroid cells from all neutron and all tracked secondary particle (photons, protons, deuterons, tritions, and alphas) interactions. Secondary photons were tracked and energy deposition was distributed along their true path, while all charged particles (namely protons and alpha particles) were treated as local deposition for computational savings because their path lengths are quite small (microns or tens of microns)

72

in comparison with size of the spatial discretization [51].

Separate energy deposition calculations were performed for each group in the 46-group DPLUS energy structure. The source energies were uniformly sampled between the lower and upper bin boundaries, making the midpoint energy identical to the average energy of each group. All 46 energy group simulations were run on the Centennial DoD cluster, an SGI ICE XA supercomputer system located at the Army Research Laboratory (ARL) DoD Supercomputing Resource Center (DSRC) [84]. Each of the MCNP6.2 computations was run on a single node (40 processors). The energy groups above some or all of the endothermic threshold energies listed in Table 2.3 created alpha, proton, and deuteron, and/or triton secondary particle tracks, which increased their runtime in comparison to the lower energy sources that could only produce secondary gamma-rays. The highest energy group took the longest to complete, approximately 103 wall-time hours, while some of the lowest energy groups took about 33 hours to finish.

3.1.2 Monte Carlo Uncertainties[2]

Monte Carlo methods are based on numerical probabilities. Each particle track history contributes a certain score, x_i, to every tally. The probability that any history will contribute a score between x and $x + dx$ is denoted by $p(x)dx$, where $p(x)$ is the probability distribution function (PDF) unique to the problem. Based on the cross-section probabilities as determined by the problem material, geometry, and source particle type and energy, a certain number of histories are required to reach a certain level of convergence. That is, what is sought in a Monte Carlo simulation is the mean (converged) value of x, or

$$\langle x \rangle = \int_0^\infty x p(x) dx. \tag{3.6}$$

---

[2]This section is adapted heavily from Section 4.1 of [85].

The PDF for any given problem is not known ahead of time; rather, it is only discovered as the simulation itself is allowed to run for a long time. Instead of trying to get the true mean $\langle x \rangle$ directly, Monte Carlo works on the principle of random sampling and instead calculates a *sample* mean,

$$\overline{x} = \frac{1}{N} \sum_{i=1}^{N} x_i, \tag{3.7}$$

where N is the number of source particle histories. By the strong law of large numbers, as $N \to \infty$, so too does $\overline{x} \to \langle x \rangle$.

The question is then: "What N is required to reach a $\overline{x}$ that is satisfactorily close to $\langle x \rangle$?" This is where uncertainty and error come into play. The estimated standard deviation S is known by the variance S^2 of the set of particle histories,

$$S^2 = \frac{1}{N-1} \sum_{i=1}^{N} (x_i - \overline{x})^2 \approx \overline{x^2} - \overline{x}^2, \tag{3.8}$$

where the average of the square of the samples is of the same form as Equation 3.7,

$$\overline{x^2} = \frac{1}{N} \sum_{i=1}^{N} x_i^2. \tag{3.9}$$

The estimated variance of the sample mean $\overline{x}$ itself is determined to be

$$S_{\overline{x}}^2 = \frac{1}{N} S^2. \tag{3.10}$$

If simulations (each with N histories) are repeated many times, it is known by the central limit theorem that the outcomes will be normally distributed (with mean $\overline{x}$ and standard deviation $S_{\overline{x}}$) about the true mean $\langle x \rangle$. Therefore, if the variance $S_{\overline{x}}^2$ is small (and subsequently the standard deviation $S_{\overline{x}}$ is small), then one can be confident that the simulation tallied values, $\overline{x}$, are very close to the true values, $\langle x \rangle$.

74

As N increases, $S_{\bar{x}}$ decreases. As $S_{\bar{x}}$ decreases, the relative error of the tally decreases. In order to achieve a satisfactory measured variance for most of the energy tally locations, each input deck was run with an N of five billion source neutron particle histories. Some of the resulting uncertainties are plotted and discussed in Section 3.2.1.1.

3.1.3 Validation/Comparison

Obtaining accurate and precise energy deposition profiles is a challenge, and this work serves as a testament to this. Considering the continuum of nuclear stand-off distances and the wide-range of asteroid sizes, shapes, compositions, etc., energy deposition profiles for a specific problem are not always generated with full radiation-transport simulations. A common method in nuclear deflection literature for quickly generating neutron energy deposition profiles is the following approximate analytical equation, which defines energy deposition based on asteroid depth d_{NEO} and angle ϕ [41]:

$$E_{dep}\left(d_{NEO}, \phi\right) = E_0 \exp\left[-\frac{d_{NEO}}{\lambda_d}\right] \cos\left(\frac{\pi\phi}{2\phi_{max}}\right), \tag{3.11}$$

where $E_0 = \frac{\eta_Y Y}{4\pi s^2 \lambda_d}$ is the deposited energy density at the surface, d_{NEO} is the depth relative to the NEO surface (as visualized in Figures 3.2b and 3.3a), λ_d is the characteristic length or penetration depth of the incident radiation, ϕ_{max} is the maximum asteroid-centered conical angle (defined in Equation 3.3), η_Y is the coupling efficiency of the source energy, Y is the total source yield, and s is the distance from the detonation to any arbitrary point on the asteroid surface. In this way, the neutron fluence (and therefore the energy deposition intensity) at any surface location is reduced by spherical divergence over distance s. This equation is derived assuming that energy is deposited throughout the asteroid as governed by the Beer-Lambert Law of exponential attenuation.

75

The MCNP6.2 energy deposition profiles will be compared to profiles generated by Equation 3.11. While it is convenient to express energy deposition as an expedient formula, in reality neutron scatter and capture reactions generate more complex energy deposition profiles. The spatial deposited energy profiles specific to a particular asteroid from the MCNP6.2 simulations were used in the subsequent hydrodynamic simulations; it was believed that these data were more accurate and precise than the approximate, more generic exponential profiles from Equation 3.11. The spatial features of energy deposition were of paramount importance for this research because of its premise in determining how neutron energy affects the asteroid deflection.

3.2 Results and Analysis

There are three pieces to this section on analyzing the neutron energy deposition results. First, the MCNP6.2 energy deposition spatial profiles for 14.1 MeV and 1 MeV source neutrons are presented and examined. Second, the energy coupling efficiencies for these two source energies are calculated. Third, profiles and efficiencies for all 46 source neutron energy groups in the DPLUS structure are provided in Appendix A.

3.2.1 Energy Deposition Profiles

Figures 3.6a and 3.6b present source-particle normalized energy deposition as profile functions of d_{NEO} depth and a selection of ϕ angles for 14.1 MeV and 1 MeV neutron sources, respectively.[3] Each plot shows energy deposition down to three-and-a-half orders of magnitude below the maximum. The solid black horizontal lines represent the melt thresholds for 50 kt and 1 Mt detonations; regions in the asteroid located at or above these lines will be melted due to sufficiently-intense energy

---

[3]The reversed view, presenting energy deposition as a function of ϕ angle across a selection of d_{NEO} depths, is contained in Appendix C in Section C.1.

deposition. These, along with the dashed black horizontal melt lines for 31.6 kt and 632 kt yields, will be discussed in greater detail in Chapter 4.

Both figures demonstrate many similar trends. First, as the penetration depth d_{NEO} increases, E_{dep} decreases. This is as expected — most energy is deposited near the surface because the initial incident neutron pulse is quickly attenuated via absorption and scattering reactions as it travels further into the asteroid medium. Second, E_{dep} decreases as the half-angle ϕ increases. This is in agreement with the intuition that more energy will be deposited near GZ than at the far-edges of the irradiated surface. The neutrons hitting the asteroid surface corresponding to larger ϕ coordinates are incident at a non-normal angle, meaning that escaping the asteroid by scattering back out into space is more likely. Even more importantly, as ϕ increases, the distance s from the detonation point-source to the asteroid surface increases, thereby reducing the incident neutron fluence and the resulting E_{dep} at these peripheral locations.

The 14.1 MeV source results in profiles that more-or-less monotonically decrease as the penetration depth d_{NEO} increases. This trend follows for all ϕ binnings and is seen in Figure 3.6a. However, Figure 3.6b, resulting from 1 MeV neutrons, shows that changing the source energy fundamentally changes the spatial distribution of the deposited energy. Two major differences in particular are observed.

First, the average slope of the E_{dep} curves between 0 to about 25 cm d_{NEO} depths is noticeably different between Figures 3.6a and 3.6b. A sharper (quicker) drop-off in this region is seen in the 1 MeV profiles as compared to the 14.1 MeV profiles, while the slopes appear essentially even at deeper depths. At and immediately beneath the asteroid surface, the energy deposition results predominately from direct neutron scatter and absorption reactions, while the energy deposited in regions deeper into the asteroid is less from neutrons and more from secondary gamma-rays, charged particles, etc. The sharper drop-off of E_{dep} between 0 and 25 cm shows that the
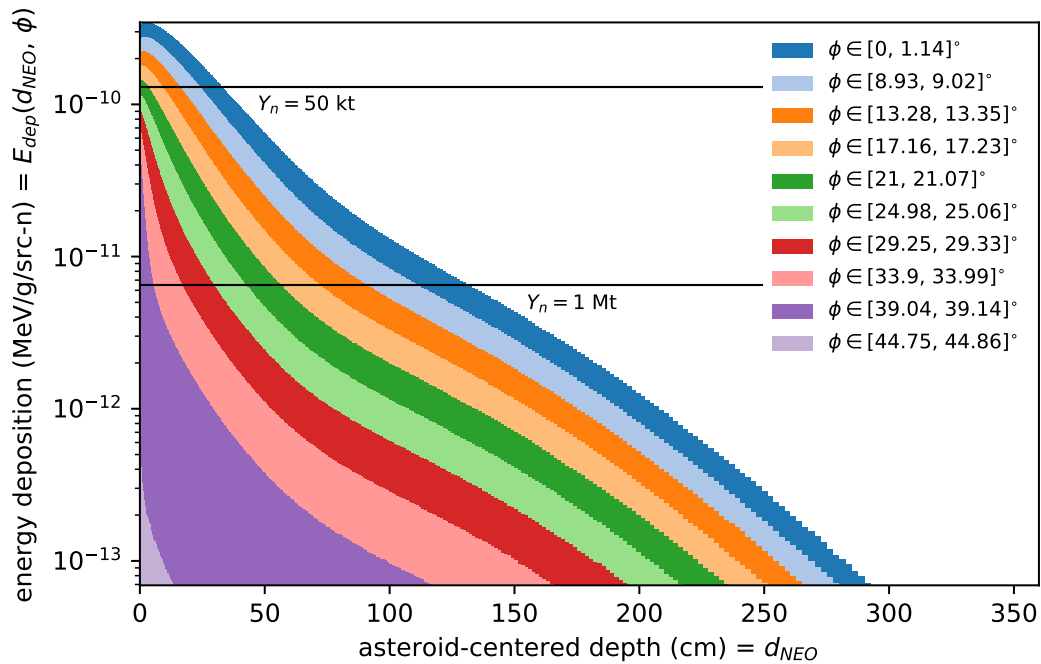
(a) Energy deposition spatial distribution from a ∼14.1 MeV neutron source (DPLUS group #3).
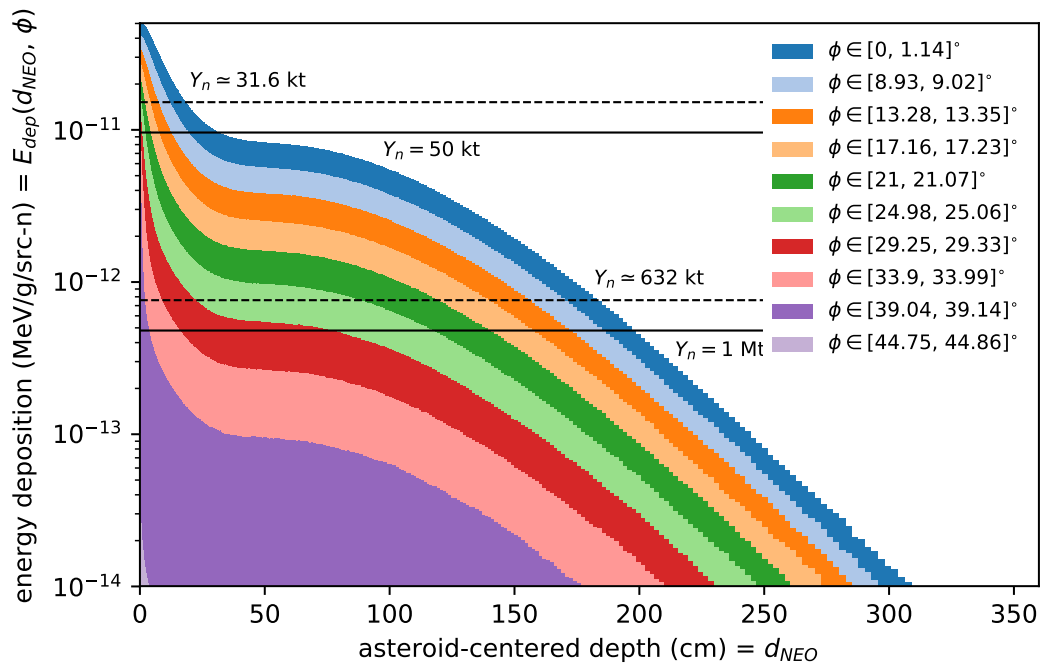
(b) Energy deposition spatial distribution from a ∼1 MeV neutron source (DPLUS group #21).

Figure 3.6. MCNP6.2 energy deposition profiles for two different neutron energy sources, 14.1 MeV fusion neutrons and 1 MeV fission neutrons. The horizontal black lines are the "melt lines," which show the depths where the melt threshold for SiO_2 is met or exceeded for select neutron yields (discussed in greater detail in Chapter 4).

78

lower-energy 1 MeV neutrons are more quickly absorbed than the more-penetrative 14.1 MeV neutrons.

Second, in the 1 MeV profiles, there is a clear "pause" in the drop-off of energy deposition in the region of the asteroid approximately 25 cm to 100 cm beneath the surface, not seen in the 14.1 MeV profiles. This is the region where the secondary gamma-rays from the exothermic (n,γ) capture reactions deposit most of their energy, forming a second pulse of energy deposition. There are a few likely reasons why this pause is not seen in the 14.1 MeV profile. For one, the 14.1 MeV neutrons are more penetrative due to their higher incident energy and therefore distribute their energy more evenly. More importantly, 14.1 MeV neutrons are more prone to be absorbed via endothermic reactions, while 1 MeV neutrons can exclusively react via elastically scatter or (n,γ) capture, which are both exothermic reaction channels (recall from Section 2.5). Thus, relative to the 14.1 MeV source, the 1 MeV source is more quickly and predominately converted to secondary gamma-rays, which in turn travel through SiO_2, forming a secondary wave of energy deposition.

An additional radiation-transport simulation provided a simple way to prove the theory that the 1 MeV pause region was primarily the result of the secondary gamma-rays. The 1 MeV energy group was re-run with exactly the same MCNP6.2 setup as before, *except* for one change: the production of secondary gamma-rays from exothermic capture reactions was turned off. Photon particles and physics were disabled in this new MCNP6.2 input deck. With this, the new energy deposition profiles would be due to neutron interactions alone, imparting energy to nuclei via scattering and/or absorption.

For the $\sim$1 MeV neutron source, Figure 3.7 shows the energy deposition profiles due to neutrons alone, alongside the profiles of the secondary gamma-rays contributing additional deposition. The neutron-only energy deposition, generated by re-

79
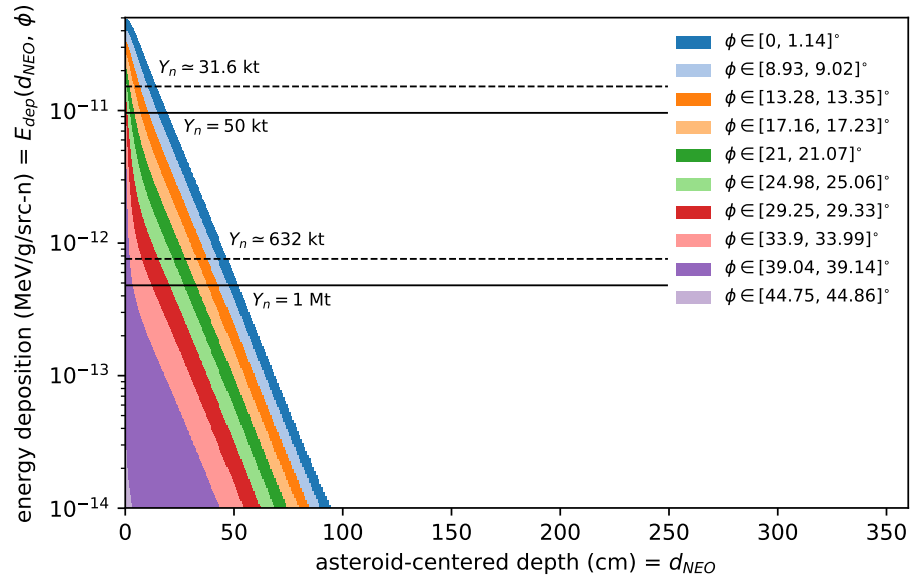
(a) Energy deposition spatial distribution resulting from ∼1 MeV neutrons *only*.
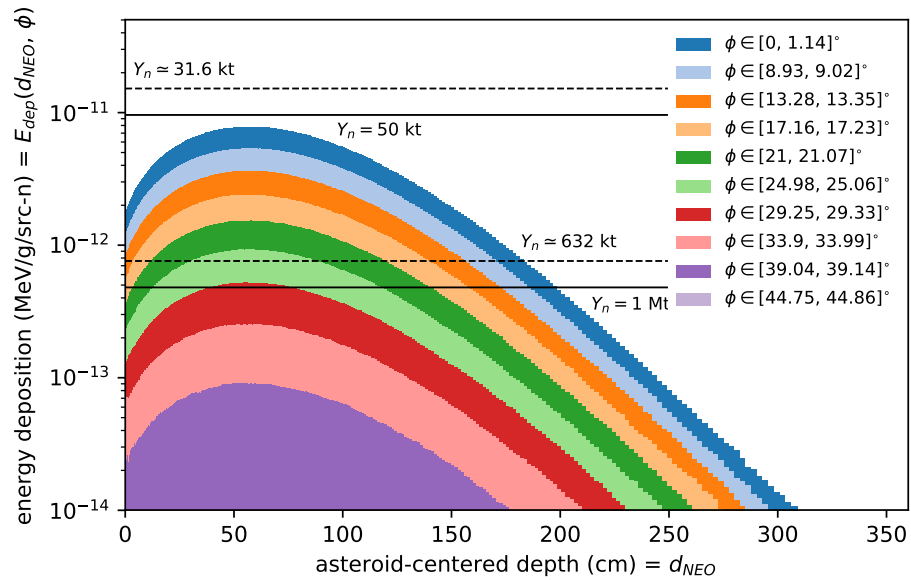
(b) Energy deposition spatial distribution resulting from (n,γ) secondary gamma-rays *only*.

Figure 3.7. Separated energy deposition profiles due to 1 MeV neutrons and their secondary gamma-rays. Figure 3.7a is the primary wave of energy deposition resulting from neutron scattering and absorption reactions in SiO_2. Figure 3.7b is a secondary pulse of energy deposition due to radiative capture gamma-rays diffusing further into the asteroid medium.

running the 1 MeV simulation with photon particles disabled, is seen in Figure 3.7a. The energy deposition profiles from neutron scattering and absorption alone generally follow a much cleaner exponential pattern than the full profiles from Figure 3.6. Most neutrons will deposit their energy near the surface at shallow d_{NEO} depths.

The deposition from capture gamma-rays alone is seen in Figure 3.7b, which was created by subtracting the neutron energy deposition (Figure 3.7a) away from the combined neutron+gamma-ray deposition (Figure 3.6b). This shows that the 1 MeV "pause" region is the result of the exponential neutron energy deposition profiles overlapping with the peak of the secondary gamma-ray deposition pulse. Most of these gamma-rays are formed once 1 MeV neutrons have lost enough energy due to several scattering events in order to be absorbed, which generally occurs some distance into the target. Because most of the (n,γ) radiative capture reactions occur at some depth, this is primary reason why the gamma-ray energy deposition peaks for d_{NEO} values around 50-80 cm, rather than at the surface as the neutron energy deposition does.

3.2.1.1   Energy Tally Uncertainties

The tally uncertainties in the energy deposition values are not shown in the aforementioned Figure 3.6 profiles for clarity in the presented results. The statistical uncertainties were only fractions of a percent for the regions with the highest energy deposition near the surface. Figure 3.8 visualizes the relative uncertainties for the energy deposition in each MCNP6.2 cell for the 14.1 MeV (top) and 1 MeV (bottom) sources, respectively.

Out to the target 4.2×10^{-15} MeV/g/src-n threshold, most of the spatial energy deposition values had uncertainties less than about 6% for the 14.1 MeV neutrons and less than about 15% for the 1 MeV neutrons. The relative smoothness of the
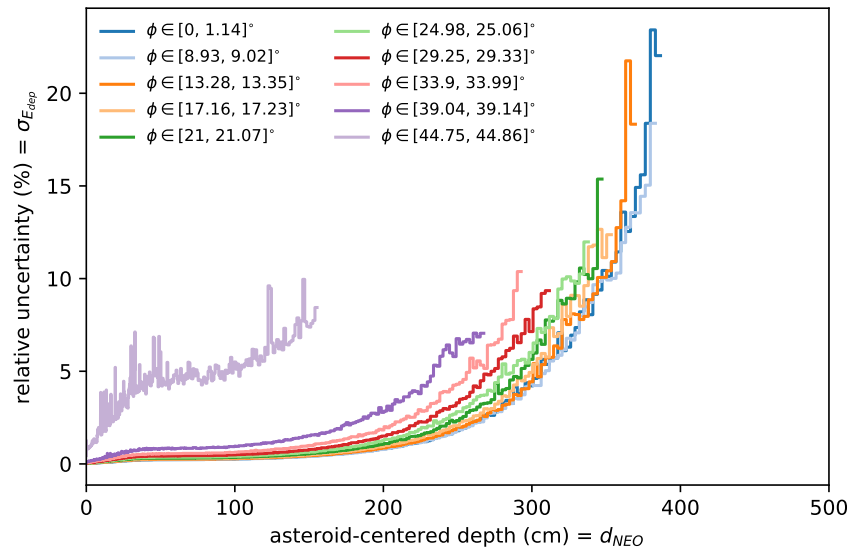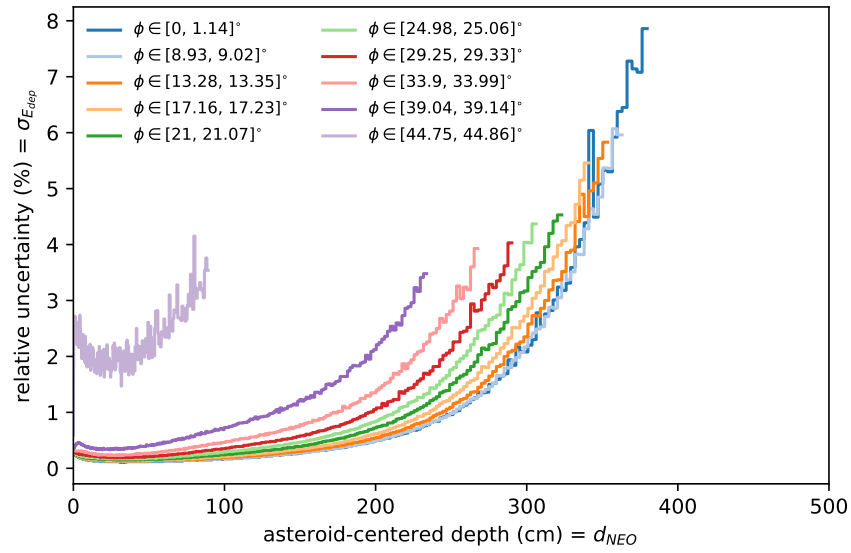
81

Figure 3.8. Relative uncertainties in the energy deposition values for the 14.1 MeV (top) and the 1 MeV (bottom) sources. These tally uncertainties were not shown in Figures 3.6a and 3.6b, as very small error bars distracted from the presented results.

profiles in Figures 3.6a and 3.6b allowed for this amount of Monte Carlo uncertainty to be deemed acceptable. As will be shown in Chapter 4, the maximum melt-depth considered in this work was ∼200 cm. The uncertainties out to d_{NEO} depths of 200 cm in Figure 3.8 are much lower than the maximum uncertainties attained at the deepest depths. The impact of these maximum uncertainties — which are still not inordinately-high, and are only present where SiO_2 remains un-melted – will be minimal in the upcoming asteroid response simulations, as the δV deflection velocity change is determined by the *melted* blow-off momentum.

For the same number of source particle tracks in the MCNP6.2 simulations, the 14.1 MeV source neutrons resulted in lower uncertainties than the 1 MeV neutrons. 1 MeV neutrons do not penetrate as far as 14.1 MeV neutrons, and thus the energy deposition resulting from a 1 MeV source primarily originates from secondary gammas as d_{NEO} increases. Due to this greater reliance on secondary particle contributions to deposited energy, the uncertainties are greater for the 1 MeV source.

3.2.1.2   Comparison to Analytical Energy Deposition Profiles

The MCNP6.2 energy deposition profiles can be compared to profiles generated by the method described in Section 3.1.3, Equation 3.11. There are two ways to use Equation 3.11 based on two possible definitions of λ_d, the "characteristic path-length" parameter. The primary definition is that λ_d is the mean-free-path, λ, of the source neutrons in the given asteroid medium [41]. For both 14.1 MeV and 1 MeV neutrons, the total microscopic cross-sections σ in barns for ^{28}Si and ^{16}O, along with the mean-free-paths λ in centimeters (via Equation 2.13) in SiO_2, are listed in Table 3.1 [52]. The total mean-free-paths in SiO_2 shown in Table 3.1 were the λ_d values used for generating 1 MeV and 14.1 MeV analytical profiles using the mean-free-path interpretation of Equation 3.11.

83

Table 3.1. Microscopic cross sections, σ, in ^{28}Si and ^{16}O for 14.1 MeV and 1 MeV neutrons, alongside the mean-free-paths, λ, in SiO$_2$.

E_{src}	Nuclide	σ	λ
14.1 MeV	^{28}Si	1.81 b	10.8 cm
	^{16}O	1.59 b	
1 MeV	^{28}Si	4.68 b	2.6 cm
	^{16}O	8.15 b	

A second way to define λ_d allows for an alternate usage of Equation 3.11. λ_d is redefined to be the penetration depth at which a fraction $(1-1/e)$ of the total energy has been deposited [47]. This definition means that radiation transport simulation results are required to calculate λ_d. A $(1-1/e)$ λ_d was calculated for each angular bin from the MCNP6.2 outputs. The total energy deposited in each conical region was calculated, and linear interpolation determined the depth where the $(1-1/e)$ fraction of this total energy was reached. Except for the differences in definitions of the mean-free-path and $(1-1/e)$ for λ_d, the two implementations of Equation 3.11 were identical.

Note that, as written, E_0 in Equation 3.11 is volumetric with units of MeV/cm^3. To directly compare Equation 3.11 profile magnitudes to their per-mass normalized MCNP6.2 counterparts, the equation was divided by the bulk SiO$_2$ density of 1.855 g/cm^3. The coupling efficiencies η_Y were taken as the η_{rel} values from Table 3.2 (see Section 3.2.2). Because the MCNP6.2 energy deposition is normalized as per source neutron (MeV/g/src-n), the yield Y within E_0 in Equation 3.11 was simply E_{src}, the energy of one source neutron (i.e. MeV/src-n). Lastly, by their nature, the MCNP6.2 profiles are discretized in both depth d_{NEO} and angle ϕ, while Equation 3.11 describes a continuum in depth and angle. To match the presentation of the MCNP6.2 profiles, a linearly-spaced survey of ϕ was taken between the lower-bound angle ϕ_{low} and upper-bound angle ϕ_{max} for each discrete conical bin. From

84

this, an array of distances s from the source along the curved asteroid surface was created, allowing for an *average* surface energy deposition E_0 along with an *average* cosine-term in Equation 3.11 to be calculated for each conical region. In this way, the Equation 3.11 profiles were discretized in angle in the same way that the MCNP6.2 results are, allowing for direct comparison.

Comparison plots showing MCNP6.2 profiles alongside the analytical equation profiles were made for all configurations of the two source energies and the two ways to define λ_d, all shown in Figure 3.9. Figures 3.9a and 3.9c show the MCNP6.2 profiles alongside the analytical equation profiles using the mean-free-path definition of λ_d for 14.1 MeV and 1 MeV source neutrons, respectively. Figures 3.9b and 3.9d visualize the profile comparison for the $(1 - 1/e)$ λ_d, again for 14.1 MeV and 1 MeV source neutrons, respectively. The dashed lines are the Equation 3.11 analytical profiles, and the solid lines are the MCNP6.2 profiles. Both the analytical profiles and the MCNP6.2 profiles are color-coded accordingly.

In general, the mean-free-path λ_d overestimates the energy deposition at the surface for most angles for both source energies (more strongly so for 1 MeV than 14.1 MeV). The mean-free-path method also performs quite poorly as d_{NEO} increases, with the Equation 3.11 lines diverging from the MCNP6.2 curves. This is due to the fundamental assumption of defining λ_d as the mean-free-path. The mean-free-path allows for an approximate measure of the *neutron* fluence as a function of depth (i.e. Equation 2.5); it does not in any way track or account for secondary particles created from neutron interactions with matter. This is one reason why the mean-free-path λ_d severely underestimates the energy deposition with increasing d_{NEO}. The neutrons from the detonation predominately interact near the asteroid surface, and as d_{NEO} increases, the energy deposited is increasingly due to secondaries, not neutrons.
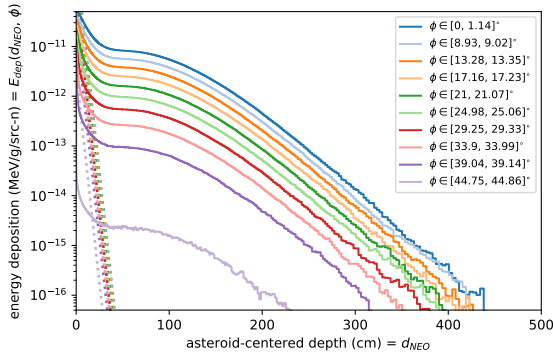
Further, this application of the analytical equation does not take into account the
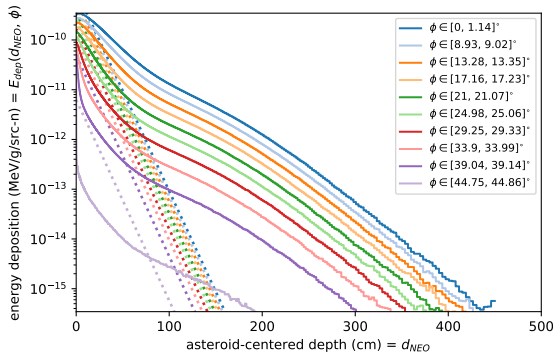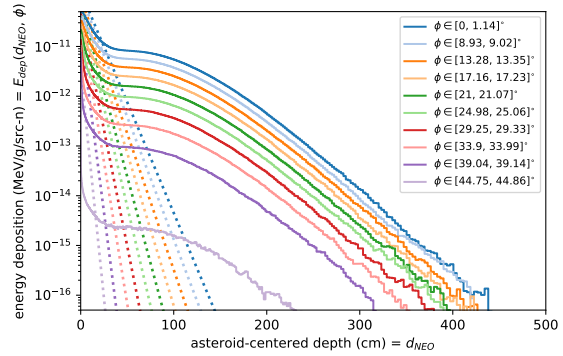
(a) 14.1 MeV source with the mean-free-path λ_d definition.
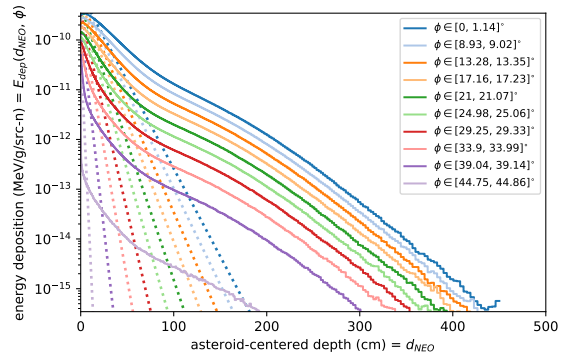
(b) 14.1 MeV source with the $(1-1/e)$ λ_d definition.

(c) 1 MeV source with the mean-free-path λ_d definition.

(d) 1 MeV source with the $(1-1/e)$ λ_d definition.

Figure 3.9. Energy deposition profiles from MCNP6.2 (solid lines) and from the analytical equation (dashed lines).

fact that scattered neutrons still have energy to be deposited. The implicit assumption here is that all interactions are absorption, thereby removing the neutron from the considered population once it has its first interaction. But clearly, not all interactions are absorption, and scattering is a significant and often dominate cross-section in SiO_2 (see Sections 2.5 and 2.6). This is yet another reason why energy deposition might be underestimated at deeper depths using the mean-free-path λ_d.

The $(1-1/e)\,\lambda_d$ in the analytical equation also results in overestimates for surface depositions from both sources. This application of Equation 3.11 somewhat matches the MCNP6.2 profiles out to a slightly deeper d_{NEO} depth than the mean-free-path definition, although the profiles do still greatly diverge. The $(1 - 1/e)\,\lambda_d$ assumes that deposited energy falls off exponentially with d_{NEO}. The energy profiles created by the 14.1 MeV source are somewhat closer to the pure exponential lines of the analytical equation than that 1 MeV profiles. The MCNP6.2 1 MeV profiles contain the marked "pause" region that strongly deviates from exponential attenuation, and as a result, the $(1 - 1/e)\,\lambda_d$ exponential model does not match the 1 MeV profiles as well.

This analytical formula relies on the simplifying assumption (or rather, approximation) that energy deposition decays purely exponentially with the path-length, and neither path-length definition for λ_d truly describes the nature of the energy-dependent profiles as seen from the MCNP6.2 outputs. Because of this, the Equation 3.11 profiles show significant differences in how the energy is spatially distributed throughout the asteroid as compared to the MCNP6.2 profiles.

The chief advantage of using an approximate equation to generate energy deposition profiles is that it is potentially much faster than constructing, running, and post-processing MCNP6.2 output. However, recall that the $(1 - 1/e)\,\lambda_d$ values were only calculable because the simulation outputs were available. Even though the $(1 - 1/e)$

λ_d version of the analytical equation seemed to produce profiles that compared some-
what better to the MCNP6.2 contours, these $(1 - 1/e)$ λ_d profiles could only be made
after having already run a Monte Carlo simulation, or at least having access to a pre-
vious set of radiation transport outputs. To some extent, this limits the practicality
of the $(1 - 1/e)$ λ_d version of the analytical formula. If energy deposition profiles
from a full Monte Carlo simulation are already available, one might as well use those
data for asteroid material response calculations.

The disadvantage of using an approximate equation is that it is only approximate;
it is not as good of a mapping of energy into an asteroid medium as results from
radiation-transport simulations. The curvatures seen in the MCNP6.2 profiles show
that energy is not strictly exponentially attenuated as it is deposited, as Equation 3.11
assumes. In general, the analytical equation was around an order of magnitude or
less off from the MCNP6.2 profiles for reasonably-shallow d_{NEO} depths at and slightly
beneath the surface, which could potentially lead to significant differences in asteroid
response. Because the energy deposition magnitude is highest at and beneath the
surface, it is most important to accurately capture the profiles in this region, where
material will be melted and/or vaporized and will be able to blow-off. At least for
low detonation yields, however, the analytical equation's dramatic underestimates of
energy deposition at deeper depths might not significantly impact the overall asteroid
deflection performance. If only a few centimeters of material beneath the surface is
melted, the extent where energy deposition results in a ΔT of only 1 K or less is not
much deeper. As such, for some low neutron yields, the sensible energy deposition
region is only on the order of a few tens of centimeters, which is where the analytical
profiles are closest to the MCNP6.2 profiles.

3.2.2 Energy Coupling Efficiencies

The E_{dep} magnitudes at GZ ($d_{NEO} \sim 0$ cm and $\phi \sim 0°$) in Figures 3.6a and 3.6b are 3.14×10^{-10} and 4.86×10^{-11} MeV/g/src-n, respectively. The 14.1 MeV neutron source results in GZ energy deposition that is $\sim$6.5 times more than the deposition resulting from the 1 MeV neutrons. Of course, the lower-energy 1 MeV neutrons arrive at the asteroid surface with less energy than the 14.1 MeV neutrons, and it follows that this would result in a lower deposition intensity at GZ.

However, it might seem strange at first glance that this difference is not identically 14.1. If the 1 MeV source is 14.1 times less in energy than the 14.1 MeV source, why is the difference in energy deposition instead a factor of $\sim$6.5? This difference is due to the non-intuitive, non-linear relationship between the energy deposited and source energy related to the neutron coupling efficiency, an incident neutron-energy-dependent parameter.

As the energy of a neutron changes, so does its cross-section for a given material. Lower-energy neutrons typically experience greater interaction probabilities in materials and in general have a lower mean-free-path than the more penetrative higher-energy neutrons. Furthermore, the probabilities of endothermic interactions occurring increases with incident neutron energy. In SiO_2, 14.1 MeV neutrons have access to a myriad of reaction channels, including exothermic elastic scattering and radiative capture (n,γ), along with various endothermic reactions: (n,p), (n,d), (n,α), and inelastic scattering. This is because the 14.1 MeV source energy is greater than the threshold E_{th} for these endothermic reactions to occur (Table 2.3). In contrast, 1 MeV neutrons traversing SiO_2 do not meet any of these thresholds and only have access to exothermic reactions: elastic scattering and (n,γ), as seen in Table 2.3 and Figures 2.5a and 2.6a. These differences in interaction mechanism probabilities and magnitudes with neutron energy result in differences in the coupled energy.

89

There are two useful ways to define coupling efficiency. First, a relative efficiency definition quantifies how much energy is deposited in comparison to all the neutron energy that actually intersects the asteroid surface, as

$$\eta_{rel} = \frac{E_{dep}}{Y_{int}}, \tag{3.12}$$

where E_{dep} is the total amount of energy deposited in the asteroid and Y_{int} is the "intercepted yield," the amount of source radiation energy that falls within the red cone of Figure 3.1a and intercepts the asteroid's surface. This quantity depends on the problem geometry; the HOB and the asteroid size define the half-angle α (Equation 3.2):

$$Y_{int} = Y_n \cdot \frac{\Omega_{cone}}{\Omega_{FOV}} = Y_n \cdot \frac{4\pi \sin^2 \frac{\alpha}{2}}{4\pi} = Y_n \cdot \sin^2 \frac{\alpha}{2}, \tag{3.13}$$

where Y_n is the total source neutron yield, Ω_{cone} is the fractional solid angle of the cone of radiation that intersects the asteroid, and Ω_{FOV} is the full solid angle field-of-view (4π). By this definition, η_{rel} purely measures the fraction of incident or *intercepted* energy that is absorbed and deposited in the asteroid. η_{rel} is "relative" to this intercepted yield Y_{int}, not to the total yield Y_n.

On the other hand, a second definition of efficiency is

$$\eta_{abs} = \frac{E_{dep}}{Y_n}. \tag{3.14}$$

Because this definition of coupling efficiency is in reference to the *total* yield Y_n, this metric is absolute — it does not factor out the fractional solid angle and therefore includes losses due to spherical divergence from the HOB. In other words, E_{dep} is now compared to all of the yield energy, even the portions of the neutron pulse that

90

radiated outwards into deep space away from the asteroid. η_{abs} will always be less than η_{rel} for a stand-off detonation because Y_{int} will always be less than Y_n.

Table 3.2 shows the relative and absolute coupling efficiencies for each of the two E_{src} neutron energies. As an example, for 14.1 MeV neutrons, η_{rel} and η_{abs} are 0.6884 and 0.1008, respectively. This means that 68.84% of the incident *intercepted* yield is deposited in the asteroid, but only 10.08% of the *total* yield is deposited.

Table 3.2. Energy coupling efficiencies for two neutron sources.

E_{src}	η_{rel}	η_{abs}
14.1 MeV	0.6884	0.1008
1 MeV	1.0896	0.1596

There are two interesting results to be drawn from these coupling efficiencies. First, both the relative and absolute coupling efficiencies for the 1 MeV neutron source are greater than the efficiencies for the 14.1 MeV source. This is in agreement with the general consensus in literature, and it is an expected result from differences in endothermic and exothermic reaction channels from the theory in Chapter 2.

Lower-energy neutrons are more readily-absorbed and receive more of a "bonus" in coupling calculations due to the extra energy produced from exothermic capture reactions. From Table 2.3, the (n,γ) radiative capture reaction generates additional energies of 8.474 MeV or 4.143 MeV when the target nucleus is ^{28}Si or ^{16}O, respectively. Due to the kinetics of conservation of energy and momentum, most of this extra energy will initially be in the form of radiation a la a secondary gamma-ray (which can, in turn, soon deposit some or all of its energy into the asteroid), while the very small remaining fraction of the Q-value will contribute to the recoil kinetic energy of the newly-formed ^{29}Si or ^{17}O nucleus.

In contrast, due to their access to endothermic reaction channels, higher-energy neutrons are required to invest (or "lose") some portion of their incident source energy

to initiate reactions like (n,p) or (n,α), which amounts to a coupling efficiency penalty.

This leads to the second notable result. η_{rel} for the 1 MeV source is greater than 1, which means that $E_{dep} > Y_{int}$, or that more energy was deposited in the asteroid than the incident energy amounted to. This is again due to 1 MeV neutrons obtaining more multi-MeV bonus energies as generated from exothermic capture reactions. Depositing more energy than what was sent to the asteroid target is only possible because enough of the 1 MeV neutrons induce the SiO$_2$ system to liberate 8.474 MeV or 4.143 MeV of extra energy.

A widely-used notional relative coupling efficiency cited and used in literature is 0.70 [34, 36, 86]. In comparison to the relative efficiencies in Table 3.2, this coupling fraction should be a reasonable approximation if the source is predominately high-energy 14.1 MeV neutrons as from a fusion device, but it underestimates the η_{rel} values resulting from a 1 MeV source, which is closer to a fission yield spectrum.

3.2.3 46-group DPLUS Profiles & Efficiencies

Figures 3.6a and 3.6b represent only two of the 46 total energy deposition calculations that were run in MCNP6.2 for this asteroid target. Plots for all 46 energy deposition profiles (one for each of the 46 energy-groups of the DPLUS bin structure, spanning 10 μeV up to 19.64 MeV) are listed in the first section of Appendix A, Section A.1. The second section of Appendix A contains a table with energy coupling efficiency values for all 46 source neutron energies. This large dataset could prove useful for future work investigating which neutron energies are most optimal for asteroid deflection.

IV. Asteroid Deflective Response

This chapter discusses the methodology behind, and analyzes the results from, the ALE3D asteroid deflection hydrodynamic simulations. The spatial distributions of deposited energy from incident neutrons, as determined from the work in Chapter 3, were imported into ALE3D and served to initialize the problem. Material response hydrodynamics via ALE3D allow for the modeling of how the energy deposition from a stand-off neutron source generates material blow-off, or ejecta with various levels of momentum. Tallying the momentums of all blow-off fragments was required to determine how the asteroid deflection δV compares for two different neutron energy sources. This allowed for an initial evaluation of how the source neutron energy affects the asteroid deflection.

4.1 Methodology

There are three pieces to this section on the asteroid deflective response methodology. First, the decisions made within the ALE3D approach are explained. Second, the expected levels of uncertainties in the blow-off momentums are justified. Third, an analytical equation for *x-ray* yields is provided to serve as potential comparison of the computed deflection velocities from the *neutron* yields in this work.

4.1.1 ALE3D Approach

An ALE3D input file (conventionally given a .ain extension identifier) consists of several input blocks to control various multi-physics for a problem [66]. As of ALE3D version 4.30.29, there are twenty different input blocks. However, only four blocks are required as a minimum specification for a hydrodynamic simulation: OUTPUT, CONTROL, REGION, and MATERIAL. For the asteroid response simulations in this

93

work, five additional input blocks were specified: HYDRO, SLIDE, ADVECTION, MESH, and BOUNDARY.

Note that the THERMAL block, which activates the thermal transport module for heat conduction and multigroup radiation diffusion, was not included in these ALE3D runs. Melted and vaporized material in the neutron energy deposition region will blow-off the asteroid surface within a few hundred microseconds, and the resulting shockwave crosses the asteroid body tens of times within a few seconds [68]. In these timescales, especially for the blow-off phase of the problem, heat transfer is not expected to exert much physical influence on the asteroid simulation. Asteroid response trials in ALE3D are run "hydro-only," with thermal energy transfer turned off, simplifying the problem and saving computational time, and there is precedence for this in past work [69].

This section on ALE3D approach is organized by these nine blocks, noting the important ALE3D physics and settings options that were selected in each block.

4.1.1.1 CONTROL Block

The CONTROL block contains generic parameters and timing controls, things that affect the way in which the code is run [66]. By default, ALE3D automatically chooses an appropriate time step based on numerical properties of the simulation. Most of the default values were implicitly kept for asteroid response simulations, as ALE3D supplies the default values for all necessary parameters that were not user-specified in the input file (this is true for all blocks in an input deck, not just for the CONTROL block). One exception to this is that the cutoff for volumetric energy (e_cut) was changed from 1.0×10^{-7} Mbar to 1.0×10^{-300} Mbar. This was done "in order for changes in energy due to Joule heating to register, especially for small time steps - otherwise the energy will be cut off and changes due to Joule heating will not

be allowed to accumulate" [66]. This change ensured that the nearly-instantaneous energy deposition was allowed to register, as discussed in Section 4.1.1.7.

The default minimum time-step (dtmin) was lowered from its default of 10 picoseconds (ps), or 1×10^{-5} microseconds (μs), to 0.01 ps, or 1×10^{-8} μs. The elements in the energy deposition region at the surface suffered significant energy densities due to the detonation yields selected in this work. Because the energy induced rapid movements and flow of materials from zone to zone, maintaining the asteroid mesh in this very violent and turbulent region required smaller time-steps at problem start-up than the default values would allow.

The maximum permissible time-step (dtmax) was changed to 0.5 μs, a massive reduction from the default of 1×10^{40} μs. Without this much-lower limiting cap on how large a time-step could grow, ALE3D would sometimes have the tendency to increase the time-step by too much, allowing for mesh instabilities to accumulate and quickly crash the simulation.

Another important timing parameter for this problem was the initial time-step value (dtinit), set to 1×10^{-5} μs. This was the arbitrary window of time close to zero, meant to approximate an instantaneous energy deposition, as discussed in Section 4.1.1.7.

Lastly, an axisymmetric geometry was selected by setting the axisym parameter to 1. The specific model of axi-symmetry is governed by the elem_integration parameter, which resides in the HYDRO block (Section 4.1.1.8). A value of 3 was assigned to elem_integration, which activates the Wilkins method for 2-D axisymmetric configurations. In this way, the asteroid simulation was run in two-dimensional, axisymmetric geometry.

This means that the asteroid in ALE3D was *not* spherical. The asteroid in ALE3D was circular. A circle is, after all, nothing more than the 2-D analog of a 3-D sphere.

As determined in Section 3.1.1.3 and as visualized in Figure 3.1a, there are 2π radians of symmetry around the y-axis in the problem coordinate system. Because of this, there is no need for a full 3-D spherical representation of the asteroid. Rather, a 2-D circle is sufficient.

More specifically, the asteroid in ALE3D was a perfect *semi*-circle. Examine Figure 3.1b. Because of the inherent symmetries of a circle and of an isotropic point-source, the top-half of the circular asteroid experiences irradiation that is exactly identical to what the bottom-half is exposed to. Once again, there is no reason to simulate both halves of a circular asteroid when only one-half would suffice.

Thus, the 3-D spherical asteroid is represented as a 2-D semi-circle in ALE3D. This is done to save computational time and memory, and this geometric approach has been used in past work [34]. This geometry also allows for finer spatial mesh resolution for a given number of elements or zones. Also, recall that energy deposition in MCNP6.2 was tallied as a 2-D function of depth d_{NEO} and angle ϕ; a semi-circular asteroid is just as compatible with these profile coordinates as a spherical asteroid would be.

Figure 4.1 shows this simple geometry of the 300 meter asteroid in the ALE3D axisymmetric coordinate plane. Because the asteroid sphere in MCNP6.2 was centered at (0, 0, 0), the asteroid semi-circle in ALE3D is also centered at the origin at (0, 0). The ALE3D x-axis is equivalent to the MCNP6.2 y-axis (in 2-D axisymmetry in ALE3D, the x-axis is always the axis of rotation), and the ALE3D y-axis is equivalent to the MCNP6.2 z-axis (i.e. compare to Figure 3.1b). The point-source (or half-point-source in this view) at $c \approx 0.414$ stand-off distance is enlarged for visibility. If this semi-circular asteroid was revolved 2π radians about the ALE3D x-axis, then the full 3-D spherical asteroid would be recovered.
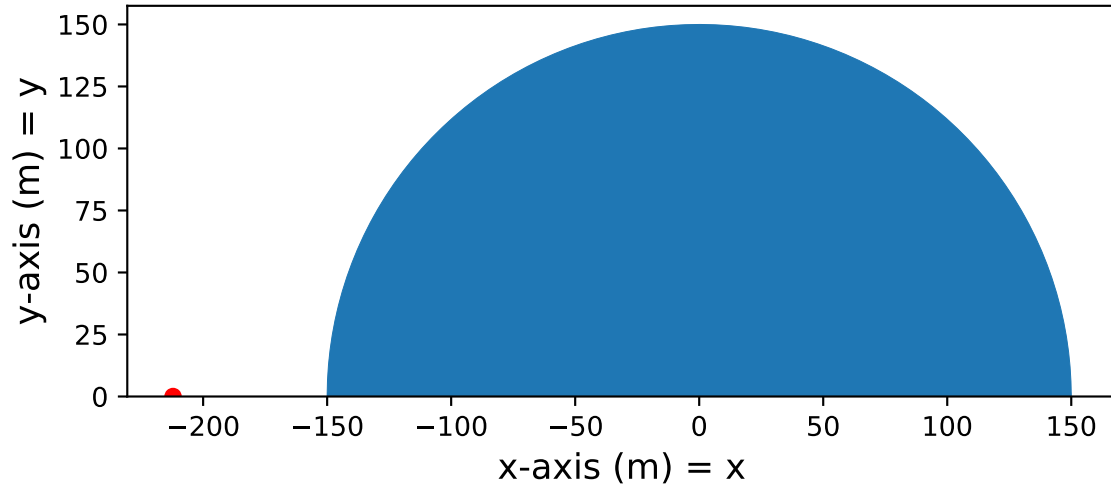
96

Figure 4.1. The 300 meter asteroid in ALE3D is semi-circular via a 2-D axisymmetric geometry. The x-axis in ALE3D is the y-axis in MCNP6.2 coordinates, and the y-axis in ALE3D is the MCNP6.2 z-axis. The red dot on the left is the point-source at $c \approx 0.414$ standoff distance.

4.1.1.2   MATERIAL Block

Each MATERIAL block in an ALE3D input file describes and defines the properties of a single material [66]. For mechanical response simulations of this homogeneous asteroid, only one MATERIAL block is necessary to define the single material: SiO_2. The material model used in this work belongs to the GEODYN library and references Livermore Equation of State (LEOS) #2210 for silicon dioxide.[1] LEOS #2210 is SiO_2 at a standard solid density of 2.65 g/cm^3 and at a reference temperature of 290.1112 K. The microporosity Φ was set to 0.30 (30%), making the bulk or effective material density of the asteroid 1.855 g/cm^3. In this way, the ALE3D material composition and density matched what was simulated in MCNP6.2 for the energy deposition.

The Cap model, which is one of the generic geologic constitutive models available in GEODYN, contributes strength characteristics to the SiO_2 material, making the

---

[1]This material model was developed by Eric Herbold of LLNL's Computational Geosciences Group.

www.manaraa.com

asteroid a rigid or cohesive body rather than rubble [66]. The Cap model is based on three pressure-dependent surfaces that constrain pressure and deviatoric stress during yielding: the moving cap surface $Y_0(p)$, the failure surface $Y_f(p)$, and the residual surface $Y_r(p)$ [66]. It defines a material history variable for damage Ω, which is assumed to be related to the total amount of bulking porosity (or dilatancy, ϕ_2) generated in the material, as,

$$\Omega = \frac{\langle \phi_2 - \phi_{cr} \rangle D}{1 + \langle \phi_2 - \phi_{cr} \rangle D}, \tag{4.1}$$

where ϕ_{cr} is a threshold value of porosity and D is the rate of softening. As damage accumulates during loading, the material softens and its strength approaches the residual curve, or minimum [66].

In a GEODYN model, ϕ_{cr} is given by strain_tofail and D by soft_rate, both in the PseudoCapYieldStrength section. For the silicon dioxide GEODYN model used in this work, strain_tofail is set to 0.0005 and soft_rate is 10. From this, the damage Ω of any zone/element in ALE3D depends only on the variable bulking porosity ϕ_2, and by Equation 4.1 it is between 0 and 1 (0% and 100%). The damage material history variable will be applied in Section 4.1.1.8.

Lastly, appropriate limits for the equation of state (EOS) were supplied by the parameters v0, eosemax, vhlimit, and eosvmax, where the supplied values were 1, 200, 1000, and 2, respectively. v0 is the initial value of relative volume (which is the 1.855 g/cm^3 reference density divided by the current density); eosemax is the maximum permissible value of volumetric energy; vhlimit is the ceiling on possible relative volumes; eosvmax is maximum relative volume for EOS evaluations. These parameter definitions were necessary to ensure that the material was initialized at standard conditions and that the EOS remained within valid specifications.

4.1.1.3 ADVECTION Block

ALE3D is a multi-physics numerical simulation code utilizing ALE (Arbitrary Lagrangian/Eulerian) techniques. It operates via a hybrid finite element (FE) and finite volume (FV) formulation to model both the fluid and the elastic-plastic material response on an unstructured grid [66]. One of its chief capabilities is advection, or mesh relaxation. Each time-step in a hydrodynamic simulation in ALE3D consists of two phases: first, a Lagrangian step that calculates the evolution of materials in the problem and updates nodal and zonal/elemental quantities, and second, an advection or re-map step that interpolates the Lagrangian-calculated variables onto a new, more favorable mesh overlay. Mesh relaxation is performed to combat mesh distortions and zonal tanglings that would otherwise cause a pure-Lagrangian code to crash.

Advection was indispensable to this problem, as the energy deposition region (where material blow-off is created) is high-temperature, high-pressure, and high in energy, which will make materials expand and distort very rapidly and violently. Furthermore, to achieve satisfactory resolution, the zone sizes were rather small. Without advection, when the simulations were set to be Lagrangian-only, crashes due to negative zonal volumes (from extreme mesh tangling) were frequent and occurred early in the simulation times. Mesh re-mapping and relaxation allowed for most elements to remain in decent condition, and fewer zones were severely twisted or distorted. Advection also allowed for the simulations to persist long-enough to reach asymptotic values for the asteroid momentum due to the blow-off impulse. Of course, this mesh relaxation process was not free, as it came with a large cost in increasing the computational time required for ALE3D to operate.

Many of the default ALE3D parameters for advection applied to this problem. Several non-default parameter values had to be specified, however. In early models, crashes occurred due to non-physical negative mass errors in certain elements. The

99

output file error messages indicated that this might be caused by the default density interpolation scheme (rhobarorder 2) allowing highly sheared zones. The alternative, rhobarorder 1, a "more accurate second order method due to the inclusion of transverse terms in the interpolated density," was specified, and this specific type of negative mass error ceased [66].

Even more importantly, the advection time-step control parameter (advdtcon) was lowered from its 0.5 default. This means that, if the advection re-mapper function determines that the mesh is moving too fast and causing stability and accuracy concerns, then the time-step will be reduced. For each time-step, the Lagrangian physics calculation of all the mesh variables is performed, and following this the advection phase occurs and the mesh is relaxed. That is, by default, there is one advection relaxation each time-step. By lowering advdtcon, if the relaxation calculations indicate that the Lagrangian phase is moving too quickly for mesh re-mapping to keep up with, then the time-step is reduced and limited accordingly. For the various simulations performed in this work, the required value for advdtcon varied. The range was from 0.1 to 0.25.

Related, the advdtmult variable, which is the multiplier that defines a floor value for the advection time constraint, was also lowered from its default of 0.1. A small value for advdtcon will reduce the time-steps if advection asks for it, but only down to a certain point. The advdtmult parameter becomes another limiting condition to ensure that the time-step does not fall to extremely low values. However, the default value for advdtmult did not allow the time-steps to decrease enough, and mesh errors from negative volumes or advection issues resulted in crashes. The value used for advdtmult varied for the set of simulations done for this thesis, but the range was between 0.01 and 0.025.

Lastly, advection iteration was enabled (it is off by default). The default 1:1 ratio

100

of one mesh relaxation per one Lagrangian time-step was not sufficient for advection to "keep up" with the moving mesh and prevent errors. For every 20 μs of simulated asteroid time, the advection iteration variable advitercnt was raised from 1 to 3 for a 0.1-or-so μs window, then set to 2 for another 0.1-or-so μs, and then lowered back to 1. When advitercnt is set to 3, this means that the advection calculations can iterate the mesh relaxation and re-mapping three times per Lagrangian step instead of just one, and when advitercnt is 2 it can perform two advection steps. Multiple advection steps are expensive with respect to computational time, but allowing this iteration every 20 μs allowed for the simulations to continue running.

4.1.1.4   SLIDE Block

A SLIDE block in ALE3D defines settings for slides, which are surface boundaries that allow misaligned or disjoint parts of the mesh to interact with each other [66]. As will be shown in Section 4.1.1.6, there are three surface boundaries within the generated asteroid mesh where nodes on one side do not align with nodes on the other side. Without slide surfaces enabled, communication across these surfaces would not have been possible, meaning that mass, energy, and momentum would not have been able to cross these boundaries. With three SLIDE blocks active (one for each of the three boundaries), the asteroid mesh behaves as it should.

These three slide surfaces were tied together by setting tiedall to 1. By default, and perhaps as suggested by its namesake, slide surfaces between two portions of a mesh allow one side to slide across the other (there is no tangential friction, by default). For a cohesive and rigid asteroid, this did not seem desirable. Instead, the slides became tied slides in order to inhibit all tangential motion along the slide surface, which in effect tied the mesh together. In this way, the zones along the slide surfaces became cohesive (i.e. normal and tangential accelerations along the surface

are combined into center-of-mass accelerations), as it is in all other locations within the solid asteroid.

These three slide surfaces were two-sided slides, requiring the user-specification of the master-side (m) and the slave-side (s). The master side is the surface "used to enforce normal velocity continuity in the final step of contact" [66]. Typically, the master-side of a two-sided slide surface is the mesh that is lower in resolution (i.e. larger zones) and the slave-side is the mesh that is higher in resolution (i.e. smaller zones). Figure 4.2 shows an example of master- and slave-sides along a slide surface boundary.
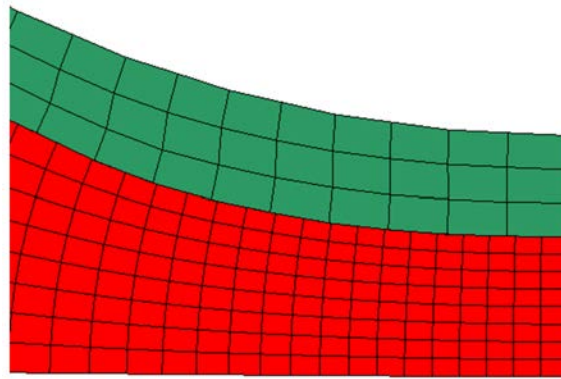
Figure 4.2. Master and slave sides of a two-sided slide surface (the boundary between the green and red meshes). Typically, the lower-resolution mesh is defined as the master-side, while the higher-resolution mesh is the slave-side. The upper mesh (green) is more coarsely zoned than the lower mesh (red), and thus the former is the master and the latter is the slave.

Additionally, when elements are eroded in a simulation (and for blow-off, element erosion is enabled, as discussed in Section 4.1.1.8), neighboring zones that were not exposed at the start of the problem suddenly find themselves with free surfaces. As the problem continues marching forward in time, these newly-exposed surfaces are not able to interact with other parts of the mesh, by default. For this problem, the autocontact flag was enabled, which creates simpler, one-sided slide surfaces on new-faces automatically as the simulation progresses. With auto-generated slides to encapsulate their free surfaces, these zones can continue to communicate with other

102

parts of the mesh.

4.1.1.5   REGION Block

A REGION block is used to initialize a portion of the mesh that has been assigned a given region number [66]. In other words, part or all of a given mesh is associated, and filled, with a pre-defined material from the MATERIAL block. There is only one material (SiO_2) in the MATERIAL block for this problem, yet the asteroid mesh is made of two regions as seen in Figure 4.3. The REGION block in the ALE3D input files is labeled by two region numbers, with region #1 corresponding to the sensible energy deposition area and region #2 consisting of the remaining asteroid body. This means that both regions in this setup refer to the same material with the same initializations, the same advection parameters, etc. The reason for creating two identical regions will be explained in Section 4.1.1.8.
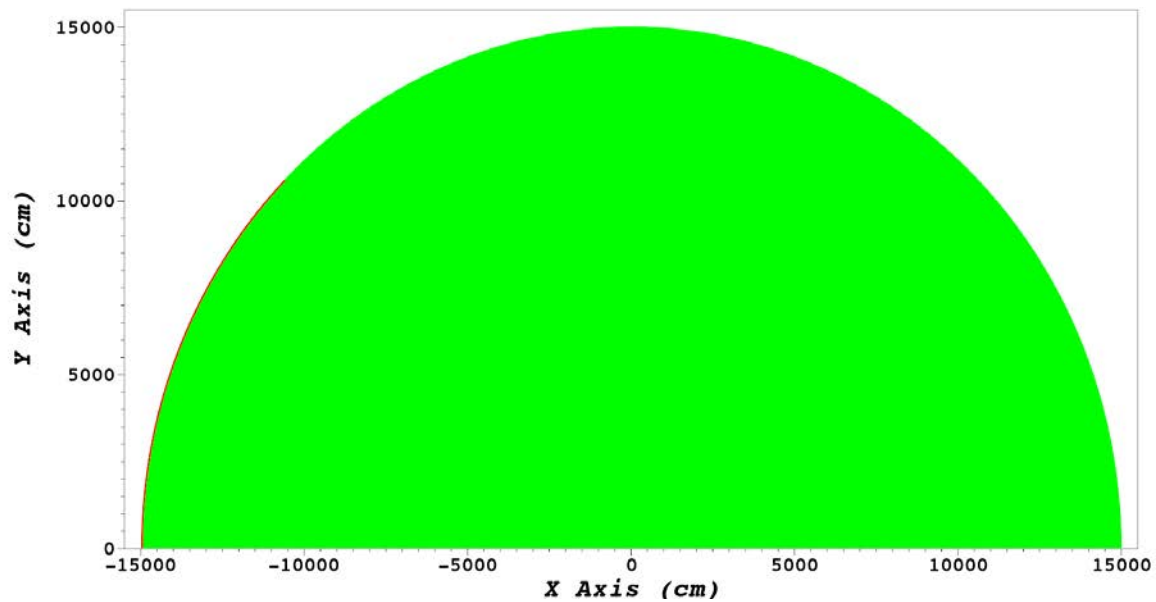
Figure 4.3. ALE3D regions of the asteroid model. The asteroid mesh is partitioned into two different regions — the zones in the green area fall into region #2, and the zones in the red area (the narrow strip along the left surface) belong to region #1. Both regions are filled with identical SiO_2 material.

Other than assigning the material name from the MATERIAL block onto these

103

regions via the matname command, the only argument in this block is advinput. These are region-based relaxation parameters (some advection settings can be specified in the REGION block or the ADVECTION block). Sub-commands within the REGION advinput are advmat 1, advtmat 0.0, and rlxwmat 1. Respectively, these settings mean that the region is allowed to advect, that advection is allowed to begin at time zero, and that the material region has a uniform weight of one. These three options were recommended when using the provided GEODYN SiO_2 material model.[2]

Three other region-based advection parameters were assigned non-default values. The region-based displacement constraint ratio (rlxdxmat) was set to 0.25, changed from a default of 0.3. This means that, during the advection re-mapping phase, the positions of the nodes for the elements in the mesh cannot move quite as much as they might otherwise want to. Changing this setting was meant to combat the occasional "too much advection" error, which appeared to be resulting from the advection re-mapper applying relaxation to the mesh too quickly per unit time. Also, the distortion test, rlxtmat, and the volume test, rlxvmat, were set to 0.1. Ordinarily, these tests are both set to 0.0 (de-activated). If they were set to 1.0, then the mesh would constantly be forced to relax. For values between 0.0 and 1.0, relaxation can be induced when zones are distorted and/or at a relative volume beyond a certain threshold. These tests were activated to combat mesh tangling issues which resulted in negative volumes and subsequent simulation crashes.

4.1.1.6   MESH Block

The MESH block defines the mesh used in an ALE3D calculation [66]. Given the desired circular shape of the 2-D asteroid, the ALE3D internal mesh generator of the form "mcircle" for generic circular geometries was applied. The quarter-type mcircle mesh is shown in Figure 4.4. Zonal spacing is uniform in the angular θ direction

---

[2]Megan B. Syal, private communication.

and, by default, also uniform in the radial r direction. The different colors signify different radial strata (shells) that can be given unique resolutions and each assigned to different region numbers.
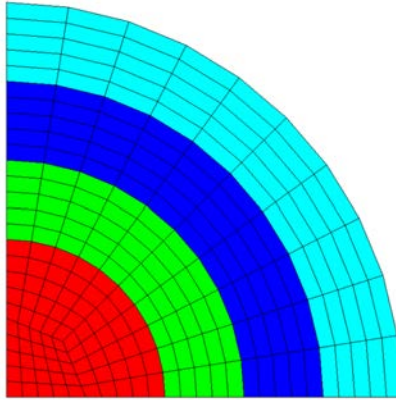
Figure 4.4. ALE3D mcircle quarter-type mesh structure. By default, zonal spacing is uniform in both r and θ. The different colors represent different shells or radial strata, providing the capability for greater resolution in certain areas of the mesh than others.

Four separate mcircle meshes, all quarter-type representing $\frac{1}{4}$ of a circle, were generated and then combined into a single mesh object. Of course, this would generate a full circle, so to restore semi-circular geometry, all four 90°-circle meshes were scaled down by a factor of two (creating meshes with 45° extents) and then rotated appropriately. The scaling is done by non-linear transform operations in ALE3D, consisting first of invpolar (inverse transform of a polar geometry to a Cartesian grid), scaling, and then polar (undoing the Cartesian mesh representation). This process is shown in Figure 4.5, demonstrated by converting a quarter circle into a fifth (72°).

The resulting positioning of each of the four 45° meshes, creating the 2-D semi-circular asteroid, is shown in Figure 4.6. The meshes are named left45, topleft45, topright45, and right45, based on their positions from left-to-right. The mesh resolution is greatest on the left, especially at the outer surface, and is gradually decreased

105
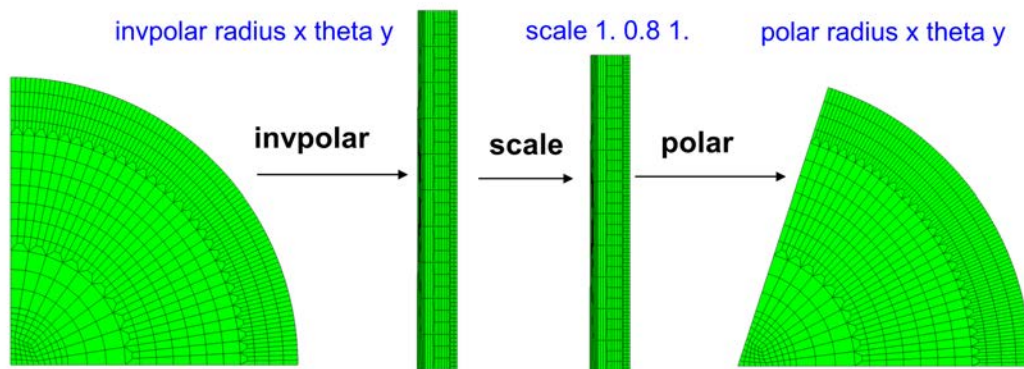
Figure 4.5. ALE3D non-linear transforms and mesh scaling. A 90° circular mesh is scaled down to a 72° extent. The process consists of the invpolar, scale, and then polar commands.

for each mesh moving to the right. While the four meshes were combined via the merge command in ALE3D, merging is not possible in the areas of the mesh where nodes do not align. Because of this, two-sided slide surfaces along the surface boundaries (labeled 1, 2, and 3) were defined to allow for these meshes to function as one. This "enables one to use slide surfaces to affect a zoning change in the middle of a region" [66]. As discussed in Section 4.1.1.4, the master-side is usually coarser in resolution and the slave-side is finer in resolution. As such, the slave-sides of these three surfaces (1s, 2s, 3s) lie to the left, where the overall mesh is higher in resolution, and the master-sides (1m, 2m, 3m) are to the right, where the mesh refinement has decreased.

The mesh resolution was altered through the use of ALE3D transition elements. There are two layers of 1-to-3 transition elements seen in Figure 4.5, which are specially-shaped trapezoidal elements that have a single face towards the center of the mesh and three faces away from the center of the mesh. For mcircle meshes, 1-to-3 transition elements increase the resolution in θ by a factor of three, i.e. increasing the number of zonal divisions in the angular direction threefold. Using several layers of transition elements in the left45 mesh, the mesh resolution achieved at the outer sur-
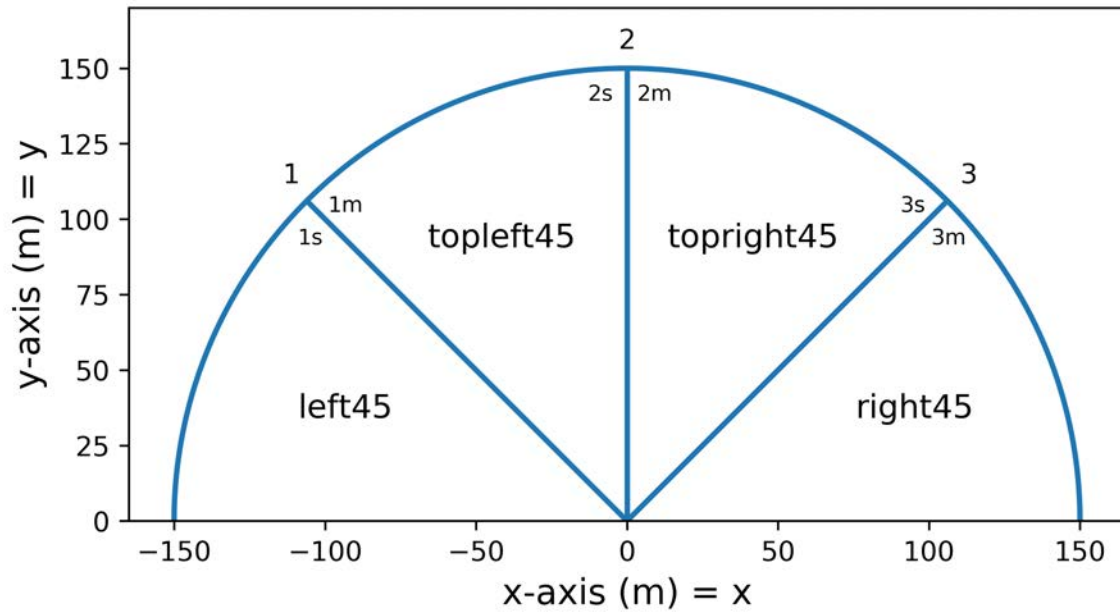
106

Figure 4.6. Four $45°$ meshes creating a semi-circular mesh. The meshes are named left45, topleft45, topright45, and right45, based on their positions from left-to-right. The mesh resolution is greatest on the left and is gradually decreased for each mesh moving to the right. The surfaces labeled 1, 2, and 3 are the three boundaries between the four meshes. Master and slave slide surfaces are defined along both sides of each of these boundaries.

107

face (in the sensible energy deposition region) was on the order of a few centimeters. Zonal resolution gradually decreased both when moving along r towards the asteroid origin and when moving along θ from the left-side of the asteroid (the irradiated side) to the right-side (the dark side). Figure 4.7 shows the finalized 2-D semi-circle asteroid mesh with variable spatial resolution.
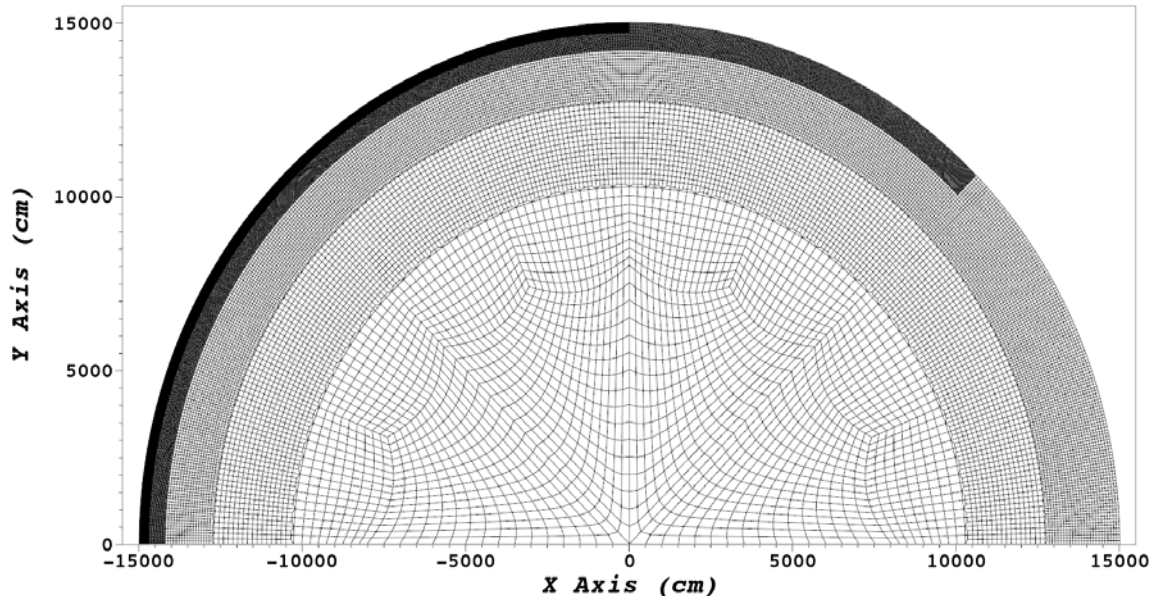
Figure 4.7. ALE3D semi-circular asteroid mesh. The mesh is most refined on the left, near the outer surface and between GZ ($0°$) and $45°$ off from GZ. This is the energy deposition region, where very high resolution was required. The mesh resolution is gradually decreased as the angle increases, moving from left to right. It is also gradually decreased when moving inwards towards the asteroid core.

This complex mesh structure was necessary to have the greatest resolution in the energy deposition region to capture the features of the rapidly-changing energy deposition profiles in Figure 3.6. Less resolution was required throughout the rest of the asteroid. This process saved several hundreds of thousands, or even millions, of additional zones that would have been required without transition element zoning and use of four sub-meshes. The computational time and memory would have been considerably higher without creating this mesh in a wise manner.

As an aside, it should be noted that the sensible energy deposition region (i.e.

108

the red area in Figure 4.3, which is the outer surface area of the left45 sub-mesh in Figure 4.6) is much longer in ϕ than it is deep in r. As will be discussed in more detail in Section 4.1.2, the maximum melt-depth resulting from the neutron energies and detonation yields that were considered in this work was about 200 cm. However, the $c \approx 0.414$ stand-off distance for the detonation source irradiates the asteroid surface from 0°-to-45°, and the arc-length L of this surface is $L = R\phi = (15{,}000 \text{ cm}) \cdot \frac{\pi}{4} \approx$ 11,781 cm. This is nearly 60 times longer than the 200 cm depth, and almost 340 times greater than a 35 cm depth, another melt-depth for a different neutron yield tested in this work. Discretizing such a long and narrow region at and beneath the surface meant that the vast majority of the zones in the entire mesh were located along this energy deposition strip.

4.1.1.7   BOUNDARY Block

The BOUNDARY block exists to define boundary and initial conditions for a problem [66]. This block was required to implement the primary initial boundary condition for these hydrodynamic simulations: the energy deposition at and beneath the asteroid surface. MCNP6.2 energy deposition profiles were imported into ALE3D by a combination of functions working in tandem: two one-dimensional tables (table), a two-dimensional table (table2d), three space tables (spacetable), and heat generation throughout space (heatgen space).

MCNP6.2 profiles were tallied in terms of depth d_{NEO}; the energy deposition at the surface was at $d_{NEO} = 0$ cm, which is equivalent to the ALE3D asteroid radial coordinates $r = 150$ m. MCNP6.2 profiles were also tallied in terms of the asteroid-centered angle ϕ. However, this angle was in reference to the left-side of the asteroid, where $\phi = 0°$ is located at GZ. ALE3D asteroid angular coordinates assign $\theta = 0°$ to the *right*-side of the asteroid, which is more standard convention for 2-D Cartesian

plane quadrants. A preparatory step for loading MCNP6.2 energy deposition into the ALE3D asteroid involved defining and mapping these differing coordinate systems to each other via two tables and two spacetables. That is, MCNP6.2's d_{NEO} was put in terms of ALE3D's r, and MCNP6.2's ϕ oriented to ALE3D's θ.

Next, a table2d was defined. This was the structure in ALE3D that contained all 256,470 energy deposition data-points from the MCNP6.2 outputs. This table was two-dimensional because the MCNP6.2 energy deposition was two-dimensional. The midpoints of each MCNP6.2 tallied cell were supplied (498 in depth, and 515 in the angle) as the discrete coordinates of the 2-D table.

Another spacetable was defined that instructed ALE3D to use MCNP6.2 coordinates on the ALE3D asteroid to interpolate and map the energy deposition onto the proper mesh locations. Given the contours in Figure 3.6, the profiles are more exponential than they are linear. As such, logarithmic interpolation of the data in this 2-D table was used, overriding the default linear interpolation.

The heatgen space method was used to activate the energy deposition spatial mapping and instill zones with internal energy. As suggested by its name, heatgen is a rate-based generation of energy over time; it is not instantaneous. The duration and timing of heatgen must be defined. The rate of generation Q_0 (or massrate, in units of energy per mass-time) must also be supplied. Recall that the MCNP6.2 energy depositions values are normalized and in units of MeV/g/srn-n. Depending on the selected neutron yield (Equation 1.1) of the detonation, a certain known number of source neutrons will scale the MCNP6.2 values accordingly.

After inspecting the heatgen formulation and performing dimensional analysis, the following equation was derived that defines the massrate Q_0 as a function of the

110

initial time-step Δt_0 and the known number of source neutrons src-n:

$$Q_0 = \frac{1.60218 \times 10^{-18} \left[\text{Mbar-cc-g}^{-1}\text{-src-n}^{-1}\right]}{\Delta t_0 \,[\mu s]} \cdot \text{src-n}\,[\text{src-n}]. \qquad (4.2)$$

The units associated with each term are shown in brackets. In total, this gives the heat generation massrate Q_0 units of $[\text{Mbar-cc-g}^{-1}\text{-}\mu s^{-1}]$. The heatgen formula for cumulative mass-based heat Q is

$$Q = Q_0 \cdot \Delta t, \qquad (4.3)$$

where Δt is the amount of time that heatgen is activated.

Δt is set to the initial time-step Δt_0 only — that is, heatgen space is only active for the very first ALE3D time-step. As stated in Section 4.1.1.1, the initial time-step dtinit was $\Delta t_0 = 1 \times 10^{-5}$ μs, which was considered a small-enough time-step such that energy deposition is approximately instantaneous. Delayed input functionality in ALE3D allowed for heatgen space to be turned off at the beginning of the second cycle, meaning that all of the energy was deposited within the first time-step only.

Q has units of $[\text{Mbar-cc-g}^{-1}]$. Recognizing that 1 Mbar-cc $= 10^5$ J, at last these units describe real energy deposition from a detonation source.[3] ALE3D now has deposited energy in terms of energy per mass at the correct spatial locations as given by the MCNP6.2 coordinates.

Lastly, there was no initial condition for the velocity of the asteroid — at time zero, the moment before energy deposition, the asteroid mesh was stationary. In reality, of course, asteroids are moving through space at great velocities. The implicit assumption here is that the ALE3D simulation-frame is a moving-frame-of-reference.

---

[3]While ALE3D can operate in any system of units, provided that the user supplies the necessary specifications, default values for inputs and outputs are expressed in LLNL's "B-division" (B-Div) units — length is in cm, mass in g, time in μs, energy in Mbar-cc, pressure in Mbar, volume in cm^3 or "cc," and temperature in K.

111

It does not matter so much what the asteroid velocity V is; what matters more is what the *change* in asteroid velocity δV is. By initializing the asteroid mesh velocity to $V = 0$, δV is simply the velocity in ALE3D that is induced by the neutron energy deposition.

4.1.1.8 HYDRO Block

The HYDRO block in ALE3D input files controls the parameters for Lagrange hydrodynamics [66]. The first two hydrodynamic parameters specified for this problem were elem_integration and hgmodel. As mentioned in Section 4.1.1.1, elem_integration was set to 3, which turned on the Wilkins 2-D axisymmetric linear operator as required for the semi-circular geometry. hgmodel was set to 4, the rotational Q hourglass control method for axisymmetric problems, as recommended in tandem with elem_integration 3.

The other notable setting in the HYDRO block for this problem was the activation of element erosion. Element erosion is the deletion of elements/zones upon reaching a certain condition or set of conditions. Often, element erosion is used to prevent mesh tangling in Lagrangian codes, where deleting poorly conditioned zones allows the problem to run longer. Even with the strict amounts of advection specified in the ALE3D input files, described in Section 4.1.1.3, some elements still became extremely distorted and in poor condition. Eroding these elements allowed the simulations to continue marching forward in time without crashing.

Element erosion deletes the mass, energy, and momentum of the eroded zones. This presents a potential problem, as it is precisely the mass and momentum of the blow-off and/or the asteroid body that must be tracked in order to determine δV. This issue was partially resolved by limiting erosion only to region 1, or the sensible energy deposition region, the red area of Figure 4.3. This was the main reason why the

112

asteroid mesh was defined by two different regions (yet both with identical properties) in Section 4.1.1.5. With this, the other component of navigating around this problem came from how δV was calculated, explained in Section 4.1.1.9.

Elements in region 2 (the green area of Figure 4.3, the majority of the massive asteroid body) could not be deleted. Region 1 is where zones are melted and/or vaporized due to the extreme heating consequences of energy deposition, and it is also where the zones are the smallest, on the order of a centimeter or a few centimeters (see Figure 4.7). Because of their small size and large amounts of energy, it is in region 1 where a small fraction of the zones will degrade in condition and require deletion to continue the hydrodynamic simulation.

For an element in the energy deposition region to be eroded and subsequently deleted, one or both of the following criteria must be met:

- The zone-centered distortion[4] mesh-quality variable must be less than or equal to 0.07.

- The elemental damage (Ω from Equation 4.1) must be 0.99 (99%) or greater.

These conditions search for zones that, in spite of the advection and mesh relaxation, are badly distorted and/or are heavily damaged (often one occurs in conjunction with the other). The thresholds of 0.07 for distortion and 0.99 for damage were somewhat arbitrary, but these values were found to allow the hydrodynamic simulations to run for longer without crashing.

---

[4]Distortion is "a measure of how well-behaved the mapping from parameter space to world coordinates is" [87]. The acceptable range for distortion is typically 0.5 to 1.0. That is, values in this range are not generally a cause for concern or a precursor to mesh issues. For a unit square, distortion is 1. As the distortion falls below 0.5, and even into the negative range, the element becomes more and more deformed.

4.1.1.9   OUTPUT Block

Commands in the OUTPUT block of an input file are options that control the output of data [66]. ALE3D was instructed to generate plot-files to visualize the asteroid every 50 μs up to 1 ms. Also, ALE3D was set to produce restart-files for every 30 minutes of physical (wall-clock) time. Restart files are SILO/HDF5 formatted files that "contain all of the information required to start an ALE3D run from that point," such that "the physics calculation can be restarted at any time from a restart file" [66].

As the earlier discussions of ALE3D methodology have implied, simulation crashes due to various computational errors occurred periodically. Because restart files were saved for every half-hour of real time, if a crash did occur, the ALE3D input file could be adjusted and re-run with reference to its most recent restart file. This avoided the unseemly idea of restarting at time zero in simulation time if a simulation threw an error a few cycles before its natural end. Each simulation took several days of physical time to run with varying amounts of wall-time hours, and restart files proved invaluable towards inching the simulated asteroid response forward in time.

A selection of variables of interest were to be included with each plot-file. Derived variables (derivedvars) are zone-centered or node-centered variables that are calculated from other fundamental hydrodynamic variables. Many quantities, including the density, kinetic energy, internal energy, specific energy, zonal velocities in the x- and y-direction, damage, and more were requested derivedvars in the OUTPUT block.

A derivedvar expression for the normal velocity in the outward direction from the asteroid center-of-mass, $v_\perp$, was required. The escape velocity v_{escape} is the velocity necessary to leave the asteroid body, but it is direction-dependent. An element should not escape, for example, if it was traveling at greater than the escape velocity, but in a direction towards the asteroid core.

114

The momentum impulse due to the evolution of the blow-off momentum is quoted in literature as occuring within a few hundred microseconds [68]. On this timescale, the entire or bulk asteroid body does not have enough time to move. As such, for the purposes of blow-off classification, the center-of-mass (CoM) of the asteroid — which is identical to the center-of-gravity when the gravitational field is uniform — was assumed to be exactly at the origin, the center of the asteroid at coordinates (0,0). Indeed, the CoM in the y-direction will always be zero (along the x-axis), through all time, due to the axisymmetric geometry. The CoM in the x-direction will slightly evolve in time both as the blow-off mass separates and as the asteroid structure itself moves to the right in the +x direction; however, the departure from x=0 should be negligible for the simulation times considered for the rapid momentum impulses in this work.

Next, considering the curvature of the asteroid zones along and beneath the surface, some additional work was required for proper application of the escape velocity threshold. A coordinate transform for each zone was required to convert zonal velocities in the x- and y-direction to the velocity $v_\perp$, or the effective speed of each zone in the outward direction referenced to the CoM:

$$v_\perp = -v_x \cdot \cos\phi + v_y \cdot \sin\phi, \tag{4.4}$$

where v_x and v_y are the zonal velocities in the x- and y-directions and ϕ is the angle between an element and the CoM at (0,0). Figure 4.8 visualizes the calculation of $v_\perp$. This $v_\perp$ is the correct velocity to evaluate against the v_{escape} threshold from Equation 1.2.

Special masked derivedvars were then defined for the asteroid mass, the asteroid momentum, the blow-off mass, and the blow-off momentum. The x-momentum for all zones across the whole mesh is stored as the momentum_x derivedvar, and the

115
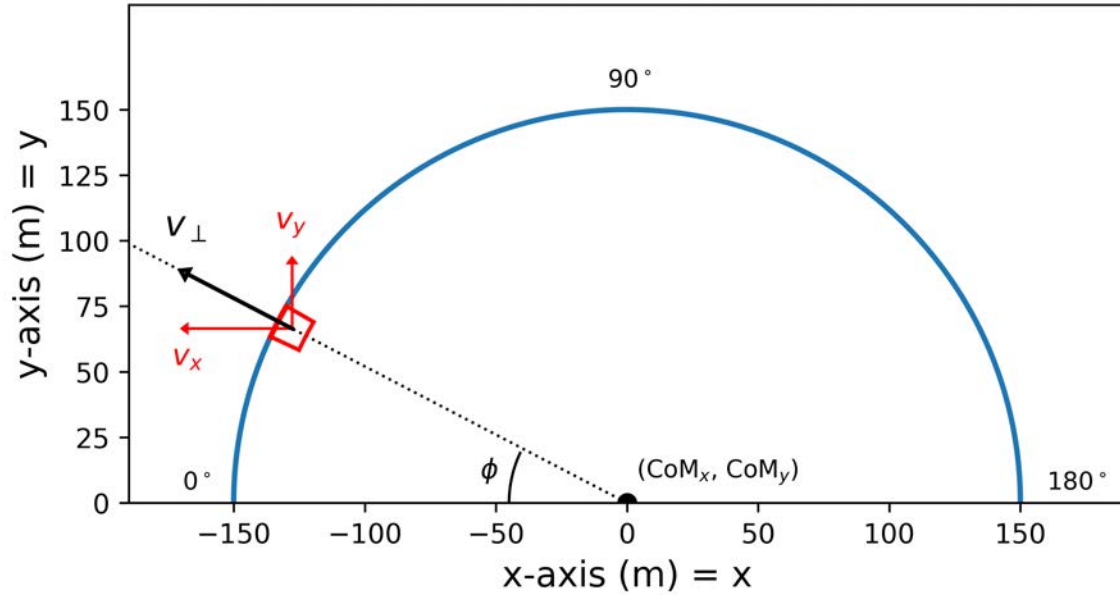
Figure 4.8. Coordinate transform of zonal velocities. Based on the angle ϕ between an element and the center-of-mass, the zonal velocities in the x- and y-directions are converted to the effective velocity $v_\perp$ in the direction where the escape velocity threshold applies. If $v_\perp$ is positive, it is pointed in the outward direction away from the asteroid. If $v_\perp$ is negative, it is pointed towards the asteroid CoM.

zmass registered variable contains the zonal masses for each element.

Variables named asteroid_momentum_x and asteroid_zmass were "masked" versions of these variables meant to track the momentums and masses of the zones that are *not* blow-off. If a zone's velocity normal to the asteroid's center-of-mass, $v_\perp$, is less than the escape velocity, v_{escape} from Equation 1.2, then its value stored in the asteroid_momentum_x array is the same as what it is in momentum_x. Otherwise, if $v_\perp > v_{escape}$, then its value in asteroid_momentum_x is set to 0. Similarly, if $v_\perp < v_{escape}$, then the asteroid_zmass value for that zone is the same as its value in zmass; otherwise, the elemental asteroid_zmass is 0. In this way, asteroid_momentum_x and asteroid_zmass are simply filtered arrays of the momentum_x and zmass variables, where the formers match the values of the latters only where $v_\perp < v_{escape}$. Thus, asteroid_momentum_x and asteroid_zmass were meant to capture all the zones that are *not* blow-off.

116

A similar masking operation applied to blowoff_momentum_x and blowoff_zmass. If a zone meets the definition of blow-off, i.e. if $v_\perp > v_{escape}$ and if the specific energy deposition (energy per unit mass) is greater than the ∼1941 J/g melt threshold for SiO_2 [48], then its values in blowoff_momentum_x and blowoff_zmass match what they are in momentum_x and zmass. Otherwise, the zonal values are zeroed in this variable. These variables were meant to group the zones that are melted and traveling at velocities above the escape threshold, i.e. the zones that are blow-off.

These masked derivedvars were defined in preparation for the time histories feature of ALE3D. Time histories (timehists) are functions in ALE3D that record the values of dynamic parameters that change over time. By default, timehists save values every cycle, i.e. every time-step, throughout the entire simulation time. Four primary timehists were activated:

1. The sum of the zonal asteroid_momentum_x, which is the total x-momentum of the asteroid body.

2. The sum of the zonal asteroid_zmass, which is the total mass of the asteroid body.

3. The sum of the zonal blowoff_momentum_x, which is the total x-momentum of the blow-off.

4. The sum of the zonal blowoff_zmass, which is the total mass of the blow-off.

An additional timehist computed the initial sum of the internal energy after the first cycle; this quantified the total amount of energy deposited in the asteroid due to the stand-off detonation source. Two other timehists saved the maximum pressures present in the mesh over time to see how shockwave intensity changes with neutron energy and/or yield.

Like all macro-scale physical interactions, asteroid deflection is bound by Newton's laws of motion. The conservation of momentum determines the change in asteroid velocity δV:

$$\frac{\delta M_{ejecta}}{M_{asteroid}} = \frac{\delta V}{-V_{ejecta}}, \tag{4.5}$$

where δM_{ejecta} is the mass of the material ejected into space (melted blow-off and/or solid ejecta), $M_{asteroid}$ is the mass of the remaining asteroid body, and V_{ejecta} is the velocity of the ejected material [36]. In other words, in the vacuum of space, when material of a certain momentum is ejected, the remaining body is imparted with an equal momentum in the opposite direction:

$$p_{ejecta} = -p_{asteroid}, \tag{4.6}$$

where

$$p_{ejecta} = \delta M_{ejecta} \cdot V_{ejecta}, \tag{4.7}$$

and

$$p_{asteroid} = M_{asteroid} \cdot \delta V. \tag{4.8}$$

Thus, there are two routes to take to apply the ideas in Equations 4.5 and 4.6 and compute δV. If the total blow-off momentum p_{ejecta} is tracked and quantified, $-p_{ejecta}$ can be substituted for $p_{asteroid}$ (via Equation 4.6) and then placed into Equation 4.8 to yield

$$\delta V = \frac{-p_{ejecta}}{M_{asteroid}}. \tag{4.9}$$

In this case, ALE3D would calculate p_{ejecta} as

$$p_{ejecta,\,x} = \sum_{i=1}^{N} \text{blowoff\_momentum\_x}_i, \tag{4.10}$$

118

where i is the index for all N elements in the asteroid mesh. This formulation is the timehist sum of blowoff_momentum_x. Unfortunately, as noted in Section 4.1.1.8, some of the zones in the energy deposition region are eroded and deleted over time if they become very poorly conditioned. As a result, the blow-off momentum is not conserved in these ALE3D simulations, and p_{ejecta} should not be relied upon.

The second avenue of calculating δV largely avoids this problem. Simply, Equation 4.8 is used directly and re-arranged to get

$$\delta V = \frac{p_{asteroid}}{M_{asteroid}}, \tag{4.11}$$

where

$$p_{asteroid,\, x} = \sum_{i=1}^{N} \text{asteroid\_momentum\_x}_i, \tag{4.12}$$

where i is the index for all N elements in the asteroid mesh. This is the timehist sum of the asteroid_momentum_x masked derivedvar in ALE3D. With Equation 4.11, δV is estimated by *excluding* the momentums of zones that meet the definition of blow-off.

The small amounts of element erosion that occur in region 1 should not have much impact on this second formulation of δV, because most of the heavily damaged and/or distorted zones that are deleted should be the result of the intense energy deposition. That is, it is much more likely that a few melted blow-off zones with negative x-momentums (i.e. having inertia towards the -x direction) will meet the thresholds for deletion than any non-melted, non-blow-off zones. Instead of Equation 4.9, Equation 4.11 was utilized; it was believed that the latter would offer a more trustworthy estimate of δV than the former.

It should be noted that shockwave propagation and crossings within the asteroid body might have an effect on the overall δV that the immediate, impulsive momentum

119

due to the initial blow-off does not capture. Pressure waves cross the asteroid on the order of tens of times over the course of seconds, which can result in additional crushed solid ejecta and some additional momentum changes [68]. Ideally, these ALE3D simulations would have run out to simulation times of several seconds, but this proved quite impractical, considering the amount of time and effort required to advance the asteroid response to only a few hundred microseconds following energy deposition. It is possible that implicit mechanics, which can sometimes be used to operate problems over longer timescales than explicit calculations, might be able to be configured and activated the moment after blow-off is concluded. Perhaps additional refinement or modification of the ALE3D input file set-up is required if shockwave crossings are desired.

As an aside, the formulation of Equation 4.11 shows that δV via the application of conservation of momentum is the same as the mass-weighted mean-value of the x-velocities of all the asteroid elements. Also, note that momentum in the y-direction is ignored; due to axisymmetry, it will always be zero. The only deflection of the asteroid that occurs is in the x-direction in ALE3D coordinates.

4.1.2 Blow-off Momentum Uncertainties[5]

The asteroid mesh resolution in the energy deposition region (red area in Figure 4.3) was on the order of centimeters. Any choice of resolution would be an approximation because homogeneous material behaves as a continuum at the macroscale. To truly test the effects of neutron energy on asteroid deflection, the resolution must be enough to resolve the differences in the energy profiles of Figure 3.6. Due to computational limitations, centimeter-scale resolution was the best that could be achieved, and this zonal sizing was found to be sufficient.

The neutron yields Y_n chosen for these simulations would partially influence if

---

[5]Parts of this section are taken from [47].

this level of refinement was acceptable. As Y_n increases, heating penetrates further into the asteroid, meaning that more material beneath the surface is melted and/or vaporized. As the extent of the melted material increases, less resolution might be needed to ascertain the differences between the two different neutron energies, because the profiles are clearly differently shaped as d_{NEO} increases. However, for lower Y_n, more refined mesh resolution would be required. In this case, the melt-depth would be smaller, and the two profiles in Figure 3.6 are somewhat more comparable in shape and extent for lower d_{NEO} depths.

In this work, two neutron yields were investigated: fifty kilotons, $Y_n = 50$ kt, and one megaton, $Y_n = 1$ Mt. In chronological order during this research process, the 1 Mt yield was the first magnitude selected somewhat arbitrarily for inspection. As will be seen in Section 4.2.2.2, the deflection velocities resulting from $Y_n = 1$ Mt neutron yields at the $c \approx 0.414$ stand-off distance are easily too large for the 300 m asteroid target. A $Y_n = 50$ kt detonation neutron yield was subsequently also selected in search of δV velocity changes that would be more amenable to an asteroid of this size to lower the risk of undesired fragmentation (discussed further in Section 4.1.3).

It is likely that 50 kt or less would be considered for asteroids in the Apophis size class (such as the one inspected in this thesis), which agrees with findings from some previous work [34]. This is not to say that the asteroid response data from the 1 Mt sources is invalid or not useful. In fact, as Section 4.2 as a whole will show, testing two dramatically different detonation intensities revealed additional results of interest.

The solid black lines in Figures 3.6a and 3.6b are the melt-lines for both $Y_n = 50$ kt and $Y_n = 1$ Mt (as labeled in the plots themselves) for both 14.1 MeV and 1 MeV neutron sources. The numerical values of these melt-lines (in MeV/g/src-n) were determined by taking the 1941 J/g melting-point threshold of SiO_2, converting units

121

from J to MeV, and scaling by the number of source neutrons required to reach either 50 kt or 1 Mt in neutron yield for each energy source, i.e. for each E_n as applied in Equation 1.1. All zones of the asteroid that are located within the volume above these melt-lines (i.e. SiO_2 material that is located at sufficiently shallow d_{NEO} and sufficiently small ϕ spatial coordinates) is melted or vaporized. Visually, for $Y_n = 1$ Mt, the maximum melt-depth for the 14.1 MeV source is somewhere close to 130 cm, while the melt-depth for the 1 MeV source extends to around 200 cm. For $Y_n = 50$ kt, both the 14.1 MeV and 1 MeV neutron profiles appear to show a melt-depth of $\sim$30-35 cm beneath GZ.

Previous work investigated how the error in the blow-off momentum changes with the hydrodynamic mesh resolution using a one-dimensional, SiO_2 slab geometry. The neutron energy source was 2.45 MeV, which is the energy imparted to neutrons coming off of D-D fusion (Equation 2.4). Energy deposition profiles were assumed to be perfectly exponential [47].

The general guideline for the minimum mesh zone size Δr in the region of energy deposition associated with a fixed error in the blow-off momentum was found to be

$$\% \text{ Error} \approx 24 \frac{\Delta r}{z_{melt}}, \tag{4.13}$$

where z_{melt} is the melt-depth for an exponentially-decaying deposition profile based on a given source yield,

$$z_{melt} = \lambda_d \ln \frac{\epsilon_0}{\epsilon_{melt}}, \tag{4.14}$$

where ϵ_{melt} is the 1941 J/g melt threshold, and ϵ_0 is the maximum energy density at the surface.

Using $z_{melt} \approx 150$ cm (a value between the 1 Mt melt-depths seen in Figures 3.6a and 3.6b) in Equation 4.13, a zone size $\Delta r = 6.25$ cm in the energy deposition

region of the asteroid mesh would result in a blow-off momentum error of only 1%. A zoning of $\Delta r = 62.5$ cm would raise the blow-off momentum error to around 10%. For 50 kt, $z_{melt} \approx 35$ cm, and therefore $\Delta r \approx 1.46$ cm corresponds to 1% error, and $\Delta r \approx 14.6$ cm might correspond to 10% error in the blow-off momentum. However, the publication that derived Equation 4.13 noted that "scenarios involving lower energy densities (resulting in shallower melt depths) are found to require higher mesh resolution," in general [47]. It would be more conservative to expect slightly higher blow-off momentum error than as predicted by Equation 4.13 for low z_{melt} melt-depths.

The ALE3D code structure does not have the necessary information to compute uncertainties or errors for hydrodynamic variables. If additional time was provided, the aforementioned mesh resolution and error study could have been re-performed in 2-D geometries simply by varying the mesh zone size and seeing how the resulting blow-off momentum changed. However, due to time constraints, the findings from Equation 4.13 were taken as true — the associated level of momentum uncertainty for a given zonal resolution in the region of melted material was assumed *sola fide*.

For $Y_n = 1$ Mt via 14.1 MeV neutrons, the zones in the energy deposition region of the asteroid mesh were 2.275-by-2.275 cm. This means that there were about 60 zones between the surface and the maximum melt-depth of $\sim$130 cm beneath GZ. By Equation 4.13, % Error ≈ 0.42 for the momentum values in this simulation.

For $Y_n = 1$ Mt via 1 MeV neutrons, Δr was set to 2.275 cm, as it was for the 14.1 MeV case. Because z_{melt} is greater (200 cm for the 1 MeV profiles), however, the expected level of blow-off momentum error is slightly less, about 0.27%.

For $Y_n = 50$ kt using 14.1 MeV neutrons, the mesh elements throughout the melt region were approximately 1.5 cm squares. There were about 23 zones between the surface and 35 cm beneath the surface, which is the approximate melt depth for

123

50 kt yields. Equation 4.13 predicts 1.03% error in the momentum from this level of resolution.

For $Y_n = 50$ kt using 1 MeV neutrons, because the melt-depth was only slightly less than 35 cm, the same $\Delta r \approx 1.5$ cm zonal resolution from the 14.1 MeV simulation was selected. With 22 zones stretching from the surface to the maximum melt-depth, the anticipated blow-off momentum error is about 1.14%.

Figures 4.9a and 4.9b show a zoomed-in view of the MCNP6.2 energy deposition profiles, as compared to Figures 3.6a and 3.6b. This view makes it easier to see what the spatial distribution of energy is for the lower $Y_n = 50$ kt neutron yield, considering the shallower melt-depths of 30-35 cm. The vertical dashed black lines depict the $\Delta r \approx 1.5$ cm mesh resolution in the radial direction in the melted region.

4.1.3 Validation/Comparison

Hydrodynamic simulations are often computationally-intensive and require long amounts of set-up and processing time. As with energy deposition, sometimes a simpler and quicker route to determining the asteroid response to a stand-off detonation is preferable. There are a few analytical formulas in literature that provide a fast estimate of the δV asteroid deflection. One such approximate formula for the velocity change due to *x-ray* yields[6] is

$$
\begin{aligned}
\delta V_{\text{x-ray}} = \frac{\alpha}{R^3} \cdot \sqrt{Y \cdot R \cdot \frac{d^2}{R+d}} \cdot \sqrt{1 - \frac{\sqrt{(1+d/R)^2 - 1}}{1 + d/R}} \\
\cdot \sqrt{\frac{2R}{d} \cdot \left[1 + \ln\left(\frac{Y}{\beta d^2}\right)\right] - \left(1 + \frac{2R}{d}\right) \cdot \ln\left(1 + \frac{2R}{d}\right)},
\end{aligned}
\tag{4.15}
$$

where α and β are material-dependent scaling constants, Y is the device x-ray yield in kilotons (kt), R is the radius of the asteroid in meters (m), and d is the stand-

---

[6]Joseph V. Wasem, private communication.
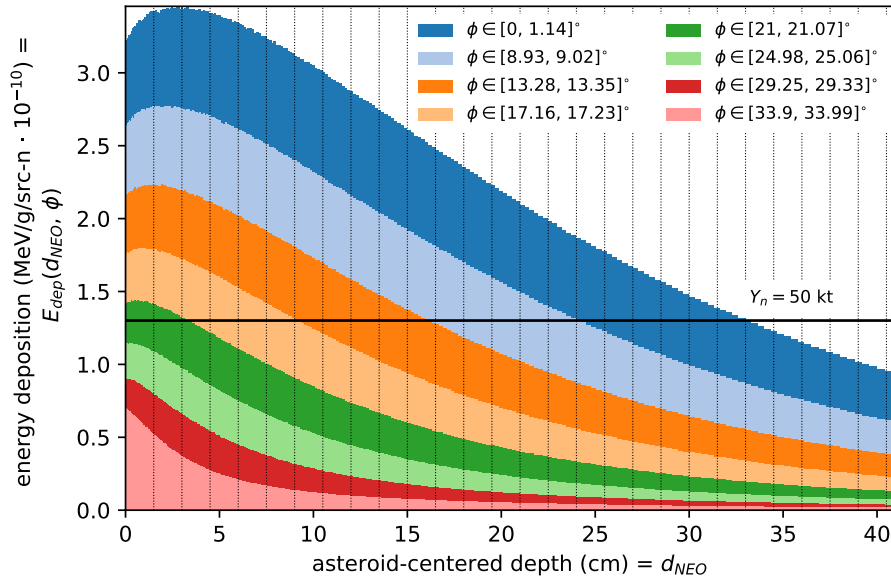
124

(a) Energy deposition spatial distribution from a ~14.1 MeV neutron source (DPLUS group #3).
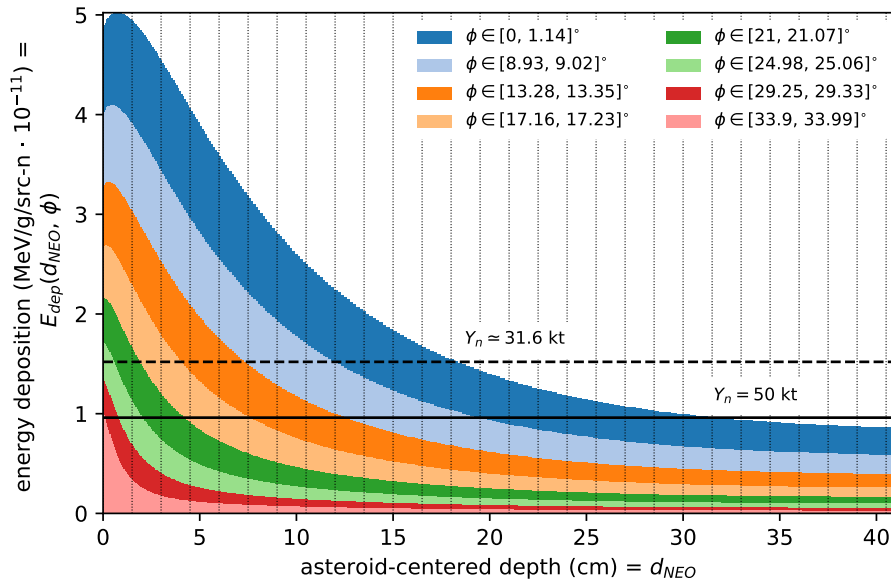
(b) Energy deposition spatial distribution from a ~1 MeV neutron source (DPLUS group #21).

Figure 4.9. Zoomed-in view of MCNP6.2 energy deposition profiles. This view is zoomed-in to the upper-left portion from Figures 3.6a and 3.6b, as relevant for shallower melt-depths associated with lower neutron yields. Note also that the E_{dep} y-axis scale is now linear. The $Y_n = 50$ kt melt-lines are shown in solid black. The $Y_n = 31.6$ kt melt-line in Figure 4.9b will be discussed in greater detail in Section 4.2.3. The vertical dashed black lines represent the ~1.5 cm zonal size resolution in the region beneath the surface where energy deposition melts material.

125

off distance of the detonation (the HOB) in meters (m). $\delta V_{\text{x-ray}}$ has units of cm/s. For non-ferrous silicate-type asteroids, $\alpha = 5750$ cm-m^2/s-kt$^{1/2}$ and $\beta = 3.16 \times 10^{-4}$ kt/m^2. To this thesis author's knowledge, an accurate analytical formula for δV resulting from *neutron* yields is not yet available in literature.

At a stand-off distance of $c \approx 0.414$, neither a 50 kt or a 1 Mt *x-ray* yield via Equation 4.15 is expected to result in $\delta V_{\text{x-ray}}$ values that are too extreme to keep the 300 m asteroid in a deflection regime. However, as mentioned in Section 1.3.2, x-rays generated from a nuclear detonation are significantly less penetrative than neutrons; because of this, x-rays are less effective than neutrons, per-source-particle, for asteroid deflection. As a result, it is anticipated that the $\delta V_{\text{x-ray}}$ values predicted from 50 kt and 1 Mt *x-ray* yields via Equation 4.15 will be underestimates of the δV velocities achieved from the 50 kt and 1 Mt *neutron* yields that are simulated in this work.

Note also that Equation 4.15 does not put any constraint on the x-ray yield Y. It simply predicts a $\delta V_{\text{x-ray}}$ for any Y, no matter how large. However, for large enough deflections on small enough asteroids, the object will break-up significantly (i.e. unwanted fragmentation). The center-of-mass of the fragments will have the predicted $\delta V_{\text{x-ray}}$ for a large Y, but the fragments themselves will be present as distributions in size and velocity. This means that Equation 4.15 cannot be used blindly. As the δV of an asteroid approaches its escape velocity v_{escape}, accidental weak disruption or fragmentation becomes difficult to avoid [34]. If the source yield is too high, then a deflection scenario instead becomes undesired disruption.

Equation 1.2 shows that v_{escape} off of an object's surface decreases as the object size or radius decreases. That is, for smaller asteroids, v_{escape} will be lower, and therefore the value of the maximum "safe" δV that avoids disruption decreases. For a spherical object with a diameter of 300 m and a bulk density of 1.855 g/cm^3, the distance r from the center to any point on the surface is 15,000 cm, and the mass M

of the body is 6.216×10^{16} g. With these values, by Equation 1.2, the escape velocity v_{escape} for blow-off pieces near the surface of this asteroid is 15.27 cm/s. For any δV values from deflection approaching or exceeding this value, regardless of the type of source yield, some degree of fragmentation or disruption is likely.

In Section 4.2.4, the asteroid deflection velocity δV calculated from ALE3D hydrodynamic simulations (via Equation 4.11) will be compared to the $\delta V_{\text{x-ray}}$ analytical approximation (Equation 4.15). Due to the nature of Equation 4.15 — namely, that it predicts asteroid velocity changes due to x-ray yields, rather than neutron yields — it is not anticipated that the analytical/x-ray $\delta V_{\text{x-ray}}$ will match the hydrodynamic/neutron δV. However, it is expected that the Equation 4.15 estimates will be less than the ALE3D simulation δV values, which would match previous findings that neutrons are the more effective source type.

4.2 Results and Analysis

There are three components to this section which analyzes the results for asteroid deflective response. First, the heatmaps of energy deposition profiles resulting from 14.1 MeV and 1 MeV source neutrons are shown in the two-dimensional asteroid geometry. Second, for an identical neutron yield, the δV values for both neutron energies are provided and discussed. Third, for an identical amount of deposited energy, the δV values from the two neutron energies are also compared.

4.2.1 Heatmaps of Asteroidal Energy Deposition Profiles

This section contains heatmaps of two-dimensional energy deposition profiles shown in semi-circular asteroid cutaways.[7] The MCNP6.2 energy deposition profiles from Figures 3.6a and 3.6b were mapped onto an ALE3D asteroid mesh and scaled by

---

[7]In Appendix B, 2-D full-circle views of these same energy deposition heatmaps are displayed in Section B.1, and 3-D $\frac{3}{4}$-sphere visuals are found in Section B.2.

127

the number of source neutrons corresponding to neutron yields of 50 kt and 1 Mt, for both 14.1 MeV and 1 MeV neutron energies. The colorbar in each of the figures below is the dimensionless quantity E_{dep}/E_{melt}, where E_{dep} is the energy deposition at a given location in J/g and where E_{melt} is the 1941 J/g melt threshold for SiO_2.

For a stand-off distance of $c \approx 0.414$ away from a 300 m diameter asteroid, the extent of the energy deposition region is much longer in ϕ than it is deep in d_{NEO}. As mentioned at the end of Section 4.1.1.6, the arc-length L of the full-size 300 m diameter asteroid from $\phi = 0°$ to $\phi = 45°$ (which is the irradiated surface area) is nearly 11,800 cm. Even compared to the maximum melt-depth considered in these simulations, 200 cm, it is a fact that the sensible energy deposition region is very long and narrow when the full 300 m asteroid size is considered. Without significantly lessening the object size to see how the energy deposition is shaped, these visuals would not be very informative or helpful. The energy deposition gradients would occupy only the very thin red area along the irradiated surface of Figure 4.3.

Instead, smaller asteroid diameters of 80 cm and 5 m for 50 kt and 1 Mt yields, respectively, were used to visualize the heating results. Mapping the energy profile contours onto smaller asteroids effectively condenses or compresses the 0°-to-45° surface into an arc-length that much smaller and more comparable to the melt-depth. This was done solely for visual-aid purposes, making it possible to see how the heating gradient changes in both depth and in angle.

4.2.1.1   Fifty Kiloton Energy Deposition Heatmaps

Figure 4.10 depicts the extent of melted material and the intensity of energy deposition in the irradiated region of a 2-D semi-circular asteroid, as would result from a 50 kt neutron yield at a $c \approx 0.414$ stand-off distance, for both 14.1 MeV neutrons (top) and 1 MeV neutrons (bottom). The colorbars are logarithmically-

scaled, and the values indicate the degree that the material is heated in reference to the 1941 J/g melt threshold of SiO_2, where SiO_2's melting point is approximately 2000 K [82]. For instance, in Figure 4.10a, the maximum energy deposition value for the 14.1 MeV neutron source is 2.66. This means that the asteroid material in the darkest red region is heated to about 5160 J/g, which is 2.66 times above 1941 J/g, with the corresponding peak temperature of 4523 K. The 50 kt yield comprised of 1 MeV neutrons, on the other hand, heats material to 5.23 times beyond the melt minimum (Figure 4.10b), reaching a maximum temperature of 8610 K.

Note that the colorbar scales are different between Figures 4.10a and 4.10b because each neutron source results in different peak energy densities. For example, the orange-red color in Figure 4.10a, with a value of 2.26, is somewhat comparable to the yellow color in Figure 4.10b, which has a value of 2.29. Both of these respective colors indicate the locations in the asteroid where material is heated to a little over twice SiO_2's melt threshold.

The darkest blue areas of the asteroid are where the energy deposition is below the melt threshold. Materials are only melted at or above 1.00, which is shown as a slightly lighter blue. In other words, only the locations marked with colors that are *not* the darkest blue are melted.

The horizontal black melt threshold lines in Figures 4.9a and 4.9b represent the melt depths (in terms of d_{NEO} beneath the surface) as a function of angle. This melt line is merely the spatial barrier that separates melted material from unmelted material. In the 2-D views of Figures 4.10a and 4.10b, the melt line is given its rightful curvature as ϕ increases when moving along the surface and away from GZ. The melt-depth below GZ is about 33 cm for the 14.1 MeV neutrons and about 31 cm for the 1 MeV neutrons, as seen by the extent of the color gradients along the x-axis (the y=0 line). This is where material is melted at its deepest beneath the surface,
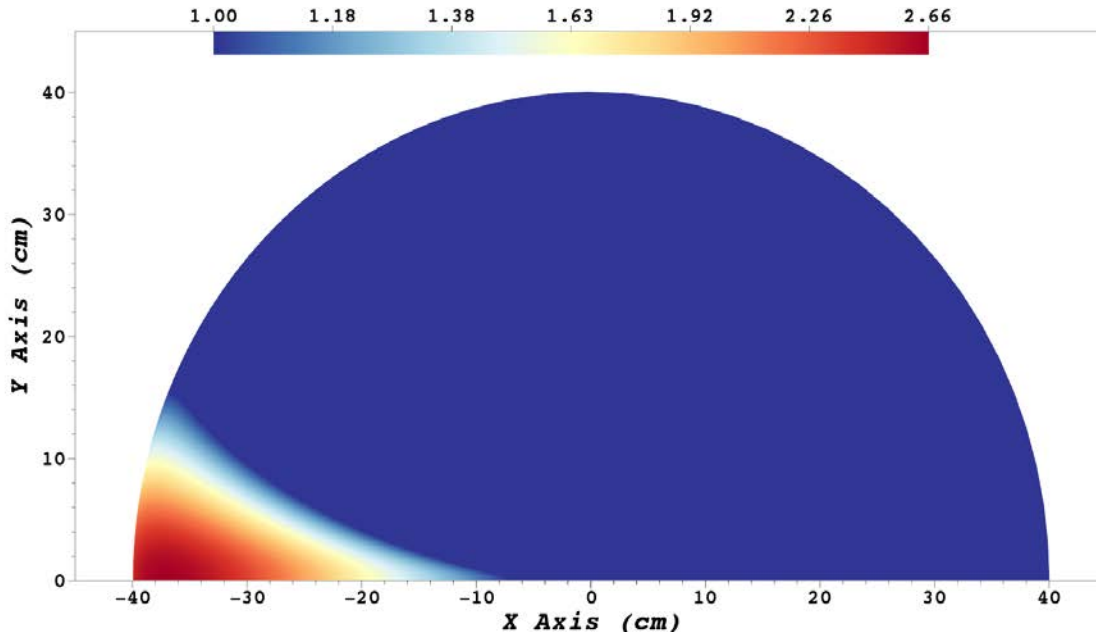
129

(a) Energy deposition heatmap from a 50 kt yield composed of 14.1 MeV neutrons.
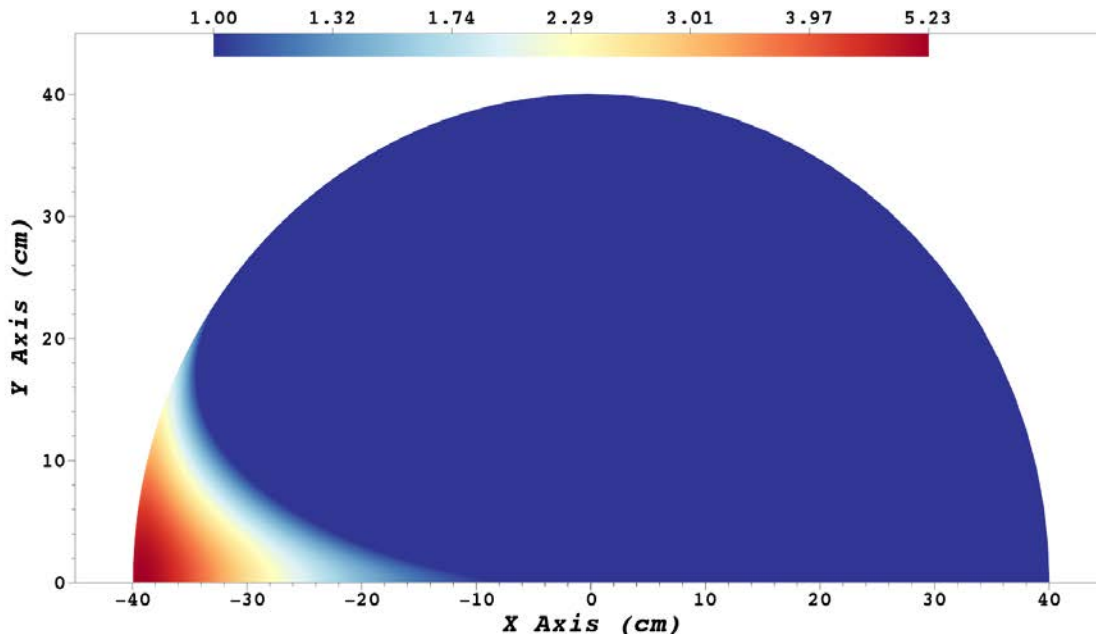
(b) Energy deposition heatmap from a 50 kt yield composed of 1 MeV neutrons.

Figure 4.10. Asteroidal energy deposition heatmaps generated from a 50 kt neutron yield, visualized on a small 80 cm asteroid. Areas with colors other than dark blue are melted. The 14.1 MeV neutrons (top) heat parts of the asteroid to 2.66 times above the melt threshold for SiO_2, while the 1 MeV neutrons (bottom) push to 5.23 times beyond the melt minimum. The maximum melt-depth for both is about 30-35 cm beneath GZ, which is located at coordinates (-40,0) cm.

both because the neutron fluence is at its strongest at the $\alpha = \phi = 0°$ line through GZ, and because this direction irradiates the asteroid at an angle exactly normal to the surface. For all other neutrons emanating from the point-source at $\alpha \in (0, 45]°$, and subsequently at locations along the asteroid surface where $\phi \in (0, 45]°$, it is seen that the melt-depths beneath the surface decrease with angle.

While the melt-depths beneath GZ are comparable, the amount of material that is melted moving along the asteroid surface away from GZ is clearly different between 50 kt's worth of 14.1 MeV neutrons and 50 kt's worth of 1 MeV neutrons. That is, the extent of the melt gradient along the surface for 1 MeV neutrons in Figure 4.10b is clearly greater than it is for 14.1 MeV neutrons in Figure 4.10a. This of course agrees with the representation of energy deposition in Figures 4.9a and 4.9b. The $Y_n = 50$ kt melt-line for 14.1 MeV neutrons extends out to approximately $\phi \in [21, 21.07]°$ (the dark green profile in Figure 4.9a), while for 1 MeV neutrons the 50 kt melt-line touches all the way out to $\phi \in [33.9, 33.99]°$ (the light red profile in Figure 4.9b).[8]

4.2.1.2 One Megaton Energy Deposition Heatmaps

Figure 4.11 shows the energy deposition heatmaps of the melted material in the irradiated region of a 2-D semi-circular asteroid, from a 1 Mt neutron yield at a $c \approx 0.414$ stand-off distance, for both 14.1 MeV neutrons (top) and 1 MeV neutrons (bottom). Again, the colorbars are logarithmically-scaled, and the values represent the E_{dep}/E_{melt} fraction. As seen in Figure 4.11a, the maximum energy deposition fractional value for 1 Mt's worth of 14.1 MeV neutrons is 53.1, which corresponds to about 103,000 J/g and peak temperatures of 52,930 K. The 1 Mt yield of 1 MeV neutrons, however, heats SiO_2 material up to 105 times beyond the melt minimum (Figure 4.11b), achieving a maximum temperature of 86,120 K.

---

[8]As easier to see in Section C.1, about 22.5° of the surface area is melted from the 50 kt 14.1 MeV source, while >35° of the outer surface is melted for 50 kt's worth of 1 MeV neutrons.
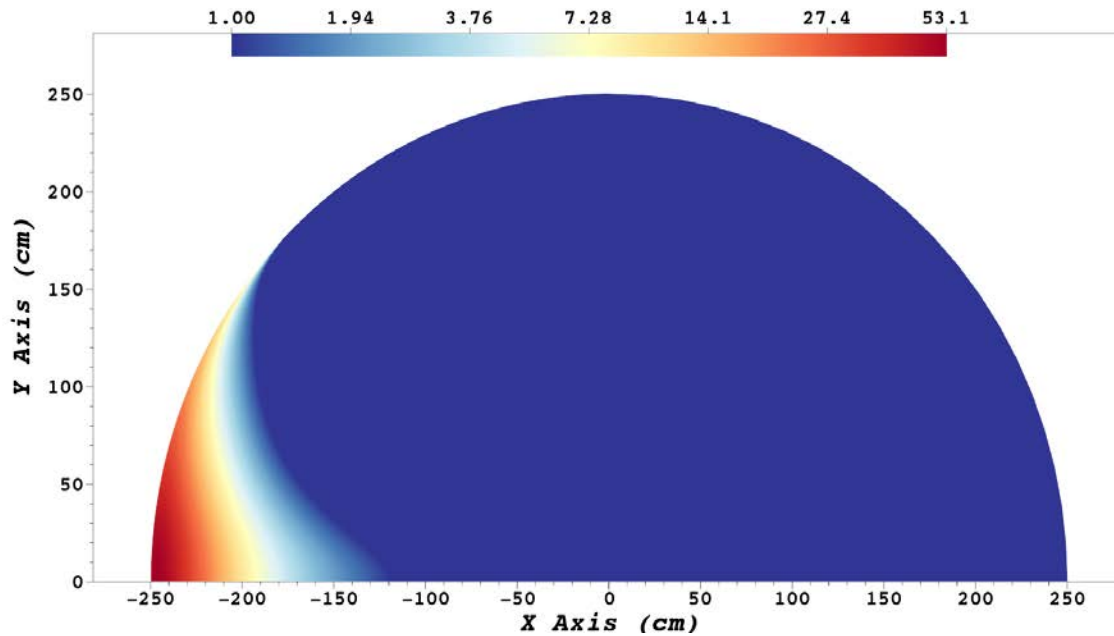
(a) Energy deposition heatmap from a 1 Mt yield composed of 14.1 MeV neutrons.
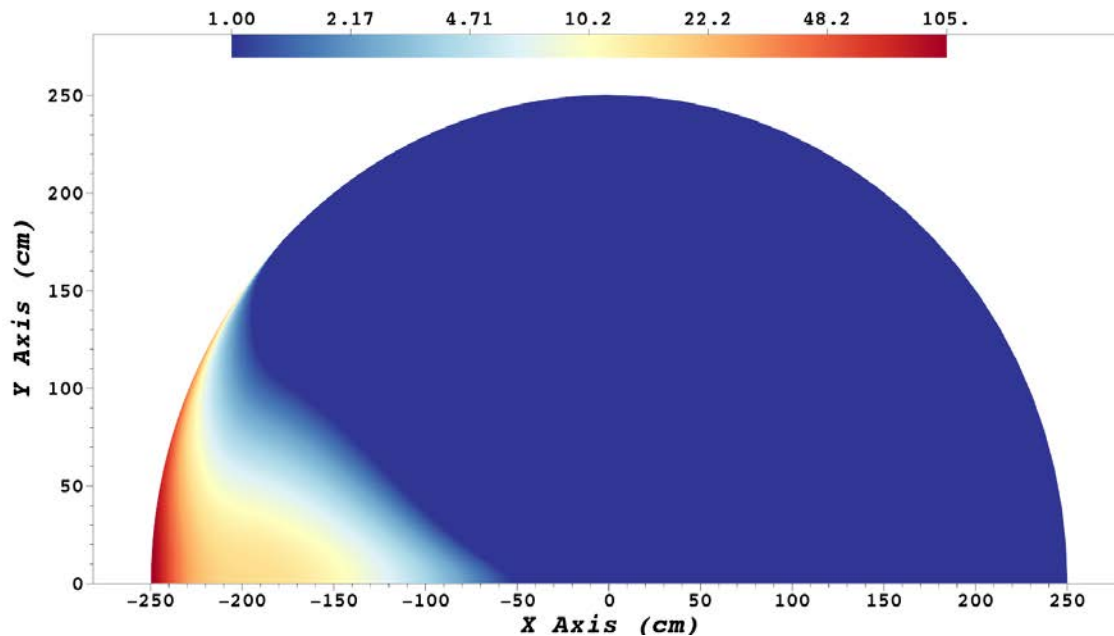
(b) Energy deposition heatmap from a 1 Mt yield composed of 1 MeV neutrons.

Figure 4.11. Asteroidal energy deposition heatmaps generated from a 1 Mt neutron yield, visualized on a small 5 m asteroid. Areas with colors other than dark blue are melted. The 14.1 MeV neutrons (top) heat parts of the asteroid to 53.1 times above the melt threshold for SiO_2, while the 1 MeV neutrons (bottom) push to 105 times beyond the melt minimum. The maximum melt-depths beneath GZ, which is located at (-250,0) cm, amount to $\sim$130 cm for 1 Mt of 14.1 MeV neutrons and $\sim$200 cm for 1 Mt of 1 MeV neutrons.

132

Note that a 1 Mt yield is 20 times greater than a 50 kt yield. Correspondingly, between the 50 kt profiles of Figure 4.10 and the 1 Mt profiles of Figure 4.11, the latter's peak energy densities are approximately 20 times greater than the peak values in the former.

As before, the colorbar scales are different between Figures 4.11a and 4.11b. The darkest red color in Figure 4.11a, with a value of 53.1, is somewhat comparable to the orange-red color in Figure 4.11b, which has a value of 48.2. These colors both mean that material is heated to about 50 times above SiO_2's melt threshold.

The melt-depth below GZ, which is located at the asteroid surface at the coordinates of (-250,0) cm, is about 130 cm for the 14.1 MeV neutrons and about 200 cm for the 1 MeV neutrons, as seen by the extent of the color gradients along the x-axis (the y=0 line). As with the Y_n = 50 kt case, this heading, i.e. traveling straight down below GZ, is where the melt-depths are maximized. The 130 cm and 200 cm depths are in agreement with the intersection of the horizontal black lines in Figures 3.6a and 3.6b with the dark blue profile — which is the region encompassing GZ, as $\phi \in [0, 1.14]^{\circ}$.

In contrast to the 50 kt energy deposition heatmaps, these 1 Mt heatmaps appear to show that an almost-equal amount of the asteroid surface meets the melt threshold for both the 14.1 MeV and 1 MeV neutrons. This is again supported by the alternative visual of the energy deposition profiles as in Figure 3.6. The Y_n = 1 Mt melt-line, both in Figure 3.6a and in Figure 3.6b, barely touches the dark purple profile profile where $\phi \in [39.04, 39.14]^{\circ}$.[9] Therefore, for both neutron energies, a 1 Mt neutron yield means that the surface area (but not the total volume) of melted material is approximately equal.[10]

---

[9]Actually, a zoomed-in view reveals that both 1 Mt melt-lines also reach the light purple profiles where $\phi \in [44.75, 44.86]^{\circ}$, though this is not visible due to the broad d_{NEO} scale in Figure 3.6.

[10]In fact, $\sim 44.96^{\circ}$ of the surface area is melted from a 1 Mt yield of either 14.1 MeV or 1 MeV sources, which is quite close to the maximum possible 45° that is irradiated at $c \approx 0.414$ stand-off.

4.2.2 Asteroid Deflection Velocities with Identical Neutron Yield

This section provides the results that compare the deflection performance — a la the asteroid velocity change δV — between 14.1 MeV and 1 MeV neutrons of equivalent neutron yield. First, a 50 kt detonation neutron yield at $c \approx 0.414$ for each source energy is simulated. Second, the response of the asteroid target from a 1 Mt neutron yield is provided.

4.2.2.1 Fifty Kiloton Neutron Yield

Table 4.1 contains the list of parameters for the ALE3D simulations where an asteroid is exposed to a 50 kt neutron yield from $c \approx 0.414$ distance away, using 14.1 MeV neutrons and 1 MeV neutrons.

To achieve equal 50 kt neutron yields, the number of 1 MeV source neutrons must be 14.1 times greater than the number of 14.1 MeV neutrons as shown in Equation 1.1. For an identical Y_n at an identical stand-off distance, the Y_{int} values are also equal. The intercepted yield was calculated by Equation 3.13, where $\alpha = 45°$ for the $c \approx 0.414$ HOB. That is, Y_{int} is simply Y_n scaled by the fractional solid angle of the red radiation cone of Figure 3.1a, which is ~ 0.1464.

Then, taking Y_{int} and multiplying by the η_{rel} values for each neutron energy from Table 3.2, the total amount of energy deposited in the asteroid, $E_{dep,tot}$, is determined. However, as determined from the internal energy timehist in ALE3D, $E_{dep,tot}^{ALE3D}$ records the true amount of energy that was deposited in the asteroid mesh. $E_{dep,tot}^{ALE3D} \neq E_{dep,tot}$ because the discretizations between the energy deposition tallied in MCNP6.2 and the asteroid mesh in ALE3D are not equivalent. The differences between the expected $E_{dep,tot}$ and the actual $E_{dep,tot}^{ALE3D}$ are extremely small, with a percent difference of less than 0.1% and less than 0.3% for 14.1 MeV and 1 MeV neutron sources, respectively.

Both asteroid meshes contained 419,136 total zones or elements. The mesh resolu-

Table 4.1. Parameters for 50 kt identical yield ALE3D simulations with two different neutron sources.

Parameter	50 kt @ 14.1 MeV/src-n	50 kt @ 1 MeV/src-n
Y_n	50 kt	50 kt
E_n	14.1 MeV	1 MeV
src-n	9.31469×10^{25}	1.26157×10^{27}
Y_{int}	7.3223 kt	7.3223 kt
η_{rel}	0.6884	1.0896
$E_{dep,tot}$	5.0410 kt	7.9785 kt
$E_{dep,tot}^{ALE3D}$	5.0364 kt	7.9573 kt
E_{dep}/E_{melt}	2.66	5.23
N	419,136	419,136
Δr	1.47 cm	1.47 cm
z_{melt}	~ 33 cm	~ 31 cm
% Error	1.03%	1.14%
$N_{E_{dep}}$	171,072	163,296
$N_{E_{dep}}/N$	0.4082	0.3896

tion where the material was melted had zones of 1.47 cm in size. Based on the slightly different melt-depths, by Equation 4.13, the 1 MeV simulation has a slightly higher uncertainty in δV. About 39-41% of all the zones in the asteroid mesh, $N_{E_{dep}}/N$, were located in the energy deposition region.

Both of these asteroid response simulations in ALE3D were run for several hundred microseconds. The anticipation was that the momentum impulse that resulted from the quickly-evolving blow-off motions would level-off within this time [68]. Indeed, this turned out to be correct. For a 50 kt yield, for both 14.1 MeV and 1 MeV neutrons, the asteroid_momentum_x timehist summation of the asteroidal zonal x-momentums reached an asymptote by $\sim$300 μs. From the beginning simulation time and up to this moment, δV was calculated via Equation 4.11; that is, by dividing the total asteroid x-momentum (g-cm/s) at each time-step by the total asteroid mass (g). This provided δV in cm/s as a function of time.

Figure 4.12 shows how δV changes during the time after the neutron energy deposition for both 50 kt's worth of 14.1 MeV neutrons and 50 kt's worth of 1 MeV neutrons. By 300 μs, δV is no longer changing significantly, as the rapid momentum impulse from the blow-off has concluded. The δV at 300 μs is 6.19 ± 0.06 cm/s for the 14.1 MeV neutrons and 9.99 ± 0.12 cm/s for the 1 MeV neutrons. This means that the 1 MeV neutrons offer about 1.61 ± 0.02 times better deflection performance than 14.1 MeV neutrons at equivalent 50 kt detonation yields. Both of these values are below the 15.27 cm/s escape velocity for this 300 m asteroid target, which means that accidental and undesired fragmentation might not occur and that a 50 kt neutron yield could be appropriate for deflecting this body.

There are several reasons why 1 MeV neutrons might be more effective than 14.1 MeV neutrons. The biggest factor is likely the large difference in the amount of energy that gets deposited in the asteroid. As listed in Table 4.1, because the 1 MeV
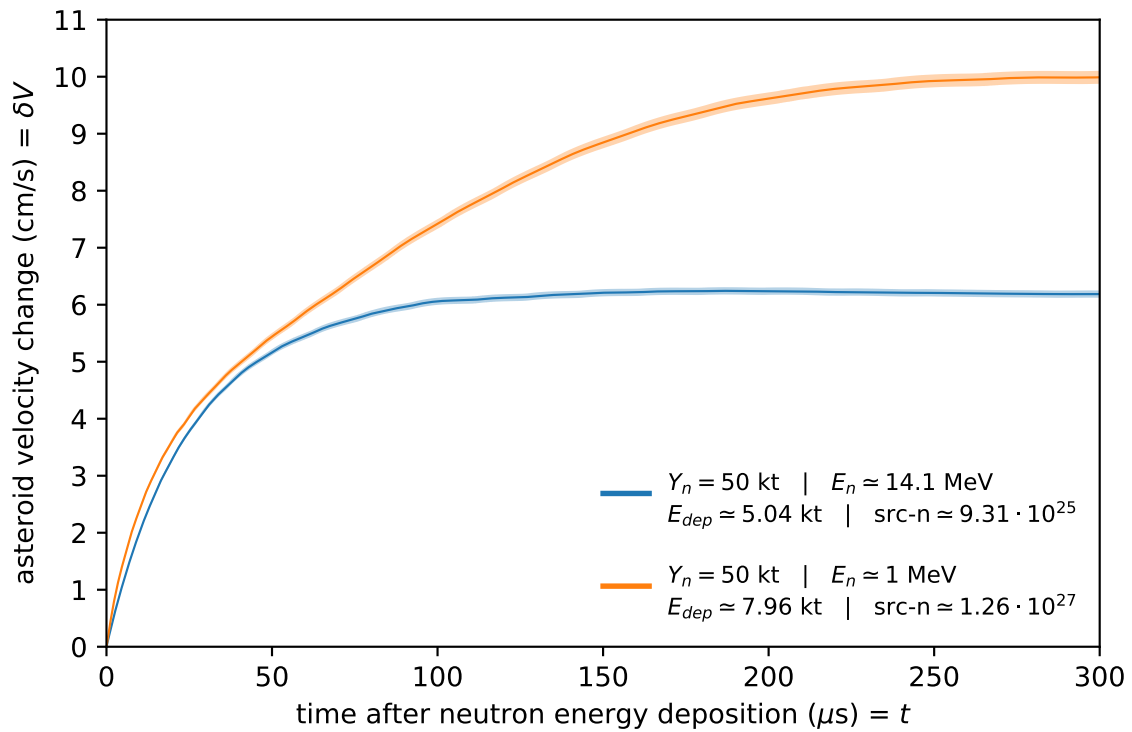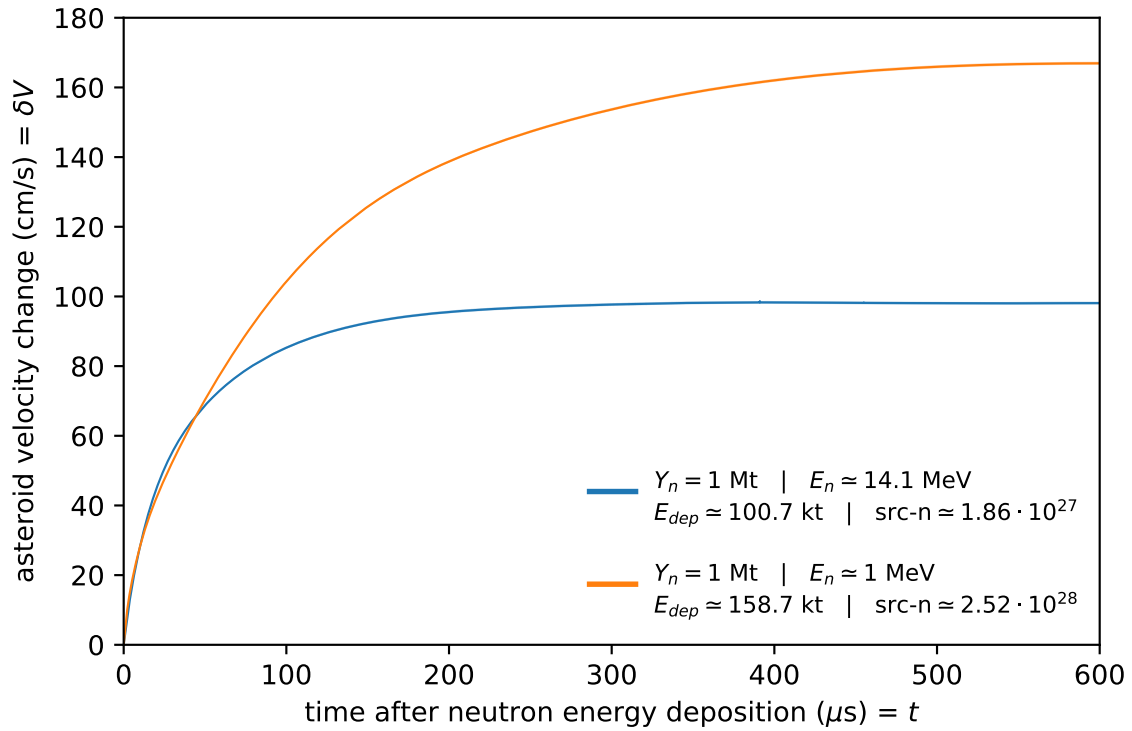
Figure 4.12. The change in asteroid velocity over time for an identical neutron yield of 50 kt. The blue line indicates the source of 14.1 MeV neutrons, and the orange line represents the 1 MeV neutrons. The bands of lighter blue and orange indicate the respective amounts of uncertainty in these δV values due to finite mesh resolution.

137

source has a much higher energy coupling efficiency than the 14.1 MeV source, the 50 kt stand-off yield allows the former to achieve 7.9573 kt of total energy deposition, while the latter reaches only 5.0364 kt. For any identical detonation yield, a 1 MeV source will always deposit 1.58 times the energy of a 14.1 MeV source, where 1.58 is the ratio of their respective η_{rel} energy coupling efficiencies. When an asteroid is provided with more energy, it is reasonable to expect that there will be more blow-off due to greater amounts of material being melted and/or material being more energetic.

Furthermore, again in Table 4.1, the peak energy density for 50 kt of 1 MeV neutrons is 5.23 times beyond SiO_2's melt threshold, while 14.1 MeV neutrons only reach 2.66 times the melt threshold. This is largely a consequence of energy deposition profile differences. Zones having a greater amount of internal energy past the melting point have a greater potential to reach faster velocities, higher kinetic energies, and therefore greater momentums. It is also possible that other differences in the spatial distribution of how energy gets deposited between the two neutron sources, visualized in Figure 4.10, affect the realized δV velocities. With these results alone, however, it is unclear if this is the case.

4.2.2.2   One Megaton Neutron Yield

Table 4.2 contains the list of parameters for the ALE3D simulations where an asteroid is exposed to a 1 Mt neutron yield from $c \approx 0.414$ distance away, using 14.1 MeV neutrons and 1 MeV neutrons.

The same parameter definitions from the 50 kt case are re-applied here. The number of source neutrons src-n, intercepted yield Y_{int}, total energy deposition $E_{dep,tot}$ and $E_{dep,tot}^{ALE3D}$, and E_{dep}/E_{melt} values in Table 4.2 are all roughly 20 times greater than their counterparts from Table 4.1. This is because the neutron yield is now 1 Mt,

138

Table 4.2. Parameters for 1 Mt identical yield ALE3D simulations with two different neutron sources.

Parameter	1 Mt @ 14.1 MeV/src-n	1 Mt @ 1 MeV/src-n
Y_n	1 Mt	1 Mt
E_n	14.1 MeV	1 MeV
src-n	1.86294×10^{27}	2.52314×10^{28}
Y_{int}	146.45 kt	146.45 kt
η_{rel}	0.6884	1.0896
$E_{dep,tot}$	100.82 kt	159.57 kt
$E_{dep,tot}^{ALE3D}$	100.68 kt	158.75 kt
E_{dep}/E_{melt}	53.1	105
N	552,896	747,200
Δr	2.275 cm	2.273 cm
z_{melt}	~ 130 cm	~ 200 cm
% Error	0.42%	0.27%
$N_{E_{dep}}$	311,040	482,112
$N_{E_{dep}}/N$	0.5626	0.6452

139

which is 20 times greater than 50 kt.

The melt-depths do not follow linear scaling with the yield; this is because the energy deposition profiles in Figure 3.6 are not linear, but rather are closer to exponential in behavior. Because these 130 cm and 200 cm z_{melt} values are still much greater than they were for 50 kt (around 30-35 cm), a slightly larger zonal discretization is acceptable, and a Δr of 2.275 cm was used for the 1 Mt case. However, the total number of zones N in the 1 Mt asteroid meshes still increased from the 50 kt set-up.

The assumed momentum errors have decreased, as well, as now there are more zones between the asteroid surface and the deepest melt-depth. Lastly, $E_{dep,tot}^{ALE3D}$ is very slightly less than $E_{dep,tot}$ once again, which is still due to the discretization differences between the tallied energy deposition in MCNP6.2 and the asteroid mesh in ALE3D.

This time, for $Y_n = 1$ Mt, the sum of the x-momentums did not approach an asymptote until around 600 μs of simulation time. It is believed that the higher energy densities and greater amounts of melted material required more time to resolve the rapid blow-off motions than in the 50 kt cases.

Figure 4.13 shows δV versus time for 1 Mt's worth of 14.1 MeV neutrons and 1 MeV neutrons. By 600 μs, δV is no longer changing significantly, as the rapid momentum impulse from the blow-off has concluded. The δV at 600 μs is 98.09 $\pm$ 0.41 cm/s for the 14.1 MeV neutrons and 166.9 $\pm$ 0.5 cm/s for the 1 MeV neutrons. Thus, 1 MeV neutrons offer about 1.70 $\pm$ 0.01 times better deflection performance than 14.1 MeV neutrons at equivalent 1 Mt detonation yields. Both of these values far exceed the $v_{escape} = 15.27$ cm/s escape velocity for this asteroid, and a certain degree of disruption would be expected if this excessive 1 Mt yield was applied at the given HOB of $c \approx 0.414$.

Again, 1 MeV neutrons are found to be better than 14.1 MeV neutrons on a

Figure 4.13. The change in asteroid velocity over time for an identical neutron yield of 1 Mt. The blue line indicates the source of 14.1 MeV neutrons, and the orange line represents the 1 MeV neutrons. The bands of lighter blue and orange indicate the respective amounts of uncertainty in these δV values due to finite mesh resolution (note: these are not visible on this scale).

141

per-detonation-yield basis. The same explanations postulated for the 50 kt case also apply here. The 1 MeV source deposits 1.58 times as much energy into the asteroid, and it offers higher maximum energy densities than the 14.1 MeV detonation does (see Table 4.2).

However, there is at least one difference of note. Before, when $Y_n = 50$ kt, the δV from 1 MeV neutrons was 1.61 ± 0.02 times higher than it was for 14.1 MeV neutrons. Now, at 1 Mt of yield, the 1 MeV neutrons offer 1.70 ± 0.01 times better deflection performance. This is somewhat interesting. In both cases, $E_{dep,tot}$ for 1 MeV neutrons is 1.58 times above what it is for 14.1 MeV neutrons. The ratio of the E_{dep}/E_{melt} ratios is also largely consistent between 50 kt and 1 Mt — for 50 kt, it is $5.23/2.66 = 1.97$, and for 1 Mt, it is $105/53.1 = 1.98$.

From this, it appears that there is another factor at play here as to why 1 MeV neutrons at 1 Mt offer an even greater advantage than they do at 50 kt. That is, there is now clearer support that the differences in the spatial distribution of energy deposition between the two neutron sources (Figure 4.11) might affect the δV velocities. If so, it appears to be more significant for 1 Mt yields than for 50 kt yields.

4.2.3 Asteroid Deflection Velocities with Identical Deposited Energy

The previous section analyzed how the neutron energies compare in deflection performance when the detonation yields are identical. Two potential explanations were considered explaining why 1 MeV neutrons achieve higher δV velocity changes. First, 1 MeV neutrons benefit from a greater energy coupling efficiency than 14.1 MeV neutrons. Because of this, for equivalent detonation yields, the total energy deposited into the asteroid target is greater by a factor of 1.58 if 1 MeV neutrons are the yield constituents rather than 14.1 MeV neutrons. With more energy to heat material near the surface, it is not much surprise that momentums are higher and therefore δV is

142

increased.

Second, the spatial distribution of the energy deposition at and beneath the asteroid surface is different for 1 MeV neutrons than it is for 14.1 MeV neutrons. This is manifested in two ways. For one, the physical shaping or contours of the energy deposition profiles are different between neutron energies. This has been seen in Figure 3.6 and in Figures 4.9, 4.10, and 4.11. A second difference in the arrangement of deposited energy is the differing peak energy densities between 14.1 MeV and 1 MeV neutrons, with the latter offering nearly double the E_{dep}/E_{melt} ratio than the former.

This section attempts to remove the potential for energy coupling differences to affect δV performance. Now, rather than comparing identical source yields, identical amounts of total energy deposition between the two neutron energies will be inspected. Any differences in the values for δV should be due only to the differing spatial distributions of deposited energy within the asteroid target.

As in Table 3.2, η_{rel} for 14.1 MeV neutrons is 0.6884, and for 1 MeV neutrons it is 1.0896 — a ratio of 1.58 between the two. Therefore, the detonation yields for the 1 MeV source will be reduced by a factor of 1.58 to remove the advantage of a better energy coupling efficiency. That is, first, a 50 kt yield of 14.1 MeV neutrons will be compared to ∼31.6 kt of 1 MeV neutrons (each depositing ∼5 kt of energy), and second, 1 Mt of 14.1 MeV neutrons is compared to ∼632 kt of 1 MeV neutrons (each depositing ∼100 kt of energy).

This section is a hypothesis test. Let us assume, as some of the results from Section 4.2.2 suggest, that the spatial distribution of deposited energy plays a minimal role in the resulting δV velocity changes. If this is true, then scaling the yield by the coupling efficiency for the 1 MeV source would result in equivalent δV values with the 14.1 MeV source. If, however, δV is still different between 14.1 MeV and 1 MeV neutron sources, then the energy deposition profiles do affect deflection performance.

143

4.2.3.1 Five Kiloton Energy Deposition

Table 4.3 contains the list of parameters for the ALE3D simulations where an asteroid is irradiated[11] by a detonation from from $c \approx 0.414$ distance away, for 50 kt's worth of 14.1 MeV neutrons and 31.6 kt's worth of 1 MeV neutrons.

The parameters in the 50 kt 14.1 MeV column are repeated from Table 4.1. The $\sim$31.6 kt yield of 1 MeV neutrons results in a lower incident Y_{int} colliding with the asteroid target, but due to a higher energy coupling efficiency, the $E_{dep,tot}$ values are equalized between these two sources. The $E_{dep,tot}^{ALE3D}$ values between the 14.1 MeV and 1 MeV neutrons are slightly different due to customized asteroid mesh resolutions for each. This difference is very small ($< 0.08\%$).

The z_{melt} melt-depth for 31.6 kt @ 1 MeV/src-n is about 19 cm, decreased from 31 cm for a 50 kt detonation yield (Table 4.1). Note that the 31.6 kt 1 MeV melt-line is shown as a dashed horizontal line in Figures 3.6b and 4.9b. To somewhat compensate for this reduction in depth, the mesh resolution in the region where zones are melted was lowered from 1.47 cm to 1.05 cm. This still resulted in a small increase in uncertainty in δV to 1.33%.

Figure 4.14 compares the δV values over time for $\sim$5 kt of total energy deposited from a source of 14.1 MeV neutrons and a source of 1 MeV neutrons. As with the 50 kt yields in Section 4.2.2.1, the impulsive motions of the blow-off zones reached an asymptote by 300 μs.

The δV at 300 μs is 6.19$\pm$0.06 cm/s for the 14.1 MeV neutrons and 6.02$\pm$0.08 cm/s for the 1 MeV neutrons. This indicates that 14.1 MeV neutrons are 1.03 ± 0.02 times more effective than 1 MeV neutrons at this equivalent E_{dep}.

---

[11]Rather than "irradiated," perhaps "irritated" is also an appropriate descriptor, characterizing the asteroid's feelings on the matter. Coincidentally, perhaps the reader is also feeling somewhat irritated by this point of the thesis. But don't despair! You will only have to read the words "neutron," "energy deposition," "source," "detonation," and "yield" approximately 8,000,000 more times before the end.

Table 4.3. Parameters for 5 kt identical deposited energy ALE3D simulations with two different neutron sources.

| Parameter	50 kt @ 14.1 MeV/src-n	31.6 kt @ 1 MeV/src-n
Y_n	50 kt	31.5913 kt
E_n	14.1 MeV	1 MeV
src-n	9.31469×10^{25}	7.97093×10^{26}
Y_{int}	7.3223 kt	4.6264 kt
η_{rel}	0.6884	1.0896
$E_{dep,tot}$	5.0410 kt	5.0410 kt
$E_{dep,tot}^{ALE3D}$	5.0364 kt	5.0324 kt
E_{dep}/E_{melt}	2.66	3.30
N	419,136	564,352
Δr	1.47 cm	1.05 cm
z_{melt}	~ 33 cm	~ 19 cm
% Error	1.03%	1.33%
$N_{E_{dep}}$	194,400	196,992
$N_{E_{dep}}/N$	0.4638	0.3491

145
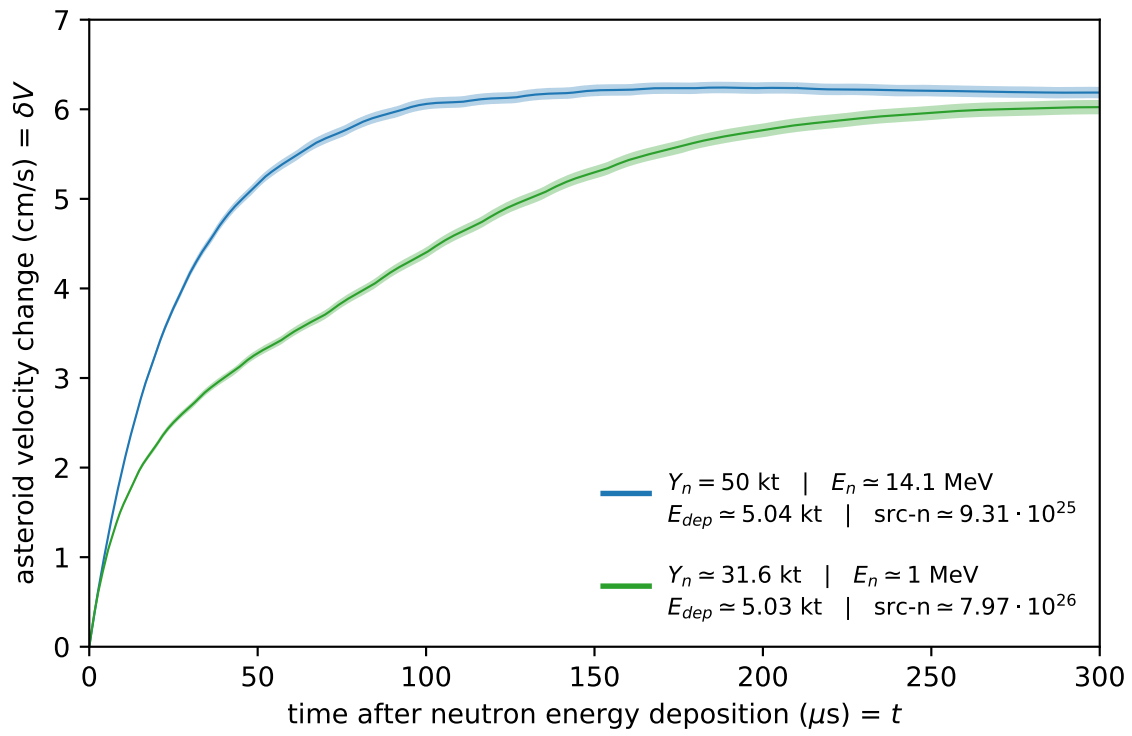
Figure 4.14. The change in asteroid velocity over time for an identical energy deposition of 5 kt. The blue line indicates the source of 14.1 MeV neutrons, and the green line represents the 1 MeV neutrons. The bands of lighter blue and green indicate the respective amounts of uncertainty in these δV values due to finite mesh resolution.

When the neutrons yields were both 50 kt in Section 4.2.2.1, the 1 MeV neutrons resulted in a 1.61 ± 0.02 higher δV than 14.1 MeV neutrons, slightly higher than the 1.58 times greater η_{rel}. Here, when the neutron yields are tuned such that the total energy deposition in the asteroid for both neutron sources is 5 kt, there is not a large, discernible difference between the deflection performance for 14.1 MeV or 1 MeV sources. The 3% increase in δV for 14.1 MeV neutrons over 1 MeV neutrons in quite small in context, especially in recognizing that the error bound on this factor is $\pm 2\%$. Furthermore, the ALE3D meshing differences caused the 1 MeV source to suffer a 0.08% penalty in terms of total energy deposition, as compared to the 14.1 MeV source.

Considering these factors, it does not appear that the spatial distribution of energy deposition significantly affects δV, at least when comparing 14.1 MeV and 1 MeV sources for 5 kt of total deposition in a SiO_2 target. Rather, both offer approximately the same performance for asteroid deflection. It seems that the magnitude of the energy deposition, determined by the neutron yield and the energy coupling efficiency, has a much stronger effect on δV than the spatial distribution.

4.2.3.2 One Hundred Kiloton Energy Deposition

Because the spatial distributions of deposited energy do change with the detonation yield, it is still prudent to see if the spatial distribution differences matter for a higher yield, $\sim$100 kt of deposition. Table 4.4 contains the list of parameters for the ALE3D simulations where an asteroid is irradiated by a detonation from $c \approx 0.414$ distance away, for 1 Mt of 14.1 MeV neutrons and 632 kt of 1 MeV neutrons.

The values in the 1 Mt 14.1 MeV column have the same values as they did in Table 4.2. The $\sim$632 kt yield of 1 MeV neutrons allows for the $E_{dep,tot}$ values to match between these two sources. As with all these simulations, the $E_{dep,tot}^{ALE3D}$ values

147

Table 4.4. Parameters for 100 kt identical deposited energy ALE3D simulations with two different neutron sources.

Parameter	1 Mt @ 14.1 MeV/src-n	632 kt @ 1 MeV/src-n
Y_n	1 Mt	631.825 kt
E_n	14.1 MeV	1 MeV
src-n	1.86294×10^{27}	1.59419×10^{28}
Y_{int}	146.45 kt	92.53 kt
η_{rel}	0.6884	1.0896
$E_{dep,tot}$	100.82 kt	100.82 kt
$E_{dep,tot}^{ALE3D}$	100.68 kt	100.30 kt
E_{dep}/E_{melt}	53.1	66.1
N	552,896	717,409
Δr	2.275 cm	2.265 cm
z_{melt}	~ 130 cm	~ 180 cm
% Error	0.42%	0.30%
$N_{E_{dep}}$	311,040	456,192
$N_{E_{dep}}/N$	0.5626	0.6359

148

are slightly below the anticipated $E_{dep,tot}$, and they are not exactly the same value for both the 14.1 MeV and 1 MeV neutrons because different asteroid mesh resolutions were constructed for each. This difference is fairly small ($< 0.4\%$).

The z_{melt} melt-depth for 632 kt @ 1 MeV/src-n is about 180 cm, decreased slightly from 200 cm for a 1 Mt detonation yield (Table 4.2). Note that the 632 kt 1 MeV melt-line is seen as a dashed horizontal line in Figure 3.6b.

Figure 4.15 shows δV over time resulting from $\sim$100 kt of total energy deposited from a source of 14.1 MeV neutrons and a source of 1 MeV neutrons. As with the 1 Mt yields in Section 4.2.2.2, the δV changes have reached an asymptote by 600 μs. The δV at 600 μs is 98.09$\pm$0.41 cm/s for the 14.1 MeV neutrons and 114.7$\pm$0.34 cm/s for the 1 MeV neutrons. By these values, for 100 kt of deposition, 1 MeV neutrons enable a velocity change that is 1.17 ± 0.01 times greater than 14.1 MeV neutrons.

In Section 4.2.3.1, when the total energy deposition was set to approximately 5 kt, both neutron source energies resulted in comparable δV values. It appeared that the differences due to the spatial arrangement of energy were not very significant. However, for 100 kt total energy depositions, the 1 MeV neutrons are easily superior to the 14.1 MeV neutrons on a per-energy-deposited basis. The δV from the 1 MeV neutrons is 17% greater than the velocity change from the 14.1 MeV neutrons. Additionally, the 1 MeV neutrons had almost 0.4% less total energy deposited than the 14.1 MeV neutrons. Clearly, at least at this amount of deposition and yield, the spatial distribution of the energy deposition in the asteroid due to 1 MeV neutrons results in higher δV than the alternative 14.1 MeV neutrons. To keep this value in perspective, recall that identical detonation yields resulted in a 61-70% effect on the velocity change, which is in the neighborhood of the 58% difference in the 14.1 MeV and 1 MeV energy coupling efficiencies.

A major characteristic difference between the two energy deposition profiles for

149
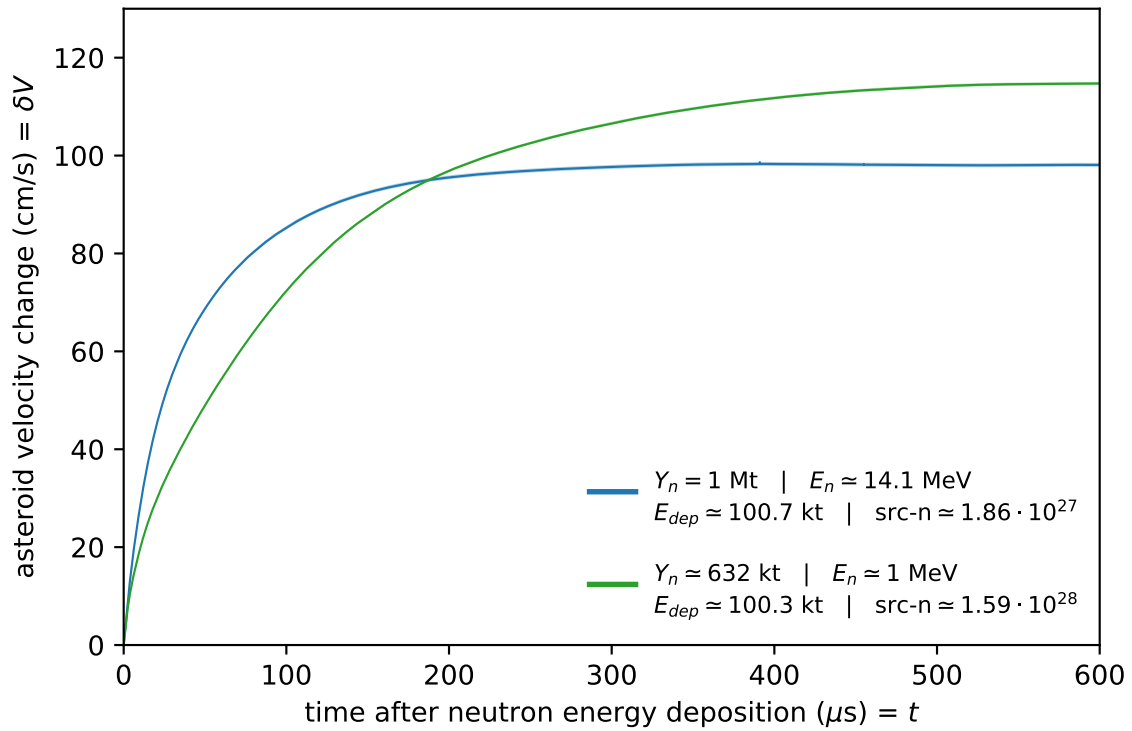
Figure 4.15. The change in asteroid velocity over time for an identical energy deposition of 100 kt. The blue line indicates the source of 14.1 MeV neutrons, and the green line represents the 1 MeV neutrons. The bands of lighter blue and green indicate the respective amounts of uncertainty in these δV values due to finite mesh resolution (note: these are not visible on this scale).

larger yields is the "pause" region of the 1 MeV source, as discussed in Section 3.2.1. As seen in Figure 3.6b, where d_{NEO} is between $\sim$40 cm to $\sim$100 cm, the energy deposition profiles level-off and remain somewhat constant for a short period, before falling back down to exponential decay. This is not a feature of the 14.1 MeV profiles from Figure 3.6a.

In earlier sections, when comparing identical 50 kt neutron yields, or when comparing identical 5 kt energy depositions, Y_n was 50 kt for 14.1 MeV neutrons and either 50 kt or 31.6 kt for 1 MeV neutrons. As seen by the melt-lines for $Y_n = 50$ kt and $Y_n = 31.6$ kt in Figure 3.6b, it is observed that the pause region of the 1 MeV profiles is not touched at these yields. That is, the asteroid materials in the pause region are not heated enough to be melted — after all, the melt depths were only 31 cm or 19 cm (Tables 4.1 and 4.3).

For these lower neutron yields, the 14.1 MeV and 1 MeV profiles in Figure 3.6 and Figure 4.9 are not dramatically different. This would explain why it was found in Section 4.2.3.1 that the spatial differences in the energy deposition profiles did not significantly change the δV, and instead it was primarily a matter of energy deposition magnitude a la coupling efficiency differences.

However, when comparing identical 1 Mt neutron yields, or when comparing identical 100 kt energy depositions, Y_n was 1 Mt for 14.1 MeV neutrons and either 1 Mt or 632 kt for 1 MeV neutrons. The melt-lines for $Y_n = 1$ Mt and $Y_n = 632$ kt in Figure 3.6b show that, at these energies, the materials in the pause region are indeed melted.

For these higher neutron yields, it is easy to see in Figure 3.6 that the energy distributions are quite different spatially between 14.1 MeV and 1 MeV neutrons, largely because of the pause feature in the latter and not in the former. This would explain the finding that δV is significantly different even at an identical magnitude

151

of 100 kt deposition — that the spatial variation does have an impact, but it is yield-dependent and based upon the shaping and contours of deposited energy itself.

If all of this is true, then at least for these 14.1 MeV and 1 MeV sources, perhaps as the neutron yield increases from 50 kt along the road to 1 Mt, the degree that the spatial profile differences impact δV steadily changes. If other, intermediate yields were simulated for each source to obtain more δV data-points, the nature of deflection's sensitivity to yield due to energy deposition profile changes would become more clear.

4.2.4 Summary of Asteroid Responses

Table 4.5 is the compilation of all δV asteroid response results for all six scenarios inspected in this work. The neutron yields Y_n, neutron energies E_n, number of source neutrons src-n, and the total energy depositions $E_{dep,tot}^{ALE3D}$ are also provided. $\delta V_{\text{x-ray}}$ is the analytical approximate velocity change calculated via Equation 4.15 for an *x-ray* equivalent yield.

Table 4.5. Summary of asteroid responses to various neutron yields, energy depositions, and source neutron energies. Y_n is the neutron yield, E_n is the energy of the source neutrons, src-n is the number of source neutrons from the detonation, Y_{int} is the amount of yield that intercepts the asteroid surface, $E_{dep,tot}^{ALE3D}$ is the *actual* total amount of deposited energy in the ALE3D model, δV is the asteroid velocity change, and $\delta V_{\text{x-ray}}$ is the analytical asteroid velocity change from x-ray yields (Equation 4.15).

Y_n	E_n	src-n	$E_{dep,tot}^{ALE3D}$	δV	$\delta V_{\text{x-ray}}$
50 kt	14.1 MeV	$9.31469 \cdot 10^{25}$	5.0364 kt	6.19 ± 0.06 cm/s	1.20 cm/s
50 kt	1 MeV	$1.26157 \cdot 10^{27}$	7.9785 kt	9.99 ± 0.12 cm/s	
31.5913 kt	1 MeV	$7.97093 \cdot 10^{26}$	5.0410 kt	6.02 ± 0.08 cm/s	0.87 cm/s
1 Mt	14.1 MeV	$1.86294 \cdot 10^{27}$	100.68 kt	98.09 ± 0.41 cm/s	7.91 cm/s
1 Mt	1 MeV	$2.52314 \cdot 10^{28}$	158.75 kt	166.9 ± 0.50 cm/s	
631.825 kt	1 MeV	$1.59419 \cdot 10^{28}$	100.30 kt	114.7 ± 0.34 cm/s	6.02 cm/s

The analytic/x-ray $\delta V_{\text{x-ray}}$ values underestimated the simulation/neutron δV val-

ues consistently and by a factor of 5-to-20. There are two obvious reasons for this. First, Equation 4.15 is an approximate formula; it cannot capture all of the physics that are modeled in a hydrodynamic simulation. Second, and more importantly, $\delta V_{\text{x-ray}}$ applies to x-ray yields, while this work investigated neutron yields. The fact that $\delta V > \delta V_{\text{x-ray}}$ matches the expectations from Section 4.1.3. It appears that neutrons are better for asteroid deflection on a per-source-yield basis than x-rays.

Interestingly, the x-ray $\delta V_{\text{x-ray}}$ values are closer to the neutron δV values for the smaller yields (50 kt and 31.6 kt) than they are for the larger yields (1 Mt and 632 kt). In an actual nuclear device detonation, the radiation impinging upon the asteroid target will include both x-rays and neutrons, and the total velocity change, δV_{total}, will be the result of energy depositions from both source types. It is possible that the neutron and x-ray contributions to δV_{total} will be comparable for smaller total detonation yields, but less-so as the total yield increases. This of course depends upon the specific energy partitioning, or how a real-world nuclear device splits the total yield between x-rays and neutrons.

It should be noted once more that the higher yields (1 Mt and/or 632 kt) tested in this work result in velocity changes that are much greater than the 15.27 cm/s escape velocity for the 300 m asteroid considered in this work. As such, yields of this class at the $c \approx 0.414$ stand-off distance would not be considered for an asteroid target of this size, if deflection without too much risk of fracture or disruption was desired. Assuming that the mass M of the spherical body is the product of its density and its volume, $\rho \cdot \frac{4}{3}\pi r^3$, then the formula for escape velocity (Equation 1.2) states that $v_{escape} \propto r$. For a δV around 167 cm/s to be less than the escape velocity, this would require an asteroid with a diameter of $\sim$4+ km. For 100 cm/s or so δV values to be more appropriate, a 2+ km object should be the target. Nevertheless, the higher yields revealed that the asteroid deflection velocity is not solely dependent on

the neutron coupling efficiency for yields that result in significantly different energy spatial deposition profiles.

Figure 4.16 shows δV versus time for all simulations. Figure 4.16a plots the δV evolution for lower neutron yields, while Figure 4.16b is for the higher neutron yields.
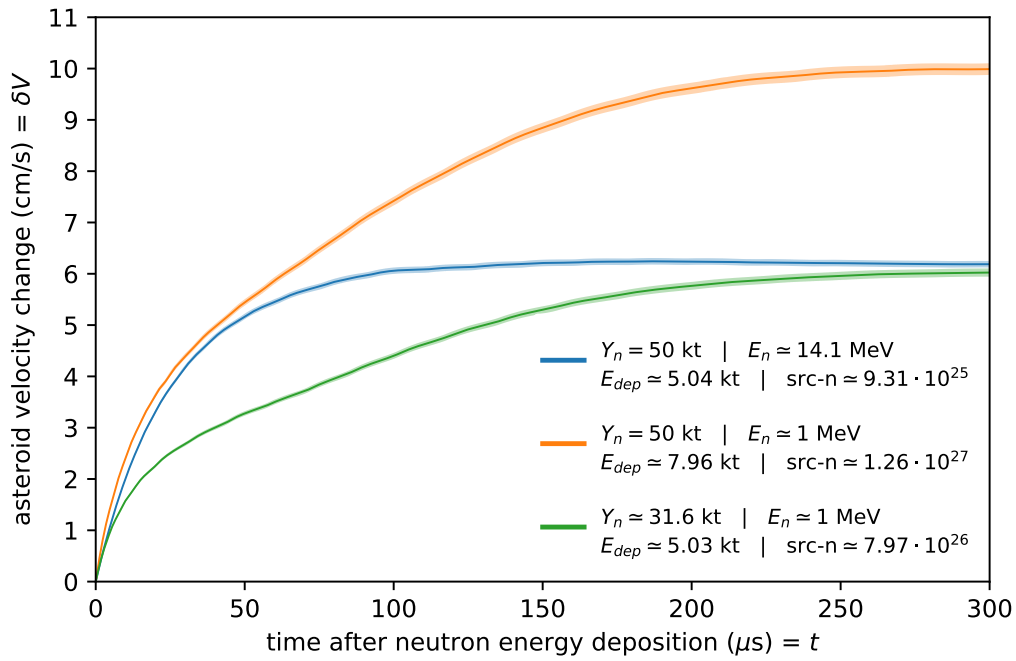
(a) The change in asteroid velocity over time for lower neutron yields.
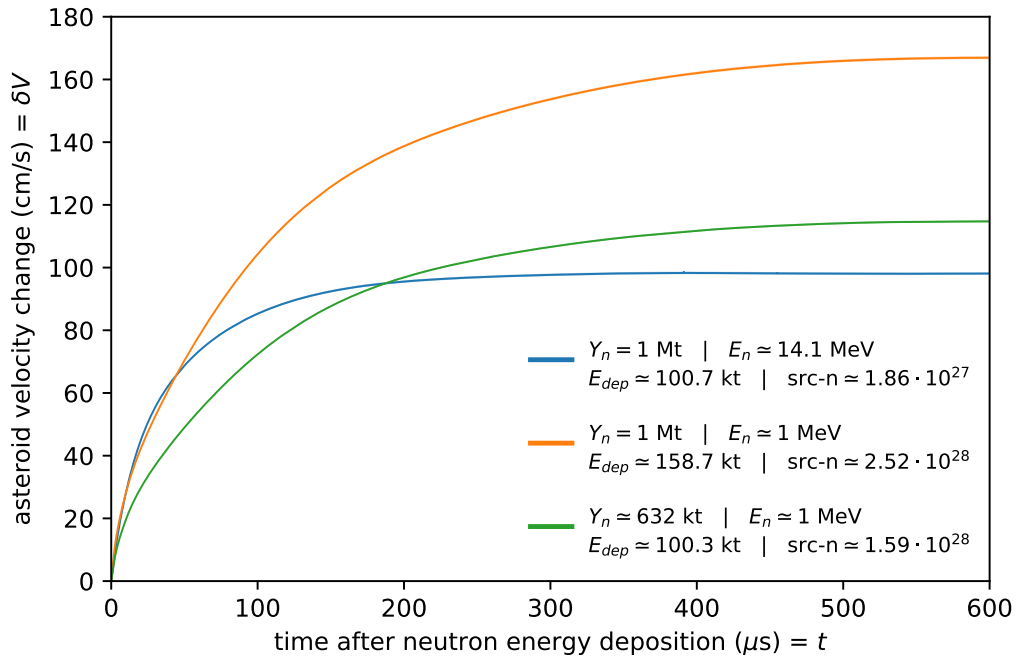
(b) The change in asteroid velocity over time for higher neutron yields.

Figure 4.16. Summary of asteroid responses to various yields, energy depositions, and source neutron energies.

V. Conclusions

5.1 Summary

This research investigated how the incident neutron energy affects asteroid deflection. A 300 m diameter asteroid target composed of SiO_2 was exposed to a nuclear device detonation at a stand-off distance of $c \approx 0.414$, which was a ~ 62.13 m height of burst above ground zero of the asteroid surface.

Two neutron energies were selected for comparison: ~ 14.1 MeV neutrons (group #3 in the DPLUS structure), as from D-T fusion reactions, and ~ 1 MeV neutrons (group #21 in the DPLUS structure), as prominent from fission reactions. Based on intuition from basic nuclear physics theory, the expectation was that different source neutron energies would result in 1) different spatial distributions of energy deposition in the target, and 2) different energy coupling efficiencies comparing the amount of energy absorbed to the amount of energy incident on the asteroid. The hypothesis was that changing the energy deposition profiles and the energy couplings would have an impact on asteroid deflection performance.

The research objectives were to answer the following questions:

1. What do the energy deposition profiles look like for various neutron source energies, and how do they compare?

2. How does energy coupling efficiency change with the energies of the incident neutrons?

3. In changing the energy deposition profile and energy coupling, what effect does neutron energy (indirectly) have on asteroid deflection?

4. What is the optimal neutron energy or energy spectrum for asteroid deflection?

156

Using a Monte Carlo radiation-transport code, MCNP6.2, questions #1 and #2 were answered. Based on the shape of a typical energy deposition profile, two general trends are observed — most energy is deposited near the asteroid surface (in depth), and most energy is deposited near ground zero, or directly beneath the source detonation (in angle). That is, energy deposition decreases as the penetration depth increases, and energy deposition also decreases as the distance from ground zero increases. Both of these results were as expected, considering that most neutron interactions will occur near the surface and that there are more neutrons per unit surface area near ground zero than far from ground zero.

In comparison, the energy deposition profiles (Figure 3.6) show that energy is deposited in quite different patterns between 14.1 MeV and 1 MeV neutrons, alone. A major difference is evident in the 1 MeV profiles (Figure 3.6b), the presence of what was dubbed the "pause" region, where the energy deposition levels-off for a period before falling back down exponentially. This is believed to be due to the much greater propensity for 1 MeV neutrons to undergo (n,γ) radiative capture reactions in SiO_2. When 14.1 MeV neutrons collide with ^{28}Si and/or ^{16}O nuclei, they have enough energy such that many different threshold nuclear reaction channels are available (Table 2.3). For 1 MeV neutrons, only elastic scatter or (n,γ) is possible. Because of this, the interactions of 1 MeV neutrons in SiO_2 can generate greater numbers of MeV-level secondary gamma-rays than 14.1 MeV neutrons. The "pause" in the 1 MeV profiles appears to be the result of thermalized neutron capture releasing a second pulse of energy deposition from the capture gamma-rays.

Results from MCNP6.2 also answered question #2 with regards to energy coupling. Table 3.2 shows that the energy coupling efficiencies are very different between 14.1 MeV and 1 MeV source neutrons. At the $c \approx 0.414$ stand-off distance away from a spherical target, an isotropic detonation at a point-source will send $\sim$14.64% of its

radiation towards the asteroid (i.e. the area of the red cone in Figure 3.1a), and the rest will be discarded to the vacuum of space. For a given neutron yield at the point of detonation, this means that only ~14.64% of the neutrons will actually intercept the asteroid and be able to deposit their energy. The relative energy coupling efficiency is the ratio of the total amount of energy deposited in the asteroid as compared to this intercepted yield. For 14.1 MeV neutrons, about 68.84% of the intercepted yield is actually absorbed by the asteroid target. For 1 MeV neutrons, almost 109% of the intercepted yield is deposited.

Noting that the 1 MeV coupling is greater than 100%, how can a greater amount of energy be deposited than what was sent towards the asteroid? It is because of the additional energy that is generated via (n,γ) reactions in SiO_2 converting mass to energy. The (n,γ) reaction channel is exothermic, meaning that it will occur with a neutron of any energy; there is no threshold. Table 2.3 shows that 8.474 MeV or 4.143 MeV of "extra" energy is generated following neutron capture on ^{28}Si or ^{16}O target nuclei, respectively. These additional Q-value energies from the (n,γ) reaction are created within the asteroid medium itself. A very small fraction of this bonus energy is immediately imparted as recoil to the ^{29}Si or ^{17}O nuclei (that is, a small amount of this Q-value energy is instantly deposited by remaining with the SiO_2 particle population), while the vast majority is initially emitted as radiation a la a gamma-ray (which can quickly deposit some, or all, of its energy into SiO_2). Therefore, since 1 MeV neutrons are more likely to undergo these energy-creating (n,γ) reactions, the coupling efficiency can increase even beyond 100%.

14.1 MeV neutrons, on the other hand, have enough energy for many endothermic reactions, which are reactions that require some amount of energy to be invested to occur. In this way, this is a net loss to coupling efficiency, as some of the 14.1 MeV neutrons will lose portions of their energy from endothermic reactions, thereby reduc-

158

ing, on average, the overall amount of energy deposition in the asteroid. However, 14.1 MeV neutrons have at least one advantage that helps keep its coupling efficiency closer to 1 MeV neutrons than might otherwise be expected. The mean-free-path for 14.1 MeV neutrons in SiO_2 is about 10.8 cm, while it is only 2.6 cm for 1 MeV neutrons (Table 3.1). This means that the average 14.1 MeV neutron will penetrate deeper beneath the asteroid surface before its first interaction. For 1 MeV neutrons, a lower mean-free-path means that they will begin to interact closer to the outer asteroid surface, increasing the odds that a decent number could leave the asteroid medium due to scattering, escaping out to space before all energy is deposited. In comparison, due to its deeper initial depth, it appears less likely that a 14.1 MeV neutron will be scattered-out of the asteroid medium, which means that it has a greater chance of depositing all of its energy. This is one reason why the coupling efficiency of 14.1 MeV neutrons is somewhat competitive with 1 MeV neutrons.

ALE3D, an arbitrary Lagrangian–Eulerian hydrodynamics code, allowed for question #3 to be answered. At equal 50 kt neutron yields (Section 4.2.2.1), 1 MeV neutrons resulted in $\delta V = 9.99 \pm 0.12$ cm/s, while 14.1 MeV neutrons achieved $\delta V = 6.19 \pm 0.12$ cm/s. These values show that 1 MeV neutrons offered about $61 \pm 2\%$ greater deflection performance at 50 kt yields. While the radial and angular extent and shapings of the energy deposition profiles in the melted region were slightly different between the two neutron sources, it is believed that most of this $\sim 61\%$ difference is explained by the differences in the magnitude of energy deposition. The ratio of the energy coupling efficiencies between 1 MeV and 14.1 MeV neutrons is 1.58. Because of this, for equal detonation yields, 1 MeV neutrons will always deposit 58% more energy in the target than the 14.1 MeV neutrons, which is quite close to the $61 \pm 2\%$ difference in δV values.

Equal 1 Mt neutron yields told a similar story (Section 4.2.2.2). 1 MeV neutrons

resulted in $\delta V = 166.9 \pm 0.5$ cm/s, while 14.1 MeV neutrons achieved only $\delta V = 98.09 \pm 0.41$ cm/s, which is a difference of 1.70 ± 0.01 between the two. Again, 58% more energy was deposited in the asteroid with 1 MeV neutrons as opposed to 14.1 MeV neutrons (158.75 kt versus 100.68 kt, as in Table 4.2), which seems to explain most of the differences. However, at 50 kt, the 1 MeV δV was $61 \pm 2\%$ better, while at 1 Mt, it is $70 \pm 1\%$ better. This discrepancy seemed to suggest that something other than the energy coupling, perhaps the differences in the energy deposition profiles, was significant for higher yields.

In an attempt to isolate any deflection performance differences due to the spatial arrangement of deposited energy, alone, new 1 MeV neutron yields were simulated. These yields were lower, suffering a penalty of 1.58, in order to remove the energy coupling efficiency advantage of 1 MeV neutrons. In this way, the comparisons would be for equalized *energy depositions*, rather than equalized detonation yields.

First, in Section 4.2.3.1, a 50 kt yield of 14.1 MeV neutrons was compared to $\sim$31.6 kt of 1 MeV neutrons (each depositing $\sim$5 kt of energy in the asteroid). This time, 1 MeV neutrons resulted in $\delta V = 6.02 \pm 0.08$ cm/s, while as before, 14.1 MeV neutrons achieved $\delta V = 6.19 \pm 0.12$ cm/s. Now, it is the 14.1 MeV neutrons that are superior, albeit only slightly so by $3 \pm 2\%$. However, considering that a 2% uncertainty is large in comparison to the 3% difference, and acknowledging that meshing differences in ALE3D caused the 1 MeV total energy deposition to be slightly (0.08%) less than the deposition from 14.1 MeV neutrons, these δV values are more-or-less the same. It appears that the differences in energy deposition profiles at these lower yields are not significant enough to strongly affect asteroid deflection.

Next, Section 4.2.3.2 compared a 1 Mt yield of 14.1 MeV neutrons to $\sim$632 kt of 1 MeV neutrons (each depositing $\sim$100 kt of energy in the asteroid). 1 MeV neutrons resulted in $\delta V = 114.7 \pm 0.34$ cm/s, while as before, 14.1 MeV neutrons achieved

160

$\delta V = 98.09 \pm 0.41$ cm/s. At this magnitude of equal energy depositions, 1 MeV neutrons are $17 \pm 1\%$ better for asteroid deflection. As energy coupling does not advantage either source here, this result shows that the energy deposition profiles can have an impact on deflection performance, and whether this effect is significant or not depends on the detonation yields. As seen by the melt-lines in Figure 3.6b, the lower yields only melted material located before the "pause" region of the 1 MeV profiles, while the higher yields heated this region. At the lower yields, perhaps the differences in the spatial arrangement of deposited energy were not large enough to change δV, but at the higher yields, the 14.1 MeV and 1 MeV profiles in the melted region are easily different due to the "pause" feature in the latter.

Question #4 remains very much open-ended. For equalized neutron yields, 1 MeV neutrons were easily better than 14.1 MeV neutrons. For equalized energy depositions in the asteroid target, 1 MeV neutrons appeared to offer either comparable or better δV values than 14.1 MeV neutrons. However, there are four very important caveats to note. First, these are only two neutron energies over the broad continuum of possible spectra to investigate, and with this alone, Question #4 must remain unanswered. Second, this is only for a single asteroid target of a given density, size, shape, and composition. Third, only two different classes of neutron yields — the larger set being 1 Mt and 632 kt, the smaller being 50 kt and 31.6 kt — were simulated in this work. Fourth, and perhaps most importantly, there are issues of practicality to be considered, as will be discussed below in Section 5.2.2.

As our knowledge increases and our technologies progress, one day, humanity might have to stop a hazardous asteroid from hurtling towards Earth. So long as we continue to work in preparation for this threat, we shall not fall as the dinosaurs did.

5.2   Future Work

5.2.1   On Re-Visiting Assumptions Made in This Work

There is an enormous amount of work that could still be done in the realm of aster-oid deflection. Some future work might involve re-visiting several of the assumptions made in this thesis.

Instantaneous energy deposition, or the approximation that the deposition and hydrodynamic timescales are well separated, is likely one of the biggest limiting assumptions in this work. If a suitable radiation-transport + hydrodynamic combined rad-hydro code is available, then it might be possible to remove the assumption of instantaneous energy deposition and instead model energy deposition and blow-off formation simultaneously. If such a code does not exist, then determining the time-line of energy deposition should be done, regardless, and implemented in the asteroid response simulations in some other manner (perhaps with variable heating rates that change over time). For example, the "Tally Time Card" functionality and/or the "time cutoff" physics option in MCNP6.2 could be applied to determine the energy deposition as a function of time.

Rather than only two neutron yields as examined in this thesis, many more require testing in order to more fully understand how sensitive the asteroid velocity changes are to different neutron energies. For example, for equal energy deposition magnitudes, this thesis found that 1 MeV neutrons are better than 14.1 MeV neutrons for deflection at higher yields, but they are either comparable or worse at lower yields. If more yields were simulated, the relative performance between these two neutron energies could be better understood.

Furthermore, neutron energies other than 14.1 MeV and 1 MeV should be investigated. Perhaps the energy deposition profiles and/or coupling from 2.45 MeV D-D fusion neutrons are even better for asteroid deflection. Even more importantly,

162

creating the energy deposition profiles from realistic neutron energy *spectra*, rather than using single energy groups or monoenergetic sources, would be more representative of the output from an actual nuclear detonation. The 46-group DPLUS dataset in Appendix A could be used to quickly and easily compute the energy deposition profiles for an arbitrary neutron energy spectrum.

Repeating the hydrodynamic simulations performed in this work and running out to several seconds to allow for shock propagation in the asteroid should be done to see how much δV changes. To accomplish this, the ALE3D input files need to be improved upon, or perhaps another hydrodynamic code that is well suited to studying the effects of asteroid diversion scenarios should be applied.

A full 3-D simulation, rather than the 2-D axisymmetric geometry considered in this work, could be done. This would require significantly more zones in order to achieve a level of resolution that is comparable to the 2-D scenario in this work, but if the computational resources are available, the 3-D effects might be of interest.

Instead of one stand-off HOB distance, perhaps a wide range could be surveyed to see if HOB changes the deflection performance due to the neutron energy. This author does not suspect that the HOB plays a large role in how successful different neutron energies are at deflection, but an investigation could be worthwhile.

Instead of only silicon dioxide at one density and porosity, other asteroid compositions and configurations could be modeled. Different asteroid shapes could be considered to see if irregular surfaces might impact which neutron energy is best, as well. This would require re-calculating energy deposition profiles for each neutron energy or spectrum of interest, for each specific asteroid target specification.

These are only some of several possible routes, parametric studies, and changes that could improve the accuracy, precision, and realism behind the results that show how neutron energy affects asteroid deflection.

163

5.2.2 On the Potential of a Modified Neutron Energy Spectra to Yield Any Practical Benefits to Asteroid Deflection

This thesis was a worthwhile academic exercise. As a first step in inspecting how neutron energy affects asteroid deflection, even though a rather limited set of data was available for analysis, some interesting results were revealed.

There is a broader and more important question, however, that is lurking in the shadows, in the black of space. Would altering the neutron energy spectrum ever be **worthwhile**? That is, is there a scenario where an asteroid target might be deflected more effectively with a neutron energy spectrum that is different from the characteristic energies of an ordinary detonation?

At first, the temptation might be to answer "Yes, of course." After all, both Sections 4.2.2.1 and 4.2.2.2 found that, on a per detonation yield basis, δV is higher for 1 MeV neutrons than it is for 14.1 MeV neutrons. Further, Section 4.2.3.2 showed that the δV from 1 MeV neutron irradiations can be greater than it is for 14.1 MeV neutrons even on a per deposition basis; even a lower neutron yield comprised of 1 MeV neutrons can outperform a higher yield made of 14.1 MeV neutrons. These results seem to indicate that it would be better for asteroid deflection if the high-energy 14.1 MeV neutrons from fusion reactions were replaced with low-energy 1 MeV neutrons as from fission.

However, this might not be the case, and it ignores issues of practicality. In fact, even though the results presented here are quite limited in extent (only inspecting two neutron energies, and only two or three detonation yields), it is almost a certainty that equal numbers 1 MeV neutrons would *not* be preferred to 14.1 MeV neutrons. How could this be?

First, the nature of the yield from a device detonation must be made explicit. A nuclear detonation liberates energy through various forms of radiation. The energy

distribution of radiation emitted from a nuclear detonation depends on the type of nuclear fuel and upon aspects of a device design. Using approximate, notional values, only 1% of the yield from a fission-based device is in the form of neutrons; for a fusion device, perhaps 20% of the total yield is given to the neutrons [39,56]. That is, for a total yield Y, the fraction Y_n/Y is 0.01 for a generic device that detonates via fission, and Y_n/Y is 0.20 for a device with a high fusion yield.

Following from this, it is understood that a nuclear explosive optimized for maximizing the neutron output is one with a high fusion to fission ratio, as stated in past work [34]. From Section 2.4, most neutrons born from fusion in nuclear explosions arise from D-T reactions, providing each neutron with $\sim$14.1 MeV of kinetic energy. Neutrons with energies of 1 MeV, in contrast, are far more likely to result from fission reactions.

1 MeV neutrons at the same neutron yield of a 14.1 MeV source achieve higher deflective velocity changes. The question then becomes: how can we synthesize 1 MeV neutrons in sufficient abundance in order to match the neutron yield of 14.1 MeV neutrons? One route would be to select nuclear devices powered by fission rather than fusion. However, taking the open-source literature Y_n/Y values at face-value (0.01 for fission and 0.20 for fusion), a fission device would require a total yield that is twenty times greater than a fusion device, in order to achieve matching neutron yields Y_n. Because the 1 MeV δV is not also 2000% beyond the 14.1 MeV δV at equivalent neutron yields — rather, in this work, it was found to be about 61-70% better for deflection — it would not make any practical sense to do this. Rather, it would be far easier and more efficient to simply opt for a fusion-based device.

If it is impractical to match the neutron yield from fusion with a fission device, then what if we were to accept the factor of 20 reduction outright? Putting aside feasibility concerns such as the fuel mass required for a nuclear explosive, for two comparable

devices with the same total yield Y, the fusion device would have $Y_n = 0.20Y$ and the fission device would have $Y_n = 0.01Y$. Could the fission device with $0.01Y$ still outperform a fusion device with $0.20Y$?

Coincidentally, this work has already provided an example that shows this is very unlikely to be the case. If we assumed that the total yield Y of a nuclear device was 5 Mt, then $Y_n = 1$ Mt (which is 20% of Y) via $E_n = 14.1$ MeV would represent a fusion device with the 0.20 neutron yield fraction. Also, when $Y_n = 50$ kt (which is 1% of 5 Mt) and $E_n = 1$ MeV, this could be roughly thought of as the 1% neutron output from a fission explosion (of course ignoring the fact that the fission neutrons come off as a spectrum). As seen in Table 4.5, δV for 50 kt of 1 MeV neutrons is only about 10% of the δV for 1 Mt of 14.1 MeV neutrons.

Producing neutrons on the order of 1 MeV directly by opting for a fission device over a fusion device does not appear that it would be worthwhile. The 20X loss in neutron yield when moving to fission from fusion might be too much to overcome, especially in light of the finding in Chapter 4 that the magnitude of the total energy deposition appears to be the strongest determinant of δV.

There is one option remaining. Perhaps the 1 MeV neutrons could be produced *from* 14.1 MeV progenitor neutrons. It has been envisioned that shells of moderating materials could be placed around, and enclose, an inner nuclear device that is optimized for neutron output. When the detonation occurs and 14.1 MeV neutrons from fusion travel through the surrounding materials, they will undergo scattering and absorption reactions (as described in Section 2.5) early on their way to the asteroid target. Some of these neutrons could lose energy by scattering reactions, while others could be absorbed and either directly or indirectly result in the release of additional neutrons from the moderator nuclei. For the neutrons that survive and escape the moderating materials and begin streaming through the void of space towards the as-

166

teroid, this transmission energy spectrum will be different than the original neutron energy spectrum from the detonation.

The average energy of the transmitted neutrons will likely be lower than the original source. Also, because most nuclei have a non-insignificant absorption cross-section, it is expected that the intensity (or number) of the transmitted neutrons will be lower than the initial amount coming off of the device detonation. The number of moderating layers, the isotopic compositions of each material, and the thickness or mass of the moderators will determine the transmission neutron energy spectrum and its intensity. In this way, starting with the initial spectrum of neutrons direct from the detonation event, various modified neutron spectra might be formed, and it is this altered set of neutron energies and numbers that will find its way to the asteroid target and irradiate the surface. As this work has shown, changing the neutron energy can have an effect on the resulting asteroid deflection.

However, there is an issue with this. Because the average weighted-energy of the transmission spectrum will almost surely be lower than the original neutron spectrum, and because the number of source neutrons that survive the journey through the moderators is probably lower than the starting intensity, the neutron yield headed toward the target will very likely be lower than it would be without the moderating materials encasing the nuclear device. That is, if both E_n and src-n in Equation 1.1 are decreased, then Y_n is lowered.

This potentially re-routes back to the earlier issues faced when considering fission devices. If the Y_n is too far decreased, then δV will be less than it would be otherwise from an unattenuated and unmodified detonation spectrum — *unless* there exists an attainable neutron energy spectrum that is more effective on a per-source-neutron basis. If a hypothetical configuration of moderating materials could generate such a spectrum with minimal losses due to absorption, then it is possible that changing the

167

neutron energy spectrum would be worthwhile as opposed to simply increasing the yield of an unmodified device.

Taking the δV and src-n values in Table 4.5, 1 MeV neutrons were clearly not more effective at deflection on a per-source-neutron basis than 14.1 MeV neutrons were. From this, the existence of such a moderator-crafted spectrum that is better, per-source-neutron, than an original detonation spectrum seems intuitively unlikely. Granted, this is a large inference to make when extrapolating from such a very small dataset, considering that this thesis considered only two neutron energies and only two yields.

If there are no known moderating materials that could generate a neutron spectrum more effective per particle than an unattenuated detonation, there is one remaining possibility that might make spectral shifting worthwhile. Like ^{28}Si and ^{16}O, many nuclei have (n,2n) or even (n,3n) reaction channels. Table 2.3 shows that the threshold energies required for the (n,2n) pathway to occur in SiO_2 are above 14.1 MeV, thereby inaccessible to most fusion neutrons. However, there exist isotopes — such as ^{2}H, ^{9}Be, ^{138}Ag, ^{23}Na, ^{27}Al, ^{39}K, ^{41}K, ^{56}Fe, ^{25}Mg, ^{26}Mg, ^{58}Ni, ^{60}Ni, and surely many others — that have (n,2n) threshold energies below 14.1 MeV [49].

If it is possible for a moderator to both shift the neutron energy spectrum *and* increase the number of neutrons from the original detonation via (n,2n) and/or (n,3n) type reactions with 14.1 MeV neutrons, then the advantages of modified neutron spectra in terms of higher energy coupling efficiencies and more beneficial spatial arrangements of deposited energy need not overcome a per-source-particle basis. While the transmission neutron yield would almost surely still be lower than an unattenuated detonation, it would not be quite as low as it would be otherwise, as long as the number of src-n could increase in order to partially offset the losses in energy per neutron (again, the relationship in Equation 1.1 is at play).

168

So, would altering the neutron energy spectrum ever be **worthwhile** for asteroid deflection? Using only what has been learned from this thesis, the answer cannot be in the affirmative. However, given the thoughts and ideas suggested in this section, it is perhaps too early to outright dismiss the notion. The best[1] answer to the question is: "More work is necessary."

---

[1]Or rather "worst," depending on your point-of-view.

Appendix A. DPLUS46 Energy Deposition Results

This appendix contains the energy deposition results for all 46 energy groups of the DPLUS structure. Group #0 in the DPLUS setup is the highest energy group, with an upper-bound of 19.64 MeV, and group #45 is the lowest energy group, with a lower-bound of 10 μeV. Section A.1 contains all 46 energy deposition profile plots, and Section A.2 contains a table recording energy coupling efficiency values for all 46 energy groups.

A.1 DPLUS Energy Deposition Profiles

The following pages in this section contain all 46 energy deposition spatial profiles for each of the 46 neutron energy groups in the DPLUS structure, beginning with group #0 (the highest energies) and ending with group #45 (the lowest-energies). Each plot presents energy deposition down to five orders of magnitude below the maximum unique to each energy group. The figure captions provide the lower-bounds, upper-bounds, and midpoints (or averages) of the neutron energy group corresponding to each of the profiles. Generally, the maximum value for the energy deposition decreases as the source neutron energy decreases. However, there are a few exceptions to this rule. For example, the peak energy deposition values increase slightly after group #32, even though source neutron energy is constantly decreasing as the group number increases.

This is attributed to the "pause" region of energy deposition that is prominent in many of the profiles, especially perhaps in group #16 and onwards. The pause is the secondary pulse of energy deposition resulting from radiative capture reactions with low-energy neutrons, an exothermic reaction channel that produces gamma-rays, as discussed in Section 3.2.1. The spatial location of the gamma-ray pause appears to change with source neutron energy, noting the shifting peak region of

170

energy deposition for lower-energy sources. The effect of the gamma-ray pause on the overall profile shaping also changes with neutron energy — sometimes it is indeed a pause or a flattening in the exponential drop-off of energy deposition, while for other energies it is shaped more like a bump or a peak.

This is a high-fidelity energy deposition dataset that could be used in future work to explore the effects of various other neutron energies and spectra on asteroid deflection. Rather than running a lengthy radiation-transport simulation for every individual spectrum of interest, the energy deposition profiles due to any arbitrary neutron energy spectrum can be immediately generated with this 46-group data, so long as the spectrum is (or can be) discretized according to the same 46-group energy boundaries as the DPLUS structure.
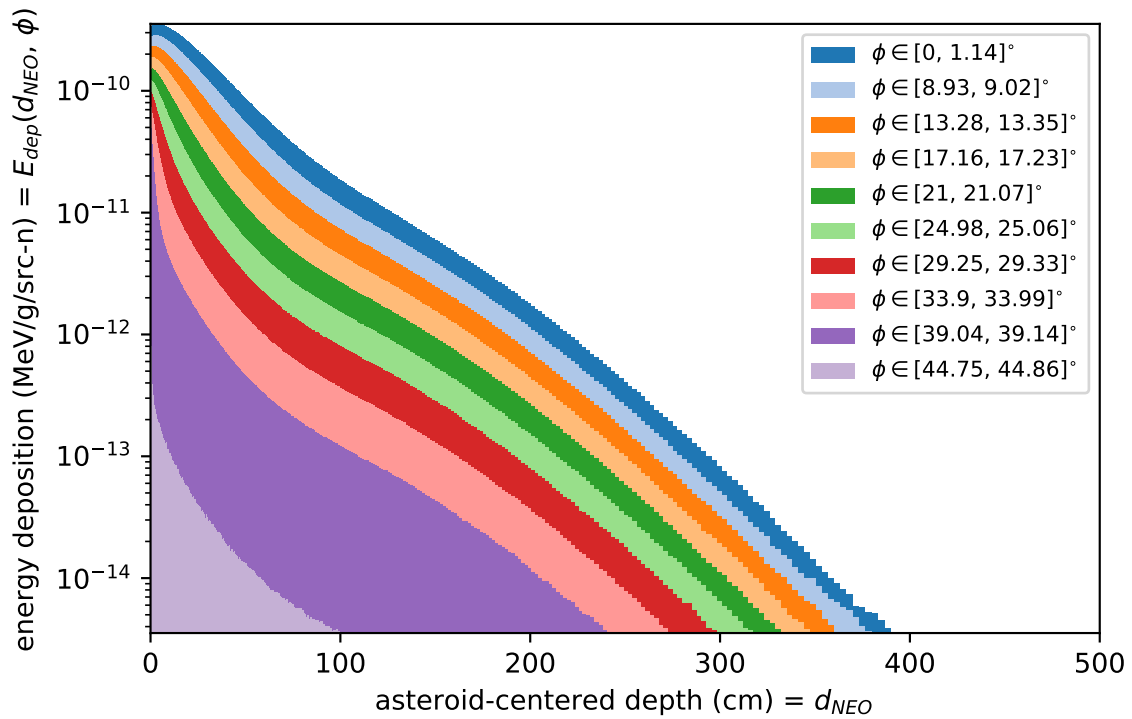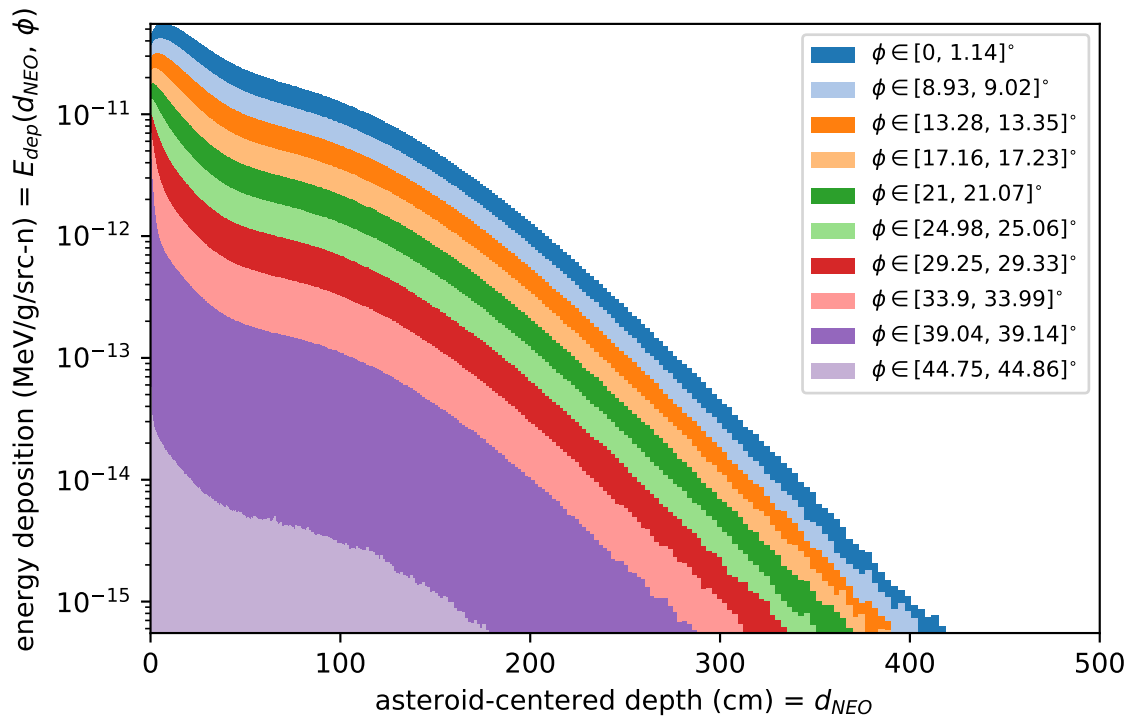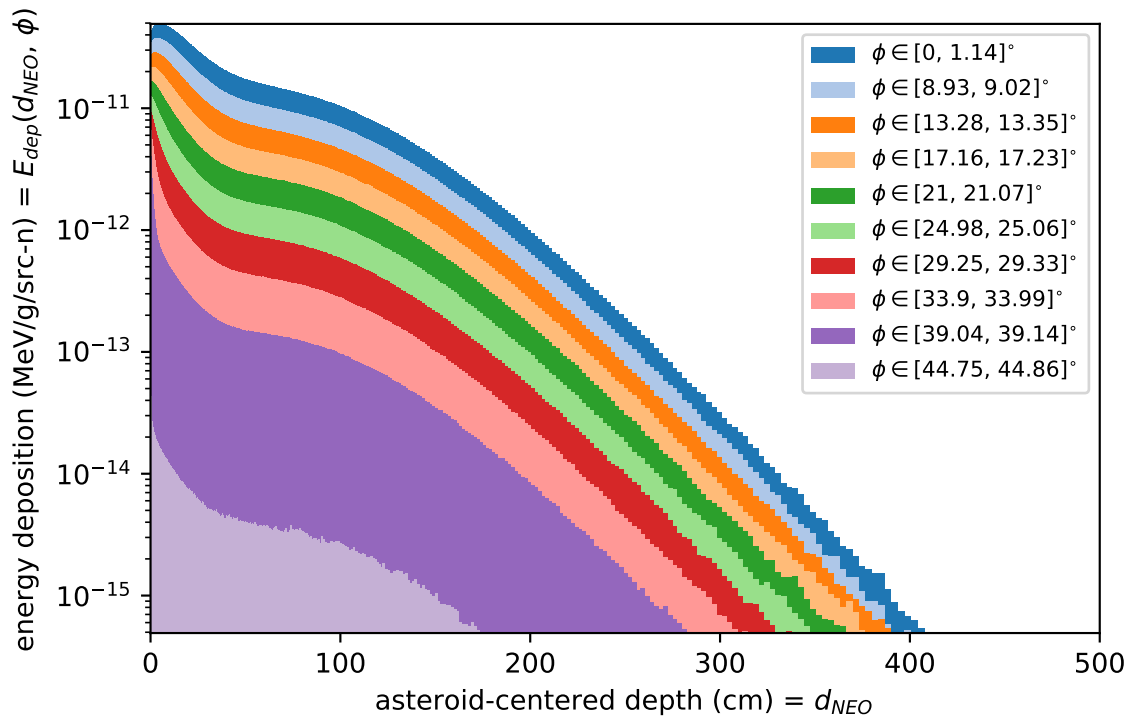
Figure A.1. DPLUS group #0 spatial energy profiles. For this energy group, the lower-boundary is 1.6905×10^1 **MeV and the upper-boundary is** 1.9640×10^1 **MeV. The midpoint or average energy is** 1.8273×10^1 **MeV.**
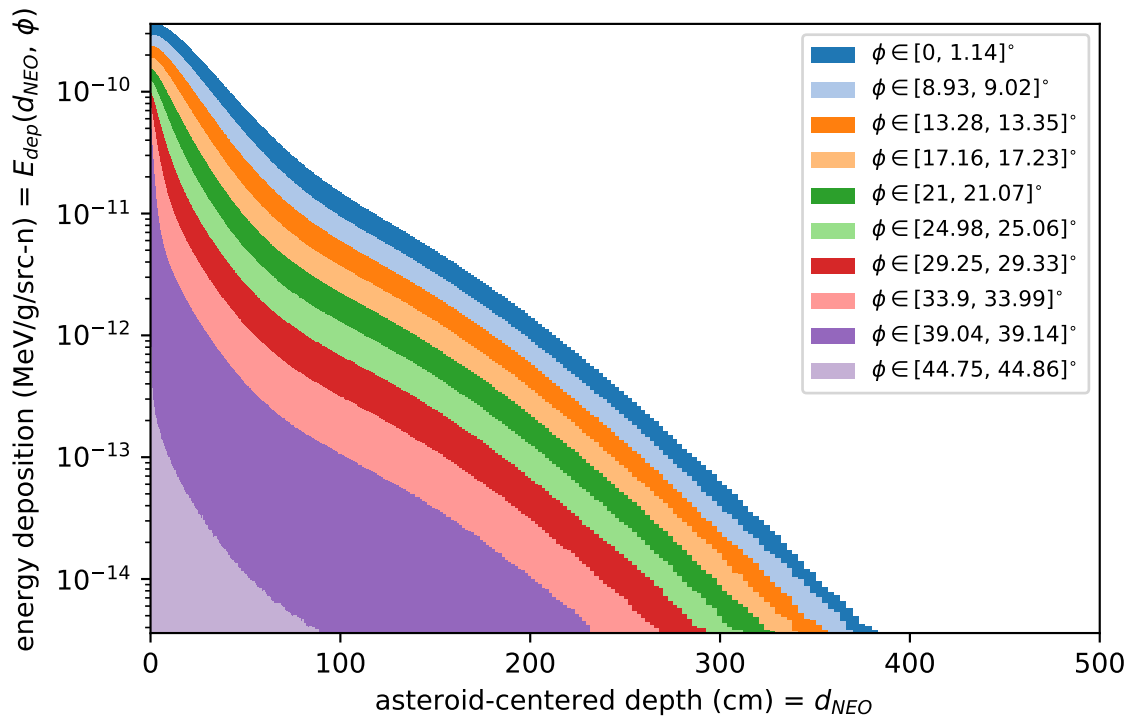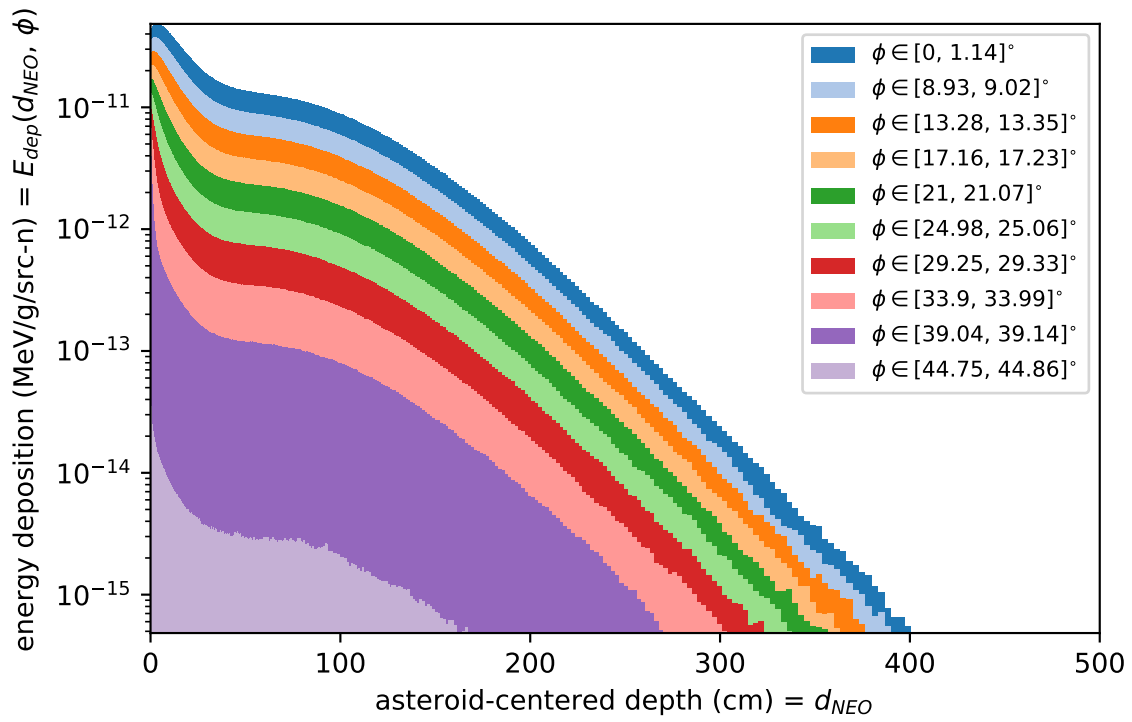
Figure A.2. DPLUS group #1 spatial energy profiles. For this energy group, the lower-boundary is 1.4918×10^1 MeV and the upper-boundary is 1.6905×10^1 MeV. The midpoint or average energy is 1.5912×10^1 MeV.
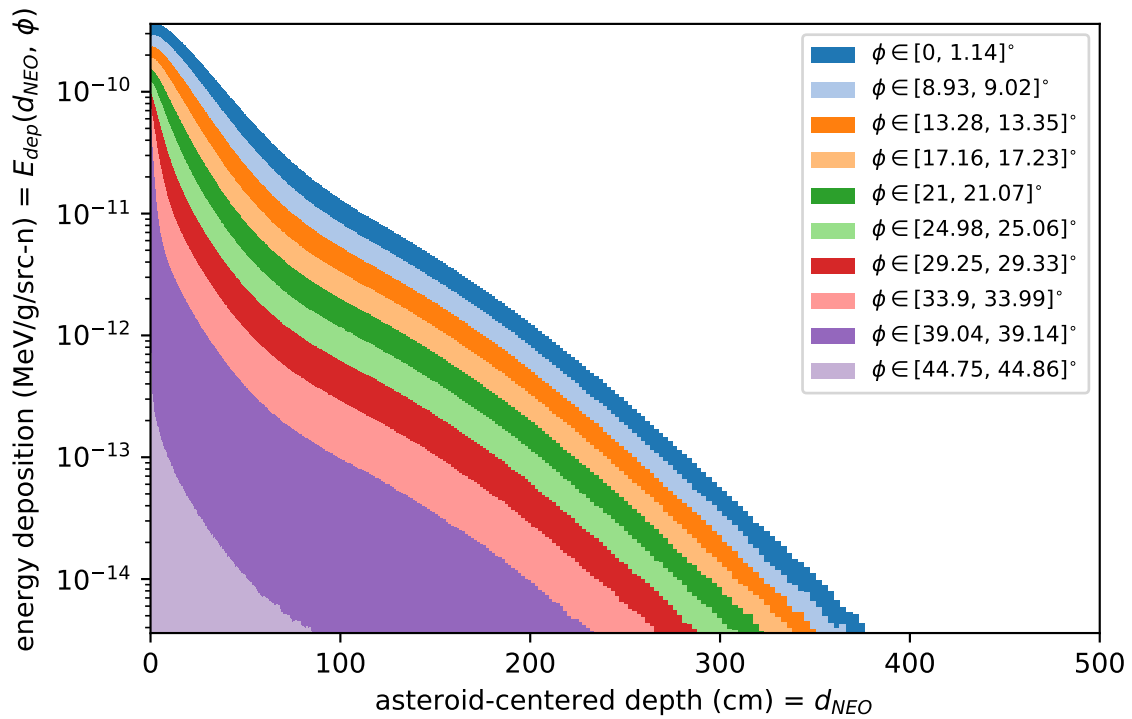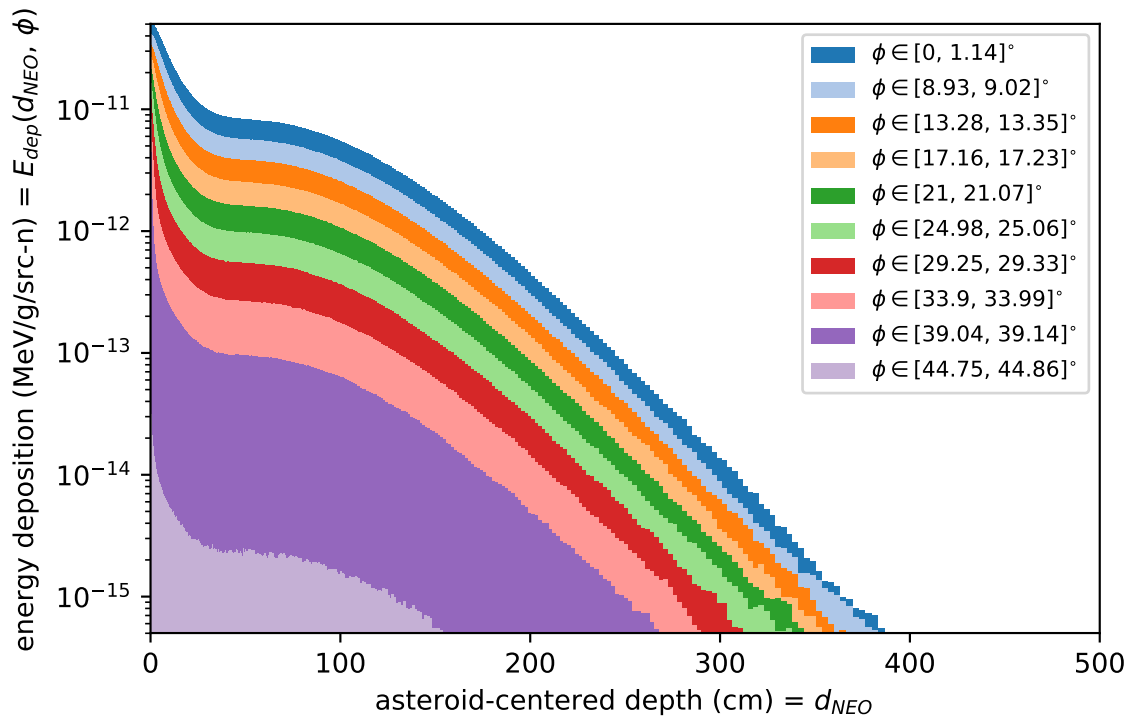
Figure A.3. DPLUS group #2 spatial energy profiles. For this energy group, the lower-boundary is 1.4191×10^1 **MeV** and the upper-boundary is 1.4918×10^1 **MeV. The midpoint or average energy is** 1.4555×10^1 **MeV.**
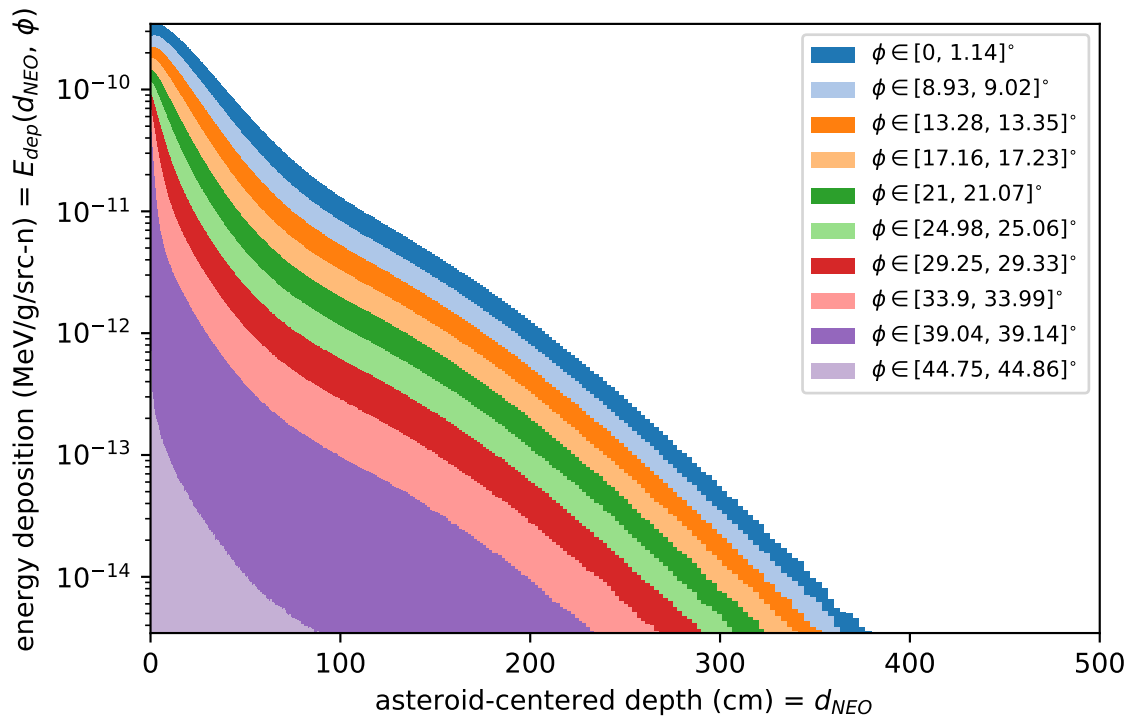
Figure A.4. DPLUS group #3 spatial energy profiles. For this energy group, the lower-boundary is 1.3840×10^1 MeV and the upper-boundary is 1.4191×10^1 MeV. The midpoint or average energy is 1.4015×10^1 MeV.
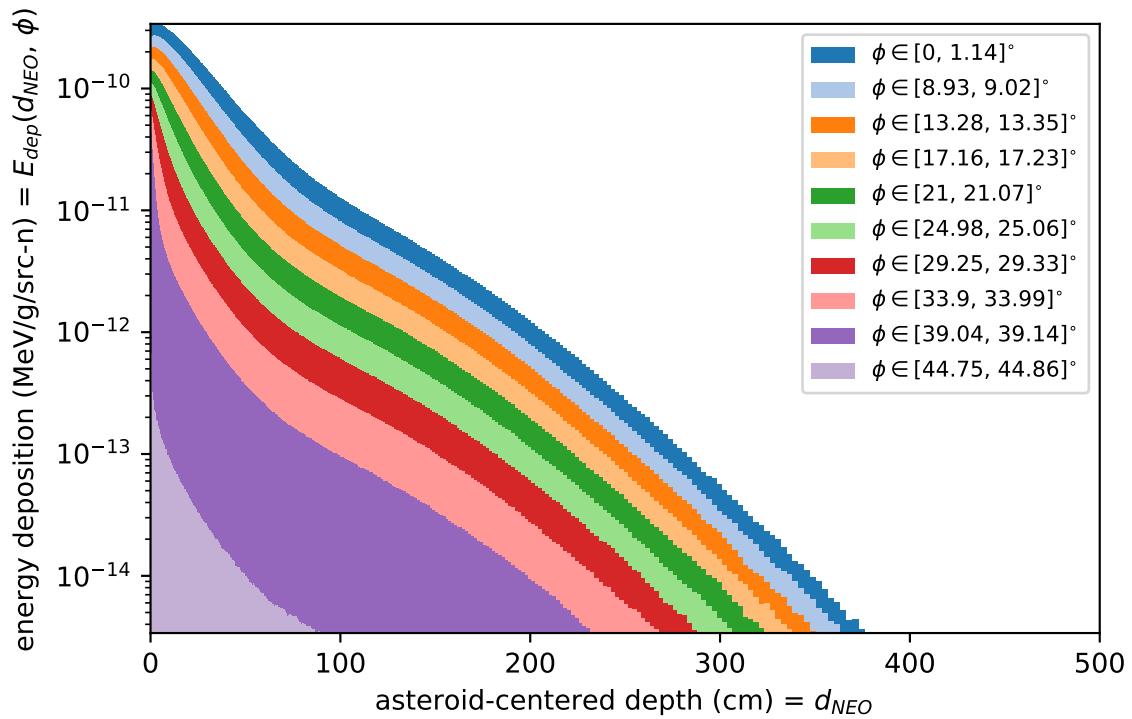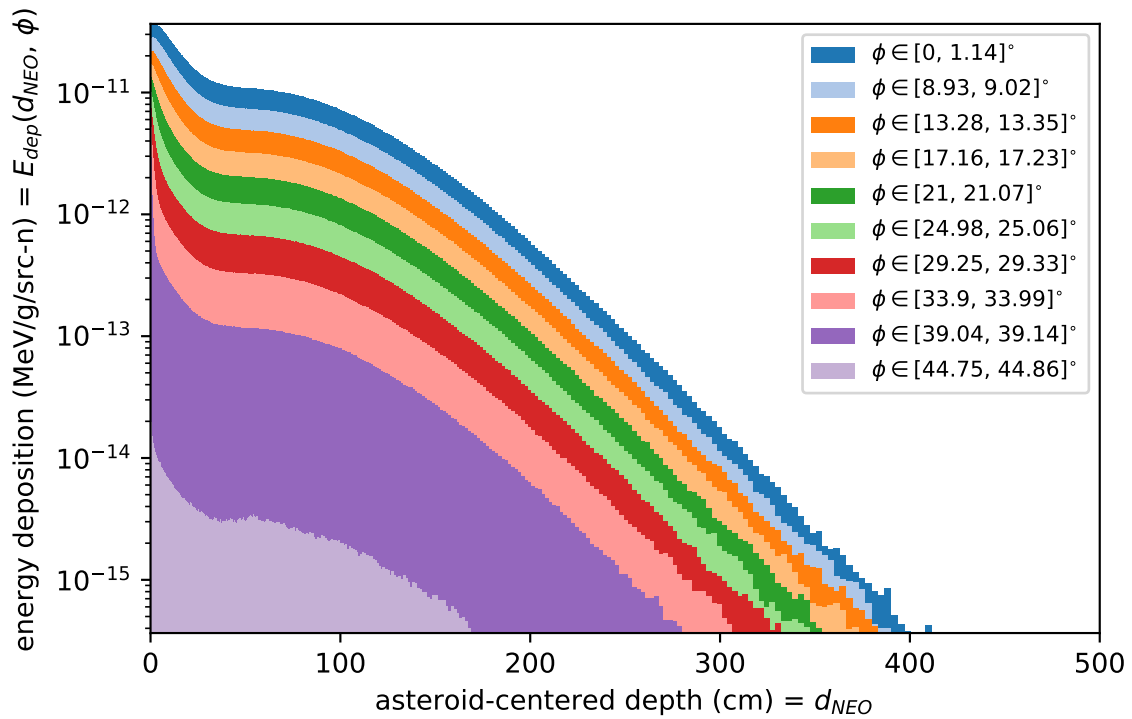
Figure A.5. DPLUS group #4 spatial energy profiles. For this energy group, the lower-boundary is 1.2523×10^1 MeV and the upper-boundary is 1.3840×10^1 MeV. The midpoint or average energy is 1.3181×10^1 MeV.
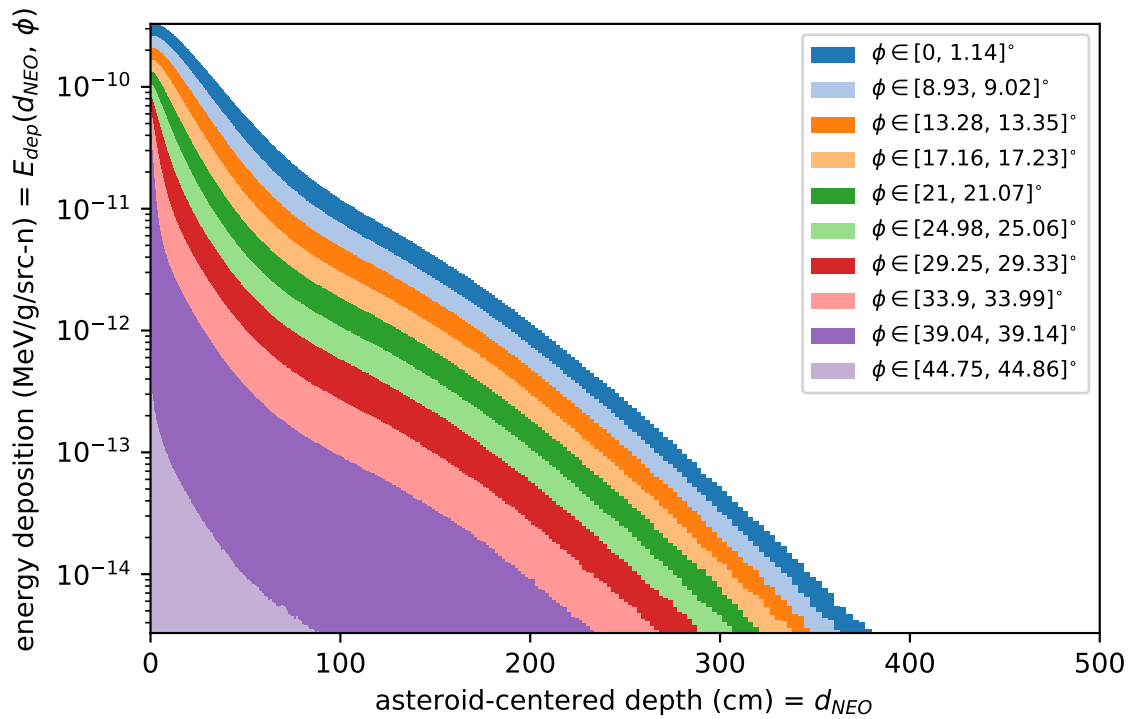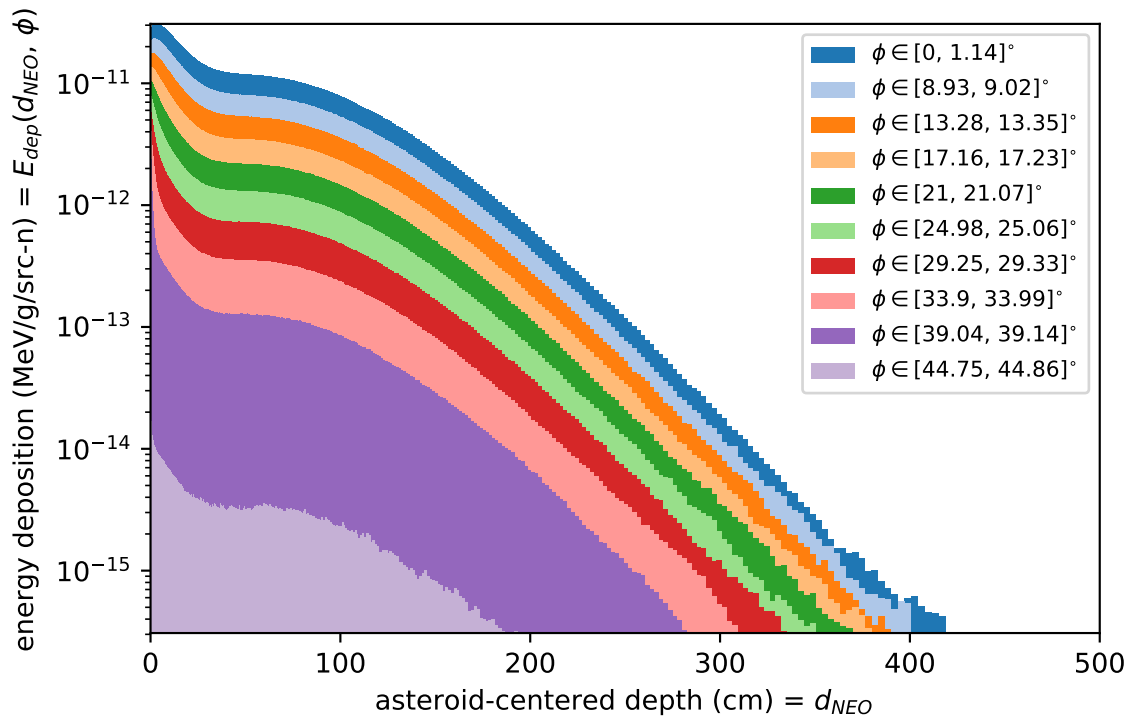
Figure A.6. DPLUS group #5 spatial energy profiles. For this energy group, the lower-boundary is 1.2214×10^1 **MeV and the upper-boundary is** 1.2523×10^1 **MeV. The midpoint or average energy is** 1.2369×10^1 **MeV.**
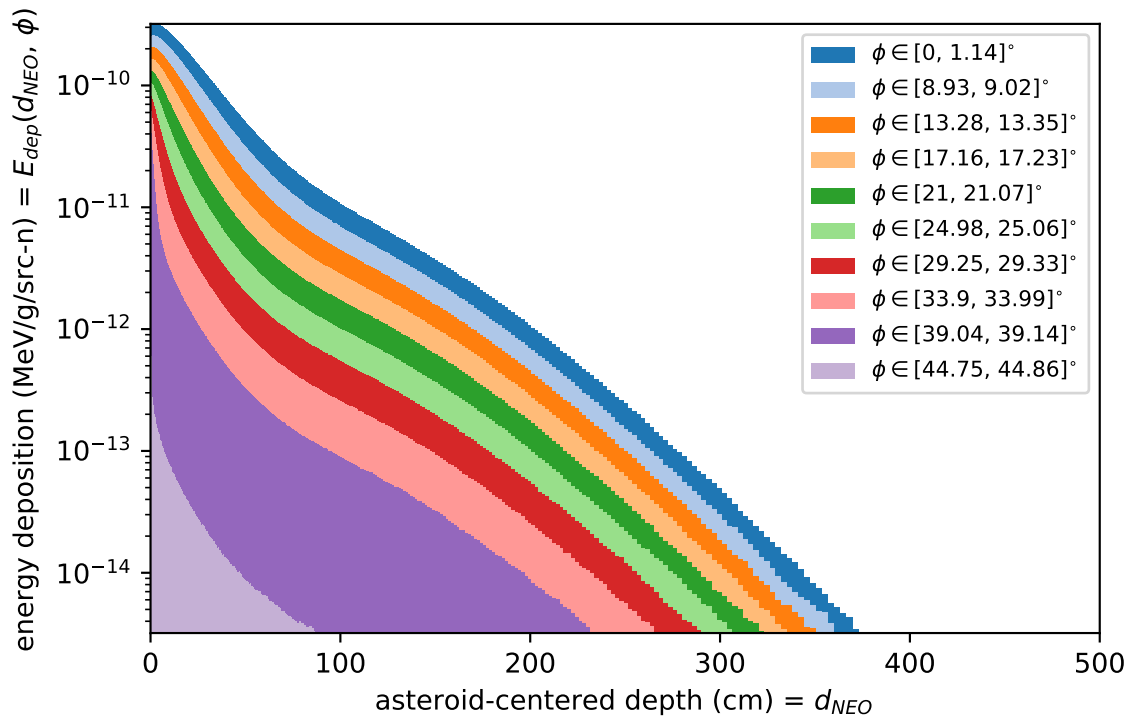
Figure A.7. DPLUS group #6 spatial energy profiles. For this energy group, the lower-boundary is 1.1052×10^1 **MeV and the upper-boundary is** 1.2214×10^1 **MeV. The midpoint or average energy is** 1.1633×10^1 **MeV.**
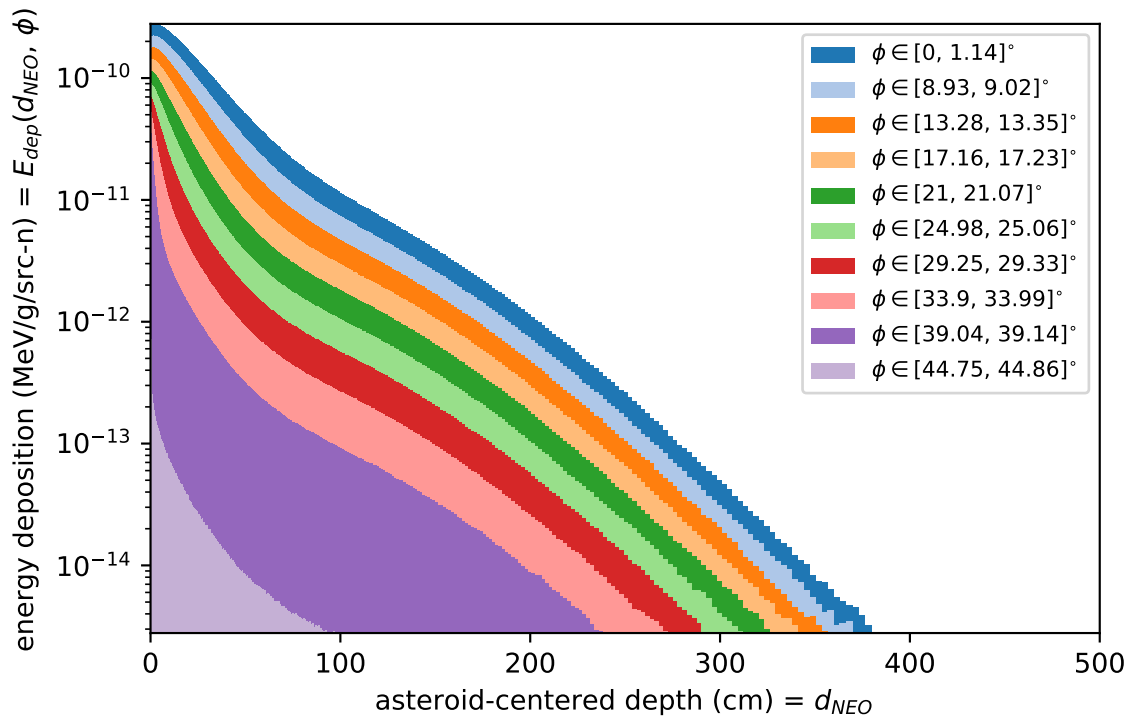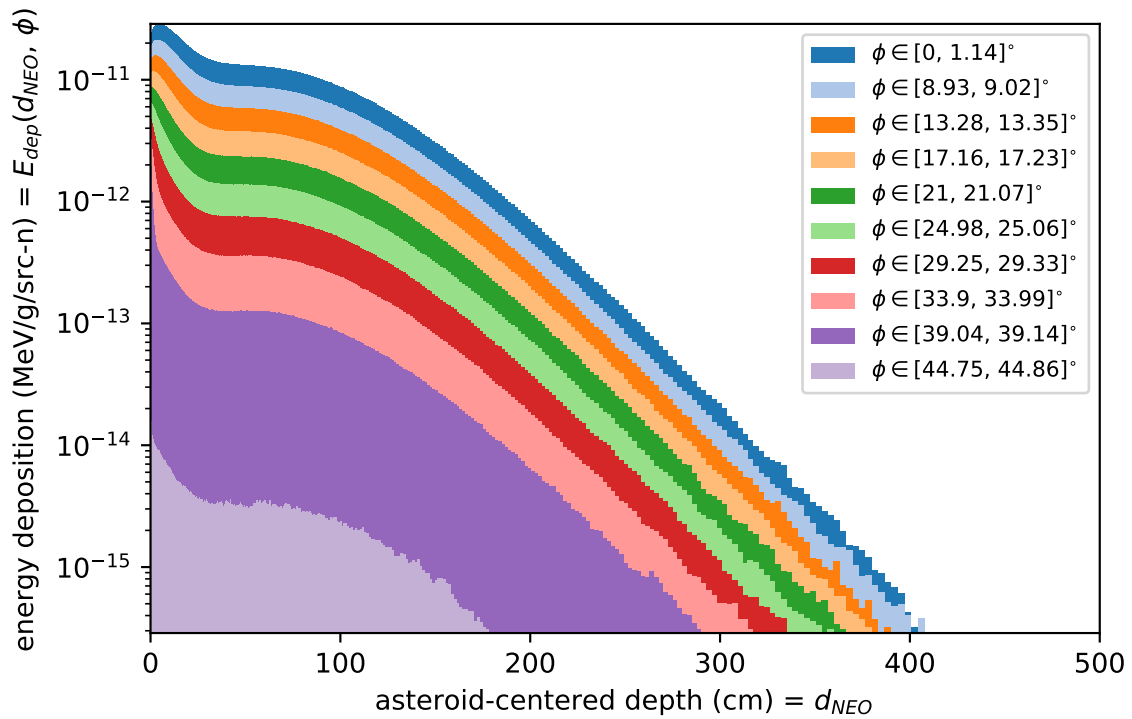
Figure A.8. DPLUS group #7 spatial energy profiles. For this energy group, the lower-boundary is 1.0000×10^1 **MeV and the upper-boundary is** 1.1052×10^1 **MeV. The midpoint or average energy is** 1.0526×10^1 **MeV.**
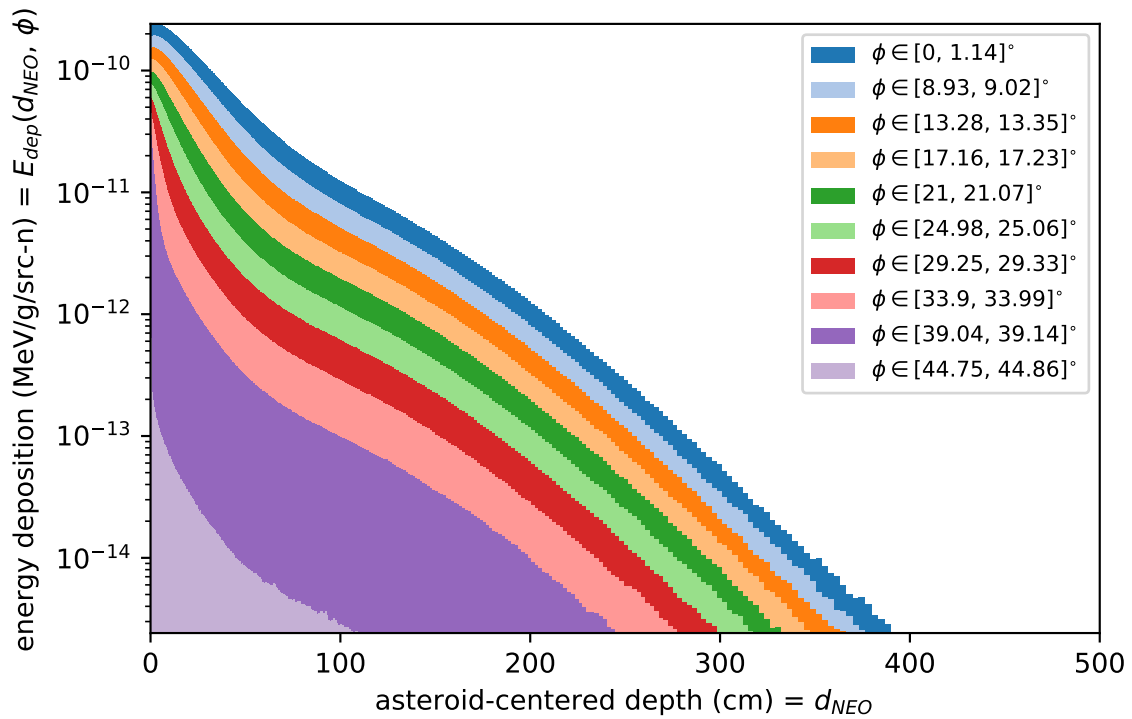
Figure A.9. DPLUS group #8 spatial energy profiles. For this energy group, the lower-boundary is 9.0484×10^{0} **MeV and the upper-boundary is** 1.0000×10^{1} **MeV. The midpoint or average energy is** 9.5242×10^{0} **MeV.**
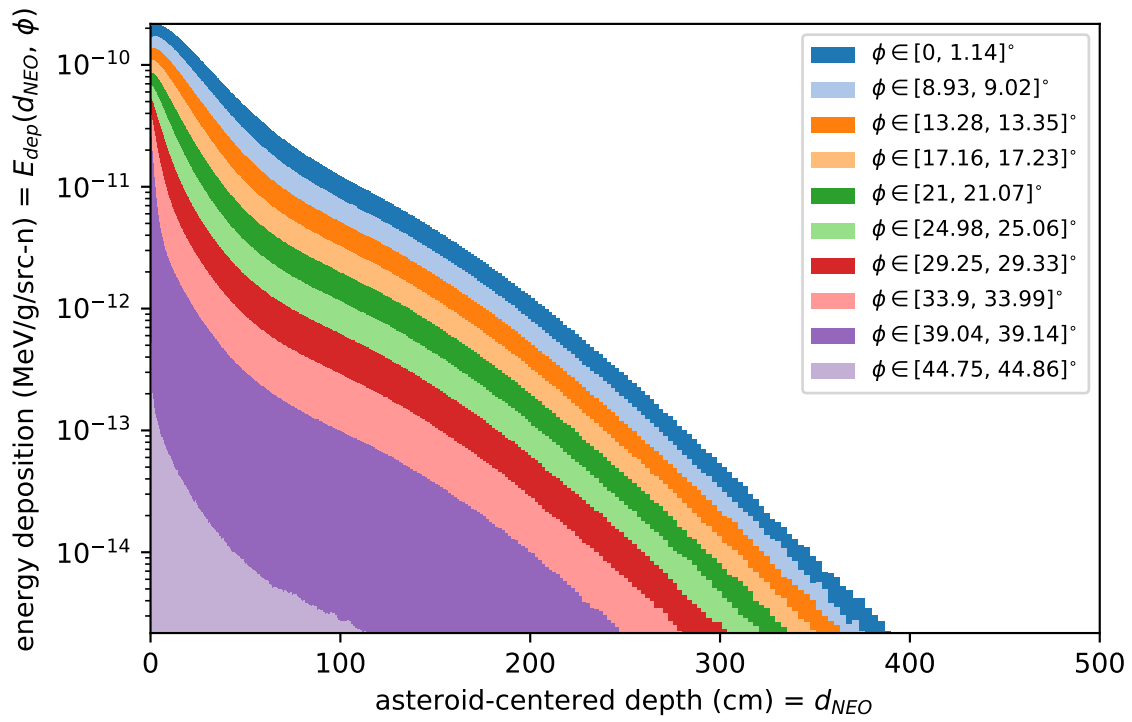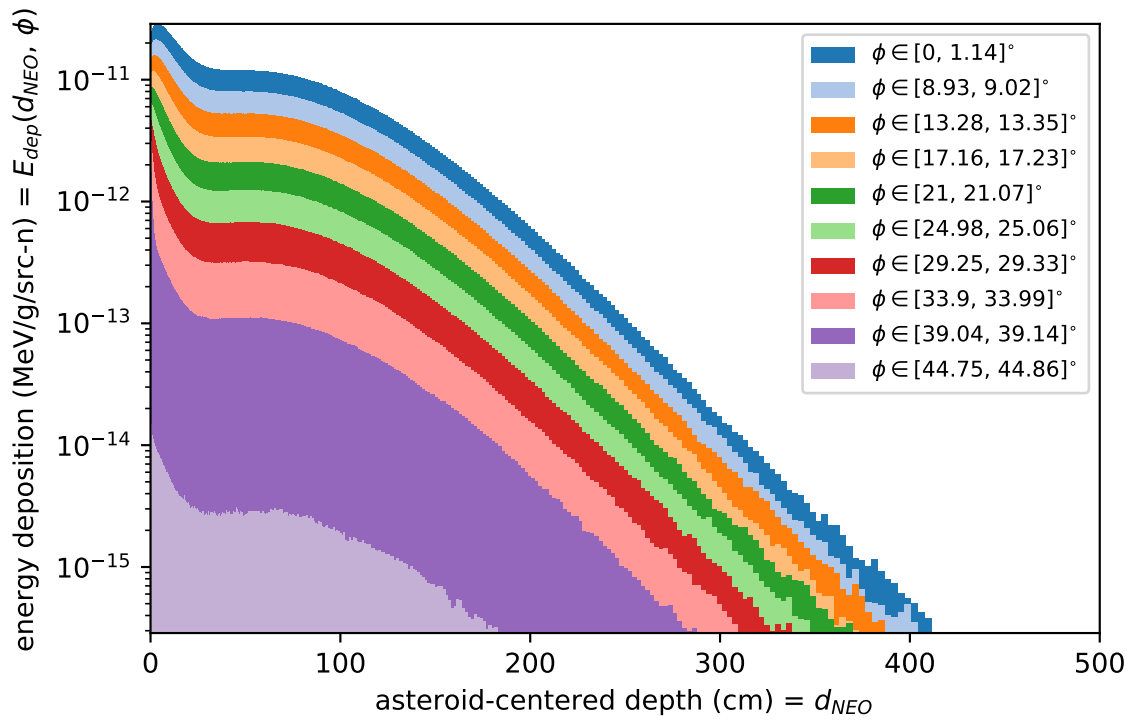
Figure A.10. DPLUS group #9 spatial energy profiles. For this energy group, the lower-boundary is 8.1873×10^0 **MeV** and the upper-boundary is 9.0484×10^0 **MeV. The midpoint or average energy is** 8.6179×10^0 **MeV.**
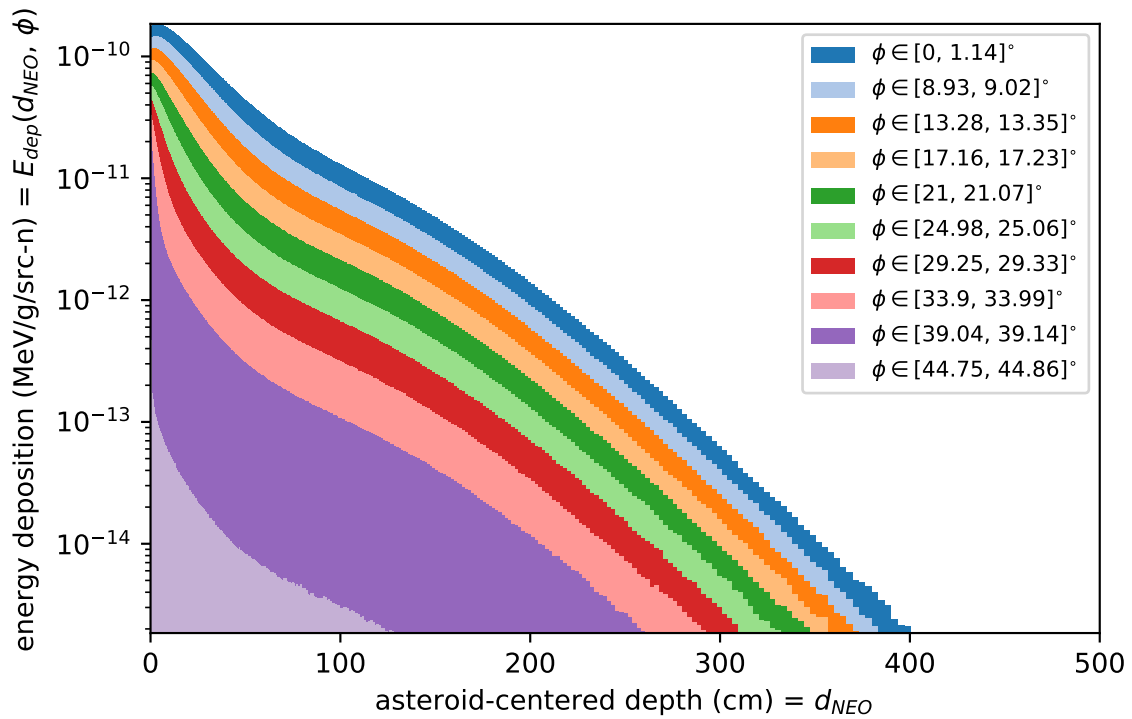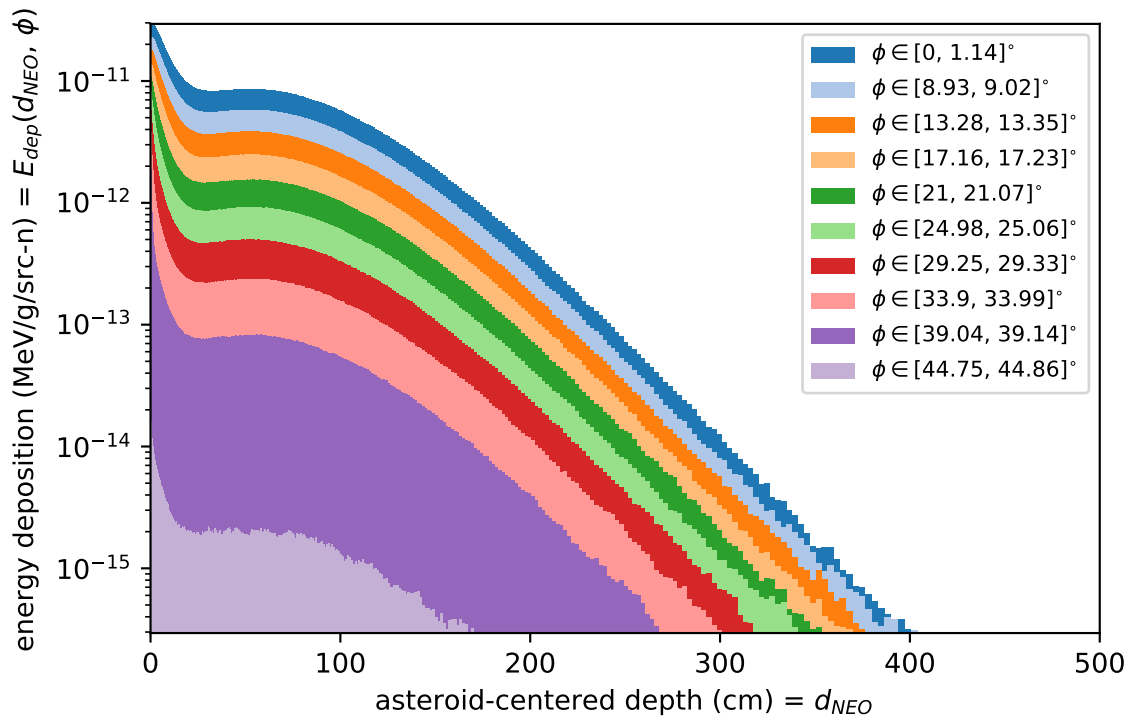
Figure A.11. DPLUS group #10 spatial energy profiles. For this energy group, the lower-boundary is 7.4082×10^0 MeV and the upper-boundary is 8.1873×10^0 MeV. The midpoint or average energy is 7.7978×10^0 MeV.
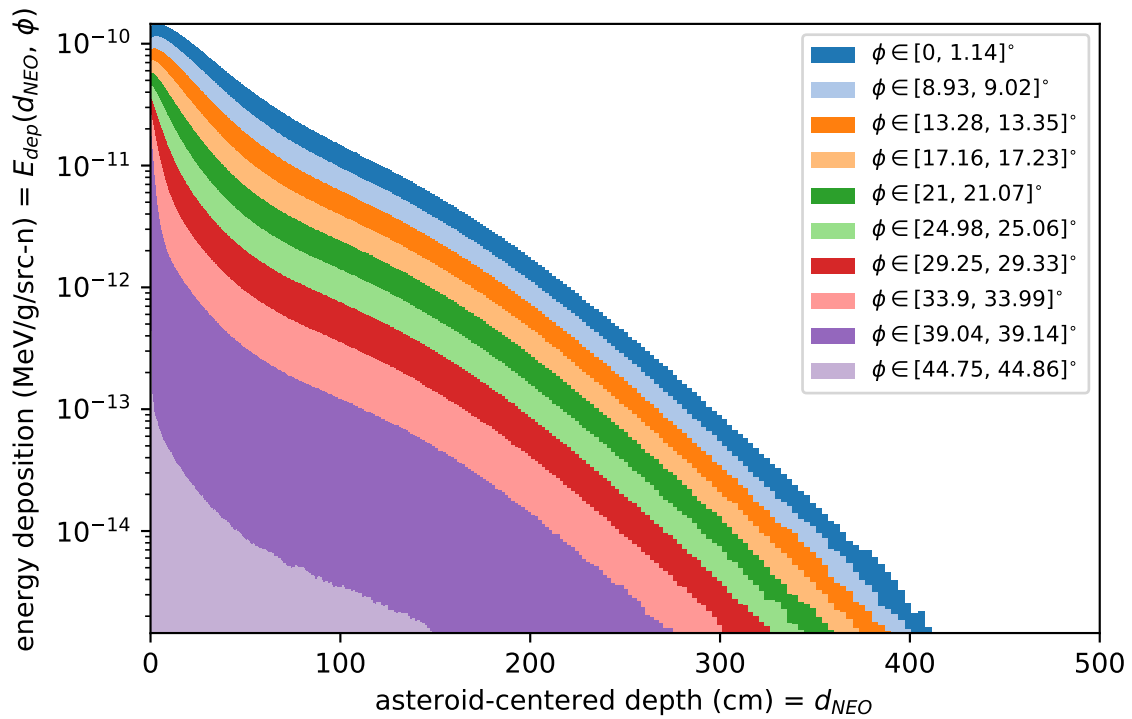
Figure A.12. DPLUS group #11 spatial energy profiles. For this energy group, the lower-boundary is 6.3763×10^0 MeV and the upper-boundary is 7.4082×10^0 MeV. The midpoint or average energy is 6.8922×10^0 MeV.
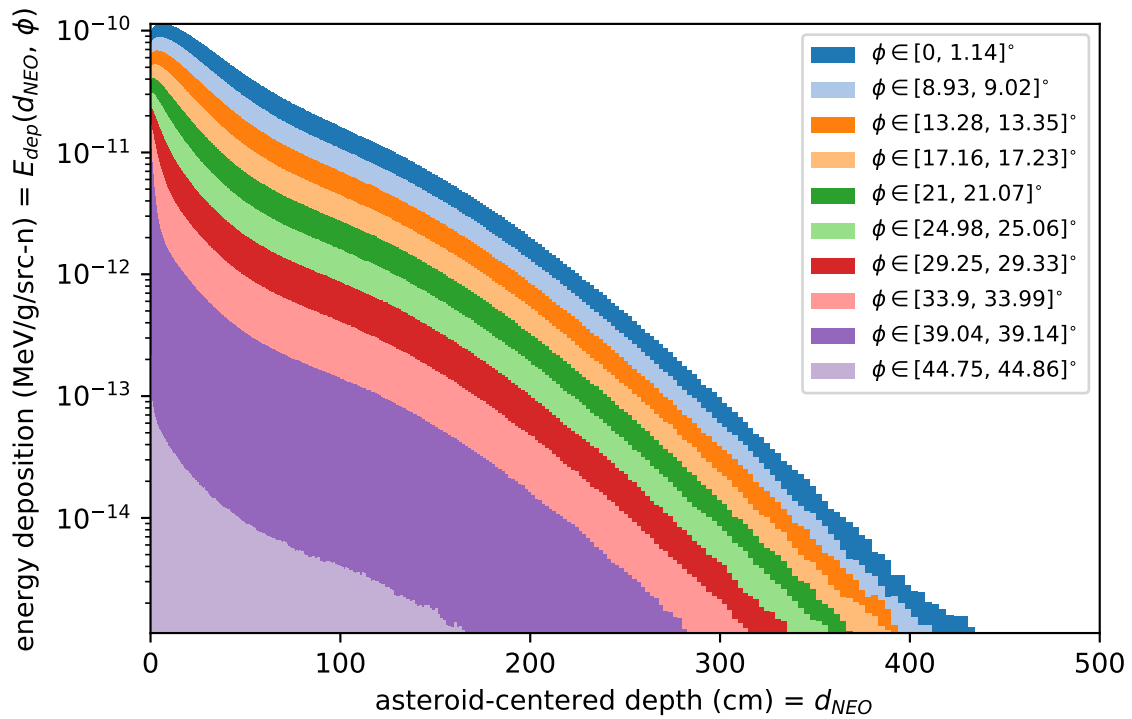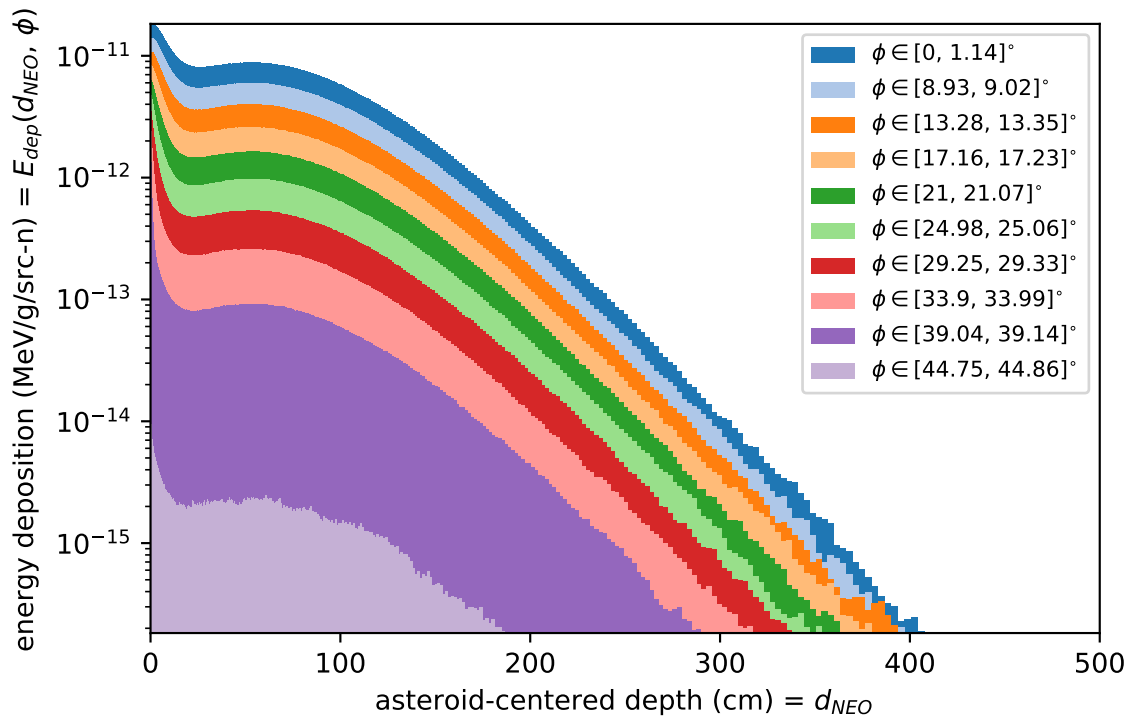
Figure A.13. DPLUS group #12 spatial energy profiles. For this energy group, the lower-boundary is 4.9659×10^0 **MeV** and the upper-boundary is 6.3763×10^0 **MeV. The midpoint or average energy is** 5.6711×10^0 **MeV.**
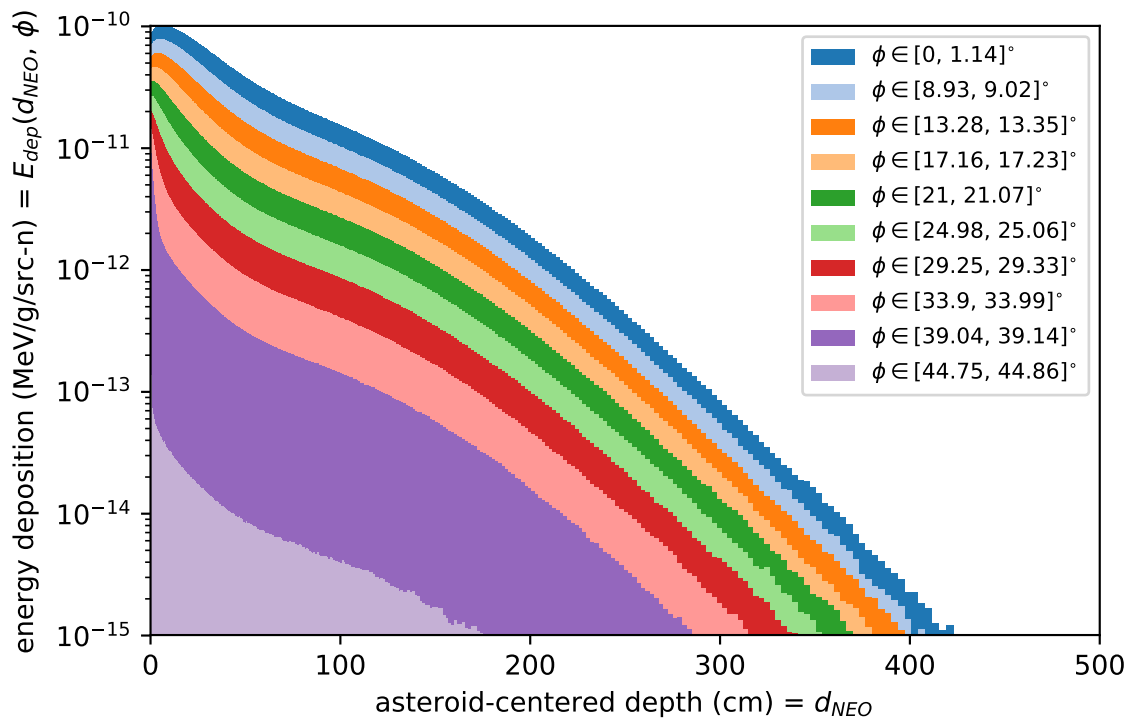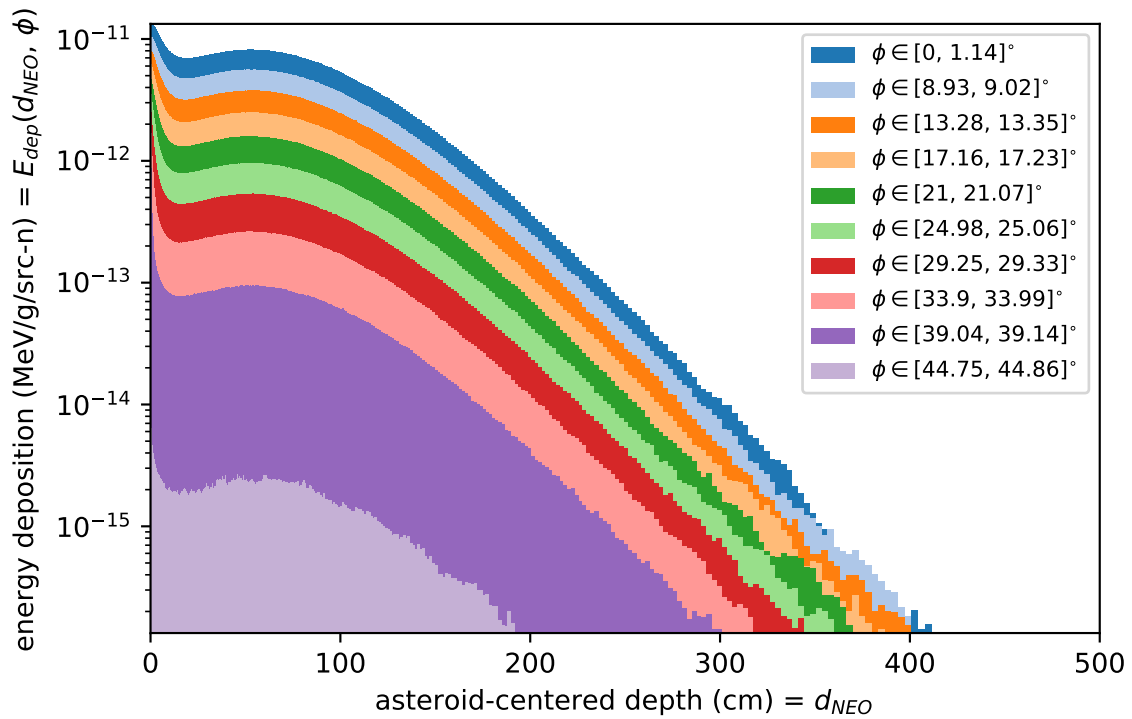
Figure A.14. DPLUS group #13 spatial energy profiles. For this energy group, the lower-boundary is 4.7237×10^0 **MeV** and the upper-boundary is 4.9659×10^0 **MeV. The midpoint or average energy is** 4.8448×10^0 **MeV.**

185
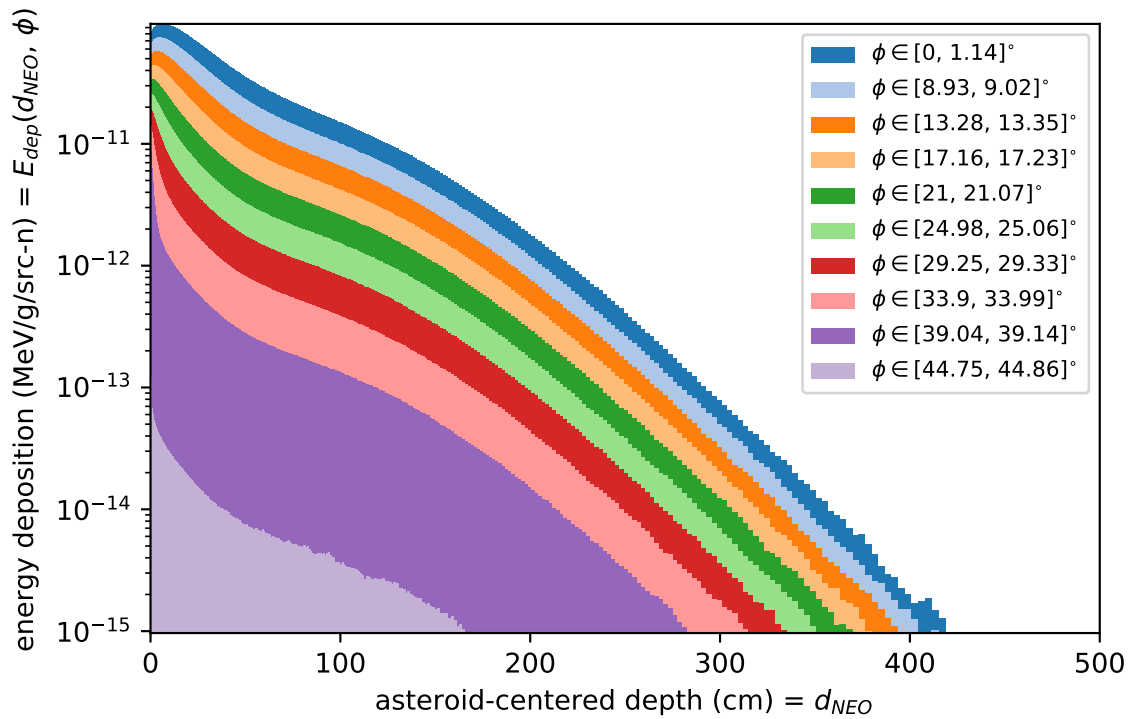
Figure A.15. DPLUS group #14 spatial energy profiles. For this energy group, the lower-boundary is 4.0657×10^0 **MeV** and the upper-boundary is 4.7237×10^0 **MeV. The midpoint or average energy is** 4.3947×10^0 **MeV.**
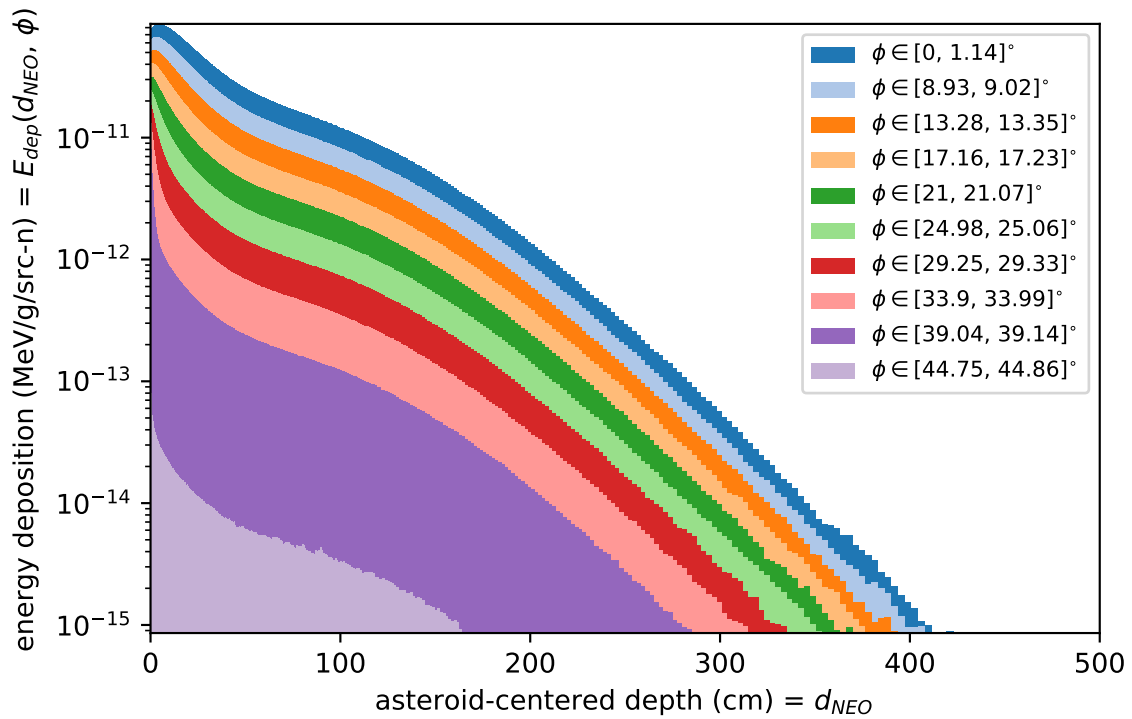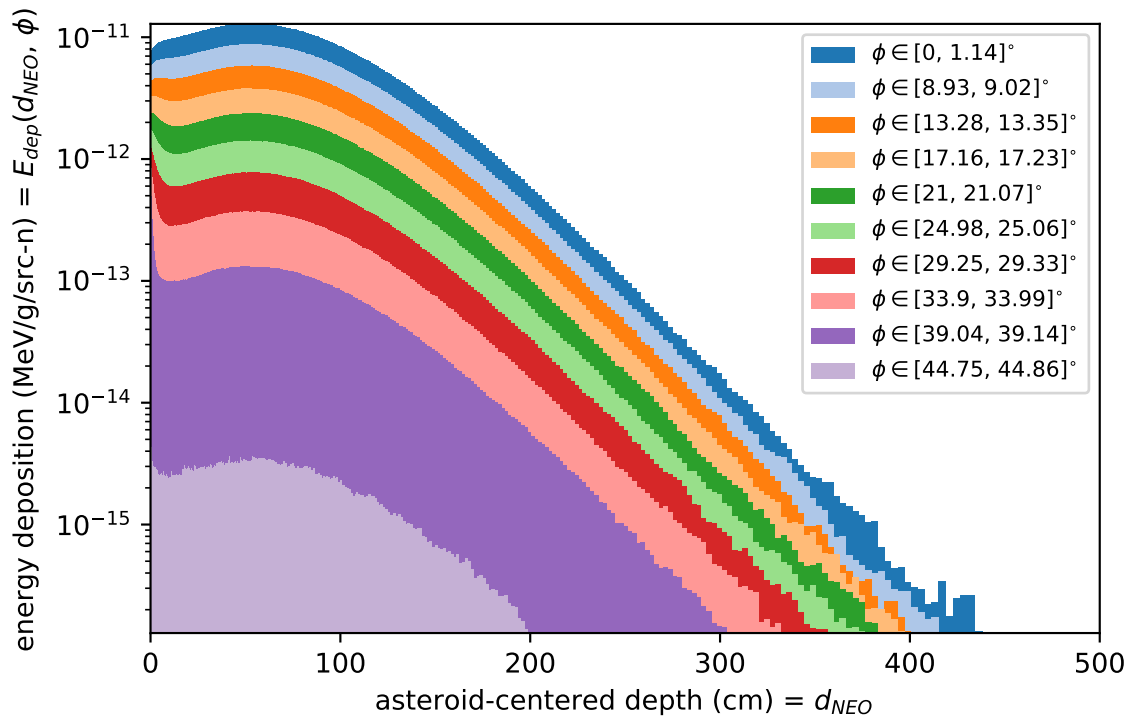
Figure A.16. DPLUS group #15 spatial energy profiles. For this energy group, the lower-boundary is 3.0119×10^0 MeV and the upper-boundary is 4.0657×10^0 MeV. The midpoint or average energy is 3.5388×10^0 MeV.
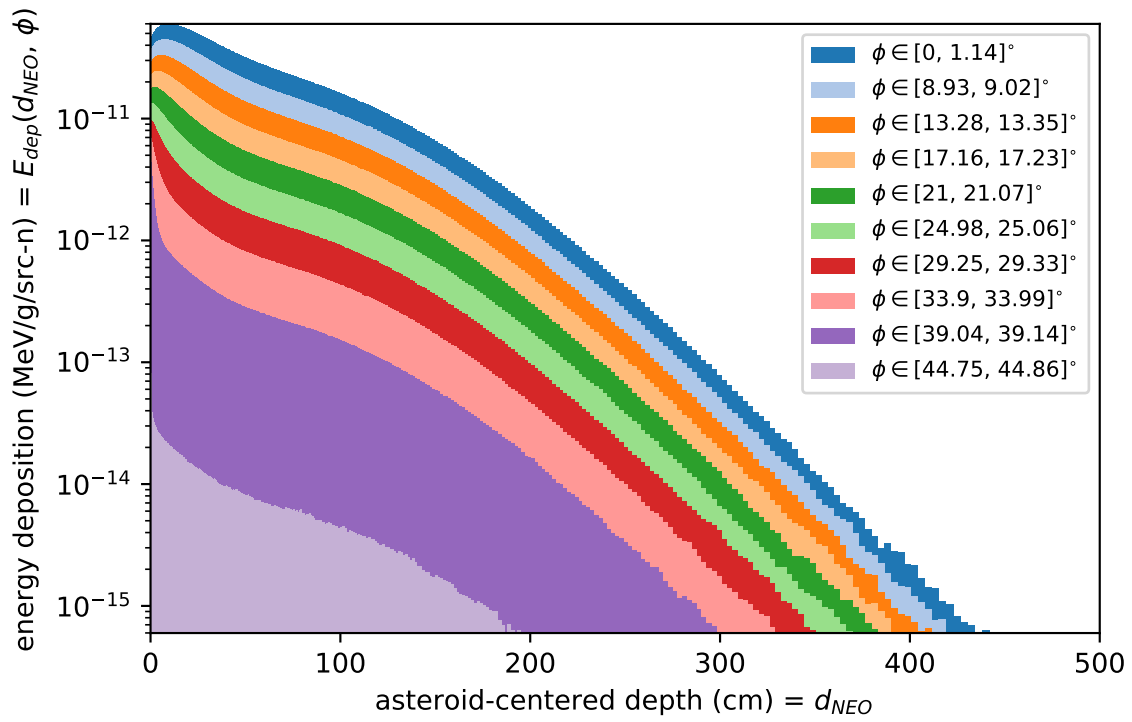
Figure A.17. DPLUS group #16 spatial energy profiles. For this energy group, the lower-boundary is 2.3852×10^0 MeV and the upper-boundary is 3.0119×10^0 MeV. The midpoint or average energy is 2.6986×10^0 MeV.
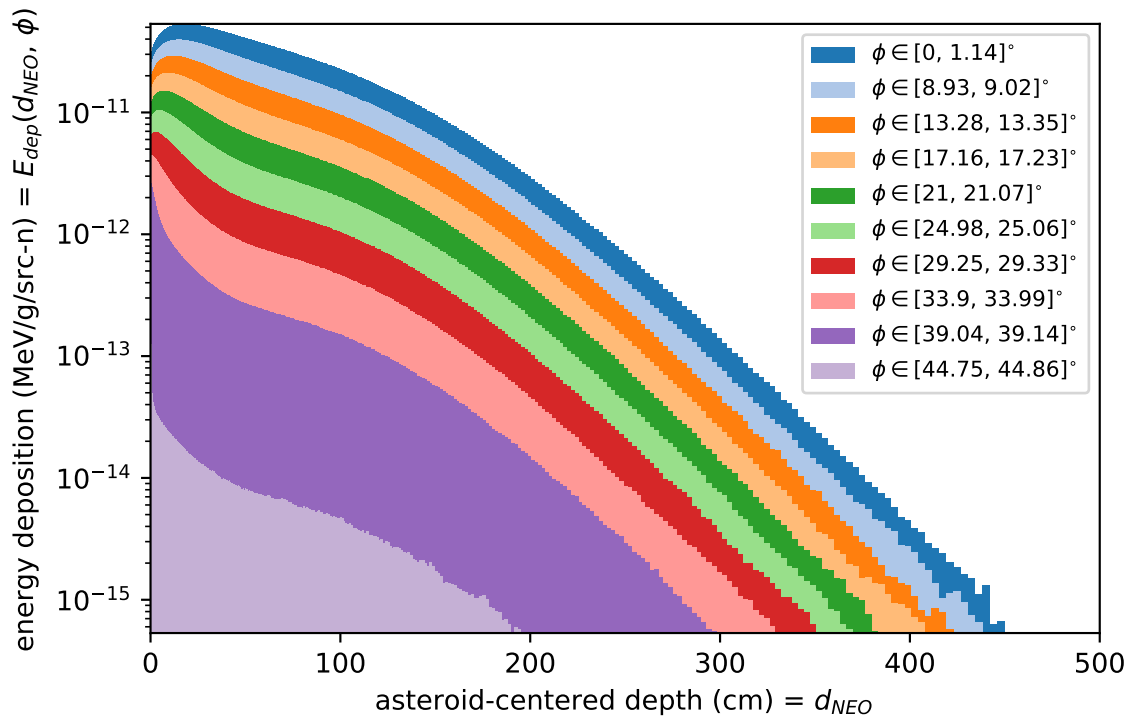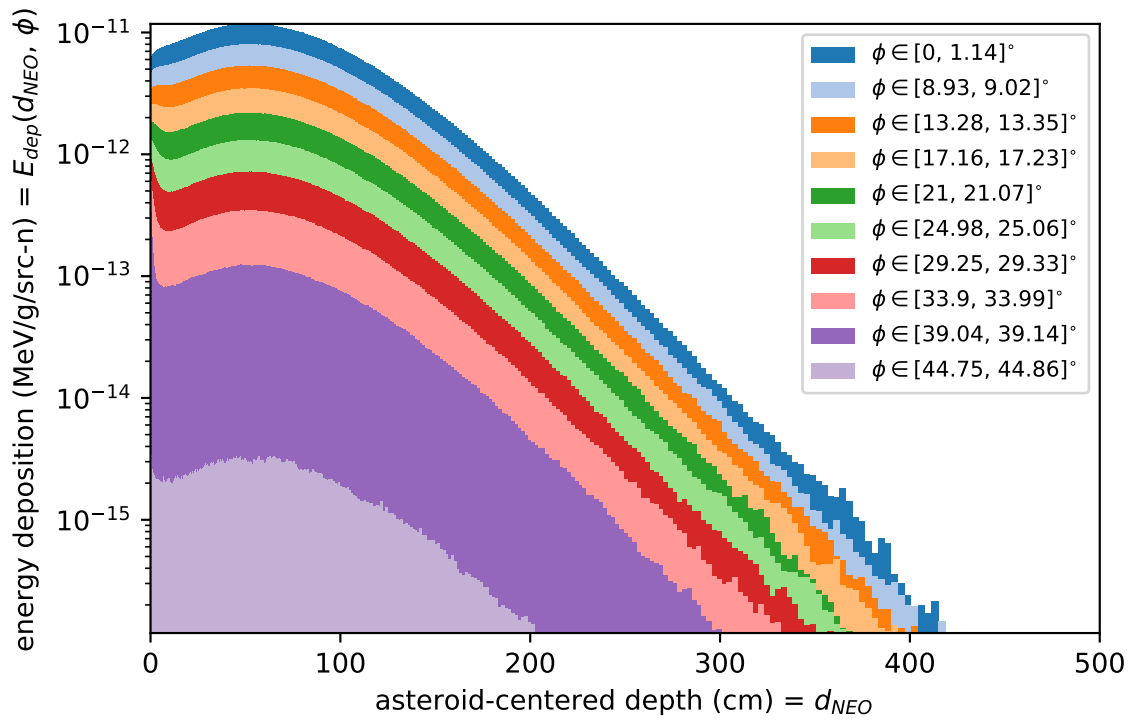
Figure A.18. DPLUS group #17 spatial energy profiles. For this energy group, the lower-boundary is 2.3069×10^0 MeV and the upper-boundary is 2.3852×10^0 MeV. The midpoint or average energy is 2.3460×10^0 MeV.
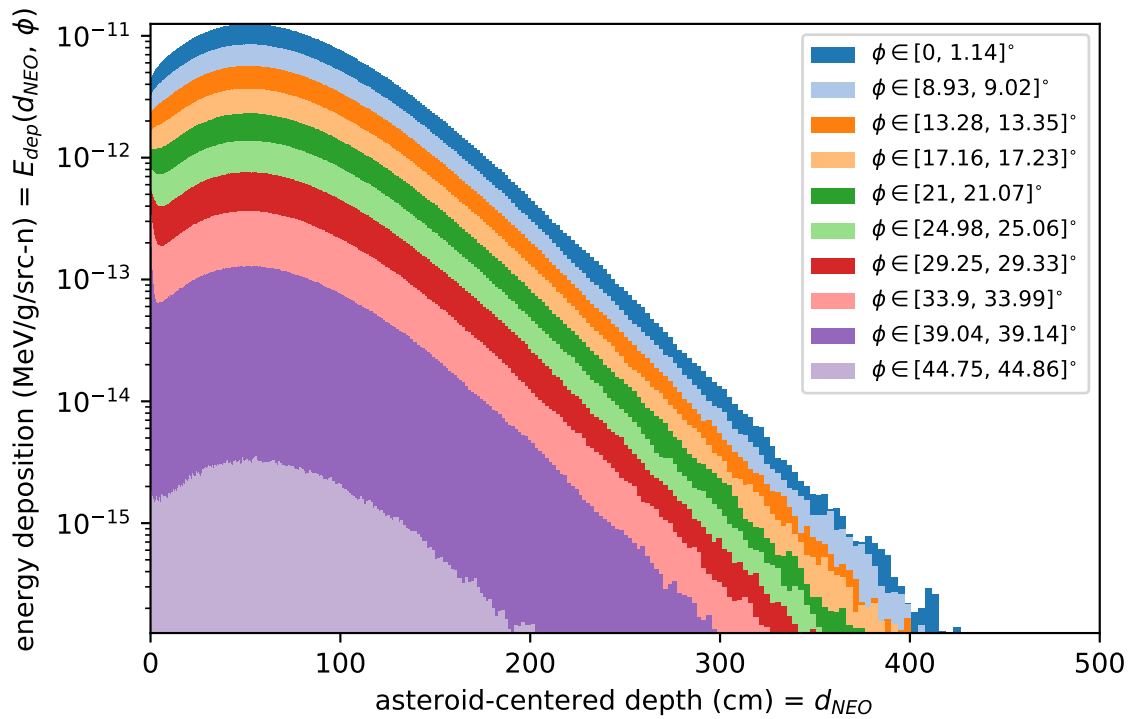
Figure A.19. DPLUS group #18 spatial energy profiles. For this energy group, the lower-boundary is 1.8268×10^0 **MeV and the upper-boundary is** 2.3069×10^0 **MeV. The midpoint or average energy is** 2.0669×10^0 **MeV.**

Figure A.20. DPLUS group #19 spatial energy profiles. For this energy group, the lower-boundary is 1.4227×10^0 MeV and the upper-boundary is 1.8268×10^0 MeV. The midpoint or average energy is 1.6248×10^0 MeV.
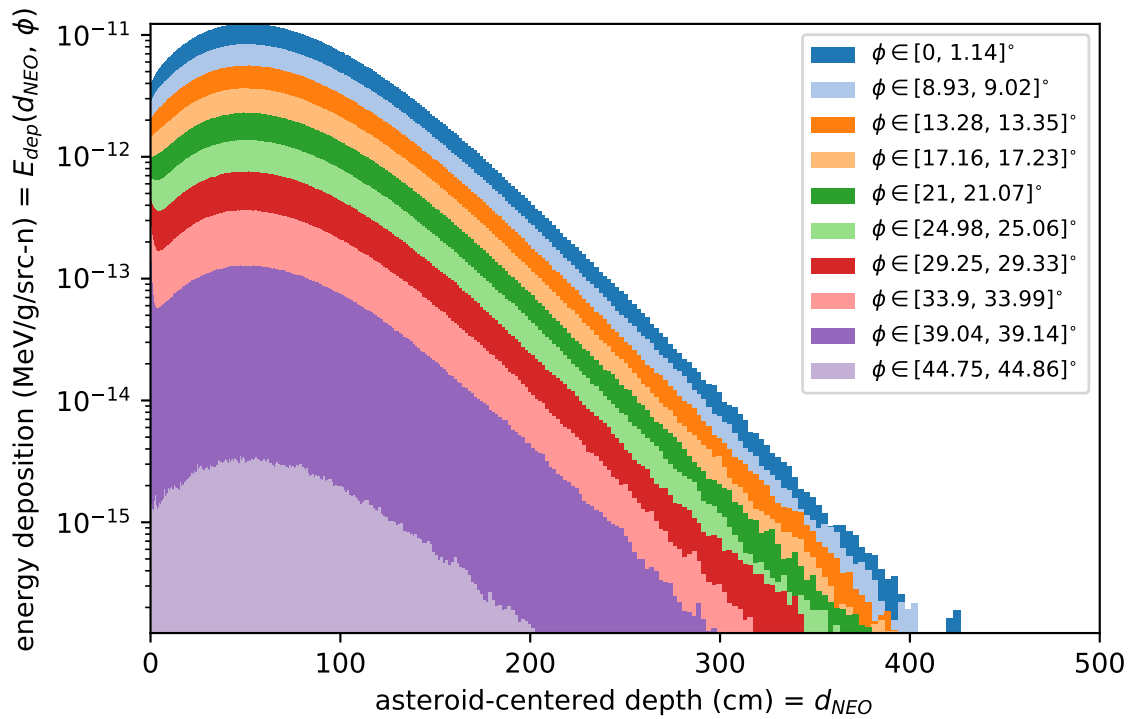
Figure A.21. DPLUS group #20 spatial energy profiles. For this energy group, the lower-boundary is 1.1080×10^0 MeV and the upper-boundary is 1.4227×10^0 MeV. The midpoint or average energy is 1.2654×10^0 MeV.
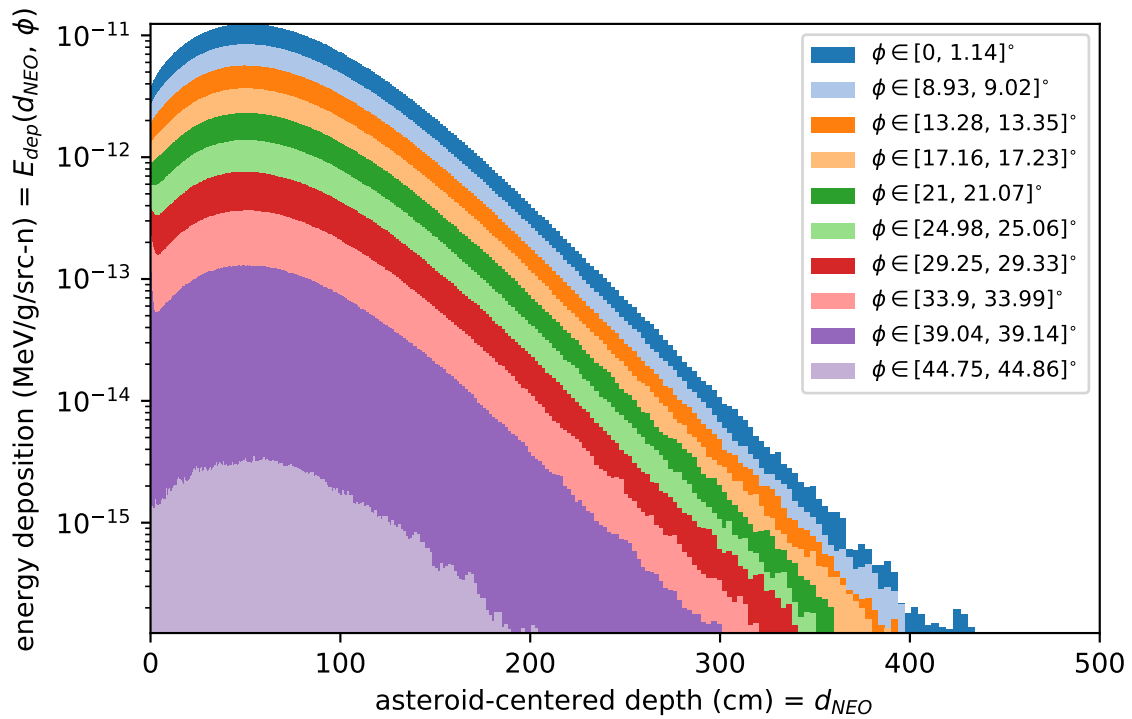
Figure A.22. DPLUS group #21 spatial energy profiles. For this energy group, the lower-boundary is 9.6164×10^{-1} MeV and the upper-boundary is 1.1080×10^0 MeV. The midpoint or average energy is 1.0348×10^0 MeV.

Figure A.23. DPLUS group #22 spatial energy profiles. For this energy group, the lower-boundary is 8.2085×10^{-1} MeV and the upper-boundary is 9.6164×10^{-1} MeV. The midpoint or average energy is 8.9125×10^{-1} MeV.
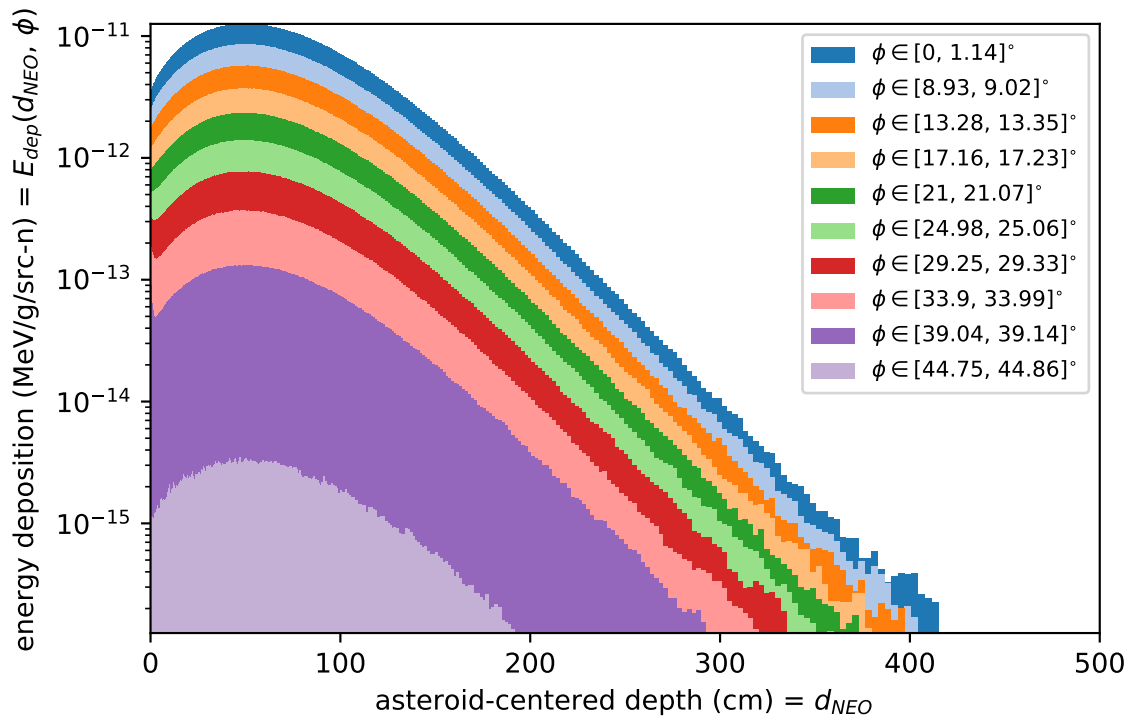
Figure A.24. DPLUS group #23 spatial energy profiles. For this energy group, the lower-boundary is 7.4274×10^{-1} MeV and the upper-boundary is 8.2085×10^{-1} MeV. The midpoint or average energy is 7.8180×10^{-1} MeV.

Figure A.25. DPLUS group #24 spatial energy profiles. For this energy group, the lower-boundary is 6.3928×10^{-1} MeV and the upper-boundary is 7.4274×10^{-1} MeV. The midpoint or average energy is 6.9101×10^{-1} MeV.
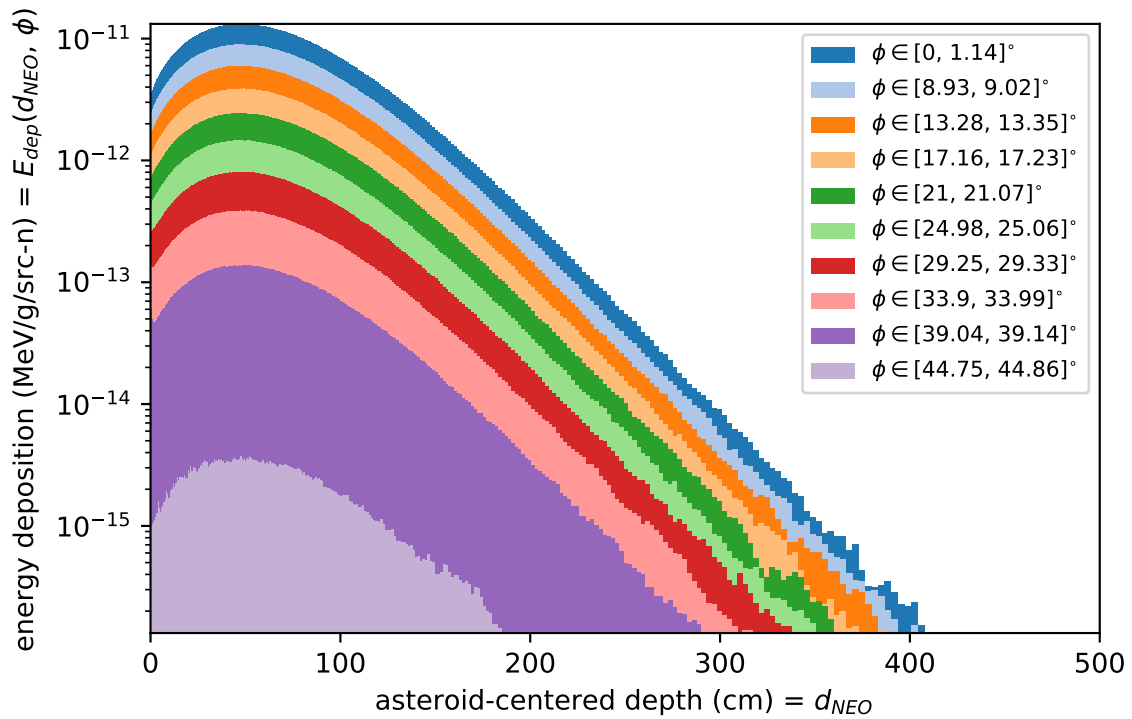
Figure A.26. DPLUS group #25 spatial energy profiles. For this energy group, the lower-boundary is 5.5023×10^{-1} MeV and the upper-boundary is 6.3928×10^{-1} MeV. The midpoint or average energy is 5.9475×10^{-1} MeV.
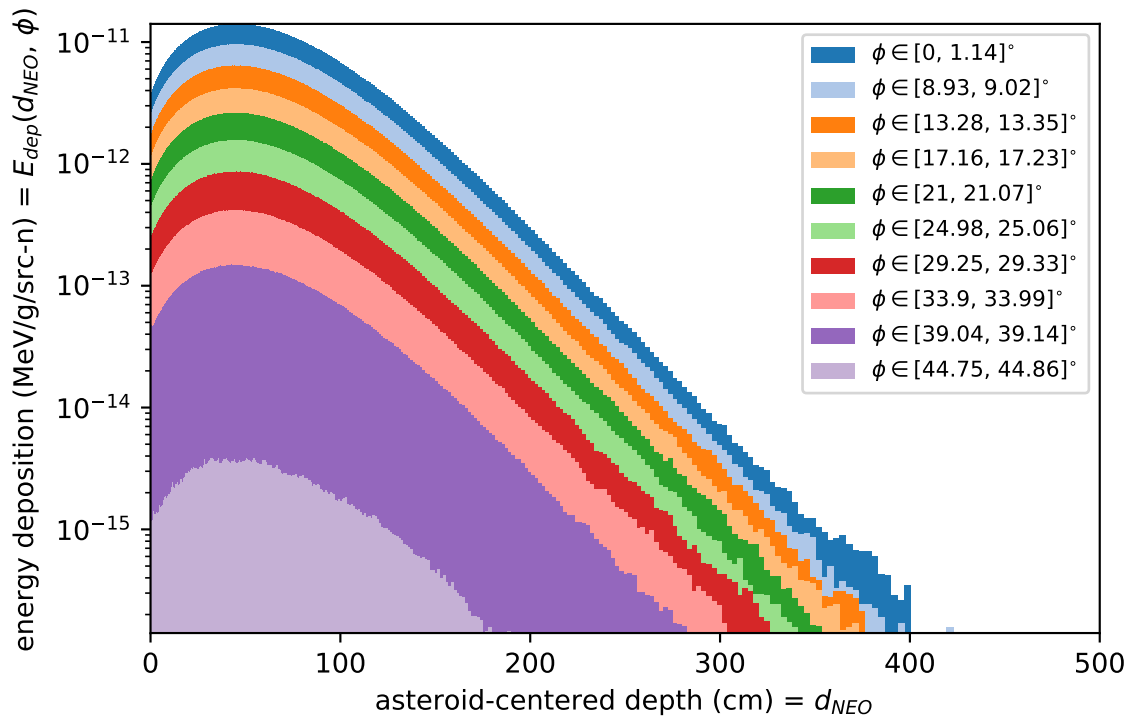
Figure A.27. DPLUS group #26 spatial energy profiles. For this energy group, the lower-boundary is 3.6883×10^{-1} MeV and the upper-boundary is 5.5023×10^{-1} MeV. The midpoint or average energy is 4.5953×10^{-1} MeV.

Figure A.28. DPLUS group #27 spatial energy profiles. For this energy group, the lower-boundary is 2.4724×10^{-1} MeV and the upper-boundary is 3.6883×10^{-1} MeV. The midpoint or average energy is 3.0804×10^{-1} MeV.
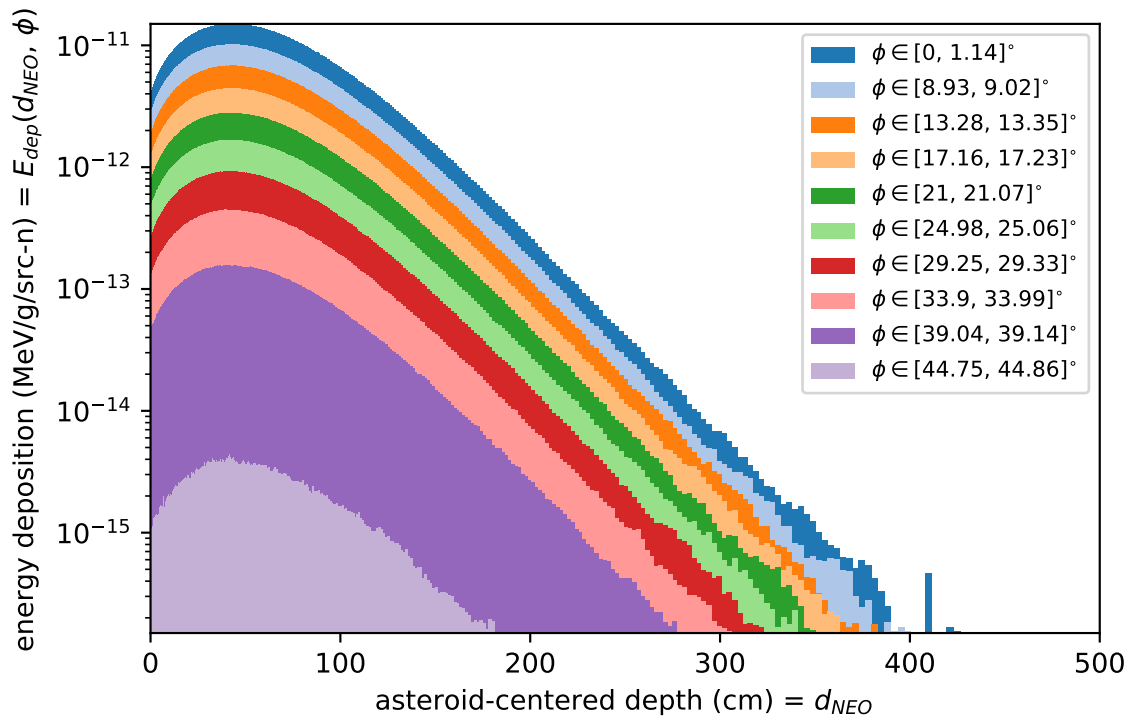
Figure A.29. DPLUS group #28 spatial energy profiles. For this energy group, the lower-boundary is 1.5764×10^{-1} MeV and the upper-boundary is 2.4724×10^{-1} MeV. The midpoint or average energy is 2.0244×10^{-1} MeV.
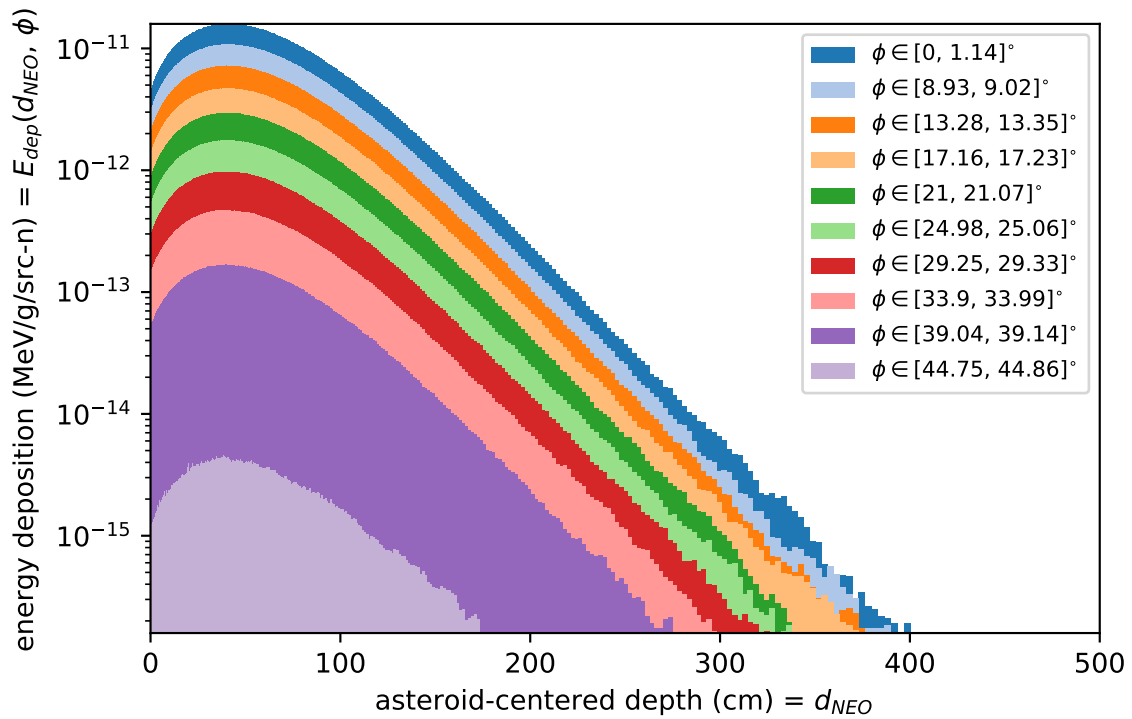
Figure A.30. DPLUS group #29 spatial energy profiles. For this energy group, the lower-boundary is 1.1109×10^{-1} MeV and the upper-boundary is 1.5764×10^{-1} MeV. The midpoint or average energy is 1.3437×10^{-1} MeV.

201

Figure A.31. DPLUS group #30 spatial energy profiles. For this energy group, the lower-boundary is 5.2475×10^{-2} MeV and the upper-boundary is 1.1109×10^{-1} MeV. The midpoint or average energy is 8.1782×10^{-2} MeV.
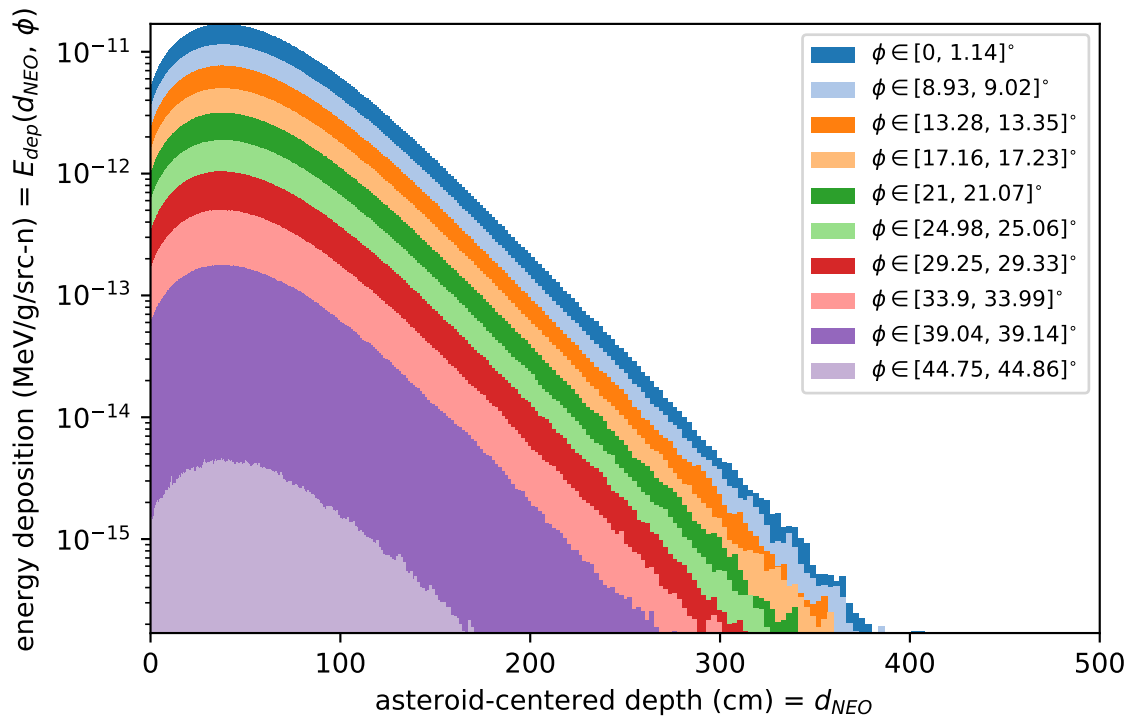
Figure A.32. DPLUS group #31 spatial energy profiles. For this energy group, the lower-boundary is 3.4307×10^{-2} MeV and the upper-boundary is 5.2475×10^{-2} MeV. The midpoint or average energy is 4.3391×10^{-2} MeV.
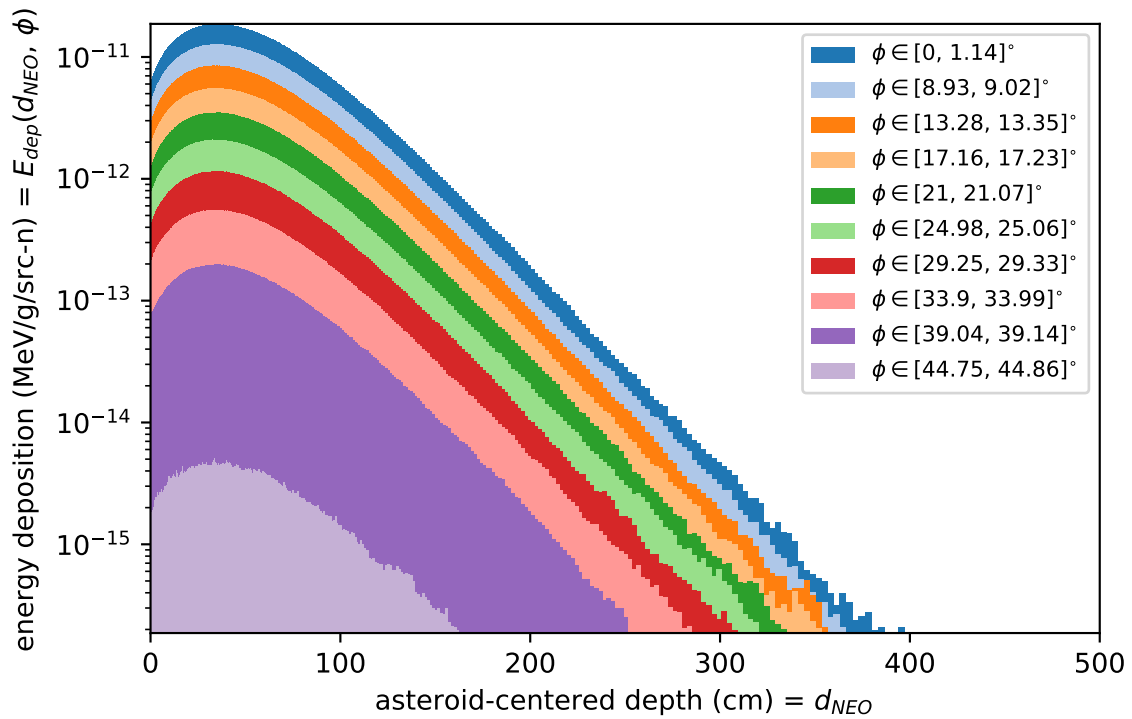
Figure A.33. DPLUS group #32 spatial energy profiles. For this energy group, the lower-boundary is 2.4788×10^{-2} MeV and the upper-boundary is 3.4307×10^{-2} MeV. The midpoint or average energy is 2.9547×10^{-2} MeV.

Figure A.34. DPLUS group #33 spatial energy profiles. For this energy group, the lower-boundary is 2.1875×10^{-2} MeV and the upper-boundary is 2.4788×10^{-2} MeV. The midpoint or average energy is 2.3331×10^{-2} MeV.
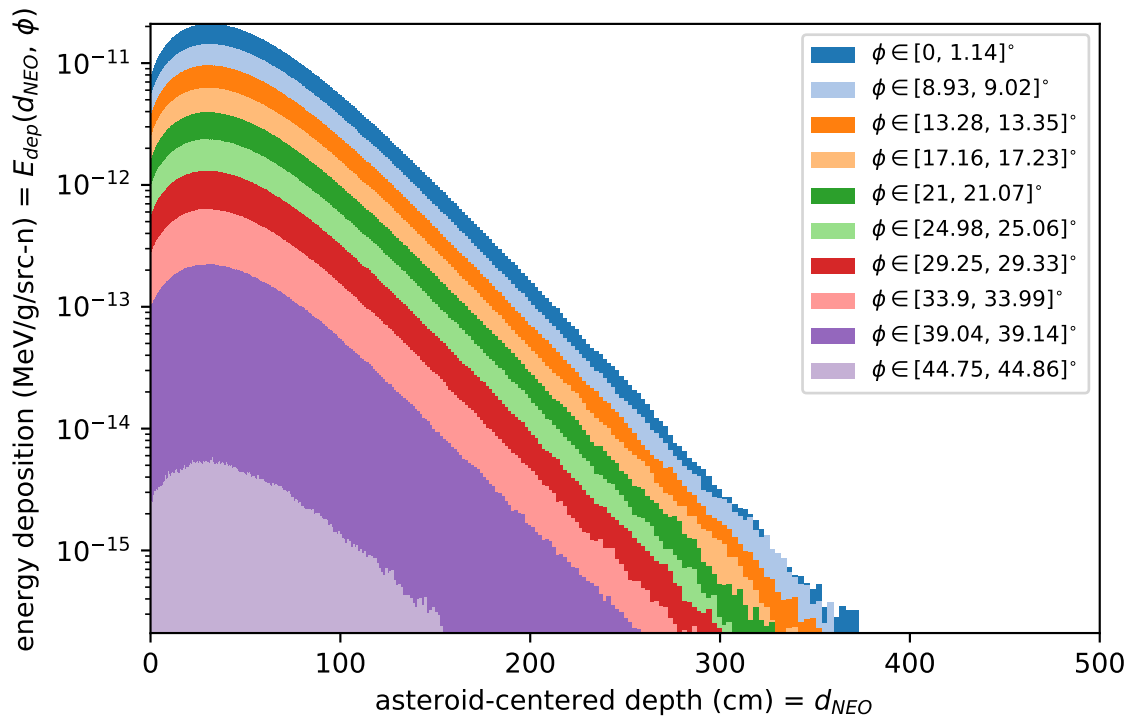
Figure A.35. DPLUS group #34 spatial energy profiles. For this energy group, the lower-boundary is 1.0333×10^{-2} MeV and the upper-boundary is 2.1875×10^{-2} MeV. The midpoint or average energy is 1.6104×10^{-2} MeV.

Figure A.36. DPLUS group #35 spatial energy profiles. For this energy group, the lower-boundary is 3.3546×10^{-3} MeV and the upper-boundary is 1.0333×10^{-2} MeV. The midpoint or average energy is 6.8438×10^{-3} MeV.
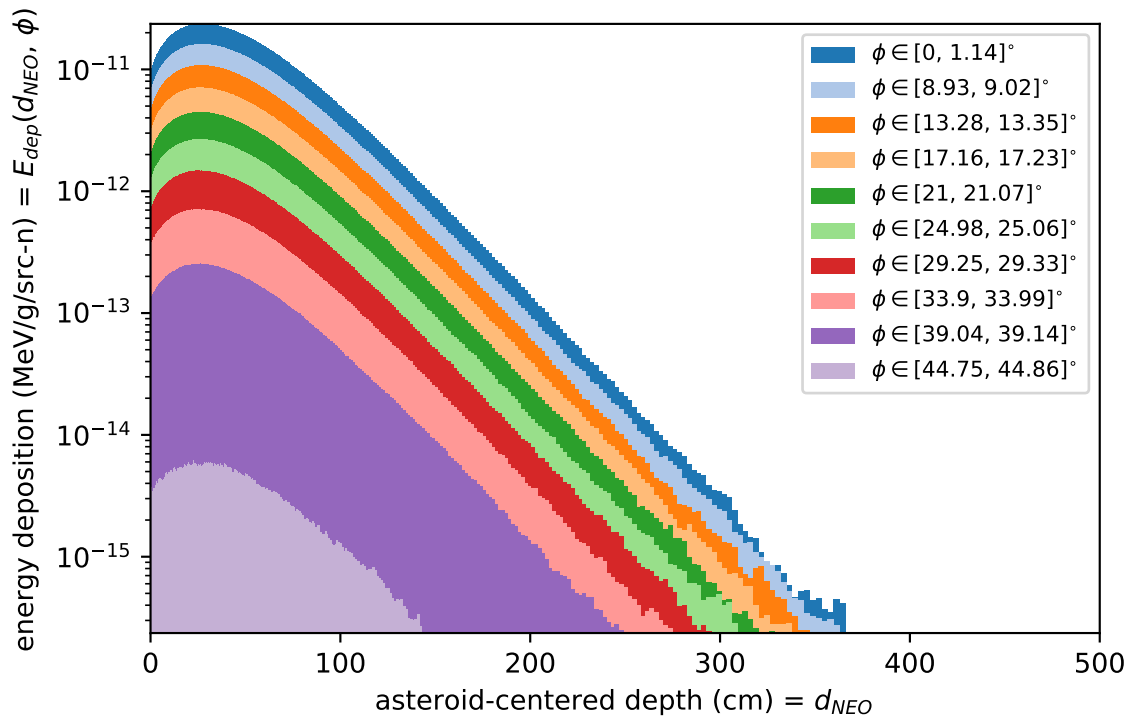
Figure A.37. DPLUS group #36 spatial energy profiles. For this energy group, the lower-boundary is 1.2341×10^{-3} MeV and the upper-boundary is 3.3546×10^{-3} MeV. The midpoint or average energy is 2.2944×10^{-3} MeV.
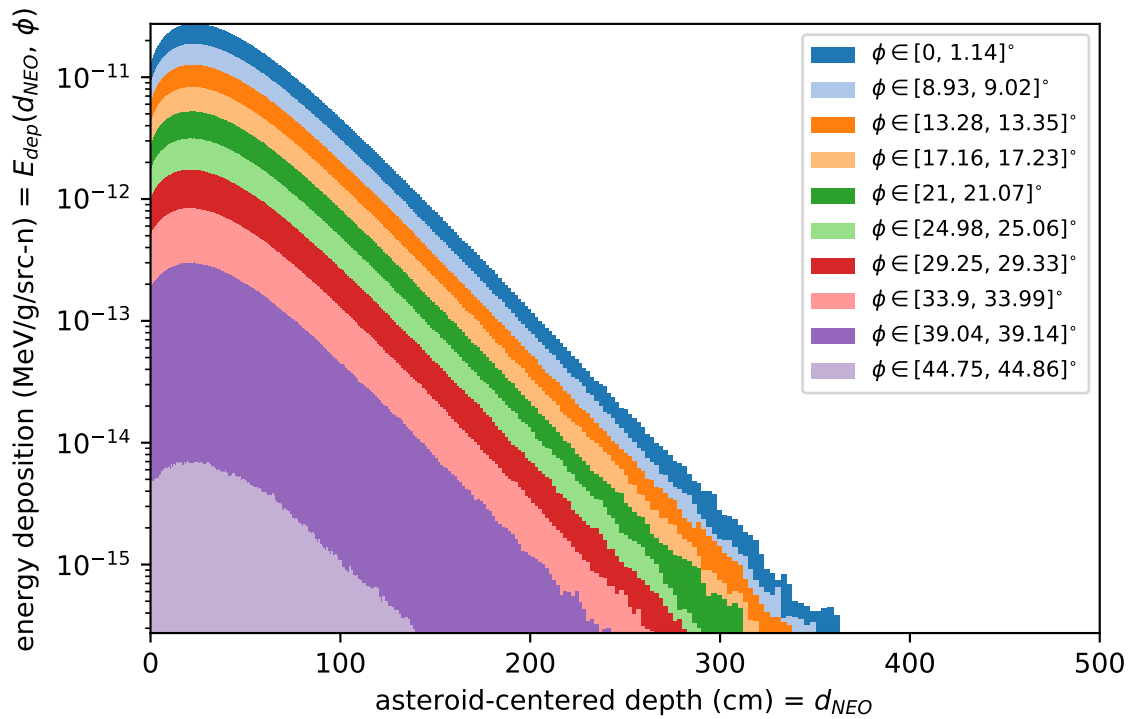
Figure A.38. DPLUS group #37 spatial energy profiles. For this energy group, the lower-boundary is 5.8295×10^{-4} MeV and the upper-boundary is 1.2341×10^{-3} MeV. The midpoint or average energy is 9.0852×10^{-4} MeV.

Figure A.39. DPLUS group #38 spatial energy profiles. For this energy group, the lower-boundary is 2.7536×10^{-4} MeV and the upper-boundary is 5.8295×10^{-4} MeV. The midpoint or average energy is 4.2916×10^{-4} MeV.
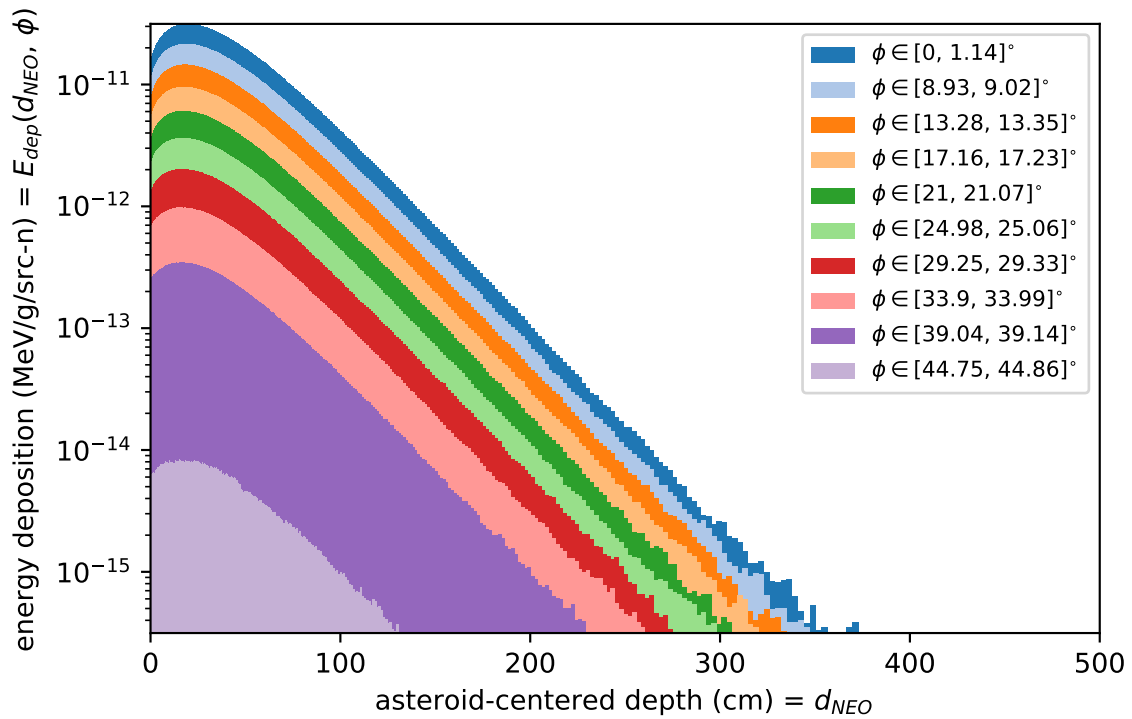
Figure A.40. DPLUS group #39 spatial energy profiles. For this energy group, the lower-boundary is 1.0130×10^{-4} MeV and the upper-boundary is 2.7536×10^{-4} MeV. The midpoint or average energy is 1.8833×10^{-4} MeV.
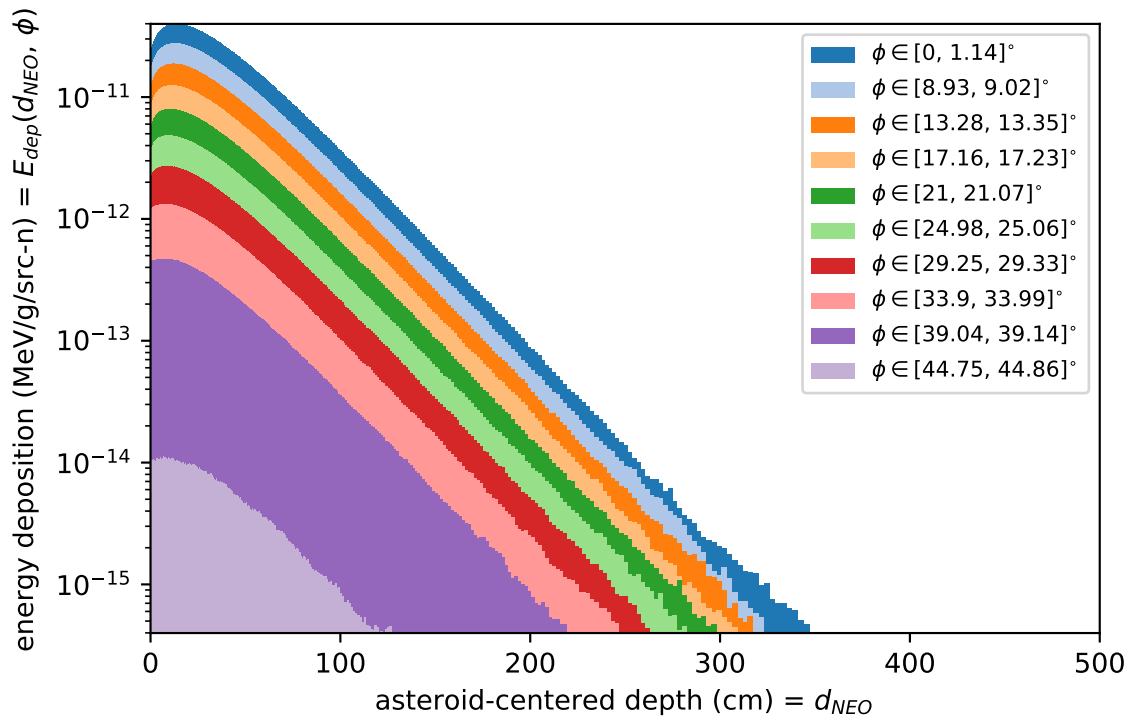
Figure A.41. DPLUS group #40 spatial energy profiles. For this energy group, the lower-boundary is 2.9023×10^{-5} MeV and the upper-boundary is 1.0130×10^{-4} MeV. The midpoint or average energy is 6.5162×10^{-5} MeV.

Figure A.42. DPLUS group #41 spatial energy profiles. For this energy group, the lower-boundary is 1.0677×10^{-5} MeV and the upper-boundary is 2.9023×10^{-5} MeV. The midpoint or average energy is 1.9850×10^{-5} MeV.

Figure A.43. DPLUS group #42 spatial energy profiles. For this energy group, the lower-boundary is 3.0590×10^{-6} MeV and the upper-boundary is 1.0677×10^{-5} MeV. The midpoint or average energy is 6.8680×10^{-6} MeV.

Figure A.44. DPLUS group #43 spatial energy profiles. For this energy group, the lower-boundary is 1.1253×10^{-6} MeV and the upper-boundary is 3.0590×10^{-6} MeV. The midpoint or average energy is 2.0921×10^{-6} MeV.

Figure A.45. DPLUS group #44 spatial energy profiles. For this energy group, the lower-boundary is 4.1399×10^{-7} MeV and the upper-boundary is 1.1253×10^{-6} MeV. The midpoint or average energy is 7.6964×10^{-7} MeV.

Figure A.46. DPLUS group #45 spatial energy profiles. For this energy group, the lower-boundary is 1.0000×10^{-11} MeV and the upper-boundary is 4.1399×10^{-7} MeV. The midpoint or average energy is 2.0700×10^{-7} MeV.

A.2 DPLUS Energy Coupling Efficiencies

Presented below in this section, Table A.1 contains a large amount of information pertaining to energy coupling efficiencies for each of the 46 DPLUS energy groups. The first few columns contain the energy structure of the DPLUS bins themselves, where E_{low}, E_{high}, and E_{mid} are the lower-bound, upper-bound, and midpoint energies for each group in MeV, respectively. Because each of these energy bins were sampled uniformly, E_{mid} is the same as the average neutron energy for each group. Note that $E_{mid} = Y_n$ if Y_n is defined to be a normalized neutron yield with units of MeV/src-n. The neutron energy E_n in Equation 1.1 is identical to this definition of a normalized Y_n.

Y_{int} is the intercepted yield from Equation 3.13, or the amount of energy that intersects and reaches the asteroid based on the $c \approx 0.414$ stand-off distance, in MeV/src-n. The fractional solid angle for this HOB is $\sim$0.1464, meaning that about 14.64% of the neutrons from the isotropic stand-off detonation are headed towards, and reach, the asteroid target. The values in the Y_{int} column of Table A.1 are simply the E_{mid} or Y_n values multiplied by $\sim$0.1464.

E_{dep} is the total amount of energy deposited in the asteroid in MeV/src-n. This is calculated by taking the cell union total MeV/g/src-n E_{dep} from all the MCNP6.2 +F6 tallies and then multiplying by the total mass of all the tallied cells.

η_{rel} and η_{abs} are the relative and absolute energy coupling efficiencies from Equation 3.12 and Equation 3.14, respectively. η_{rel} is E_{dep} divided by Y_{int}, while η_{abs} is E_{dep} divided by Y_n. η_{rel} will always be less than η_{abs} for a stand-off nuclear detonation. When $\eta_{rel} > 1$, it is explicitly known that the energy deposition contributions from secondary particles or photons provided a bonus to energy coupling.

As seen in Table A.1, as the energy levels of the source neutrons decrease, the energy coupling efficiencies into the SiO$_2$ asteroid target generally increase. There

218

are a few small exceptions to this — for example, group #17 has $\eta_{rel} = 1.5658$ resulting from its $Y_n = 2.3460$ MeV, while group #18 has $\eta_{rel} = 1.2143$ resulting from its $Y_n = 2.0669$ MeV. In general, however, the energy coupling efficiency is inversely proportional to neutron energy.

Note that the lowest energy group #45 has an energy coupling value in the millions, $\eta_{rel} = 7.6419 \times 10^6$. While incredibly large, this is perhaps to be expected. The average source energy for this group is $Y_n = 0.207$ eV. At this energy level in a SiO_2 medium, the only nuclear reaction channels that are open are elastic scattering and exothermic radiative capture, as seen in Figures 2.5a and 2.6a. The energy of the secondary gamma-rays that are produced from (n,γ) capture reactions are close to 8.474 MeV and 4.143 MeV for ^{28}Si and ^{16}O, respectively. That is, 0.207 eV neutrons interact with silicon and oxygen nuclei in such a way that gamma-rays in the MeV regime are generated. This energy difference between the incident neutrons and the secondary gamma-rays is in the millions, and thus it is not much surprise that η_{rel} is also in the millions.

Table A.1. Energy coupling efficiencies for all 46 DPLUS energy groups. E_{low}, E_{high}, and E_{mid} are the lower-bound, upper-bound, and midpoint (average) energies in MeV for each group. $E_{mid} = Y_n$ for a normalized neutron yield with units of MeV/src-n (this is E_n in Equation 1.1). Y_{int} is the intercepted yield from Equation 3.13, or the amount of energy that intersects and reaches the asteroid target based on the $c \approx 0.414$ standoff distance, in MeV/src-n. E_{dep} is the total amount of energy deposited in the asteroid in MeV/src-n. η_{rel} and η_{abs} are the relative and absolute energy coupling efficiencies from Equation 3.12 and Equation 3.14, respectively. η_{rel} is E_{dep} divided by Y_{int}, while η_{abs} is E_{dep} divided by Y_n.

Group #	E_{low}	E_{high}	$E_{mid} = Y_n$	Y_{int}	E_{dep}	η_{rel}	η_{abs}
0	$1.6905 \cdot 10^1$	$1.9640 \cdot 10^1$	$1.8273 \cdot 10^1$	$2.6759 \cdot 10^0$	$1.6663 \cdot 10^0$	$6.2271 \cdot 10^{-1}$	$9.1194 \cdot 10^{-2}$
1	$1.4918 \cdot 10^1$	$1.6905 \cdot 10^1$	$1.5912 \cdot 10^1$	$2.3302 \cdot 10^0$	$1.5208 \cdot 10^0$	$6.5264 \cdot 10^{-1}$	$9.5576 \cdot 10^{-2}$
2	$1.4191 \cdot 10^1$	$1.4918 \cdot 10^1$	$1.4555 \cdot 10^1$	$2.1315 \cdot 10^0$	$1.4447 \cdot 10^0$	$6.7780 \cdot 10^{-1}$	$9.9262 \cdot 10^{-2}$
3	$1.3840 \cdot 10^1$	$1.4191 \cdot 10^1$	$1.4015 \cdot 10^1$	$2.0525 \cdot 10^0$	$1.4130 \cdot 10^0$	$6.8844 \cdot 10^{-1}$	$1.0082 \cdot 10^{-1}$
4	$1.2523 \cdot 10^1$	$1.3840 \cdot 10^1$	$1.3181 \cdot 10^1$	$1.9304 \cdot 10^0$	$1.3696 \cdot 10^0$	$7.0952 \cdot 10^{-1}$	$1.0391 \cdot 10^{-1}$
5	$1.2214 \cdot 10^1$	$1.2523 \cdot 10^1$	$1.2369 \cdot 10^1$	$1.8113 \cdot 10^0$	$1.3026 \cdot 10^0$	$7.1917 \cdot 10^{-1}$	$1.0532 \cdot 10^{-1}$
6	$1.1052 \cdot 10^1$	$1.2214 \cdot 10^1$	$1.1633 \cdot 10^1$	$1.7036 \cdot 10^0$	$1.2040 \cdot 10^0$	$7.0676 \cdot 10^{-1}$	$1.0350 \cdot 10^{-1}$
7	$1.0000 \cdot 10^1$	$1.1052 \cdot 10^1$	$1.0526 \cdot 10^1$	$1.5415 \cdot 10^0$	$1.1329 \cdot 10^0$	$7.3491 \cdot 10^{-1}$	$1.0763 \cdot 10^{-1}$
8	$9.0484 \cdot 10^0$	$1.0000 \cdot 10^1$	$9.5242 \cdot 10^0$	$1.3948 \cdot 10^0$	$1.0486 \cdot 10^0$	$7.5181 \cdot 10^{-1}$	$1.1010 \cdot 10^{-1}$
9	$8.1873 \cdot 10^0$	$9.0484 \cdot 10^0$	$8.6179 \cdot 10^0$	$1.2621 \cdot 10^0$	$9.4784 \cdot 10^{-1}$	$7.5103 \cdot 10^{-1}$	$1.0999 \cdot 10^{-1}$
10	$7.4082 \cdot 10^0$	$8.1873 \cdot 10^0$	$7.7978 \cdot 10^0$	$1.1420 \cdot 10^0$	$8.6316 \cdot 10^{-1}$	$7.5586 \cdot 10^{-1}$	$1.1069 \cdot 10^{-1}$
11	$6.3763 \cdot 10^0$	$7.4082 \cdot 10^0$	$6.8922 \cdot 10^0$	$1.0093 \cdot 10^0$	$7.8290 \cdot 10^{-1}$	$7.7565 \cdot 10^{-1}$	$1.1359 \cdot 10^{-1}$
12	$4.9659 \cdot 10^0$	$6.3763 \cdot 10^0$	$5.6711 \cdot 10^0$	$8.3051 \cdot 10^{-1}$	$6.9965 \cdot 10^{-1}$	$8.4243 \cdot 10^{-1}$	$1.2337 \cdot 10^{-1}$
13	$4.7237 \cdot 10^0$	$4.9659 \cdot 10^0$	$4.8448 \cdot 10^0$	$7.0950 \cdot 10^{-1}$	$6.2448 \cdot 10^{-1}$	$8.8017 \cdot 10^{-1}$	$1.2890 \cdot 10^{-1}$
14	$4.0657 \cdot 10^0$	$4.7237 \cdot 10^0$	$4.3947 \cdot 10^0$	$6.4359 \cdot 10^{-1}$	$5.8679 \cdot 10^{-1}$	$9.1174 \cdot 10^{-1}$	$1.3352 \cdot 10^{-1}$
15	$3.0119 \cdot 10^0$	$4.0657 \cdot 10^0$	$3.5388 \cdot 10^0$	$5.1825 \cdot 10^{-1}$	$4.6507 \cdot 10^{-1}$	$8.9739 \cdot 10^{-1}$	$1.3142 \cdot 10^{-1}$
16	$2.3852 \cdot 10^0$	$3.0119 \cdot 10^0$	$2.6986 \cdot 10^0$	$3.9519 \cdot 10^{-1}$	$4.7157 \cdot 10^{-1}$	$1.1933 \cdot 10^0$	$1.7475 \cdot 10^{-1}$
17	$2.3069 \cdot 10^0$	$2.3852 \cdot 10^0$	$2.3460 \cdot 10^0$	$3.4357 \cdot 10^{-1}$	$5.3797 \cdot 10^{-1}$	$1.5658 \cdot 10^0$	$2.2931 \cdot 10^{-1}$
18	$1.8268 \cdot 10^0$	$2.3069 \cdot 10^0$	$2.0669 \cdot 10^0$	$3.0268 \cdot 10^{-1}$	$3.6753 \cdot 10^{-1}$	$1.2143 \cdot 10^0$	$1.7782 \cdot 10^{-1}$
19	$1.4227 \cdot 10^0$	$1.8268 \cdot 10^0$	$1.6248 \cdot 10^0$	$2.3794 \cdot 10^{-1}$	$2.9624 \cdot 10^{-1}$	$1.2450 \cdot 10^0$	$1.8233 \cdot 10^{-1}$
20	$1.1080 \cdot 10^0$	$1.4227 \cdot 10^0$	$1.2654 \cdot 10^0$	$1.8531 \cdot 10^{-1}$	$2.4287 \cdot 10^{-1}$	$1.3106 \cdot 10^0$	$1.9194 \cdot 10^{-1}$
21	$9.6164 \cdot 10^{-1}$	$1.1080 \cdot 10^0$	$1.0348 \cdot 10^0$	$1.5155 \cdot 10^{-1}$	$1.6513 \cdot 10^{-1}$	$1.0896 \cdot 10^0$	$1.5957 \cdot 10^{-1}$
22	$8.2085 \cdot 10^{-1}$	$9.6164 \cdot 10^{-1}$	$8.9125 \cdot 10^{-1}$	$1.3052 \cdot 10^{-1}$	$1.8618 \cdot 10^{-1}$	$1.4265 \cdot 10^0$	$2.0890 \cdot 10^{-1}$
23	$7.4274 \cdot 10^{-1}$	$8.2085 \cdot 10^{-1}$	$7.8180 \cdot 10^{-1}$	$1.1449 \cdot 10^{-1}$	$1.9029 \cdot 10^{-1}$	$1.6620 \cdot 10^0$	$2.4340 \cdot 10^{-1}$
24	$6.3928 \cdot 10^{-1}$	$7.4274 \cdot 10^{-1}$	$6.9101 \cdot 10^{-1}$	$1.0120 \cdot 10^{-1}$	$1.9980 \cdot 10^{-1}$	$1.9744 \cdot 10^0$	$2.8914 \cdot 10^{-1}$
25	$5.5023 \cdot 10^{-1}$	$6.3928 \cdot 10^{-1}$	$5.9475 \cdot 10^{-1}$	$8.7100 \cdot 10^{-2}$	$1.7870 \cdot 10^{-1}$	$2.0517 \cdot 10^0$	$3.0046 \cdot 10^{-1}$
26	$3.6883 \cdot 10^{-1}$	$5.5023 \cdot 10^{-1}$	$4.5953 \cdot 10^{-1}$	$6.7297 \cdot 10^{-2}$	$1.2905 \cdot 10^{-1}$	$1.9176 \cdot 10^0$	$2.8082 \cdot 10^{-1}$
27	$2.4724 \cdot 10^{-1}$	$3.6883 \cdot 10^{-1}$	$3.0804 \cdot 10^{-1}$	$4.5111 \cdot 10^{-2}$	$1.2075 \cdot 10^{-1}$	$2.6768 \cdot 10^0$	$3.9201 \cdot 10^{-1}$
28	$1.5764 \cdot 10^{-1}$	$2.4724 \cdot 10^{-1}$	$2.0244 \cdot 10^{-1}$	$2.9647 \cdot 10^{-2}$	$1.0630 \cdot 10^{-1}$	$3.5857 \cdot 10^0$	$5.2511 \cdot 10^{-1}$
29	$1.1109 \cdot 10^{-1}$	$1.5764 \cdot 10^{-1}$	$1.3437 \cdot 10^{-1}$	$1.9677 \cdot 10^{-2}$	$1.5085 \cdot 10^{-1}$	$7.6661 \cdot 10^0$	$1.1227 \cdot 10^0$
30	$5.2475 \cdot 10^{-2}$	$1.1109 \cdot 10^{-1}$	$8.1782 \cdot 10^{-2}$	$1.1977 \cdot 10^{-2}$	$1.3375 \cdot 10^{-1}$	$1.1167 \cdot 10^1$	$1.6354 \cdot 10^0$
31	$3.4307 \cdot 10^{-2}$	$5.2475 \cdot 10^{-2}$	$4.3391 \cdot 10^{-2}$	$6.3545 \cdot 10^{-3}$	$1.3519 \cdot 10^{-1}$	$2.1275 \cdot 10^1$	$3.1157 \cdot 10^0$
32	$2.4788 \cdot 10^{-2}$	$3.4307 \cdot 10^{-2}$	$2.9547 \cdot 10^{-2}$	$4.3271 \cdot 10^{-3}$	$1.3086 \cdot 10^{-1}$	$3.0241 \cdot 10^1$	$4.4287 \cdot 10^0$
33	$2.1875 \cdot 10^{-2}$	$2.4788 \cdot 10^{-2}$	$2.3331 \cdot 10^{-2}$	$3.4168 \cdot 10^{-3}$	$1.3013 \cdot 10^{-1}$	$3.8085 \cdot 10^1$	$5.5774 \cdot 10^0$
34	$1.0333 \cdot 10^{-2}$	$2.1875 \cdot 10^{-2}$	$1.6104 \cdot 10^{-2}$	$2.3584 \cdot 10^{-3}$	$1.3004 \cdot 10^{-1}$	$5.5140 \cdot 10^1$	$8.0751 \cdot 10^0$
35	$3.3546 \cdot 10^{-3}$	$1.0333 \cdot 10^{-2}$	$6.8438 \cdot 10^{-3}$	$1.0023 \cdot 10^{-3}$	$1.3182 \cdot 10^{-1}$	$1.3152 \cdot 10^2$	$1.9261 \cdot 10^1$
36	$1.2341 \cdot 10^{-3}$	$3.3546 \cdot 10^{-3}$	$2.2944 \cdot 10^{-3}$	$3.3600 \cdot 10^{-4}$	$1.3594 \cdot 10^{-1}$	$4.0459 \cdot 10^2$	$5.9251 \cdot 10^1$
37	$5.8295 \cdot 10^{-4}$	$1.2341 \cdot 10^{-3}$	$9.0852 \cdot 10^{-4}$	$1.3305 \cdot 10^{-4}$	$1.4043 \cdot 10^{-1}$	$1.0555 \cdot 10^3$	$1.5457 \cdot 10^2$
38	$2.7536 \cdot 10^{-4}$	$5.8295 \cdot 10^{-4}$	$4.2916 \cdot 10^{-4}$	$6.2848 \cdot 10^{-5}$	$1.4472 \cdot 10^{-1}$	$2.3027 \cdot 10^3$	$3.3722 \cdot 10^2$
39	$1.0130 \cdot 10^{-4}$	$2.7536 \cdot 10^{-4}$	$1.8833 \cdot 10^{-4}$	$2.7580 \cdot 10^{-5}$	$1.5013 \cdot 10^{-1}$	$5.4432 \cdot 10^3$	$7.9714 \cdot 10^2$
40	$2.9023 \cdot 10^{-5}$	$1.0130 \cdot 10^{-4}$	$6.5162 \cdot 10^{-5}$	$9.5427 \cdot 10^{-6}$	$1.5813 \cdot 10^{-1}$	$1.6570 \cdot 10^4$	$2.4267 \cdot 10^3$
41	$1.0677 \cdot 10^{-5}$	$2.9023 \cdot 10^{-5}$	$1.9850 \cdot 10^{-5}$	$2.9070 \cdot 10^{-6}$	$1.6830 \cdot 10^{-1}$	$5.7896 \cdot 10^4$	$8.4787 \cdot 10^3$
42	$3.0590 \cdot 10^{-6}$	$1.0677 \cdot 10^{-5}$	$6.8680 \cdot 10^{-6}$	$1.0058 \cdot 10^{-6}$	$1.7947 \cdot 10^{-1}$	$1.7844 \cdot 10^5$	$2.6131 \cdot 10^4$
43	$1.1253 \cdot 10^{-6}$	$3.0590 \cdot 10^{-6}$	$2.0921 \cdot 10^{-6}$	$3.0639 \cdot 10^{-7}$	$1.9367 \cdot 10^{-1}$	$6.3210 \cdot 10^5$	$9.2568 \cdot 10^4$
44	$4.1399 \cdot 10^{-7}$	$1.1253 \cdot 10^{-6}$	$7.6964 \cdot 10^{-7}$	$1.1271 \cdot 10^{-7}$	$2.0772 \cdot 10^{-1}$	$1.8429 \cdot 10^6$	$2.6989 \cdot 10^5$
45	$1.0000 \cdot 10^{-11}$	$4.1399 \cdot 10^{-7}$	$2.0700 \cdot 10^{-7}$	$3.0314 \cdot 10^{-8}$	$2.3166 \cdot 10^{-1}$	$7.6419 \cdot 10^6$	$1.1191 \cdot 10^6$

220

Appendix B. Asteroidal Energy Deposition Heatmaps

This appendix contains the heatmaps of asteroidal energy deposition profiles in a full-circle, two-dimensional view, and in reconstructed three-dimensional views.

B.1   2-D Asteroidal Energy Deposition Heatmaps

Below, the semi-circle heatmaps in Figures 4.10 and 4.11 were reflected across the ALE3D x-axis due to symmetry. This creates a 2-D circular energy deposition heatmap for each of the two yields and for each of the two neutron energies.

As before, areas with colors other than dark blue are melted. The colorbar values are unitless, representing the E_{dep}/E_{melt} ratio of energy densities at a given spatial location, where 1.0 is melted, 2.0 is melted to twice beyond the 1941 J/g melt threshold for SiO_2, and so forth. For visualization purposes only, the heating contours resulting from 50 kt neutron yields are shown on an 80 cm diameter asteroid, and for 1 Mt yields the asteroid size is 5 m.

The full-circle heatmaps could be envisioned as if the spherical asteroid was cut cleanly through the center, and then the halves separated, at the moment of energy deposition. It is the opinion of this paper's author that the full-circle views are "very cool." So go ahead, scroll on down!
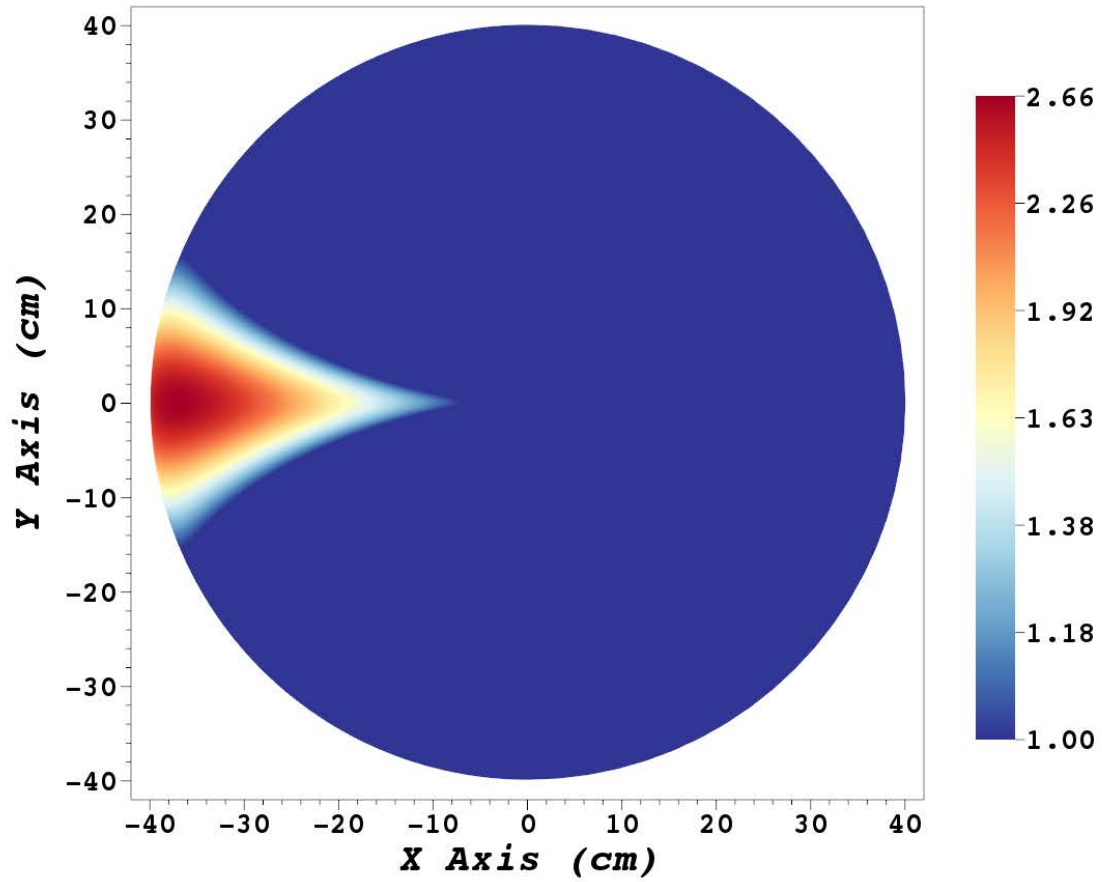
Figure B.1. Energy deposition heatmap from a 50 kt yield composed of 14.1 MeV neutrons, full-circle view.
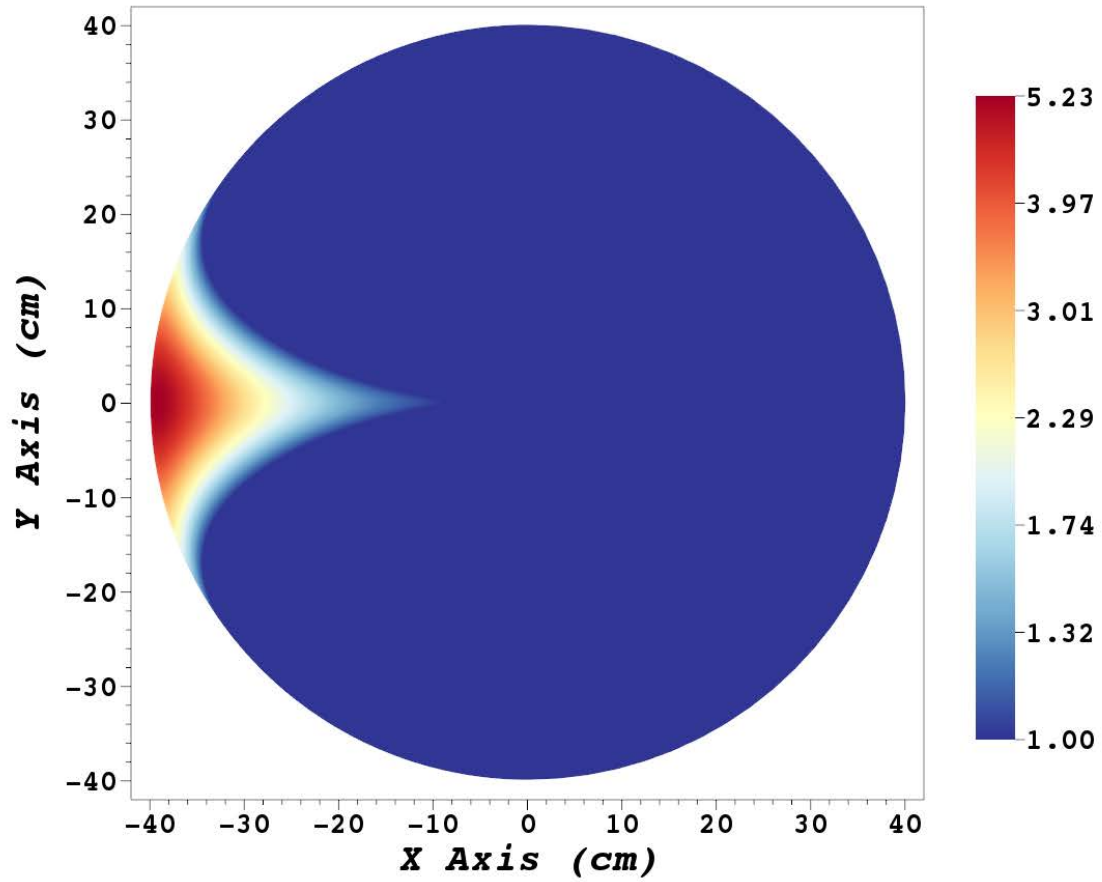
Figure B.2. Energy deposition heatmap from a 50 kt yield composed of 1 MeV neutrons, full-circle view.

223
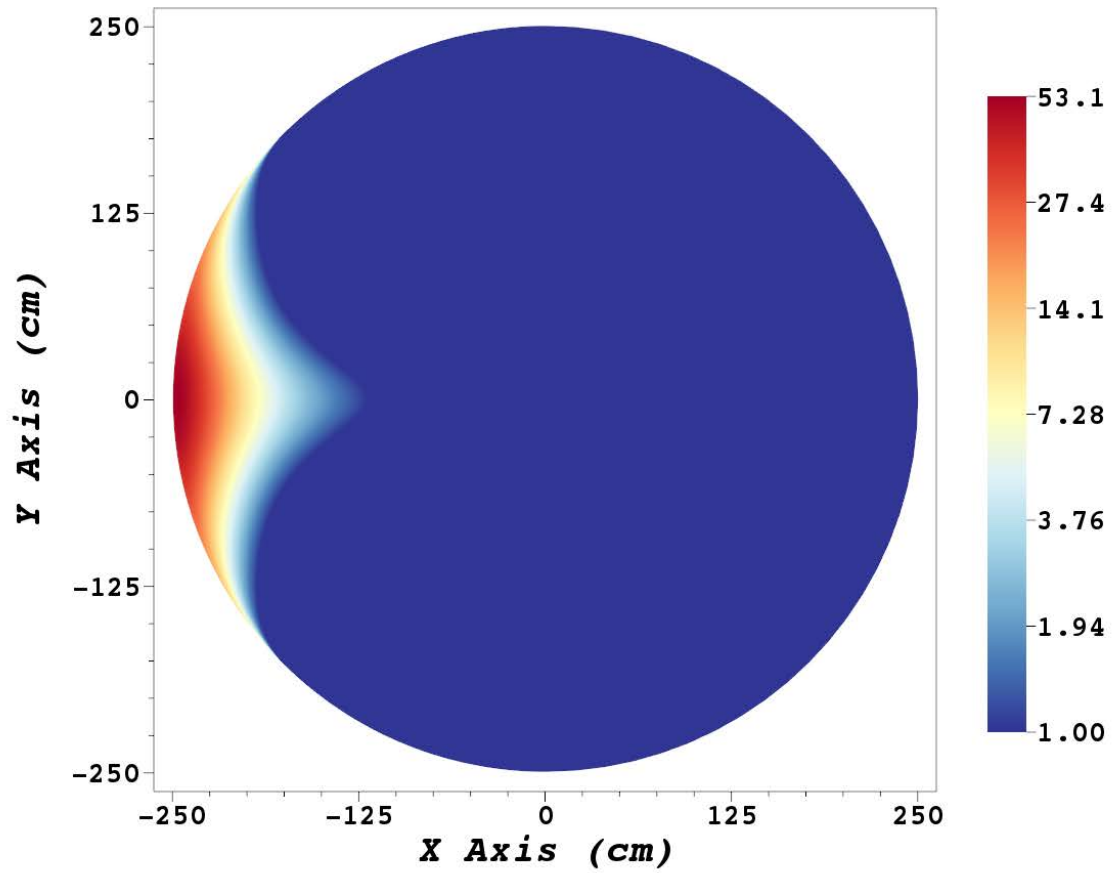
Figure B.3. Energy deposition heatmap from a 1 Mt yield composed of 14.1 MeV neutrons, full-circle view.
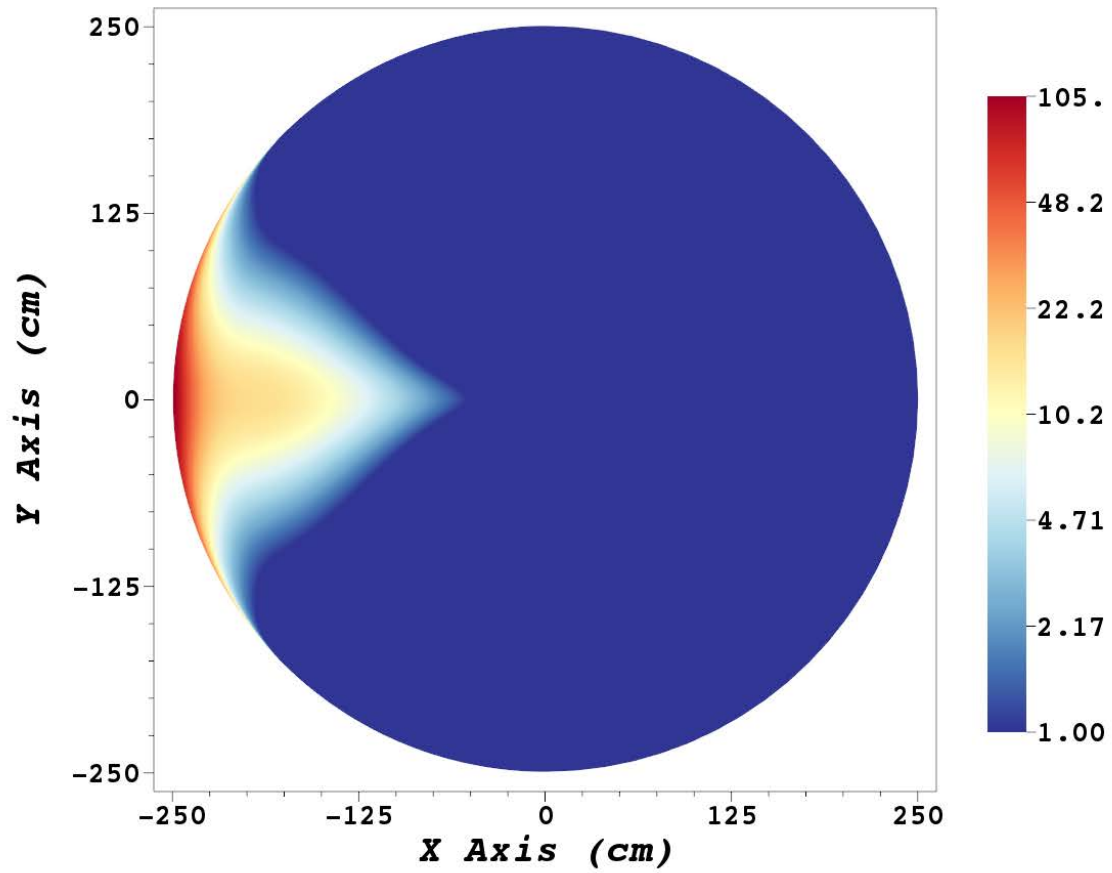
Figure B.4. Energy deposition heatmap from a 1 Mt yield composed of 1 MeV neutrons, full-circle view.

B.2 3-D Asteroidal Energy Deposition Heatmaps

Below, the semi-circle heatmaps in Figures 4.10 and 4.11 were revolved 270° about the axisymmetric axis. In this way, the original 3-D spherical asteroid shape is recovered (or, at least 75% of it is). The quarter cutaway allowed for both the surface energy deposition and the inner deposition to be displayed simultaneously.

If zoomed-in on one of the below figures, it might be possible to see longitudinal-type lines on the outer asteroid surface, all crossing through the GZ "pole." This is simply an artifact of the visualization software. The 2-D semi-circle was rotated about the axisymmetric axis over a discrete number of increments. 70 total planes of rotation within the 0°-to-270° revolution were used to create this filled 3-D shape. This is also why the outer asteroid surface might not appear to be perfectly smooth, if examined very closely.

First, the set of 3-D energy deposition heatmaps formed from 50 kt neutron yields are shown, followed by a similar set for 1 Mt yields. On each page, the deposition resulting from the 14.1 MeV neutron source is shown on top, and the deposition due to 1 MeV neutrons is on the bottom. There are five different 3-D perspectives included for each of the two yields.

For each side-by-side comparison of the results from 14.1 MeV and 1 MeV neutrons, a few caveats are warranted. The energy deposition heatmap colorscales are different between the two neutron sources, though they are both shown using the same range of colors. Recall that, for equivalent neutron yields, the 1 MeV deposition results in peak energy densities that are about twice the maximums from the 14.1 MeV neutron source. That is, the darkest red color shown in the 1 MeV figures below represents an energy deposition intensity that is nearly two times greater in value than the darkest red color in the 14.1 MeV heatmaps. The colorbars were omitted from the 3-D views contained below in an effort to avoid clutter, as these 3-D

226

visuals are somewhat more for show than they are for tell. However, each 3-D figure is shown with the exact same colorbar as its corresponding 2-D full-circle representation from Section B.1. One commonality among all colorbar scales is that the darkest blue corresponds to below the melt threshold. In this way, the relative shape and extent of the melted material (that is, the non-dark-blue portions of the heatmaps) can be easily compared between the two neutron source energies.

Also, these 3-D energy deposition heatmaps are displayed on the same miniature asteroids as before for 2-D, again only for visual purposes. The axes labels and coordinates are not shown, again in an effort to reduce clutter. For the 50 kt yield, the asteroid diameter is 80 cm, and for the 1 Mt yield, the asteroid is 5 m. If the 3-D heatmaps were instead shown on the full-size 300 m asteroid target, the appearance of the angular energy deposition on the outer surface would not change. However, on a 300 m scale, the radial energy deposition inside the asteroid would be compressed into an extremely thin layer beneath the surface (once more, the melt depths are tens of centimeters, which would hardly be visible on a 300 m object). For each side-by-side image of the deposition from 14.1 MeV and 1 MeV neutrons, the *relative* melt penetration depths do still have meaning. For example, it is clear that 1 Mt of 14.1 MeV neutrons (Figure B.13a) melts less material beneath the surface than 1 Mt of 1 MeV neutrons (Figure B.13b), because the latter shows melt-colors that push deeper into the asteroid than the former.

Alright, enough talk. You are here for 3-D energy deposition figures that might be even cooler (or is it hotter?) than the 2-D heatmaps. Go for it!
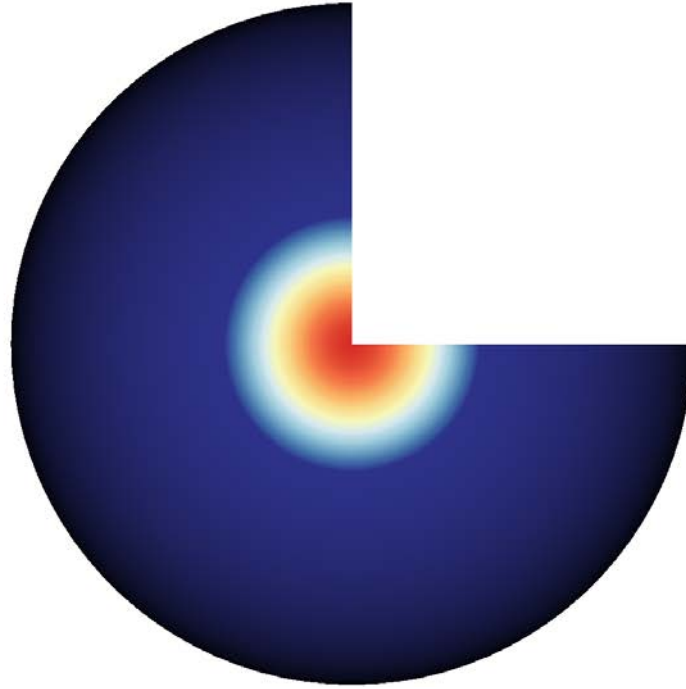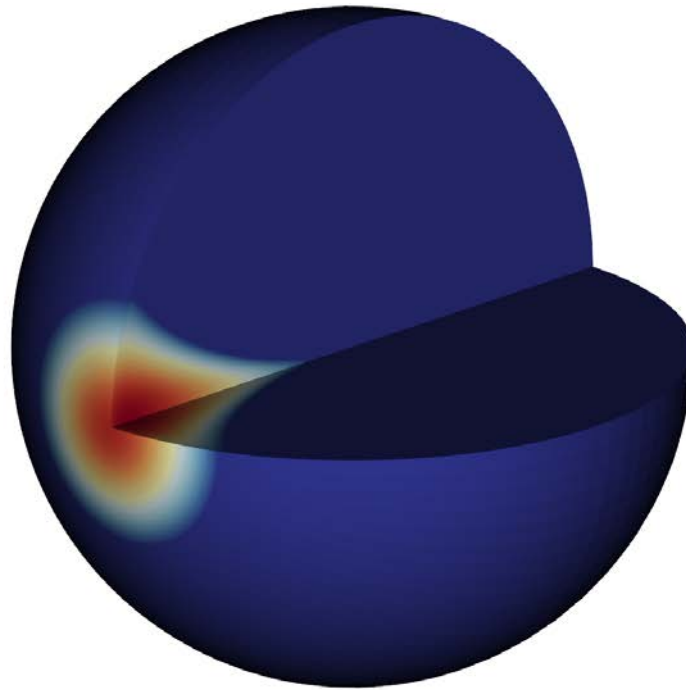
(a) Energy deposition heatmap from a 50 kt yield composed of 14.1 MeV neutrons.
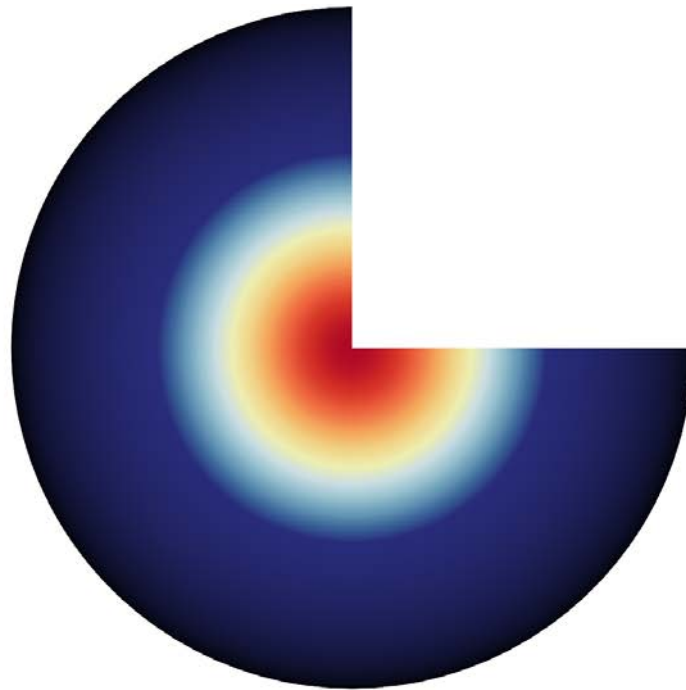
(b) Energy deposition heatmap from a 50 kt yield composed of 1 MeV neutrons.

Figure B.5. Energy deposition heatmaps from 50 kt neutron yields of 14.1 MeV and 1 MeV neutrons, view A. This is the "device-view" as from Figure 3.4a, looking directly at the irradiated outer asteroid surface.
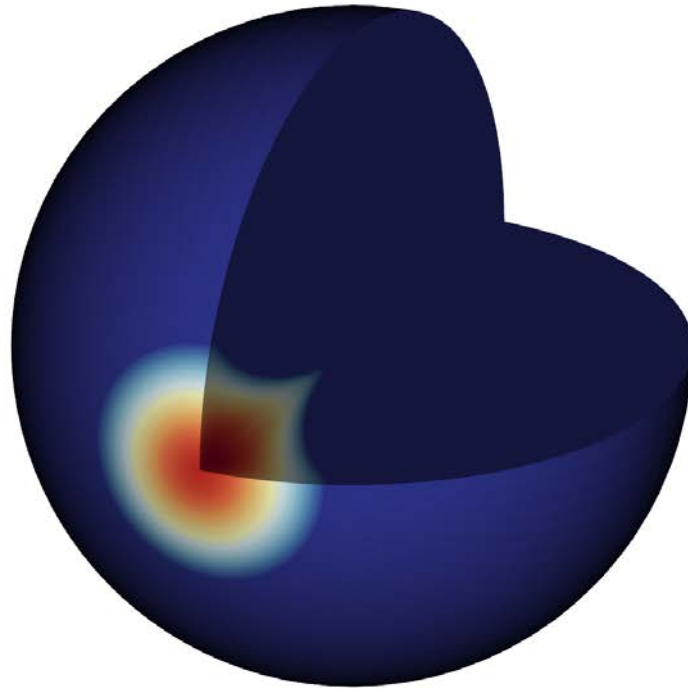
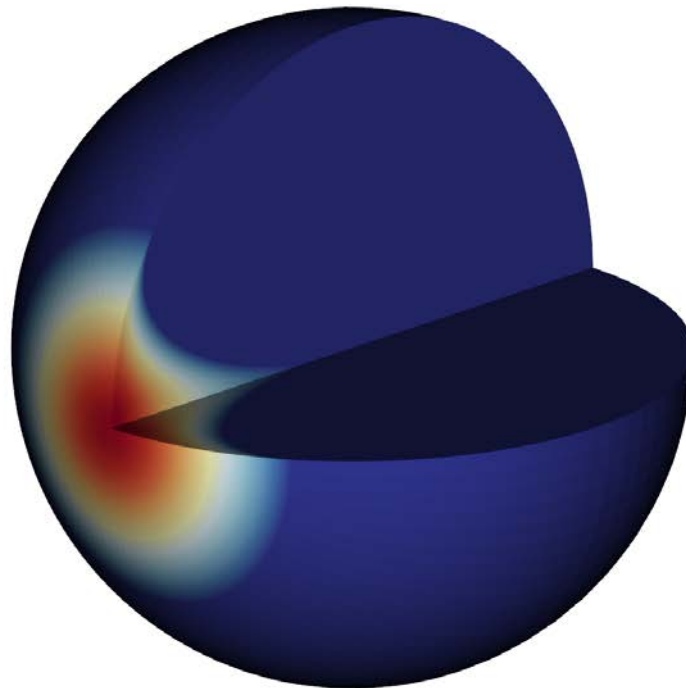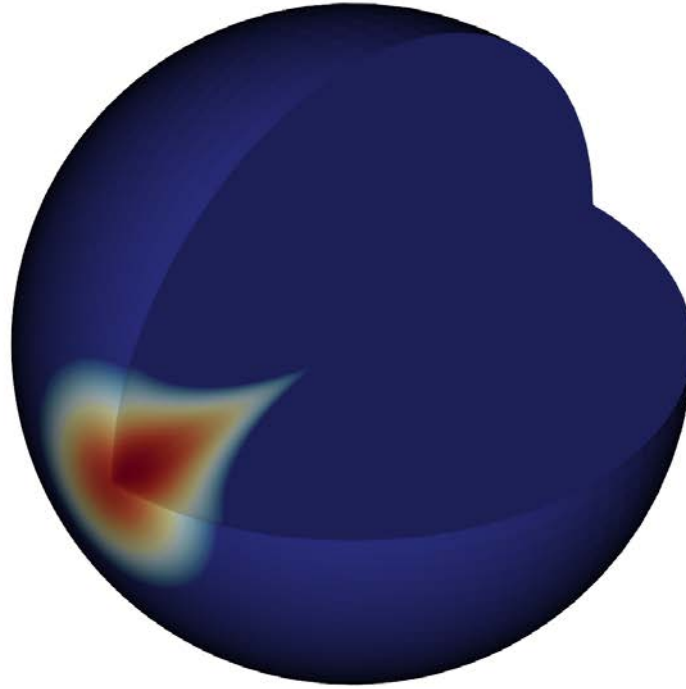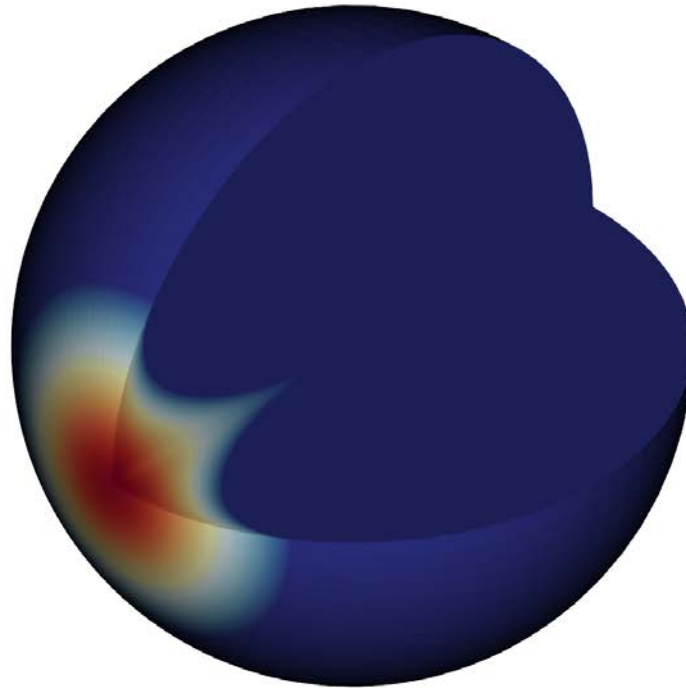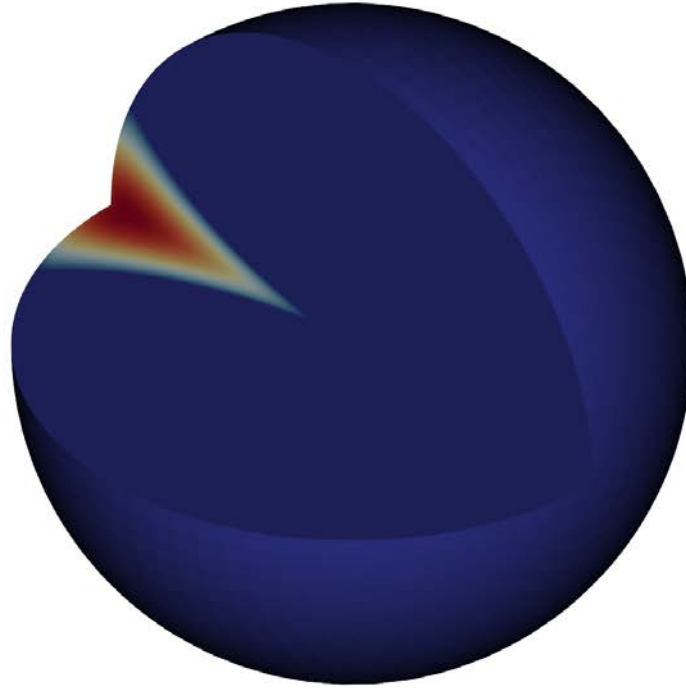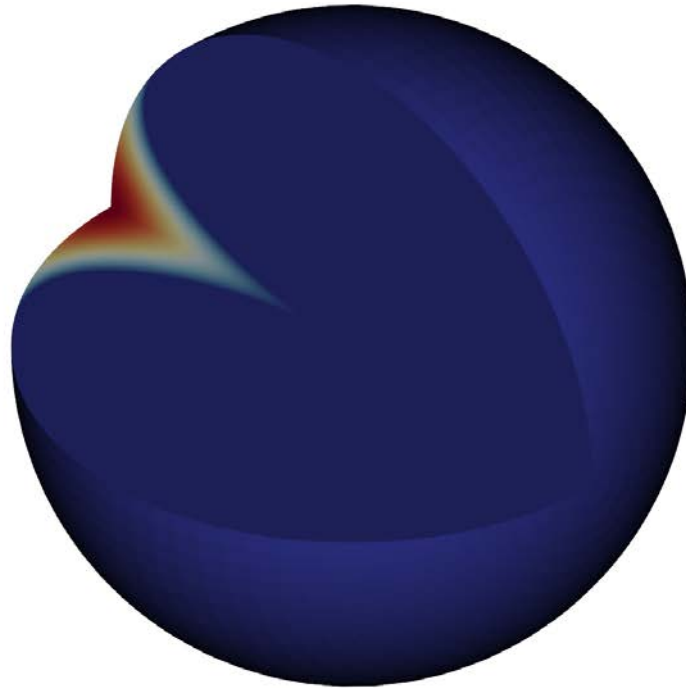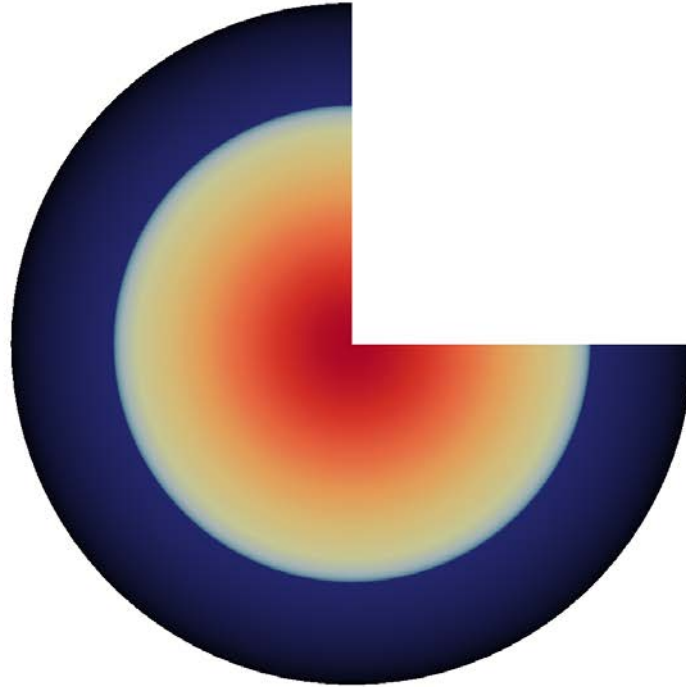(a) Energy deposition heatmap from a 50 kt yield composed of 14.1 MeV neutrons.
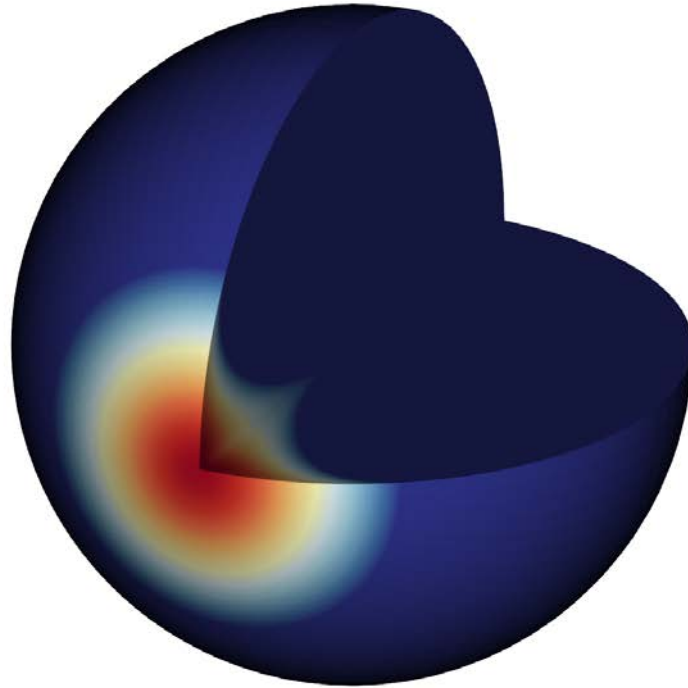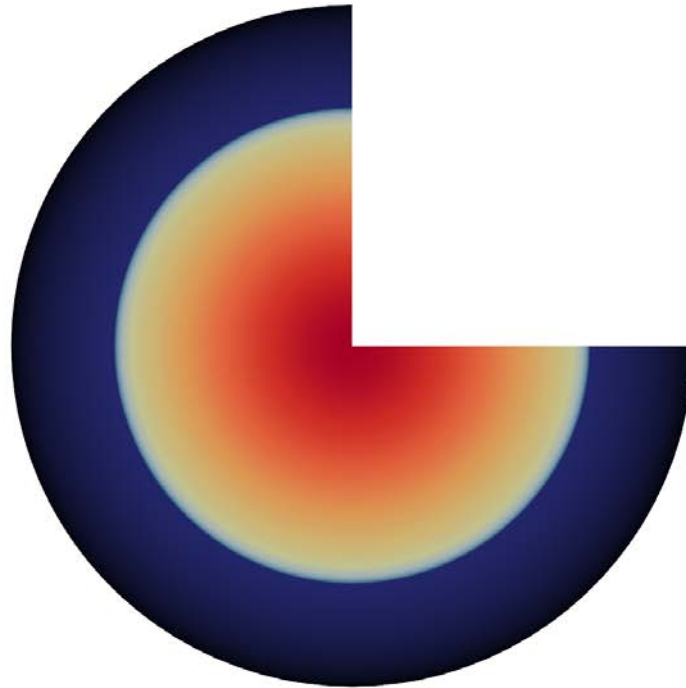

(b) Energy deposition heatmap from a 50 kt yield composed of 1 MeV neutrons.

Figure B.6. Energy deposition heatmaps from 50 kt neutron yields of 14.1 MeV and 1 MeV neutrons, view B. This is the first of the off-axis views in the spirit of Figure 3.1a.

229

(a) Energy deposition heatmap from a 50 kt yield composed of 14.1 MeV neutrons.

(b) Energy deposition heatmap from a 50 kt yield composed of 1 MeV neutrons.

Figure B.7. Energy deposition heatmaps from 50 kt neutron yields of 14.1 MeV and 1 MeV neutrons, view C. This is the second of the off-axis views in the spirit of Figure 3.1a.
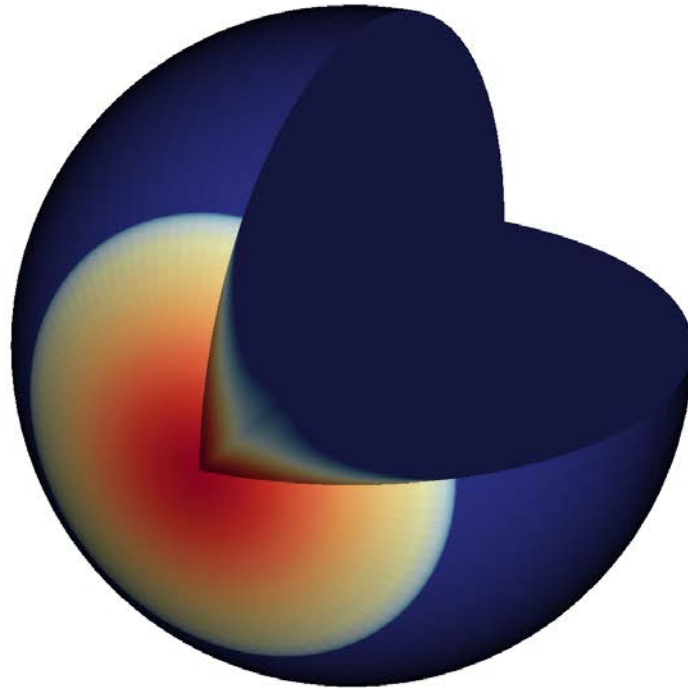
(a) Energy deposition heatmap from a 50 kt yield composed of 14.1 MeV neutrons.

(b) Energy deposition heatmap from a 50 kt yield composed of 1 MeV neutrons.

Figure B.8. Energy deposition heatmaps from 50 kt neutron yields of 14.1 MeV and 1 MeV neutrons, view D. This is the third of the off-axis views in the spirit of Figure 3.1a.

(a) Energy deposition heatmap from a 50 kt yield composed of 14.1 MeV neutrons.

(b) Energy deposition heatmap from a 50 kt yield composed of 1 MeV neutrons.

Figure B.9. Energy deposition heatmaps from 50 kt neutron yields of 14.1 MeV and 1 MeV neutrons, view E. This is the final off-axis view, looking into-and-through the asteroid from the "dark" side away from the detonation.

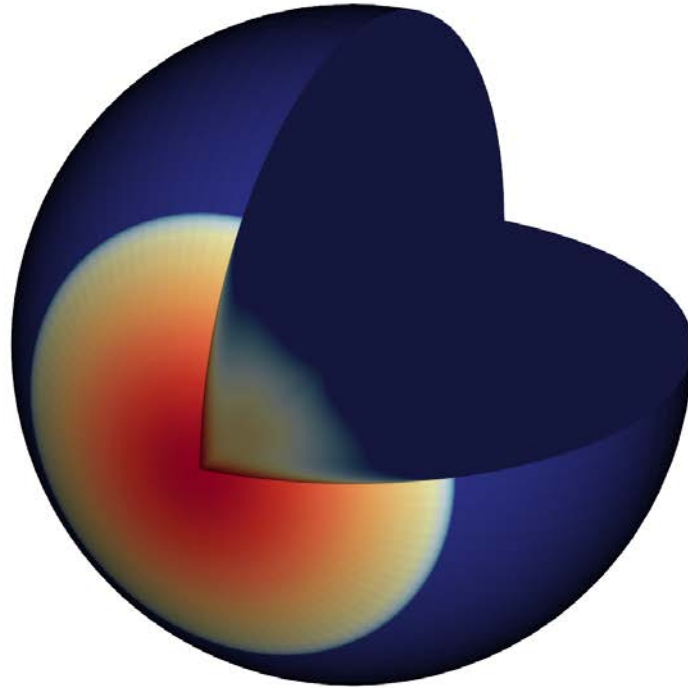(a) Energy deposition heatmap from a 1 Mt yield composed of 14.1 MeV neutrons.

(b) Energy deposition heatmap from a 1 Mt yield composed of 1 MeV neutrons.

Figure B.10. Energy deposition heatmaps from 1 Mt neutron yields of 14.1 MeV and 1 MeV neutrons, view A. This is the "device-view" as from Figure 3.4a, looking directly at the irradiated outer asteroid surface.
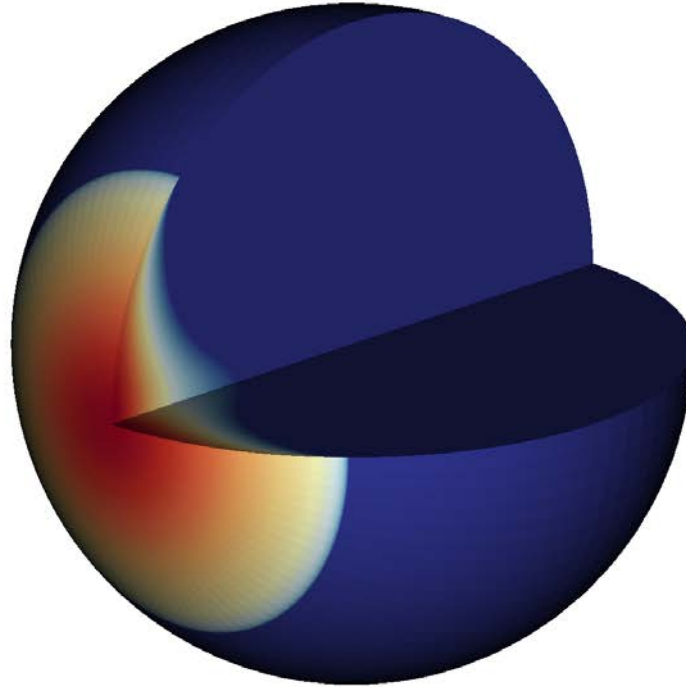
233

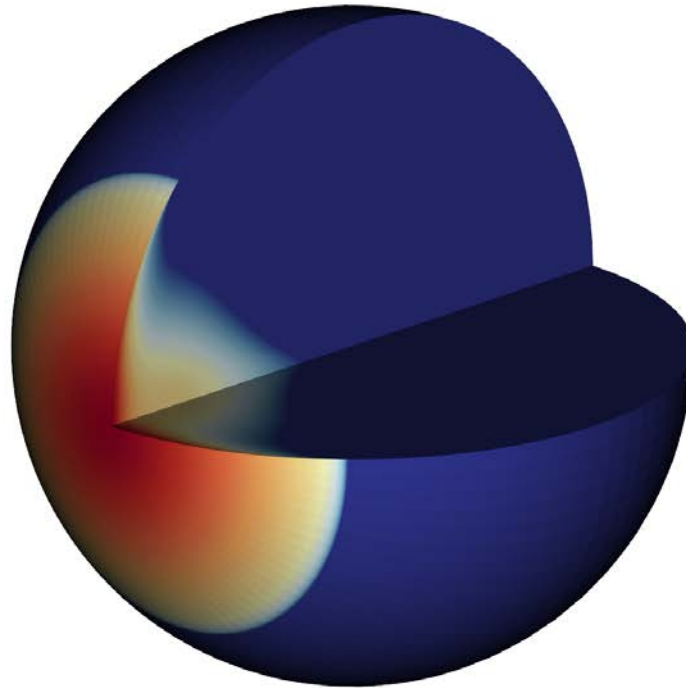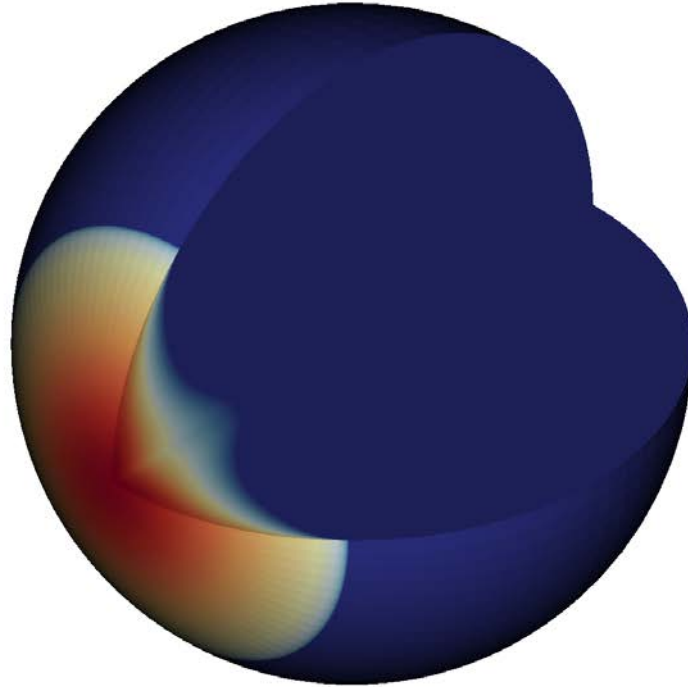(a) Energy deposition heatmap from a 1 Mt yield composed of 14.1 MeV neutrons.

(b) Energy deposition heatmap from a 1 Mt yield composed of 1 MeV neutrons.

Figure B.11. Energy deposition heatmaps from 1 Mt neutron yields of 14.1 MeV and 1 MeV neutrons, view B. This is the first of the off-axis views in the spirit of Figure 3.1a.

234

(a) Energy deposition heatmap from a 1 Mt yield composed of 14.1 MeV neutrons.
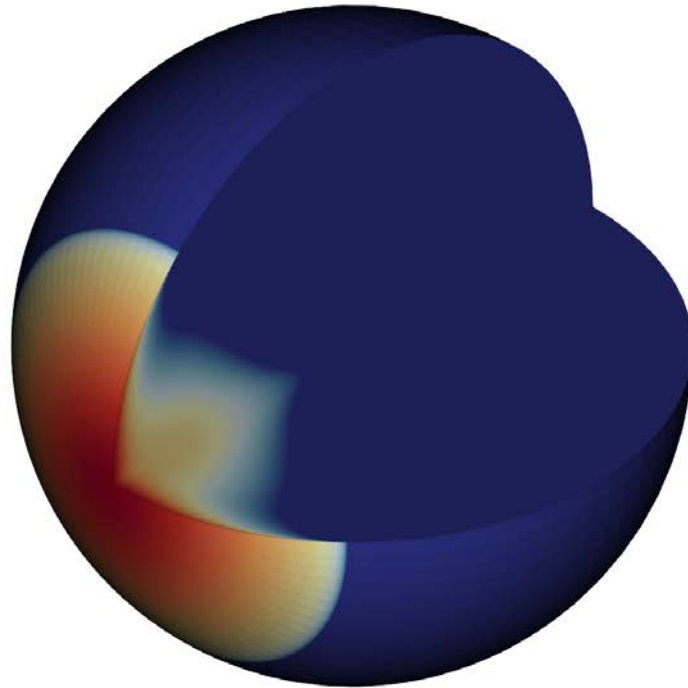

(b) Energy deposition heatmap from a 1 Mt yield composed of 1 MeV neutrons.

Figure B.12. Energy deposition heatmaps from 1 Mt neutron yields of 14.1 MeV and 1 MeV neutrons, view C. This is the second of the off-axis views in the spirit of Figure 3.1a.
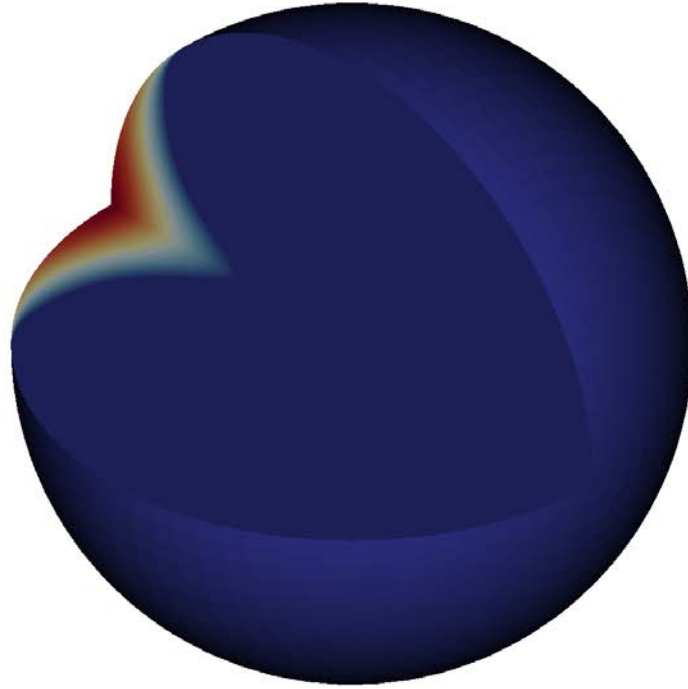
235

(a) Energy deposition heatmap from a 1 Mt yield composed of 14.1 MeV neutrons.
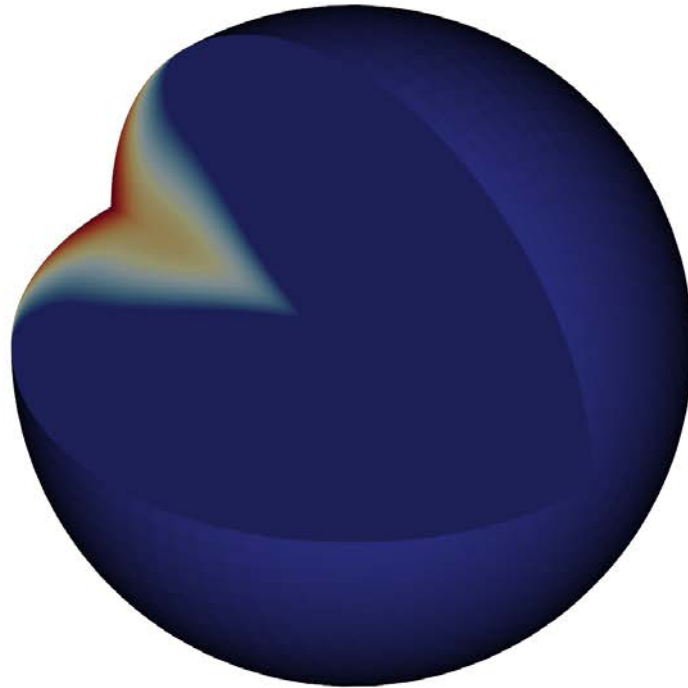

(b) Energy deposition heatmap from a 1 Mt yield composed of 1 MeV neutrons.

Figure B.13. Energy deposition heatmaps from 1 Mt neutron yields of 14.1 MeV and 1 MeV neutrons, view D. This is the third of the off-axis views in the spirit of Figure 3.1a.

236

(a) Energy deposition heatmap from a 1 Mt yield composed of 14.1 MeV neutrons.

(b) Energy deposition heatmap from a 1 Mt yield composed of 1 MeV neutrons.

Figure B.14. Energy deposition heatmaps from 1 Mt neutron yields of 14.1 MeV and 1 MeV neutrons, view E. This is the final off-axis view, looking into-and-through the asteroid from the "dark" side away from the detonation.

237

Appendix C. Miscellany

This appendix contains miscellaneous figures to briefly supplement Chapter 3 on neutron energy deposition and Chapter 4 on asteroid deflective response.
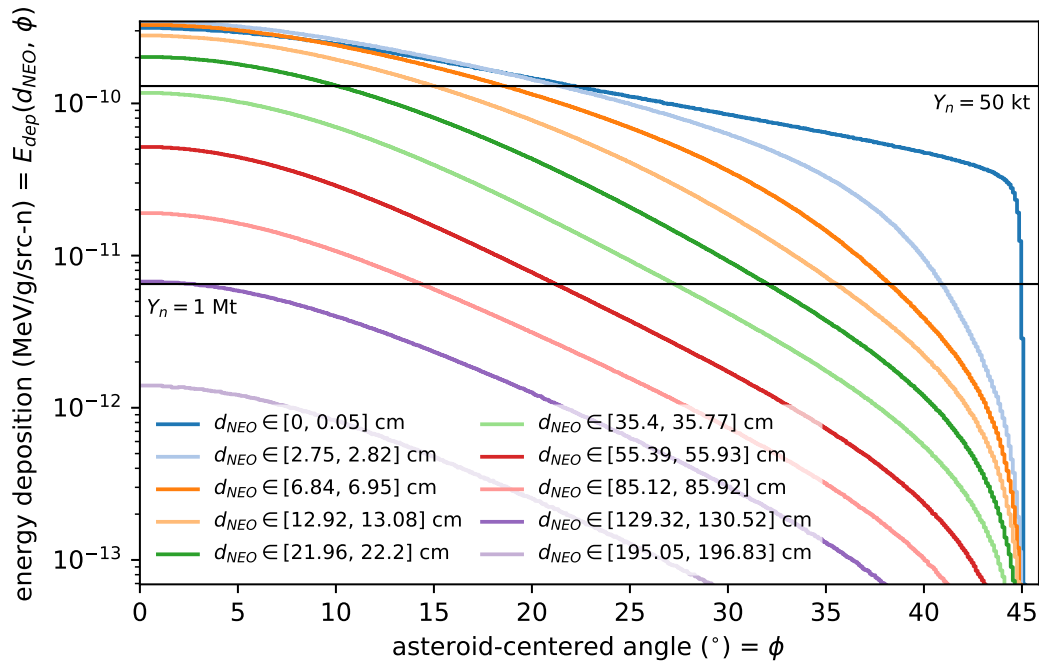
C.1   Reversed Energy Deposition Profiles

In Section 3.2.1, Figure 3.6 showed energy deposition as a function of d_{NEO} depth for a survey of ϕ angles. Below, Figure C.1 visualizes the same data, but in a reversed view — energy deposition as a function of ϕ angle for a survey of d_{NEO} depths.

Figure 3.6 made it easier to discern the melt depths due to the given neutron yields in this work. The intersection of the horizontal melt-lines with each colored depth reveals the angular extent of melted material in the asteroid for the given yields. Figure C.1, however, makes it easier to see these "melt angles." For example, for the $Y_n = 50$ kt melt-line, the blue lines (the energy depositions at the very surface of the asteroid) in Figure C.1a and Figure C.1b reveal a significant difference in the melted surface area. It appears that $\sim 22.5°$ of the surface area is melted from the 50 kt 14.1 MeV source, while a $>35°$ extent of the outer surface is melted for 50 kt's worth of 1 MeV neutrons. The fact that the 50 kt 1 MeV source melted a greater surface area than the 14.1 MeV neutrons was seen in 2-D back in Figure 4.10, and seen in 3-D in Figure B.5.

It was observed that the melt depth decreased as ϕ increases, or when moving away from GZ. Similarly, the melt angle decreases as d_{NEO} increases, i.e. when moving deeper beneath the surface. The melt depth was maximized along the $\phi = 0°$ angle (beneath GZ), and in turn, the melt angle is maximized along the $d_{NEO} = 0$ cm depth (at the outer surface).

The same trends noted before in Section 3.2.1 are still visible in Figure C.1. As the ϕ angle away from GZ ($0°$) increases, the energy deposition decreases. As the d_{NEO}

238

(a) Energy deposition spatial distribution from a ~14.1 MeV neutron source (DPLUS group #3).
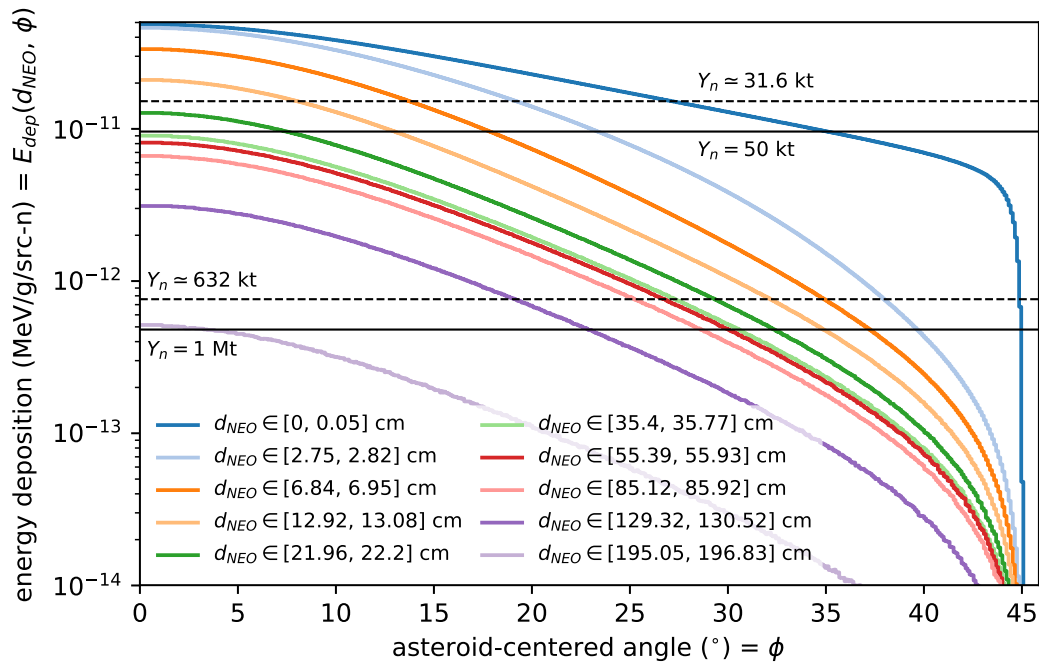
(b) Energy deposition spatial distribution from a ~1 MeV neutron source (DPLUS group #21).

Figure C.1. MCNP6.2 energy deposition profiles for two different neutron energy sources, 14.1 MeV fusion neutrons and 1 MeV fission neutrons. Figure 3.6 displayed energy deposition as a function of d_{NEO} depth across a selection of ϕ angles. This figure is the reversed view, showing energy deposition as a function of ϕ angle across a selection of d_{NEO} depths.

depth beneath the surface increases, the energy deposition (in general) decreases. Some exception to this is evident at locations near GZ (small angles + shallow depths) in Figure C.1a, noting that both the light blue line ($d_{NEO} \in [2.75, 2.82]$ cm) and the dark orange line ($d_{NEO} \in [6.84, 6.95]$ cm) surpass the dark blue line ($d_{NEO} \in [0, 0.05]$ cm).

Note that this phenomena was observed, but not highlighted or discussed, in the main body of this thesis. Figure 4.9, the zoomed-in view of the MCNP6.2 energy deposition profiles, showed that the energy deposition for some of the profiles was more intense at very shallow depths than at the outer surface. That is, for angular locations close to GZ, the energy deposition peaked where $d_{NEO} > 0$ cm. This is most likely the so-called "boundary layer effect" that has been observed in previous energy deposition calculations [60]. It is possible that less energy might be deposited at the surface than at slightly beneath the surface due to the greater likelihood that particles interacting near the surface will scatter away from the asteroid and be lost to the void of space.

In the original E_{dep} vs. d_{NEO} perspective in Figures 3.6 and 4.9, the melt angle could be estimated by noting which profile the melt-lines touched that represented the maximum angle. For example, in Figure 4.9b, the $Y_n = 50$ kt melt-line for 1 MeV neutrons extends out to approximately $\phi \in [33.9, 33.99]°$ (the light red profile) for shallow d_{NEO} depths. While the true 50 kt melt angle for 1 MeV neutrons is more easily and accurately read from Figure C.1b, where it is slightly greater than 35° at the outer surface, the E_{dep} vs. d_{NEO} perspective still permitted a rough estimate.

In a similar manner, the melt depth for a given yield can be estimated from the E_{dep} vs. ϕ display in Figure C.1. For instance, the dark purple line of Figure C.1a is barely above the 14.1 MeV 1 Mt melt threshold for small values of ϕ (i.e. near GZ, where the melt depth is maximized). This dark purple line corresponds to depths

of $d_{NEO} \in [129.32, 130.52]$ cm, which matches the $\sim$130 cm melt-depth estimated from Figures 3.6a and 4.11a. The same is seen in Figure C.1b for the light purple curve ($d_{NEO} \in [195.05, 196.83]$ cm), which pushes just past the melt-line near $\phi = 0°$, agreeing with the observation from Figures 3.6b and 4.11b that the melt-depth for 1 Mt of 1 MeV neutrons was about 200 cm.

As in Figure 3.6b, the "pause" region formed in the 1 MeV neutron energy deposition profiles is also apparent in Figure C.1b — it is just less obvious. Note that the light green line ($d_{NEO} \in [35.4, 35.77]$ cm), the dark red line ($d_{NEO} \in [55.39, 55.93]$ cm), and the light red line ($d_{NEO} \in [85.12, 85.92]$ cm) are all closer in proximity to each other than any of the other profiles in Figure C.1. This range of $\sim$35-86 cm is within the "pause" region (which was estimated in Section 3.2.1 to be roughly 25 cm to 100 cm beneath the surface). Even though the d_{NEO} depth increases by tens of centimeters in this region, the energy deposition magnitudes throughout these locations are nearly the same, which is only possible in the "pause" region where the energy deposition radial slopes are almost flat.

Lastly, the general smoothness of the profiles in Figure 3.6 along the d_{NEO} axis was a testament to the selected energy deposition discretization in the radial direction. Now, in Figure C.1, the overall smoothness of the profiles along the ϕ axis shows that the spatial discretization in the angular direction was appropriate and sufficient.

C.2 Blow-Off Visualization Example

As seen in Figure 4.16, the asteroid velocity change δV due to blow-off converges after a few hundred microseconds. This is because the prompt blow-off momentum finishes evolving in this time-span. While the small blow-off fragments are traveling very quickly with enough kinetic energy to escape the asteroid body, after a few hundred microseconds, they have not yet traveled very far away from the surface.

As an example, Figure C.2 visualizes the blow-off that results from a 1 Mt yield of 14.1 MeV neutrons, 1 ms (or 1000 μs) after the initial energy deposition. The red zones are blow-off, while the blue zones are the remaining, majority asteroid body.[1] It is easy to see that, while the red blow-off has indeed moved slightly to the left away from the asteroid, not enough time has passed for it to escape further. If the simulations were continued, and if the ALE3D input file was improved to allow for element erosion and conversion, then the blow-off would continue on its determined path outwards into space, never to return to the asteroid.
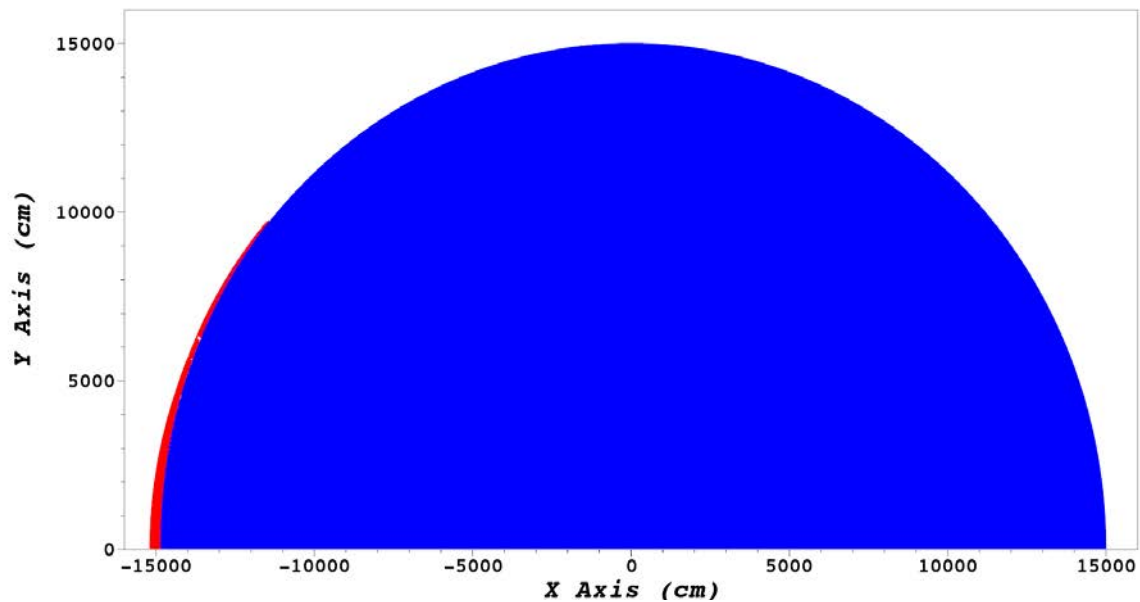

Figure C.2. The blow-off, 1 ms after the energy deposition from 1 Mt of 14.1 MeV neutrons. The zones colored red are blow-off (i.e. energy density is beyond the melt threshold, and travel speeds are greater than the escape velocity), while the blue zones comprise the remaining, majority asteroid body.

---

[1] Even for an excessive 1 Mt yield, the blow-off is obviously only a very small fraction of the total asteroid mass. Similar figures for 50 kt yields, which melt much less material and therefore generate less blow-off, were omitted, as the red blow-off fraction was so small that it was hardly visible.

Bibliography

1. I. Couronne, "Killer asteroid flattens New York in simulation exercise," *Phys.org*, 4 May 2019. [Online]. Available: https://phys.org/news/2019-05-killer-asteroid-flattens-york-simulation.html

2. G. L. Dillow, "How an Asteroid Could Destroy the World Before Impact," *Literary Hub*, 20 June 2019. [Online]. Available: https://lithub.com/how-an-asteroid-could-destroy-the-world-before-impact/

3. "About the Department of Defense (DOD)." [Online]. Available: https://archive.defense.gov/about/

4. "U.S. Strategic Command - About," January 2018. [Online]. Available: https://www.stratcom.mil/About/

5. D. Morrison, "The Spaceguard Survey: Report of the NASA International Near-Earth-Object Detection Workshop," *National Aeronautics and Space Administration*, 25 January 1992.

6. T. Ahrens and A. Harris, "Deflection and fragmentation of near-Earth asteroids," *Nature*, 3 December 1992.

7. D. K. Lynch, "Near-Earth Asteroids: What are they and where do they come from?" *Geology.com*, 2007. [Online]. Available: https://geology.com/articles/near-earth-asteroids.shtml

8. "In Depth - Asteroids," *National Aeronautics and Space Administration*, 19 December 2019. [Online]. Available: https://solarsystem.nasa.gov/asteroids-comets-and-meteors/asteroids/in-depth/

9. N. T. Redd, "Asteroid Belt: Facts & Formation," *Space.com*, 5 May 2017. [Online]. Available: https://www.space.com/16105-asteroid-belt.html

10. C. Q. Choi, "Asteroids: Fun Facts and Information About Asteroids," *Space.com*, 20 September 2017. [Online]. Available: https://www.space.com/51-asteroids-formation-discovery-and-exploration.html

11. I. de Pater and J. J. Lissauer, "Planetary Sciences," *Cambridge University Press*, 16 March 2015.

12. L. Carter, "How are asteroid compositions and classifications determined? (Intermediate)," *Cornell University Astronomy Department*, 2019. [Online]. Available: http://curious.astro.cornell.edu/our-solar-system/72-our-solar-system/comets-meteors-and-asteroids/asteroids/295-how-are-asteroid-compositions-and-classifications-determined-intermediate

13. "Asteroids: Structure and composition of asteroids," *European Space Agency*, 2019. [Online]. Available: https://www.esa.int/Science_Exploration/Space_Science/Asteroids_Structure_and_composition_of_asteroids

14. S. D. Pippo, "Near-Earth Objects and Planetary Defence," *United Nations Office for Outer Space Affairs*, June 2018. [Online]. Available: https://www.unoosa.org/documents/pdf/smpag/st_space_073E.pdf

15. J. Horner, "Why dangerous asteroids heading to Earth are so hard to detect," *The Conversation*, 22 March 2019. [Online]. Available: https://theconversation.com/why-dangerous-asteroids-heading-to-earth-are-so-hard-to-detect-113845

16. "National Near-Earth Object Preparedness Strategy and Action Plan," *Office of Science and Technology Policy*, June 2018.

17. P. Chodas, "Discovery Statistics," *NASA JPL Center for Near Earth Object Studies*, 24 December 2019. [Online]. Available: https://cneos.jpl.nasa.gov/stats/totals.html

18. "Effects of Nuclear Weapon Testing by the Soviet Union," *Comprehensive Nuclear-Test-Ban Treaty Organization*, 2019. [Online]. Available: https://www.ctbto.org/nuclear-testing/the-effects-of-nuclear-testing/the-soviet-unionsnuclear-testing-programme/page-4-effects-of-nuclear-weapon-testing-by-the-soviet-union/

19. "Planetary Defense Frequently Asked Questions," *National Aeronautics and Space Administration*, 22 April 2019. [Online]. Available: https://www.nasa.gov/planetarydefense/faq

20. "Orbits of Potentially Hazardous Asteroids (PHAs)," *NASA JPL*, 2 August 2013. [Online]. Available: https://www.jpl.nasa.gov/spaceimages/details.php?id=PIA17041

21. P. Chodas, "NEO Basics," *NASA JPL Center for Near Earth Object Studies*, 2019. [Online]. Available: https://cneos.jpl.nasa.gov/about/neo_groups.html

22. "NASA Asteroid Database: What Can You Learn About Our Solar System?" *Science Buddies*, 19 April 2018. [Online]. Available: https://www.sciencebuddies.org/science-fair-projects/project-ideas/Astro_p039/astronomy/nasa-asteroid-database-what-can-you-learn-about-our-solar-system#background

23. P. Tricarico, "The near-Earth asteroid population from two decades of observations," *Elsevier Icarus*, 6 December 2016. [Online]. Available: http://orbit.psi.edu/~tricaric/pdf/Tricarico_NEA_population_Icarus_2017.pdf

24. W. Clavin, "NASA Survey Counts Potentially Hazardous Asteroids," *NASA JPL*, 16 May 2012. [Online]. Available: https://www.jpl.nasa.gov/news/news.php?release=2012-138

25. W. K. Hartmann, "The Impact That Wiped Out the Dinosaurs," *Planetary Science Institute*, 2019. [Online]. Available: https://www.psi.edu/epo/ktimpact/ktimpact.html

26. "K-T Event," *NASA JPL*, 2019. [Online]. Available: https://www2.jpl.nasa.gov/sl9/back3.html

27. H. Weitering, "This Is NASA's New Plan to Detect and Destroy Asteroids Before They Hit Earth," *Space.com*, 20 June 2018. [Online]. Available: https://www.space.com/40943-nasa-asteroid-defense-plan.html

28. C. Chyba, P. Thomas, and K. Zahnle, "The 1908 Tunguska explosion: atmospheric disruption of a stony asteroid," *Nature*, 1993. [Online]. Available: https://doi.org/10.1038/361040a0

29. P. Brown, J. Assink, L. Astiz *et al.*, "A 500-kiloton airburst over Chelyabinsk and an enhanced hazard from small impactors," *Nature*, 2013. [Online]. Available: https://doi.org/10.1038/nature12741

30. "List of asteroid close approaches to Earth in 2019," *Wikipedia*, 27 December 2019. [Online]. Available: https://en.wikipedia.org/wiki/List_of_asteroid_close_approaches_to_Earth_in_2019

31. "Detection of Near-Earth Asteroids," *Open Philanthropy*, March 2013. [Online]. Available: https://www.openphilanthropy.org/research/cause-reports/asteroid-detection

32. T. Malik, "NASA Maps Dangerous Asteroids That May Threaten Earth (Photos)," *Space.com*, 14 August 2013. [Online]. Available: https://www.space.com/22369-nasa-asteroid-threat-map.html

33. "Threats from Space: A Review of U.S. Government Efforts to Track and Mitigate Asteroids and Meteors (Part I and Part II)," *United States Congress Committee on Science, Space, and Technology*, 10 April 2013. [Online]. Available: https://www.govinfo.gov/content/pkg/CHRG-113hhrg80552/pdf/CHRG-113hhrg80552.pdf

34. M. B. Syal, D. S. Dearborn, and P. H. Schultz, "Limits on the use of nuclear explosives for asteroid deflection," *Lawrence Livermore National Laboratory*, 17 November 2012.

35. R. A. Hyde, "Cosmic Bombardment," *Lawrence Livermore National Laboratory*, 19 March 1984.

36. D. Dearborn, "21st Century Steam for Asteroid Mitigation," *Lawrence Livermore National Laboratory*, 16 March 2004.

37. D. Dearborn, S. Patenaude, and R. Managan, "The Use of Nuclear Explosives To Disrupt or Divert Asteroids," *Lawrence Livermore National Laboratory*, 2 March 2007.

38. "Near-Earth Object Survey and Deflection Analysis of Alternatives," *National Aeronautics and Space Administration*, March 2007.

39. J. P. Sanchez, C. Colombo, M. Vasile, and G. Radice, "Multicriteria Comparison Among Several Mitigation Strategies for Dangerous Near-Earth Objects," *Journal of Guidance, Control, and Dynamics*, 15 August 2008.

40. R. Adams, J. Campbell, R. Hopkins, W. S. Smith *et al.*, "Near Earth Object (NEO) Mitigation Options Using Exploration Technologies," *National Aeronautics and Space Administration*, 1 January 2007.

41. J. C. Sanders, "Near Earth Object Collisional Mitigation Via Intense Neutron and Photon Sources: a Study in Asteroid Interdiction and Energy Coupling," *Oregon State University Honors Baccalaureate Thesis*, 2006.

42. R. Rhodes and D. Beller, "The Need for Nuclear Power: Viewpoint on the World's Challenging Energy Future," *International Atomic Energy Agency*, 2000.

43. D. Dearborn, M. Bruck Syal, B. Barbee, G. Gisler, K. Greenaugh, K. Howley, R. Leung, J. Lyzhoft, P. Miller, J. Nuth, C. Plesko, B. Seery, J. Wasem, R. Weaver, and M. Zebenay, "Options and uncertainties in planetary defense: Impulse-dependent response and the physical properties of asteroids," *Acta Astronautica*, 2020.

44. C. Bridgman, "Introduction to the Physics of Nuclear Weapons Effects," *Defense Threat Reduction Agency*, July 2001.

45. Sir Isaac Newton, "Philosophiæ Naturalis Principia Mathematica," *London*, 5 July 1687.

46. K. Howley, J. Wasem, D. Dearborn, R. Managan, and P. Miller, "Lower Limits on NEO Deflection Velocities from Melt and Vapor Blow-off Momentum," *International Academy of Astronautics Planetary Defense Conference*, 7 April 2013.

47. K. Howley, R. Managan, and J. Wasem, "Blow-off momentum from melt and vapor in nuclear deflection scenarios," *Lawrence Livermore National Laboratory*, 2014.

48. R. Managan, K. Howley, and J. Wasem, "Efficient and Accurate Mapping of Nuclear-Energy Deposition," *Lawrence Livermore National Laboratory*, 2015.

49. A. Ferguson, "Analysis of Neutron Effects for Asteroid Disruption," *Air Force Institute of Technology*, March 2016.

50. J. P. Lestone, "Watt parameters for the Los Alamos Model: Subroutine getab," *Los Alamos National Laboratory*, 2007.

51. D. Pelowitz, "MCNP6 User's Manual," *Los Alamos National Security LLC*, 2008.

52. D. Brown, "Evaluated Nuclear Data File (ENDF)," *Brookhaven National Laboratory*, 2 February 2018. [Online]. Available: https://www.nndc.bnl.gov/exfor/endf00.jsp

53. "Arbitrary Lagrangian-Eulerian 3D and 2D Multi-Physics Code," *Lawrence Livermore National Laboratory*, 2019. [Online]. Available: https://wci.llnl.gov/simulation/computer-codes/ale3d

54. S. W. Mosher *et al.*, "ADVANTG—An Automated Variance Reduction Parameter Generator," *Oak Ridge National Laboratory*, August 2015.

55. S. Glasstone and P. J. Dolan, "The Effects of Nuclear Weapons," *United States Department of Defense and Department of Energy*, 1977.

56. P. Hammerling and J. Remo, "NEO Interaction with Nuclear Radiation," *Acta Astronautica*, 6 September 1995.

57. A. K. Jain, B. Maheshwari, S. Garg, M. Patial, and B. Singh, "Atlas of Nuclear Isomers," *Nuclear Data Sheets*, September 2015.

58. "Gamma decay," *Encyclopædia Britannica*, 20 July 1998. [Online]. Available: https://www.britannica.com/science/gamma-decay

59. E. Y. Aristova, A. A. Aushev, V. K. Baranov, I. A. Belov, S. A. Bel'kov, A. Y. Voronin *et al.*, "Laser Simulations of the Destructive Impact of Nuclear Explosions on Hazardous Asteroids," *Journal of Experimental and Theoretical Physics*, 3 September 2017.

60. R. Weaver, P. Miller, K. Howley *et al.*, "Los Alamos and Lawrence Livermore National Laboratories Code-to-Code Comparison of Inter Lab Test Problem 1 for Asteroid Impact Hazard Mitigation," *Los Alamos National Laboratory*, 15 January 2016.

61. D. Brown and J. Wendel, "Scientists Planning Now for Asteroid Flyby a Decade Away," *NASA JPL*, 29 April 2019. [Online]. Available: https://www.jpl.nasa.gov/news/news.php?feature=7390

62. B. Barbee, M. B. Syal, and G. Gisler, "NEA Mitigation Studies for Short Warning Time Scenarios," *15th Meeting of the NASA Small Bodies Assessment Group (SBAG)*, 30 June 2016.

247

63. "Data Available from the Minor Planet Center," *The International Astronomical Union Minor Planet Center*, 2019. [Online]. Available: https://www.minorplanetcenter.net/data

64. "Nuclide Table," *Korea Atomic Energy Research Institute*, 2019. [Online]. Available: http://atom.kaeri.re.kr:8080/ton/index.html

65. D. T. Britt, D. K. Yeomans, K. R. Housen, and G. Consolmagno, "Asteroid Density, Porosity, and Structure," *Asteroids III, University of Arizona Press*, 2002. [Online]. Available: https://www.lpi.usra.edu/books/AsteroidsIII/pdf/3022.pdf

66. A. L. N. III and D. M. Dawson, "ALE3D User's Manual," *Lawrence Livermore National Laboratory*, 24 April 2018.

67. D. B. Henry, "The temperature of an asteroid," *Physique theorique*, 1991.

68. M. B. Syal, J. M. Owen, C. D. Raskin, D. S. Dearborn, and P. L. Miller, "Integrated Blowoff and Breakup Calculations for Asteroid Deflection by Nuclear Ablation," *International Academy of Astronautics Planetary Defense Conference*, 16 May 2017. [Online]. Available: https://iaaweb.org/iaa/Scientific%20Activity/conf/pdc2017/IAA-PDC-17-04-01ab.pdf

69. B. Kaplinger, B. Wie, and D. Dearborn, "Nuclear fragmentation/dispersion modeling and simulation of hazardous near-Earth objects," *Acta Astronautica*, 17 November 2012.

70. R. G. Brown, "Escape Velocity, Escape Energy," *Duke University Physics*, 12 April 2004. [Online]. Available: https://webhome.phy.duke.edu/~rgb/Class/phy51/phy51/node9.html

71. J. E. Turner, "Atoms, Radiation, and Radiation Protection," *Wiley-VCH Publishing*, 2007.

72. J.-L. Basdevant, J. Rich, and M. Spiro, "Fundamentals in Nuclear Physics," *Springer Publishing*, 2005.

73. K. S. Krane, "Introductory Nuclear Physics," *John Wiley & Sons Publishing*, 1988.

74. B. N. Taylor, "Molar mass and related quantities in the New SI," *Metrologia*, 24 February 2009. [Online]. Available: https://tsapps.nist.gov/publication/get_pdf.cfm?pub_id=901156

75. R. Kobes and G. Kunstatter, "The Strong Nuclear Force and Binding Energy," *University of Winnipeg - Physics 1501 Modern Technology*, September 1999. [Online]. Available: https://theory.uwinnipeg.ca/mod_tech/node178.html

76. E. E. Lewis, "Fundamentals of Nuclear Reactor Physics," *Academic Press*, 1 February 2008.

77. R. Nave, "The Most Tightly Bound Nuclei," *HyperPhysics*, 2019. [Online]. Available: http://hyperphysics.phy-astr.gsu.edu/hbase/NucEne/nucbin2.html#c1

78. H. M. Kristensen, "The Basics of Nuclear Weapons: Physics, Fuel Cycles, Effects and Arsenals," *Federation of American Scientists*, 8 February 2016. [Online]. Available: https://fas.org/wp-content/uploads/2014/05/Brief2016_CNP-MIIS_.pdf

79. "Fissile material," *United States Nuclear Regulatory Commission*, 21 March 2019. [Online]. Available: https://www.nrc.gov/reading-rm/basic-ref/glossary/fissile-material.html

80. U.S. Department of Energy, "Nuclear Physics and Reactor Theory," *DOE Fundamentals Handbook, Volume 1 of 2*, January 1993. [Online]. Available: https://www.standards.doe.gov/standards-documents/1000/1019-bhdbk-1993-v1/@@images/file

81. J. Watterson, "Elastic scattering," *CERN, the European Organization for Nuclear Research*, 2007. [Online]. Available: https://indico.cern.ch/event/145296/contributions/1381141/attachments/136909/194249/lecture26.pdf

82. B. El-Kareh, "Fundamentals of Semiconductor Processing Technologies," *Kluwer Academic Publishers*, 1995. [Online]. Available: http://www.iue.tuwien.ac.at/phd/filipovic/node26.html

83. E. W. Weisstein, "Circle-Line Intersection," *MathWorld, A Wolfram Web Resource*, 2019. [Online]. Available: http://mathworld.wolfram.com/Circle-LineIntersection.html

84. "Unclassified Systems: Centennial," *Department of Defense High Performance Computing*, 20 November 2019. [Online]. Available: https://centers.hpc.mil/systems/unclassified.html#Centennial

85. J. Shultis and R. E. Faw, "An MCNP Primer," *Kansas State University*, 2011.

86. P. Bedrossian, "Neutrons and Granite: Transport and Activation," *Lawrence Livermore National Laboratory*, April 2004.

87. C. J. Stimpson, C. D. Ernst, P. Knupp, P. P. Pebay, and D. Thompson, "The Verdict Geometric Quality Library," *Sandia National Laboratories*, March 2007.

REPORT DOCUMENTATION PAGE

Form Approved
OMB No. 0704–0188

1. REPORT DATE *(DD–MM–YYYY)*	2. REPORT TYPE	3. DATES COVERED *(From — To)*
26–03–2020	Master's Thesis	October 2018 - March 2020

4. TITLE AND SUBTITLE

Neutron Energy Effects on Asteroid Deflection

5a. CONTRACT NUMBER

5b. GRANT NUMBER

5c. PROGRAM ELEMENT NUMBER

6. AUTHOR(S)

Horan IV, Lansing S., Civilian

5d. PROJECT NUMBER

5e. TASK NUMBER

5f. WORK UNIT NUMBER

7. PERFORMING ORGANIZATION NAME(S) AND ADDRESS(ES)

Air Force Institute of Technology
Graduate School of Engineering and Management (AFIT/EN)
2950 Hobson Way
WPAFB OH 45433-7765

8. PERFORMING ORGANIZATION REPORT NUMBER

AFIT-ENP-MS-20-M-101

9. SPONSORING / MONITORING AGENCY NAME(S) AND ADDRESS(ES)

National Nuclear Security Administration
1000 Independence Ave SW
Washington, DC 20585
NNSA NA-115
POC: Lt Col Whit Dailey, PhD — Program Manager, Nuclear Survivability
      Whitman.Dailey@nnsa.doe.gov / (202) 992-4385

10. SPONSOR/MONITOR'S ACRONYM(S)

NNSA

11. SPONSOR/MONITOR'S REPORT NUMBER(S)

12. DISTRIBUTION / AVAILABILITY STATEMENT

Distribution Statement A. Approved for public release; Distribution Unlimited.

13. SUPPLEMENTARY NOTES

This material is declared work of the U.S. Government and is not subject to copyright protection in the United States.

14. ABSTRACT

In the future, a hazardous asteroid will find itself on a collision course with Earth. It is an inevitability; the question is not if, but when. For asteroids of moderate size or larger, a nuclear device is one of humanity's only technologies capable of mitigating this threat via deflection on a timescale of less than a decade. This work examined how changing the output neutron energy from a nuclear device detonation affects asteroid deflection. The notional asteroid target was 300 meters in diameter and composed of silicon dioxide at 1.855 g/cm^3.

To calculate the energy deposition in the asteroid that results from a neutron source, the Monte Carlo radiation-transport code, MCNP6.2, was applied. MCNP6.2 simulations were performed for neutrons of various energies radiating towards the asteroid surface. The neutron energy was found to have an impact in terms of 1) the spatial distribution of energy deposition, and 2) the energy coupling efficiency.

To model the mechanical response of the asteroid due to a spatially-varying energy deposition, the hydrodynamics code, ALE3D, was employed. The energy deposition outputs from MCNP6.2 served as inputs into the model representation of the asteroid in ALE3D. The momentum impulse imparted onto the asteroid body due to rapidly-evolving melted and/or vaporized blow-off ejecta was quantified.

From this, the asteroid velocity change, or δV, was determined for two different neutron yields (50 kt and 1 Mt) and for two different source neutron energies (14.1 MeV from fusion and 1 MeV from fission). Underexplored in literature, the distribution of deposited energy and the energy coupling were both found to affect the asteroid deflection. The magnitude of energy deposition, as determined by the neutron energy and the coupling, generally appears to be the more significant factor.

15. SUBJECT TERMS

Neutron, Asteroid, Nuclear Device, Nuclear Detonation, Nuclear Explosive, Nuclear Radiation, Stand-off, Asteroid Deflection, Asteroid Mitigation, Energy Deposition, Material Response, Monte Carlo, MCNP, MCNP6.2, Hydrodynamic, ALE3D, Energy Deposition Profile, Energy Coupling Efficiency, Asteroid Velocity Change, Planetary Defense, Blow-off

16. SECURITY CLASSIFICATION OF:			17. LIMITATION OF ABSTRACT	18. NUMBER OF PAGES	19a. NAME OF RESPONSIBLE PERSON
a. REPORT	b. ABSTRACT	c. THIS PAGE			Holland, Darren E., AFIT/ENP
U	U	U	UU	263	19b. TELEPHONE NUMBER *(include area code)* (937) 255-6565 x4697; Darren.Holland@afit.edu

Standard Form 298 (Rev. 8–98)
Prescribed by ANSI Std. Z39.18